POLITECNICO
MILANO 1863

Department of Chemistry, Materials and Chemical Engineering “G. Natta”

Doctoral Program in Materials Engineering and Nanotechnology

Pulsed anodizing treatments to increase the corrosion resistance of CP titanium in acidic environment

Doctoral dissertation of:

Luca Casanova

Supervisor:

Professor Marco Ormellese

Tutor:

Professor MariaPia Pedeferri

Chair of PhD program:

Professor Chiara Bertarelli

PhD cycle: XXXIV

Alcune parole dedicate alle persone che hanno profondamente influenzato il completamento di questo percorso…

Un ringraziamento speciale va alla mia amata **Sofia** per la scelta di fidanzarsi con un ingegnere nonchè per aver sopportato le assenze dovute alla passione dedicata al presente progetto di ricerca.

Alla mia **famiglia** ed i miei **amici** per avermi aiutato a diventare quello che sono oggi, ve ne sarò sempre grato.

Ai fantastici **colleghi** che hanno contribuito a rendere questa esperienza ancora più interessante.

Al **prof. Ormellese** per i consigli ed il sostegno ricevuto.

Contents

Abstract

Titanium and its alloys offer a great opportunity and reliability when applied in those industrial applications where the contact with an aggressive solution, or the occurrence of too serious consequences in case failure, limit the use of other common structural materials like iron or aluminum. For those reasons common fields of Ti implementation, listed in order of market demand, are: aerospace, chemical, nuclear, and naval industry. In all cases, the contact with acidic environments can severely affect the protective properties of the thin oxide layer that naturally grows on the metal. This is particularly true when dealing with sulfuric acid often present, for example, in the stratosphere where airliners fly or during metal pickling and synthesis of several chemicals like fertilizers. Followed from those observations, electrochemical surface treatment, like plasma electrolytic oxidation (PEO), offers a great deal to improve surface properties upon the growth of a thick (even several microns) and hard conversion coating.

The aim of this research is to optimize PEO surface treatments for titanium grade 2 tested for corrosion resistance in a solution of hot concentrated sulfuric acid (typically 10 %v/v at 60 °C, a common environment adopted in metal pickling applications). In the first part of the thesis, the role of the main technological parameters, like frequency and amount of cathodic polarization, was investigated according to a detailed characterization made possible upon the use of transmission electron microscopy (TEM). This allowed to probe the material structure, at the scale of the nanometers, according to the use of electron energy loss spectroscopy (EELS). Detailed structural maps were constructed improving knowledge about the barrier layer, i.e., the morphological region of PEO oxides directly in contact with the metal and responsible for the corrosion resistance, and the porous region, i.e., the oxide portion directly in contact with the external environment. It was verified that upon the use of pulsed PEO with hybrid duty cycles, repeated at high frequency (1000 Hz), it was possible to limit the amount of oxygen vacancies and to promote the formation of the most thermodynamically stable TiO_2 polymorph, i.e., rutile.

The latter verifications were found to be fundamental in characterizing the corrosion response of the coatings, particularly in acidic environments, where the presence of electronic defects can favour protons reduction and consequent atomic hydrogen ingress inside the oxide layer. The corrosion mechanism was investigated through the use of electrochemical impedance spectroscopy (EIS) allowing to extract proton diffusivities of oxides produced according to different PEO conditions. Accordingly, a clear correlation between technological parameters, synthesized materials, and corrosion response was established.

Chapter 1 Anodizing treatments on titanium

Titanium is a special transition metal element whose high popularity, in many industrial fields, comes from the tendency to preserve its integrity thanks to the formation of a highly stable, compact, and adherent oxide layer over its surface. The present peculiarity makes Ti a desirable material for applications requiring high stability and corrosion resistance, while making its production and workability a rather expensive and sometimes prohibitive choice. Discovered by Reverend William Gregor in 1791 in England (Manaccan valley, Cornwall), it owes its name from the German chemist, who found the new element in the form of rutile. The first attempts to purify the metallic form of the element should be adduced to William Justin Kroll, a Luxembourgish metallurgist who reduced $TiCl_4$ with Ca obtaining metallic Ti. Up to now the Kroll's process is still the major actor in the field of Ti production, however its high energy requirement and long extraction time poses a lower limit to the price of the metal which generally, for commercially pure grades (e.g. Ti grade 2) oscillates around 20 $/Kg. For this reason, Ti finds applications where budget is not a restriction or where its use is mandatory like in the biomedical field. After this brief general introduction *section 1.1* has the aim to collect the main technological processes to extract and refine metallic Ti.

1.1 Production of metallic Ti

1.1.1 Extraction

Still nowadays Kroll's process is the most employed solution for metallic Ti extraction from its ores. The raw material is initially treated with chlorine and coke involving inevitable production of greenhouse gas according to **Equation 1**

$$TiO_2 + (x + y)C + 2Cl_2 \rightarrow TiCl_4 + xCO + yCO_2 \quad (1)$$

and the formation of $TiCl_4$ which is then reduced thanks to the addition of Mg (or even Na in the so-called Hunter process) at high temperature (~ 800-900 °C) according to **Equation 2**.

$$TiCl_4 + 2Mg \rightarrow Ti + 2MgCl_2 \quad (2)$$

Ti reduction is an exothermic process requiring the reaction to proceed for several days in a closed stainless-steel vessel and inert Ar atmosphere. After the reaction is almost completed cooling of titanium sponge and removal of unreacted products occurs. Economic and environmental constraints limit the application of extraction processes to ores containing more than ~ 90 % of TiO_2, thus imposing the utilization of rutile only. As the natural availability of the latter polymorph is decreasing

with time synthetic rutile can be produced from ilmenite ($FeTiO_3$) for example by leaching in sulfuric or hydrochloric acid [1].

After extraction, a porous titanium sponge containing a high level of contaminants is obtained requiring post-treatments, for refinement purpose, analyzed in *section 1.1.2*.

Alternative routes for metallic titanium extraction can be summarized as follows:

- *FFC Cambridge process:* based on electro de-oxygenation of TiO_2 in molten calcium chloride. In this process titanium dioxide pellets are inserted in an electrolytic cell as the cathode, with an electrolyte temperature generally held at 950 °C using a graphite electrode as the anode. Oxygen delivered from the ore then reacts with the anode producing CO/CO_2. The inventor claimed the process to be around 5 times faster and ~ 30 to 40 % cheaper than the Kroll's process [2].
- *OS process:* the Ono-Suzuki process [3] is a calcio thermic reduction of TiO_2. Calcium is dissolved in molten $CaCl_2$ and TiO_2 pellets immersed and reduced in the liquid. De-oxidized Ti metal agglomerates and deposits to form a granular sponge. The reaction by-product (CaO) is then decomposed electrochemically by reaction with a carbon anode and Fe cathode applying a cell potential of 3 V, leading to the formation of liquid Ca at the cathode, dissolved in $CaCl_2$, and carbon dioxide at the anode. As the electrolytic reaction, of CaO decomposition and TiO_2 reduction, occurs in the same reaction bath the energy consumption is claimed to be smaller than the Kroll's process.
- *Armstrong process:* it uses almost the same chemistry of the Hunter's process; however, the reactor scheme and the way reactants are supplied is totally different. In this process $TiCl_4$ is introduced in a continuous flow of Na melt in a tubular reactor resulting in rapid reduction of titanium in the form of powder separated from Na and NaCl according to washing, distillation, and filtration.
- *Electrochemical reduction of TiO_2:* at research level in India DMRL (Defense Metallurgical Research Laboratory) they tried to extract metallic Ti according to a cathodic treatment of titanium dioxide powder immersed in a molten $CaCl_2$ heated at 950-975 °C using a graphite anode with an applied DC voltage of 3-3.2 V. Quite recently Shi *et al.* [4] proposed the electrolytic reduction of titanium dioxide in a solution of $LiCl\text{-}Li_2O$ at 650 °C using a cathodic reduction potential of -0.3 V with respect to the Li/Li^+ redox couple. However, the author incurred in the formation of highly stable and reversible rection intermediates, like $LiTiO_2$, limiting the overall reduction efficiency.

1.1.2 Refinement

After production of the Ti sponge purification from the molten salts and other contaminants, generally entrapped in the porous Ti matrix, occurs. A common procedure is separation through vacuum arc remelting. A strong DC current of several kA is used to ignite an arc between Ti and a counter electrode leading to metal melting. During the process Ar is supplied in the chamber to avoid contamination and consequent oxidation while a compressive stress is applied to compact the material in the form of an ingot. The technology offers an easy control over the melting rate providing the opportunity to tune microstructure and porosity, but also the chance to eliminate harmful contaminants through evaporation, like: O, H and N. In this step several alloying elements could be added to obtain the desired composition depending on which several Ti grades can be defined and listed in the next section.

1.2 Titanium grades

ASTM (American Society for Standard and Materials) was the first to introduce a detailed classification of titanium and its alloys. The first four grades describe different compositions of commercially pure titanium with level of impurities, listed in **Table 1**, scaling with the grade.

Table 1: elemental composition of commercially pure titanium grades [5]

ASTM	O % (max)	Fe % (max)	C % (max)	N % (max)	H % (max)
Grade 1	0.18	0.20	0.10	0.03	0.015
Grade 2	0.25	0.30	0.10	0.03	0.015
Grade 3	0.35	0.30	0.10	0.05	0.015
Grade 4	0.40	0.40	0.10	0.03	0.015

The workhorse among all the Ti alloys, according to annual production, is for sure Ti grade 5, also called Ti-6V-4Al, offering higher mechanical properties than unalloyed Ti at the expense of a lower corrosion resistance provided by the addition of V and Al. Noteworthy is Ti grade 7, the outliers Ti grade in terms of corrosion resistance keeping comparable mechanical properites to commercially pure Ti grade 2. In fact, the alloy is almost equivalent to Ti grade 2 differing only by the addition of ~ 0.12-0.25 % of Pd responsible for boosting the metal's passivation. Other Ti alloy grades are listed below (impurity levels are not indicated):

- *Grade 5*: 6 %V + 4 %Al
- *Grade 6*: 5 %Al + 2.5 %Sn
- *Grade 8*: 8 %Al + 1 %V + 1 %Mo
- *Grade 9*: 3 %Al + 2.5 %V
- *Grade 10*: 11.5 %Mo + 6 %Zr + 4.5 %Sn
- *Grade 11*: similar to Ti Grade 1 but with 0.12 < %Pd < 0.25

- *Grade 12*: 0.2-0.4 %Mo + 0.6-0.9 %Ni
- *Grade 13, 14, 15*: 0.5 %Ni + 0.05 %Ru
- *Grade 17*: 0.04-0.08 %Pd
- *Grade 18*: 3% aluminium, 2.5% vanadium and 0.04 to 0.08% palladium. This grade is identical to Grade 9 in terms of mechanical characteristics. The added palladium gives it increased corrosion resistance.
- *Grade 19* contains 3% aluminium, 8% vanadium, 6% chromium, 4% zirconium, and 4%
- molybdenum.
- *Grade 20* contains 3% aluminium, 8% vanadium, 6% chromium, 4% zirconium, 4%
- molybdenum and 0.04% to 0.08% palladium.
- *Grade 21* contains 15% molybdenum, 3% aluminium, 2.7% niobium, and 0.25% silicon.
- *Grade 23* contains 6% aluminium, 4% vanadium, 0.13% (maximum) oxygen. Improved
- ductility and fracture toughness with some reduction in strength.
- *Grade 24* contains 6% aluminium, 4% vanadium and 0.04% to 0.08% palladium.
- *Grade 25* contains 6% aluminium, 4% vanadium and 0.3% to 0.8% nickel and 0.04% to 0.08%
- palladium.
- *Grades 26*, 26H, and 27 all contain 0.08 to 0.14% ruthenium.
- Grade 28 contains 3% aluminium, 2.5% vanadium and 0.08 to 0.14% ruthenium.
- *Grade 29* contains 6% aluminium, 4% vanadium and 0.08 to 0.14% ruthenium.
- *Grades 30* and *31* contain 0.3% cobalt and 0.05% palladium.
- *Grade 32* contains 5% aluminium, 1% tin, 1% zirconium, 1% vanadium, and 0.8%
- molybdenum.
- *Grades 33* and *34* contain 0.4% nickel, 0.015% palladium, 0.025% ruthenium, and 0.15%
- chromium.
- *Grade 35* contains 4.5% aluminium, 2% molybdenum, 1.6% vanadium, 0.5% iron, and 0.3%
- silicon.
- *Grade 36* contains 45% niobium.
- *Grade 37* contains 1.5% aluminium.
- *Grade 38* contains 4% aluminium, 2.5% vanadium, and 1.5% iron.

1.3 Oxide formation

In this chapter focus will be given to the natural tendency of titanium to form an oxide even in presence of a small amount of atmospheric oxygen or water vapor. This occurrence comes from the high reactivity of the metal thanks to the very cathodic redox potential of the couple Ti/Ti^{+2} ~ -1.63

V_{SHE} [6]. According to X-ray Photoelectron Spectroscopy (XPS) experiments, carried out at the end of the 90[s] [7,8], the structure of the native oxide film was characterized as formed by TiO_2 only. In fact, traces of sub-oxides like Ti_2O_3 and TiO were initially recognized as artefacts introduced by the sputtering procedure, (with Ar^+ or H^+ ion beam) used to ablate the material, necessary to obtain in depth characterization. Only after the development of in-situ oxidation tests, carried out inside the chamber of an XPS apparatus, the very first layers of titanium suboxide were detected [8–10] and attributed to a natural occurrence. This can be seen by looking at the Ti 2p spectrum, highlighted in **Figure 1** and clearly showing in b), where upon dosing with 6 L of oxygen fingerprints of TiO_2 (458.8 eV), Ti_2O_3 (457.5 eV), TiO (455.1 eV) and Ti (454.1 eV) manifested. However, beyond a certain dose of O_2 the oxide chemistry levelled towards almost all TiO_2 (spectrum e)), as the electrons of the first few suboxide layers, in contact with the metal and excited by the x-ray beam, were prevented to reach the detector by scattering events in the thick TiO_2 layer. On the other hand, as temperature was raised to 850 °C, in absence of O_2, spectrum f) shown features only related to metallic Ti and TiO, confirming the Ti^{2+}- bearing oxide as the first layer in touch with the metal.

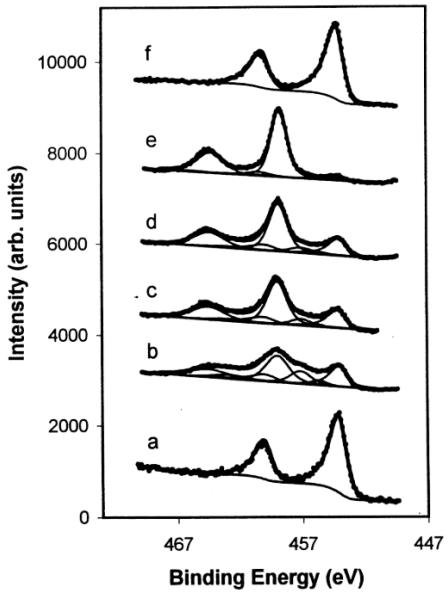

Figure 1: Ti 2p XPS spectra of **a** clean Ti sample and after successive O_2 dosing **b**, **c**, **d**, **e**. In spectrum **f** de-oxidation due to heating at 850 °C occurred [8–10].

This evidence allowed to conclude that the metal spontaneously covered with a first layer of titanium sub - oxide characterized by 2+ and 3+ cation oxidation states, i.e., TiO and Ti_2O_3. Then the structure of the upper portion of the oxide layer evolved towards TiO_2 according to the scheme highlighted in **Figure 2**.

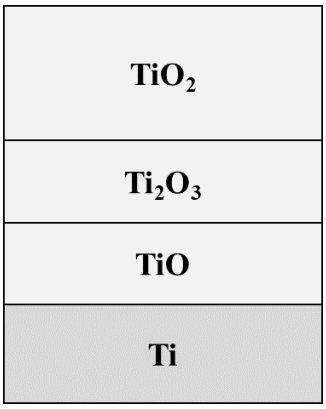

Figure 2: schematic diagram of the natural Ti oxide.

To further confirm the three-layers model, of the native oxide growing on Ti, Pouilleau *et al.* [11] collected XPS spectra at different take - off angles (θ), noticing that the TiO_2 component was higher for θ tending to 40 °, confirming its stronger accumulation in correspondence of the surface. The contrary held true in case of Ti_2O_3 and TiO where a total TiO_x thickness ~ 6.1 nm rose according to **Equation 3**

$$d_{TiO_x} = \lambda_{Ti}^{TiO_x} \sin(\theta) \ln\left(\frac{I_{Ti}^{\infty}}{I_{Ti}}\right) \quad (3)$$

with I_{Ti} the intensity of the Ti signal in presence of the oxide, I_{Ti}^{∞} the Ti signal of a sample sputtered with Ar^+ (supposed to be almost oxide free) and $\lambda_{Ti}^{TiO_x}$ the attenuation length of e^- in TiO_2.

Having clarified the oxide stoichiometry, developed over the Ti surface when exposed to an oxidizing environment, the next section will introduce the reader to the main technological processes used to increase the thickness of this natural oxide scale. Attention will be focused on the different ways by which energy can be supplied to the system to fulfill this task, i.e., chemical, thermal, and electrochemical energy.

1.3.1 Chemical oxidation of titanium

Chemical oxidation can be a valid alternative route when thermal and electrochemical oxidation appears to be prohibitive as occurs, for example, during in-situ oxide repairing. Chemical oxidation in fact, does not require any supply of external current, finding its driving force directly from the chemicals used and placed in touch with the workpiece. As a consequence, there is no need for using an electrochemical cell or a hoven, saving space and equipment costs. First attempts regard the use of hydrogen peroxide to allow the grow of thick and almost contaminations free titanium oxides. Nanci *et al.* [12,13] used for example a mixture of H_2SO_4/H_2O_2, claiming to decrease surface contamination with good reproducibility. According to XPS analysis they confirmed the gradient

composition of the oxide, previously highlighted by the studies of McCafferty *et al.* [7], also suggesting that upon chemical oxidation part or even almost all the sub-oxides are converted into TiO_2. Wang *et al.* [14] instead used a mixture of 8.8 M H_2O_2/0.1 M HCl at 80 °C finding an almost linear proportionality between treatment time and oxide thickness. Also nano structuring can be carried out using chemical oxidation: Wu *et al.* [15] prepared titanium dioxide nanorods by using a solution of 30 wt.% of H_2O_2 to oxidize the metal at 80 °C for 72 h. They also observed the opportunity to modulate the structure upon addition of selected ionic species favoring respectively:

- F^- and SO_4^{-2} → anatase formation
- Cl^- → rutile stabilization

Literature results, collected up to now, do not deal with chemical oxidation for corrosion resistance enhancement but rather are focused on surface functionalization for biomedical application. Thanks to recent investigation carried out by Prando *et al.* [16,17] a solution of 10 M NaOH + 10 M H_2O_2 was optimized for Ti protection against 0.5 M ammonium bromide, a chemical found to induce strong localized attacks on Ti. The author verified an optimum performing the chemical treatment at 60 °C for 12 h. A mechanism of chemical oxidation in alkoxide and hydrogen peroxide was proposed according to **Equation 4** to **8**

$$M^{n+} + H_2O_2 \rightarrow M^{(n+1)+} + OH^{\cdot} + OH^- \quad (4)$$

$$M^{n+} + OH^{\cdot} \rightarrow M^{(n+1)+} + +OH^- \quad (5)$$

$$OH^{\cdot} + H_2O_2 \rightarrow H_2O + HO_2 \quad (6)$$

leading to the competing formation of TiO_2 and oxygen gas:

$$Ti + 2H_2O_2 \rightarrow TiO_2 + 2H_2O \quad (7)$$

$$2H_2O_2 \rightarrow 2H_2O + O_2 \uparrow \quad (8)$$

As opposed to Al, Zn, Sn, and other amphoteric elements, whose contact with OH^- determine the formation of soluble metal hydroxides, Ti readily passivates with hydroxide ions forming a thick and protective oxide layer.

Also Liu *et al.* [18] studied chemical oxidation of Ti for corrosion resistance purpose. They found a beneficial effect in using a solution of 2 M H_2O_2 with the addition of 0.1 M HCl. Presence of chlorides was found to be particularly beneficial in enhancing the electrochemical response in de-aerated sulfuric acid as the presence of the halogen, in such a small quantity, was found to promote oxide thickness.

1.3.2 Thermal oxidation of titanium

Thermal oxidation is a widely adopted alternative to produce titanium oxide generally characterized by a mixture of anatase and rutile crystal structures. The technique is relatively simple, requiring only the introduction of the sample in a hoven in oxygen containing atmosphere. In this way, playing with final temperature allows to tune morphology and relative amount of both TiO_2 polymorphs. The morphology of Ti oxides grown by this technology is generally porous, with thicknesses even reaching 10 - 20 µm. Oxidation kinetics is very fast in the first minutes of the reaction, driven by the initially high driving force dependent proportional to the high temperature gradient. Then, as a steady state is reached, final thickness establishes proportionally to the temperature adopted, a trend generally well approximated by a parabola. Saturation is a consequence of the too high energy required for diffusion of oxygen ions and metal cations to occur as the oxide thickness overcomes a critical value. To further boost the oxidation kinetics T and oxygen partial pressure should be increased, favoring a higher titanium activity in correspondence of the oxide surface and faster oxygen ions diffusion. According to Lin *et al.* [19] the oxidation process can be divided into five main steps: *1* initial absorption of oxygen, *2* oxygen diffusion, *3* formation of a thin oxide, *4* oxide growth, *5* formation of a thick oxide layer. Aniołek *et al.* [20] grown a thermal oxide at 600, 700, and 800 °C using different treatment times and obtained, upon XRD analysis, the formation of an upper layer of rutile and an oxygen solid solution in correspondence of the metallic substrate with formula Ti_3O. A similar result was reached by several authors [21–24] finding a titanium dioxide top layer and an oxygen diffusion layer beneath it even ~ 10 µm thick [25].

Structural aspects

Anatase is the metastable TiO_2 polymorph generally formed at lower temperatures with respect to other structures like rutile. The reason behind this evidence can be twice:

- *From a structural point of view*: anatase has a less constrained geometry thanks to a larger lattice compared to rutile (overall rutile volume decrease ~ 8 % [26] due to contraction along the c-axis). This can give an easier way to TiO_6 octahedra to arrange in space making easier its stabilization.
- *Thermodynamic perspective*: even if rutile is more stable (lower Gibbs free energy with respect to anatase [27]) anatase surface free energy is lower [28,29], thus favoring crystallization at lower T.

Apart from thermodynamics, the anatase to rutile transformation is highly dependent on a multitude of factors influencing the reaction kinetics. This causes the transformation to not follow a rigorous transition T but rather to span over a wide thermal window between 400 to 1200 °C [30,31] depending on *raw material*, *synthesis method*, and *experimental procedure* used to evaluate the transition T.

Furthermore, as the anatase to rutile transition is reconstructive in nature (involving breaking and reformation of bonds) it does not occur instantly but rather it takes several time to complete, thus enlarging the number of possible contributions affecting the final structure. Some of them are related to morphological features, like grain size and particle aspect ratio, but also to processing conditions like heating rate, volume, nature of the sample container, and presence of impurities which can act as nucleation centers. Among the technological factors affecting the transition, Diamanti *et al.* [32], working on Ti anodization, reported anatase and rutile formation temperatures as dependent on the type of pretreatment undergone. For example, an oxide produced at higher voltage and then successively thermally treated demonstrated an anatase formation temperature decreased from 500 to 400 °C attributing the effect to morphological modifications induced in the oxide layer upon the use of higher forming voltage. *Crystalline defects* in the form of oxygen vacancies or *element inclusions* strongly affect the phase transition. Oxygen vacancies in particular, were found to favor rutile stabilization [33,34] while impurities can exert a profound influence on the kinetics of anatase to rutile transformation. Substitutional elements, for example, can speed up the transition if the impurity favors oxygen vacancy formation, while in case of interstitials the effect is a little bit more complex and dependent on quantities like size, valence, and amount. In any case, if the solubility limit of the dopant is overcome rutile formation is enhanced according to heterogeneous nucleation. According to previous information a classification on the effect of the addition of different elements, based on their chemical nature, is given.

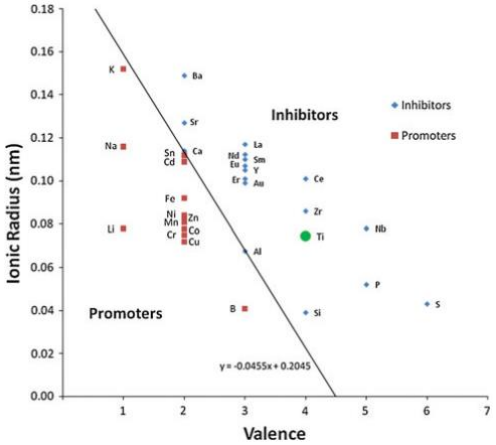

Figure 3: Valence/ionic radius plot of cations promoting or inhibiting anatase to rutile transformation. The plot was provided by Hanaor *et al.* [26].

- *Cationic dopants*: a rather simple discrimination on the influence of cation valence on promoting or even retarding the anatase to rutile transition can be visualized in **Figure 3** [35,36], and the concept summarized as follows:

- If cation valence < 4: oxygen vacancy formation is enhanced → rutile stabilization
- If cation valence > 4: oxygen vacancy annihilation → anatase stabilization
- *Carbon doping:* carbon is a well-known reducing agent for the TiO_2 system thus promoting, according to **Equation 9** to **11**, oxygen vacancies (affecting rutile stabilization), Ti suboxide, and titanium carbide formation:

$$TiO_2 + xC \rightarrow TiO_{2-x} + xCO \quad (9)$$

$$TiO_2 + C \rightarrow TiO + CO \quad (10)$$

$$TiO_2 + 2C \rightarrow TiC + CO_2 \quad (11)$$

Consequently, C is expected to promote rutile formation even if no reports at all are present in literature demonstrating such a result.

- *Anionic dopants*: generally, it is reasonable to assume that doping using anions results in oxygen vacancies filling. Again, the effect on the transformation can be rationalized in terms of size and charge effects.

- *Doping with nitrogen:* from the point of view of size, N is only 6 % larger than oxygen, so a destabilization induced mechanism of the sub-lattice leading to rutile formation is not expected. On the other hand, focusing on charge neutrality principle, the formation of three oxygen vacancies every time two N^{3-} are added (as Ti^{5+} is not allowed) should favor rutile formation. However, to the best of our knowledge no reports are present in literature showing the influence of N addition on rutile formation.
- *Doping with fluorine:* fluorine is considered to be an inhibitor of the rutile transformation [37]. F is around 6 % smaller than oxygen and if F^{1-} is considered, the smaller anionic charge requires the Ti^{4+} to Ti^{3+} reduction to occur. These observations result in lattice constraints, due to the higher Ti^{3+} ionic radii, decreasing the molecular mobility necessary for the transformation to occur.
- *Chlorine doping:* chlorine is considered a phase transition inhibitor [38]. The reason comes from its high size, inducing stearic hindrance, (~ 33 % larger than O) making the transition less probable.

Morphological aspects

Apart from structural modification, morphology is also claimed to depend profoundly on technological parameters. An example is reported by Muñoz-Mizuno *et al.* [39] applying thermal oxidation over previously synthetized titanium dioxide nanotubes by electrochemical route. He found T to increase nanotubes diameter from 500 to 560 °C even if above 580 °C a densification effect, due to sintering and crystallization, occurred. This was confirmed also by other authors [40,41] founding the collapse of the nanotubular geometry, promoting the formation of nanopores, for T > 600 °C. Also roughness was found to increase with temperature [39,42], a strategy particularly beneficial to promote cellular adhesion. Chen *et al.* [43] thermally oxidized Ti between 750 - 950 °C looking for hardness and tribological properties optimization. They found thickness, hardness and tribological performances to scale with oxidation T with a maximum at 850 °C. After this threshold oxide delamination and other morphological defects appeared.

Bansal *et al.* [44] observed the formation of spherical particles with radius ~ 10 nm treating Ti in the range 200 - 300 °C. From 400 to 500 °C a rather compact and porous free morphology established while as T was raised beyond 600 °C grain growth prevailed with respect to nucleation, resulting in large clusters of titanium oxide (~ 800 - 1000 nm) and high porosity.

Kumar *et al.* [45] noticed no oxide spallation treating Ti at 650 °C for 48 h. Furthermore, the surface appeared to be relatively smooth up to 16 h, while beyond this value a considerable amount of surface roughness developed according to the nucleation of large grains. Thickness was also found to be highly dependent on treatment time, passing from 3.5 to 19 μm from 8 to 48 h of treatment.

Aniołek *et al.* [20] observed modifications if increasing T of 100 °C from 600 to 700 °C, where the higher T resulted in a finer morphology sign that agglomeration contributed to form a more compact oxide. Things are different if working at 800 °C where the higher driving force allowed grain growth resulting in a rougher morphology.

Corrosion behavior

As previously said, heating at high temperature induces rutile stabilization and sintering due to crystallization. Consequently, beneficial effects are expected for what concern the electrochemical response of the material towards harsh environments. This was confirmed by Muñoz-Mizuno *et al.* [39] finding an optimum for samples treated at 600-620 °C and tested in Ringer's solution. According to Wang *et al.* [46] a too high temperature (~ 800 °C) or a too long treatment time can cause oxide spallation resulting loss of metal protection and biological properties. For this reason, the author

suggests using a maximum T of ~ 450 °C adjusting the treatment time to 6 h, increasing thickness but also preserving a good oxide architecture.

Bansal *et al.* [44] studied thermal oxidation of Ti in the T range 200 - 900 °C optimizing process parameters for corrosion resistance in body fluid. He claimed to obtain best electrochemical performances by treating the metal at 500 °C according to the formation of an anatase – rutile - Ti_2O_3 mixture combined with pores closure.

Kumar *et al.* [45] investigated the effect of treatment time on the corrosion resistance in a Ringer's solution of CP - Ti treated at 650 °C. He found corrosion resistance, oxide thickness and hardness to scale with treatment time, obtaining good performances with 48 h heating.

Bloyce *et al.* [47] used thermal oxidation of CP - Ti to protect the metal from immersion in 10 % HCl at boiling T. He compared the treatment with palladium - treated thermal oxidation and plasma nitriding finding a beneficial effect in using thermal oxidation. Also Jamesh *et al.* [25] characterized thermal oxides, in acidic solution of nitric and HCl, finding important improvement with respect to bare Ti thanks to the formation of ~ 20 μm thick oxide offering a physical barrier towards proton diffusion.

Arslan *et al.* [21] thermally treated Ti for 8 h at 850 °C inducing higher roughness upon using different emery paper grades during pre-polishing. He noticed a decreased corrosion resistance upon roughness increase.

Bailey *et al.* [22,23] verified that T and treatment time increase the thickness of the oxygen diffusion layer inside the metal offered a further contribution in favoring metal protection against a solution of 0.9 % NaCl.

1.3.3 Electrochemical oxidation of titanium

Several processes can be grouped inside the heading of the present section depending mainly on one of the most important parameter in electrochemical oxidation, i.e., *voltage*. Based on that, a first classification can be proposed collecting several technologies allowing the formation of an oxide scale driven by an electrochemical potential applied between an anode (the workpiece) and a cathode:

- *Standard anodizing:* a well-known relatively simple process involving the raise of the cell potential below the spark voltage, i.e., the value in correspondence of which the electrolyte in contact with the positive electrode start to be ionized. In this condition of growth the coating is allowed to thicken according to a high field migration of oxygen anions, starting their path from

the oxide electrolyte region, combining with Ti metal cations coming from the substrate. A very different technique, exploiting higher voltages, will be covered in the next section.

- *Plasma electrolytic oxidation (PEO):* a relatively recent process involving the formation of plasma - chemical reactions in correspondence of the electrode surface. Here the potential is raised beyond the spark limit producing hard ceramic - like coatings with important oxide thickness increase and porous morphologies often requiring a sealing procedure [48].
- *Micro - arc oxidation (MAO):* several authors [49–52] sustain MAO and PEO to be two sides of the same coin while some others [53,54] consider MAO an extension of the PEO process manifesting when the voltage is so high that small sparks become substituted by destructive arcs with large size and long life - time. In the present dissertation the terms will be used interchangeably propending for the more common PEO terminology.
- *Soft spark PEO:* this recent variant of the PEO process refers, as the name suggests, to a modulation (softening) of the plasma activity during the oxidation process. This rather complex event generally manifests by a sudden decrease in voltage, light, and acoustic emission resulting in a more compact, thick, and high quality deposit.

1.3.4 Standard anodizing

Titanium anodizing was introduced for the first time by the British aerospace industry in 1923 and in the US leading to the formulation of two updated standards:

- *AMS 2487*: this norm specifies the properties of Ti oxides as well as the requirements for anodization carried out at pH < 12.4. These coatings are classified as abrasion resistant (type - 2).
- *AMS 2488*: this standard refers to anodization performed in a solution with pH > 13 producing thick and protective oxides mainly for type - 2 and type - 3 applications (type - 1 is less common).

Depending on application type - 1 (uncommon) is followed by those processes intended for the production of high - T coatings, type - 2 mainly for abrasion and corrosion resistance giving to the object a distinctive gray color, and type - 3 also called “color anodizing”, is specific for coatings used in the medical and dental field.

It is possible to say that generally standard anodizing allows the formation of compact mainly amorphous or at least semi - crystalline coatings. Process can be controlled galvanostatically or potentiostatically, the former finding wider industrial application as it allows control over the kinetics and overall process duration. In both cases the process requires a positive voltage applied to the metal in an electrochemical cell containing a counter electrode (generally an insoluble metal like activated Ti) and an electrolyte providing the required ionic conduction necessary to close the circuit. Common

electrolytic solutions, used for corrosion and wear applications, are acids (generally sulfuric or phosphoric), salts (like sodium sulfate, ammonium sulfate…) or bases like NaOH or KOH. The oxide growth appears mainly affected by the following parameters: – current density – final voltage – treatment duration – electrolyte composition – pH – T and concentration – solution stirring – surface finishing and chemical composition of the Ti electrode.

If the process is performed in potential - controlled regime (45 V in this example) current, *I*, monitoring can allow the process to be described by three main steps as in **Figure 4**.

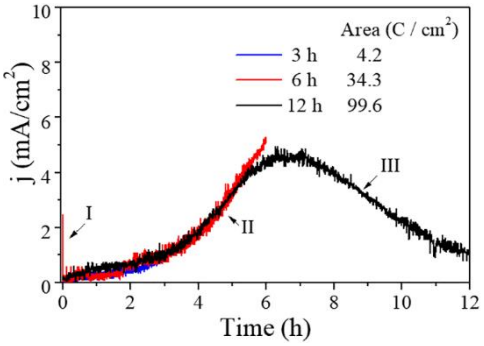

Figure 4: current trend during standard anodizing in potential-control regime.

Initially the trend presents a sudden drop due to the formation of the first few layers of oxide, stage I, then *I* increases (stage II) according to the reaction of Ti^{4+} with hydroxyls leading to the formation of a thick layer of TiO_2, acting as a barrier towards further ionic migration, causing inevitable *I* drop (stage III).

Structural aspects

A rigorous control over the oxide growth rate, attained by adjusting the current density and the final voltage, can favor the development of certain crystal structures. For example upon using higher current density it is possible to increase the oxide fraction converted to anatase, as it is possible to see in **Figure 5** [55] where according to higher values (in a range 100 ÷ 1080 $A \cdot m^{-2}$), in 0.5 M H_2SO_4, a progressively higher anatase intensity resulted.

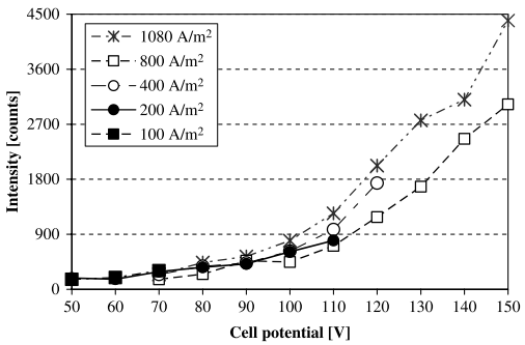

Figure 5: Anatase intensity peak Vs cell potential for different anodization current densities [55].

Also *V* allows to increase the amount of crystal phase present. Considering constant current density (1080 $A \cdot m^{-2}$) and previous electrolyte the following trend can be highlighted (**Figure 6**).

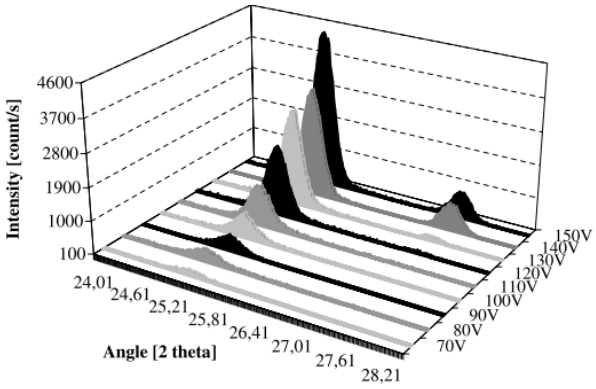

Figure 6: XRD plot collecting main anatase and rutile peaks at different cell voltages [55].

The diffractogram was magnified around the main anatase (~ 25.5 °) and rutile (~ 27.5 °) peaks. As the *V* is increased beyond the spark limit (*V* ~ 130 V in present conditions) the process shifts from standard anodizing to plasma electrolytic oxidation (PEO) involving the formation of a high quantity of anatase and rutile.

Morphological aspects

Morphology is mainly affected by the final voltage used during the conversion treatment. Here in **Figure 7** it is reported an example of Ti grade 1 anodizing in 1.2 M H_2SO_4 performed by Mizukoshi *et al.* [56]. The treatment was performed galvanostatically (8 $mA \cdot cm^{-2}$) and images collected during progressively increasing process time indicate the development of a porous surface as the cell *V* reached 210 V after 33 min (well beyond the spark voltage threshold). With the treatment progress pore diameter increases and eventually adjacent pores coalesce leading to an increase of the overall surface roughness.

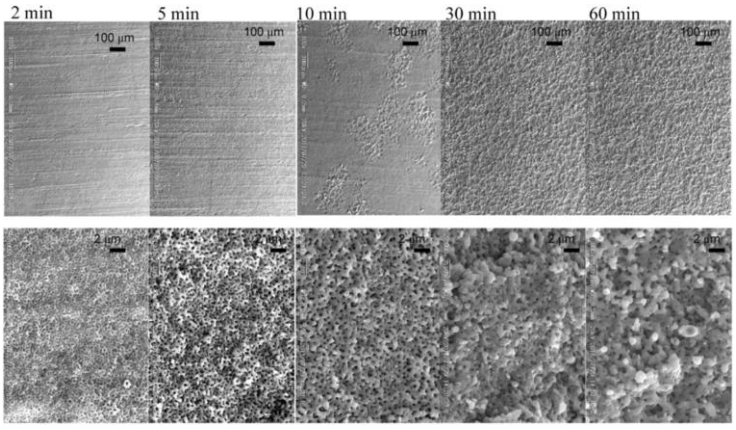

Figure 7: morphological variation induced during standard anodizing of Ti grade 1 [56].

Apart from porosity *V* highly affects surface coloring. This is due to an interference phenomenon between light and the oxide layer, leading to different colors depending on oxide thickness. In fact, the path travelled by the radiation through the coating plays a preponderant role in determining the color hue. This in turns will be dependent on which frequencies will be promoted by constructive interference. However, beyond a certain *V*, thickness increases too much and the interference phenomena causes frequencies to move outside the visible spectrum resulting in coatings with opaque gray tonality (this occurs e.g. at ~ 120 V in 0.5 M sulfuric acid).

Having established the correlation between coating thickness and surface optical properties a simple experiment can be used to calculate oxide thickness simply evaluating its reflectance according to a spectrophotometer apparatus. With the aim of doing that, knowledge of the refractive index *n* (found to be *V* dependent according to material density variations [57]) of the material and the wavelength λ giving construction interference (collected in correspondence of the maximum of the reflectance curve) it is possible to use **Equation 12** (Bragg's interference law) to evaluate the coating thickness d [58]:

$$n\lambda = 2d \sin\theta \tag{12}$$

where θ is the angle of incidence of light over the material.

Corrosion behavior

Even the application of a relatively low *V* can improve the corrosion response of Ti anodic coatings. This was observed for example by Karambakhsh *et al.* [57] working between 0 ÷ 80 V for oxides optimization in Ringer's solution. The following trend (**Figure 8**) was obtained:

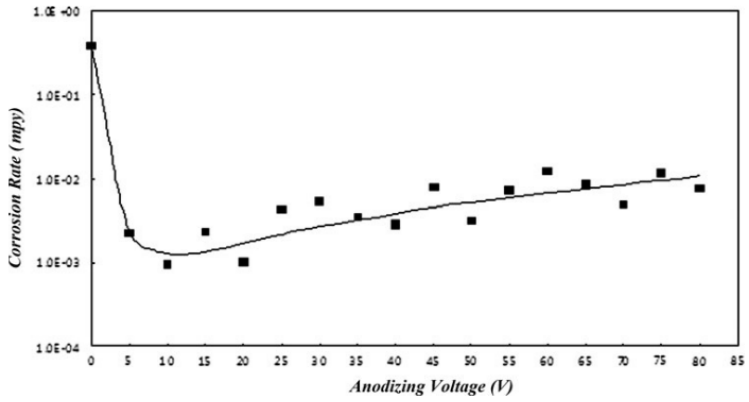

Figure 8: corrosion rate (mpy) dependence on anodization voltage [57].

All the treatments outperformed pristine Ti grade 2 even if the benefits, provided by the conversion coating, appeared to be non - monotonic with the cell potential. A maximum in corrosion resistance

in fact, was obtained for treatments performed at 10 V representing a good compromise between thickness and absence of surface porosity (both getting bigger with *V*).

Similar results were obtained by Saraswati *et al.* [59] working on Ti-6Al-4V. The author found that anodizing in 1 M KOH in a *V* interval 10 ÷ 30 permitted the formation of effective barrier coatings. In particular, despite the slight porosity increase experienced when increasing the *V*, the corrosion response seemed to be mainly affected by the thickness enhancement observed when increasing *V* and evaluated according to potentiodynamic plots of **Figure 9**.

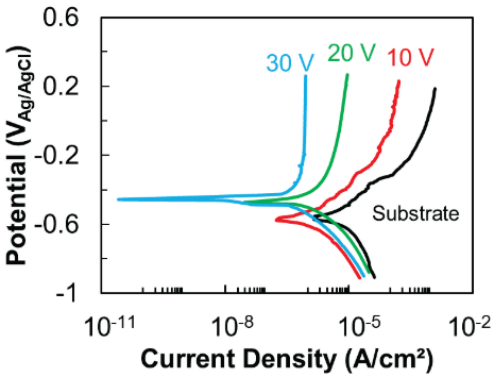

Figure 9: potentiodynamic plots for Ti-6Al-4V samples anodized at different voltages [59].

Higher anodization *V* caused the corrosion potential, E_{corr}, to move anodically and the corrosion current, i_{corr}, and the current in correspondence of the passive branch, i_{pass}, to decrease considerably.

Also Prando *et al.* [60] studied the corrosion response of Ti electrodes anodized below the spark voltage limit. The author found an optimum for Ti oxides, grown in 0.5 M H_2SO_4, using 40 V reached according to 20 $mA \cdot cm^{-2}$. Also increasing the voltage from 20 to 50 V seemed to be beneficial on Ti-6Al-4V anodized in H_3PO_4 [61] for corrosion resistance in artificial saliva, ringer's and simulated acid rain solution. Voltage dependence of the corrosion behavior of unalloyed Ti was also studied by Kahar *et al.* [62] testing the electrode in 3.5 % NaCl and 0.1 N H_2SO_4. The author found an optimum in corrosion resistance, in both electrolytes, for an oxide layer synthesized in 10 % KOH at 50 V.

According to this brief literature survey and the presence of a maximum of corrosion resistance for relatively low values of *V*, it appears evident the need to apply another strategy to increase the protectiveness of anodic coatings grown on Ti. For this reason the present dissertation, and the following section, will be devoted to the investigation of plasma electrolytic oxidation regime, a technique exploiting plasma chemical reactions in conjunction to high field ionic migration.

1.3.5 Plasma electrolytic oxidation (PEO)

Plasma electrolytic oxidation, always abbreviated as PEO, is a rather recent technique, with TRL ~ 4 ÷ 6 [63], actually employed in the research field but also present in some industrial companies like Keronite (UK), Tagnite (US), and Ceratronic in France. For this reason the process can be considered far from being completely understood, thus requiring further study particularly on the mechanism behind the oxide growth and plasma ignition. Despite that, the process offers the opportunity to considerably enlarge the voltage window, which practically remains limited only by the set-up adopted, permitting to enhance considerably the opportunity for functionalization. Despite the set-up used during the conversion treatment is similar to the one used during standard anodizing the mechanism of oxide synthesis is totally different:

- *Standard anodizing*: as previously said, the oxide grows according to a continuous migration of ions due to the high field produced inside the dielectric material.
- *PEO*: the metal is oxidized directly inside the plasma and the oxide forms as the plasma cools down. This causes a PEO oxide to be continuously destructed and reconstructed, as the metal used for oxide formation comes directly from substrate evaporation.

PEO was born initially as a surface treatment for Al and Mg where thanks to the insulating nature of their oxides, inducing the formation of strong electric field, the process well develops. Also Ti demonstrates to be PEO treatable, even if it is difficult to obtain coatings with thickness > 20 µm [64] as due to the semiconductive nature of TiO_2 lower electric fields, compared to previous metals, are expected to establish. Furthermore, as the enthalpy variation [65] of Ti to give TiO_2 is lower, and more similar to the energy gain of H oxidation (to give water), than the one of Al (to give Al_2O_3) and Mg (for MgO formation) water oxidation is expected to be more competitive thus decreasing the amount of oxygen used to react with Ti. For these reasons, PEO can be successfully applied generally only to so called “valve metals”, i.e., Al – Mg – Ti – Ta – Zr – Nb – Be. This terminology comes from the natural tendency of those materials to form a stable oxide, over their surface, acting as a rectifier, i.e., allowing e^- to flow through the oxide only when the electrode is made the cathode, as a result of the action of the metal - oxide junction.

PEO mechanism:

Several attempts were done to understand the physics behind the oxidation mechanism in a complex phenomenon like PEO involving: plasma, liquid, vapor, and solid phases. According to literature they can be divided into two main categories:

- Models describing the oxidation mechanism
- Models describing plasma ignition

Models describing the oxidation mechanism

Starting from the first category Klapkiv *et al.* [66] sustained Al oxidation to occur according to the model of the steam and gas vial formation. In this case in correspondence of the discharge channel, resulting from the failure of the first layers of oxide grown electrochemically, a gas vial with T ~ 2000 K established at the electrolyte side as in **Figure 10**. According to the author the discharge channel is responsible for substrate melting and subsequent evaporation, while in the gas vial H_2O dissociation with consequent formation of atomic O, H, OH radicals and other electrolytic species occurred. The author suggested that within the time of existence of the gas vial (supposed to be even longer than the one of the discharge channel) the EDL failed, allowing a considerable mass transport towards and inside the oxide layer. After condensation, the still present high T favored polymorphic transitions of the oxide.

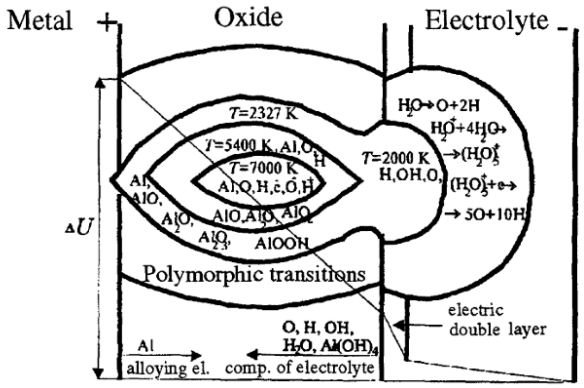

Figure 10: schematic drawing of the gas vial model [66].

Sundararajan *et al.* [67] accounted, on Al treated by PEO, for a discharge mechanism in continuous evolution, creating a connection for mass transfer between the top coating layer and the oxide - metal interfacial region. Deviations from thicknesses evaluated according to Faraday's law were attributed to a constant oxide volume deposited in the form of the common pancake like morphology, highlighted in **Figure 11 b** [68], reach in Al and typical of destructive discharges.

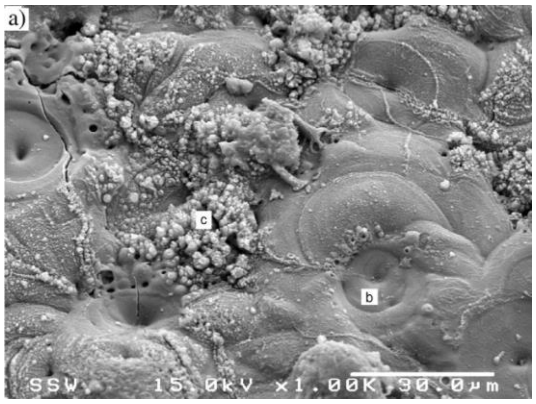

Figure 11: SEM surface overview of **b** the pancake like morphology and **c** the nodular region [68].

As the process develops discharges become less distributed in space while their power increases resulting in pancakes with larger holes. This strongly affected the microstructure where due to the continuous contact with the relatively cold electrolyte rapid quenching favored γ-Al_2O_3 to accumulate on the coating surface. On the other hand, the harder and more stable α-Al_2O_3 developed as the consequence of heat accumulation at the coating bottom.

Yerokhin *et al.* [69] gave an interpretation of the Al oxidation mechanism as composed by two concomitant reactions, i.e.: electrochemical surface oxidation and plasma chemical reaction. According to a computer simulation the author demonstrated the phases present in the coating as mainly dependent on relative amount of previously cited current contributions.

Matykina *et al.* [70] instead performed sequential PEO treatments over Al in alkaline solution containing ^{18}O isotope verifying the reaction site, leading to alumina formation, to be localized in the deeper coating region near the barrier layer. This allowed to conclude the process as mainly controlled by transport of O - species in the inner part of the coating, resulting in ions and radicals formation according to plasma interactions.

Models describing plasma ignition

Hussein *et al.* [71,72] were the first to successfully apply in - situ optical emission studies during PEO of Al. According to their evidences plasma can be ignited following three types of mechanisms, a result confirmed by also other independent authors [73]:

- *Type - A*: surface plasma, not involving the deeper coating regions, ignited in correspondence of small features sizes, like defects, leading to electric field amplification beyond water breakdown.
- *Type - B*: dielectric discharges involving all the coating thickness. They are generally thought to be ignited in correspondence of the metal substrate according to the electron avalanche theory. Their occurrence can be roughly predicted, based on material type, according to this simple

formula: $\frac{3}{2}E_g$ (where E_g indicates the band gap of the material) representing the energy necessary to accelerate a valence e^-, causing oxide breakdown, proportional to the material band gap.

- *Type - C*: plasma emission mainly occurring below the oxide surface in correspondence of holes filled with gas and electrolyte.

An interesting perspective was introduced by Dehnavi *et al.* [68] working on Al in an aqueous electrolyte of KOH containing sodium silicates. The author focused the analysis on the effect of duty cycle on discharge modulation. He found that the use of low duty (lower applied polarization) allowed to decrease the intensity of a single discharge even if the total number was dramatically increased (constant *I* experiments). As a result, the higher plasma spatial density allowed to limit the amount of foreign elements adsorbed on the surface, like Si, according to the forces exerted by the molten Al ions ejected from the substrate. Cheng *et al.* [74] instead widened the spark mechanisms previously proposed, hypothesizing the occurrence of other two additional forms of plasma, i.e.:

- *Type - D*: plasma ignited in large holes separating inner barrier and outer porous layer.
- *Type - E*: strong discharges, forming pancake morphology, confined to the outer portion of the oxide layer (considered less penetrant with respect to *type - B*).

Corrosion behavior

PEO coatings are generally classified as highly resistant to corrosive attacks thanks to the relatively high thickness and extreme adherence. Wang *et al.* [75], for example, enhanced the corrosion response of ZrO_2 PEO coatings by increasing the amount of cathodic polarization. This allowed to decrease the number and intensity of destructive *type - B* discharges, to increase thickness, and also to decrease the porosity according to sintering. Su *et al.* [76] studied the effect of increasing the working frequency (from 100 to 1000 Hz) and improved the polarization resistance of Mg coatings by two orders of magnitude justifying the result in terms of a less damaged structure obtained when using higher frequency. Concerning electrolyte composition Salami *et al.* [77] found that the use of 30 $g \cdot L^{-1}$ Na_2SiO_3 was the best choice to improve the corrosion resistance imparted by PEO oxides on Mg substrates. Asoh *et al.* [78] instead studied the effect of adding alcohols like ethylene glycol (EG), glycerol (GLY), and ethanol to a solution of sodium phosphate for PEO applied on Mg. He founded important benefits in terms of coating quality by using both EG and GLY like: higher thickness, compactness and decrease of roughness, all factors providing important corrosion resistance enhancement. Shokouhfar *et al.* [79] compared the PEO process, over Ti electrodes, using two different solutions: sodium phosphates and sodium silicate. The author found the former to favor corrosion resistance as smaller pores were left by the plasma activity. Hussein *et al.* [80] instead studied the addition of silicon oxalate

(So_x) and citrate (Sc_i) to an alkaline borate electrolyte during PEO treatment Al. He found the preferential adsorption of So_x and Sc_i as an important strategy to locally smooth the detrimental action of the plasma. In this way the corrosion resistance of the coating, tested in 3.5 % NaCl, was largely improved.

Providing the generally high corrosion resistance imparted by PEO coatings grown over Ti substrates the selection of a suitable aggressive environment will be the focus of the next section. Attention will be paid to strong reducing acids responsible, in general, to make the stability of the anodic layer a reason of concern.

Chapter 2 Selection of the aggressive environment

Keeping in mind one the main objective of the present thesis, i.e., the study of titanium oxide debonding, different acidic solutions were tested in order to assess the most aggressive environment for Ti grade 2 and the most corrosion resistance Ti grade 7 alloy, the latter containing ~ 0.2% of Pd responsible to boost the passivation of the metal making its application suitable for very aggressive acidic solutions. Generally speaking titanium has a good corrosion resistance owing to a thin, compact, and well adherent oxide layer extremely stable in a huge variety of environments. Despite that, even Ti oxide can lose its protectiveness when in contact with strong reducing acids, particularly in case of environments with low oxygen partial pressure. To overcome this weakness, it is possible to perform surface treatments or change the composition of the metal adding proper alloying elements. Following the latter procedure, two strategies can be addressed:

- nobility by alloying
- variation of anodic or cathodic overvoltage

A famous example, of modifications of the cathodic process responsible for Ti corrosion, i.e. hydrogen evolution reaction (HER), was introduced in the 1950s by Tomashov *et al.* [81] who demonstrated the role of metal additions like Pd or Pt to reduce HER overvoltage thus moving E_{corr} in the passivation region.

The acids analyzed in the present work (sulfuric, phosphoric, hydrochloric, sulfamic, and oxalic) are for sure the most employed in the manufacturing and chemical industry. In particular *sulfuric acid* production volume is so huge that it can be used as an indicator of the industrialization level of a country. It is mainly employed for the production of fertilizers like ammonium sulfate [82], for the synthesis of chemicals like hydrochloric and nitric acids, in the metallurgical field and during pickling operations. As a consequence high concentrations ~ 10 – 20 %v/v and T are required, making the bare metal particularly susceptible to uniform attacks. Some ions can be strategically used to decrease the aggressiveness of sulfuric acid like Fe^{3+}, Cu^{2+}, and Cl^-, favoring titanium passivation [83]. Apart from sulfuric, also *phosphoric* is very common in the chemical industry, for example in the production of phosphates or as a catalyst during the synthesis of ethanol [84]. It is also used in the electronic field for the processing of PCB and semiconductors [85] but also in the beverage industry as an acidulant in many soft drinks. It can also work pretty well as an etchant for the removal of mineral substances depositing over apparatus used for water treatments. Ti grade 2 (UNS R50400) generally guarantees a good protection to H_3PO_4 until 30 % concentration at T_{room} and in presence of oxygen [83,86].

HCl is a common mineral acid mainly derived from the reaction of chlorine with water. It is generally used for oil wells cleaning even if its use is sometimes limited by the high aggressiveness and the formation, upon reaction, of hazardous hydrogen gas. According to that the use of Ti grade 2 is only advisable for T < 75 °C provided the concentration remains << 10 %v/v. In case of higher temperatures/concentrations Ti grade 7 is strongly suggested, manifesting an appreciable stability up to 37.1 % v/v at 15 °C or 10 %v/v at 100 °C. Beyond these values Pt or Ta should be used. *Sulfamic acid* is an inorganic acid generally available in dry form and considered relatively strong in solution with water. Sometimes it substitutes HCl for metallic and ceramic cleaning operations favoring rust and lime scale removal without the drawbacks of HCl. Ti grade 2 shows relatively high stability up to 10 %v/v at 75 °C which can be considered as an upper limit above which the corrosion rate becomes unacceptable (~ 1 mm·year^{-1}) [87].

Oxalic acid is a strong organic acid mainly used in the pharmaceutical industry as a purifying agent. It is naturally present in human saliva, tooth tartar, and teeth with a concentration ranging from 0.09 mmol·L^{-1} for man to 0.17 mmol·L^{-1} for woman [88]. Titanium, which is one of the most employed material for dental prosthesis sustains oxalic acid up to 5 %v/v at 35 °C, while for concentration ~ 10 %v/v at 60 °C the corrosion rate becomes very high (~ 11.4 mm·year^{-1}) [83].

2.1 Materials and Methods

Having established the importance of the former chemicals, especially if considering the high probability for Ti to be in contact with them, immersion tests have been performed (ASTM G31 [89]) in acidic environment in a 1 L Pyrex balloon, a condition sufficient to guarantee a solution volume – specimen area ratio of 1 L·cm^{-2}.

Table 2: concentration and T of acids used in the present investigation.

Acid	Concentration (%v/v)	T (°C)
Sulfuric	10	50
	10	60
Phosphoric	30	60
	40	35
	50	35
	60	35
Hydrochloric	2	60
	40	35
	50	35
	60	35
Sulfamic	10	60
Oxalic	10	50
	10	60

Reflux condenser have been adopted to avoid evaporation thanks to the use of a cryostat/thermostat Julabo 200F for temperature control of the fluid circulating in the coil wound of the condenser. **Table 2** summarizes concentrations and temperatures used in the present assessment for Ti grade 2 in the acids studied. Tests and data on Ti grade 7 have been collected in the same condition and results reported and discussed only for weight - loss variations relevant for the resolution of our experimental apparatus. Temperatures and concentrations were selected according to literature data availability for direct comparison, economic, and safety reasons. Titanium coupons were washed in deionized water, sonically cleaned in ethanol for 5 min, and dried by compressed air. The metal was pickled in Kroll's solution (2 %v/v HF + 4 %v/v HNO_3) prior to immersion. This allowed to measure the initial weight (W_1) using a Mettler Toledo MS105 balance (resolution 10^{-5} g) after 5 minutes immersion in the testing solution. A procedure for corrosion product removal was adopted according to ASTM G1 [90] in a 20 $g \cdot L^{-1}$ of NaOH polarizing the sample cathodically with current density of 300 $A \cdot m^{-2}$. Prior to final weighting (W_2) samples were put in a vacuum desiccator for 24 h. Corrosion rates (CR) (expressed in $mm \cdot year^{-1}$) were evaluated according to **Equation 13**

$$CR = \frac{k(W_1 - W_2)}{A \cdot t \cdot \gamma} \quad (13)$$

where γ = material density (in $kg \cdot m^3$), A = exposed surface area (m^2), t = immersion time (h), and k = $8.76 \cdot 10^4$ is a constant used for unit conversion.

Planned intervals corrosion tests were performed considering three relevant time windows of immersion: 24 h (T_{24}), 48 h (T_{48}), and 72 h (T_{72}), plus further 24 h (sample "B") of immersion of a new sample in the solution previously used for 72 h (this sample has been extracted after 24 h). In this way it was possible to study: *1* the variation in metal corrodibility (from 24 to 72 h) *2* the variation of solution aggressivity (according to sample "B"). Previous criteria can be summarized in **Table 3** used to define unchanged, increased, or decreased solution corrosiveness (S) as well as the metal corrodibility (M).

Table 3: criteria defined for planned interval test analysis.

Acid	Criterion	Status
Solution corrosiveness (S)	$T_{24} = B$	Unchanged
	$B < T_{24}$	Decreased
	$B > T_{24}$	Increased
Metal corrodibility (M)	$T_{72} = T_{24}$	Unchanged
	$T_{72} > T_{24}$	Increased
	$T_{72} < T_{24}$	Decreased

An optical microscope, LEICA DL ML, was used to evaluate the corrosion morphology while roughness was investigated using laser profilometry collecting 500 points per mm of linear scan.

A Metrohm Autolab PGSTAT equipped with a FRA32M module for EIS was used for electrochemical measurements of a standard three - electrode cell with a saturated silver/silver chloride reference electrode ($SSC_{sat.}$) and an Amel Pt counter electrode. A salt bridge, filled with agar – agar and KCl, allowed to protect the reference electrode from the acidic solution. Electrochemical tests have been performed on both titanium grade 2 and grade 7 immersed in HCl, H_2SO_4 ,H_3PO_4, oxalic acid, and sulfamic acid at 0.5 $mol \cdot L^{-1}$ concentration. EIS tests were always performed at the corrosion potential (E_{corr}), after 1 h of stabilization, and using a sinusoidal signal of 10 mV_{rms} considering a frequency spectrum between 10 mHz and 100 kHz. Ten impedance points were acquired by the system for each decade of frequency and the corresponding spectra fitted according to the use of the software Nova 2.1. As the solution conductivity was generally high data were not corrected for ohmic drops.

The cathodic behavior was scanned with 10 $mV \cdot min^{-1}$ from +0.1 V/E_{corr} up to -1 V/E_{corr}. Origin software was used to extract Tafel parameters by a linear regression method. Tests was conducted following ASTM G5 [91] prescriptions considering a repetition of three.

2.2 Results

Table 4 collects CR of Ti grade 2 immersed in 10 %v/v *sulfuric acid* at 50 and 60 °C.

Table 4: results in terms of CR for Ti grade 2 immersed in H_2SO_4.

Acid	Conc. (%v/v)	T (°C)	Sample	CR ($mm \cdot year^{-1}$)	M	S
H_2SO_4	10	50	T_{24}	3.76	↑↑	↑↑
			T_{48}	4.50		
			T_{72}	5.20		
			B	6.20		
H_2SO_4	10	60	T_{24}	8.08	↑↑	↑↑
			T_{48}	11.17		
			T_{72}	14.16		
			B	14.40		

CR demonstrate strong dependence on T and immersion time. It will be shown H_2SO_4 to be the chemical promoting the highest CR values with respect to other acids.

Table 5: results in terms of CR for Ti grade 2 immersed in H_3PO_4.

Acid	Conc. (%v/v)	T (°C)	Sample	CR (mm·year^{-1})	M	S
H_3PO_4	30	60	T_{24}	2.59	=	=
			T_{48}	2.57		
			T_{72}	2.65		
			B	2.38		
H_3PO_4	40	35	T_{24}	0.71	=	↓
			T_{48}	0.47		
			T_{72}	0.43		
			B	0.39		
H_3PO_4	50	35	T_{24}	1.58	↑	↓↓
			T_{48}	0.10		
			T_{72}	0.33		
			B	0.29		
H_3PO_4	60	35	T_{24}	0.41	↓	↑
			T_{48}	0.69		
			T_{72}	0.52		
			B	0.65		

In fact, sulfates are well known to complex stronger to Ti^{4+} ions (with $Ti(OH)_3HSO_4$ [92], demonstrated by Beukenkamp *et al.* [93] to be the preponderant species up to 2 M concentration, responsible to inhibit re-oxidation) than other anions such as Cl^- and PO_4^{2-}. As CR of sample B is almost two times the one of sample T_{24} it is possible to say that solution aggressiveness largely increased with time. T was found as the main agent responsible for aggressivity of *phosphoric acid*, in fact, the CR obtained for H_3PO_4 30 %v/v at 60 °C was around one order of larger magnitude with respect to the one obtained using a lower T (35 °C) but larger content of acid (60 %v/v) (see **Table 5** above).

Table 6: results in terms of CR for Ti grade 2 immersed in HCl.

Acid	Conc. (%v/v)	T (°C)	Sample	CR (mm·year^{-1})	M	S
HCl	2	60	T_{24}	0.05	↑↑	↑↑
			T_{48}	0.07		
			T_{72}	1.13		
			B	1.76		
HCl	6	50	T_{24}	0.80	=	↑
			T_{48}	1.05		
			T_{72}	0.98		
			B	0.98		
HCl	10	60	T_{24}	3.97	↑↑	↑↑
			T_{48}	5.64		
			T_{72}	6.65		
			B	6.40		

Furthermore, an increase of $[H_3PO_4]$ at constant T did not produce appreciable increase of CR, perfectly correlating with the observed decrease of solution aggressivity S when using 40 %v/v at 35 °C.

On the other hand, even *hydrochloric acid* 2 %v/v at 60 °C raised the CR, averaged over 72 h of immersion, beyond 1 mm·year^{-1} (**Table 6**). Also in this case metal self - passivation and formation of protective corrosion products were not effective to preserve the metallic substrate, as a result the metal corrodibility (M) increased with immersion time.

The use of 10 %v/v and 60 °C induced the CR to rise up to 6.65 mm·year^{-1} over 72 h of test thereby making the use of Ti grade 2 a dangerous material selection. Also, in this case when T > 50 °C S increased with time.

Table 7: results in terms of CR for Ti grade 2 immersed in sulfamic acid.

Acid	Conc. (%v/v)	T (°C)	Sample	CR (mm·year^{-1})	M	S
Sulfamic	10	60	B	0.35	↑	↑↑
			T_{24}	0.34		
			T_{48}	0.47		
			T_{72}	1.92		

Due to the relatively high stability of commercially pure titanium in *sulfamic acid*, immersion tests were performed in a solution 10 %v/v at 60 °C. While M demonstrated only a slightly increase, S varied more than five times with the immersion time (**Table 7**). This evidence can find justification by monitoring the pH, evaluated at t = 0 h and t = 72 h, and corresponding to 3.8 and 2.0.

Even if Ti is generally not attacked by organic acids, *oxalic acid* was demonstrated to be more aggressive than HCl when high concentration and temperature are employed. CR was always > 1.5 mm·year^{-1}, saturating towards ~ 10 mm·year^{-1} at t = 72 h in 10 %v/v at 60 °C (**Table 8**). During immersion in this solution a strong color variation towards pale violet manifested [94,95] due to the formation of Ti^{3+} complex with the oxalate anion. However, the restoration of the original transparent color indicated that almost all the Ti^{3+} complexes were oxidized to Ti^{4+}. No color variation was encountered at all in case of solution T < 60 °C, corroborating the influence of T in favoring the stability of the complex hexaacquatitanium (III).

Table 8: results in terms of CR for Ti grade 2 immersed in oxalic acid.

Acid	Conc. (%v/v)	T (°C)	Sample	CR (mm·year^{-1})	M	S
Oxalic	10	50	T_{24}	1.89	↑	=
			T_{48}	1.83		
			T_{72}	2.09		
			B	1.74		
Oxalic	10	60	T_{24}	5.67	↑	↑
			T_{48}	8.45		
			T_{72}	9.75		
			B	6.46		

Thanks to previous results it was verified how the use of Ti grade 2 should be avoided when dealing with H_2SO_4 and oxalic acids in case of hot concentrated solutions (10 %v/v at 60 °C). According to that, Ti grade 7 was tested in these environments and results reported in **Table 9**.

Table 9: results in terms of CR for Ti grade 7 immersed in H_2SO_4 and oxalic acid.

Acid	Conc. (%v/v)	T (°C)	Sample	CR (mm·year^{-1})	M	S
H_2SO_4	10	60	T_{24}	0.54	↓	↑
			T_{48}	0.29		
			T_{72}	0.22		
			B	0.73		
Oxalic	10	60	T_{24}	0.12	↑	↑
			T_{48}	0.15		
			T_{72}	0.22		
			B	0.21		

The addition of Pd was found to be very effective in promoting the decrease of the CR of even 1 order of magnitude. M slightly decreased with time in presence of sulfuric acid while the opposite was found to occur for oxalic acid, in accordance with the color shift of the solution, indicating the formation of stable complexes.

Corrosion morphology, of Ti grade 2 immersed in all previous acidic solutions, considering experimental conditions 10 %v/v at 60 °C, was investigated by optical microscopy (see **Figure 12**) and average crater areas were evaluated using ImageJ software.

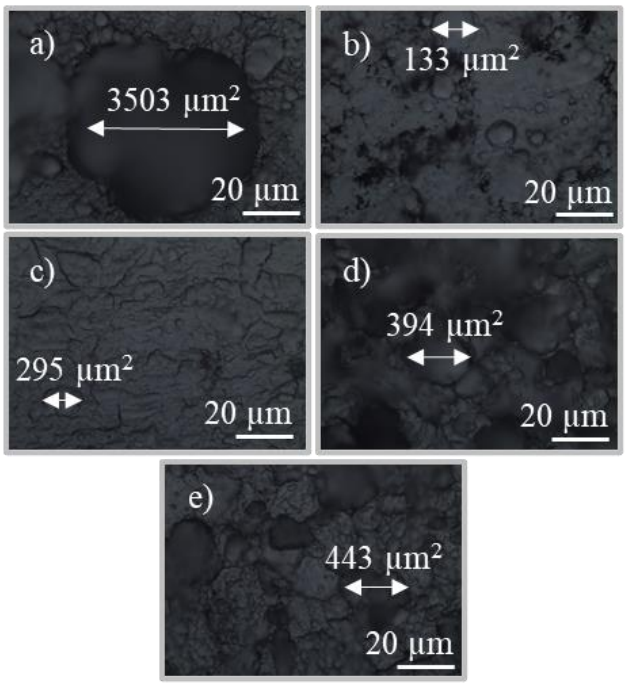

Figure 12: corrosion morphology of Ti grade 2 immersed in **a** HCl, **b** H_2SO_4, **c** H_3PO_4, **d** oxalic, and **e** sulfamic acid.

Greater craters were observed when dealing with HCl, evidencing the highest prominence of Cl^- to induce strong localized dissolution while the smaller depression regions were evidenced in tests conducted in sulfuric acid corroborating the uniformity of the attack. **Table 10** summarizes all the roughness parameters (R_a, R_{max}, R_q, R_z, and R_t) extracted according to laser profilometry performed (see **Figure 13**) on samples immersed for 24 and 72 h, in the most aggressive condition (10 %v/v at 60 °C), for all the acids.

Table 10: roughness parameters extracted according to laser profilometry performed over Ti grade 2 exposed in different acidic solutions.

Sample	HCl		H_2SO_4		H_3PO_4		Sulfamic		Oxalic	
	T_{24}	T_{72}	T_{24}	T_{72}	T_{24}	T_{72}	T_{24}	T_{72}	T_{24}	T_{72}
R_a (µm)	1.0	1.8	0.7	0.8	0.5	0.5	0.6	0.8	1.9	2.6
R_q (µm)	1.3	2.6	0.9	1.2	0.6	0.6	0.7	0.9	2.4	3.2
R_z (µm)	7.0	14.2	6.2	7.4	3.4	3.7	4.1	5.4	12.4	17.0
R_t (µm)	8.4	16.1	7.1	11.4	3.8	4.4	4.5	6.2	14.2	19.1
R_{max} (µm)	8.3	15.3	7.0	11.4	3.5	4.2	4.2	5.9	13.5	17.7
Area (µm^2)	283	3503	37	30	22	313	94	177	113	336
Depth (µm)	2	8	0.5	1.5	0.2	0.7	0.8	3.0	1.5	5.0

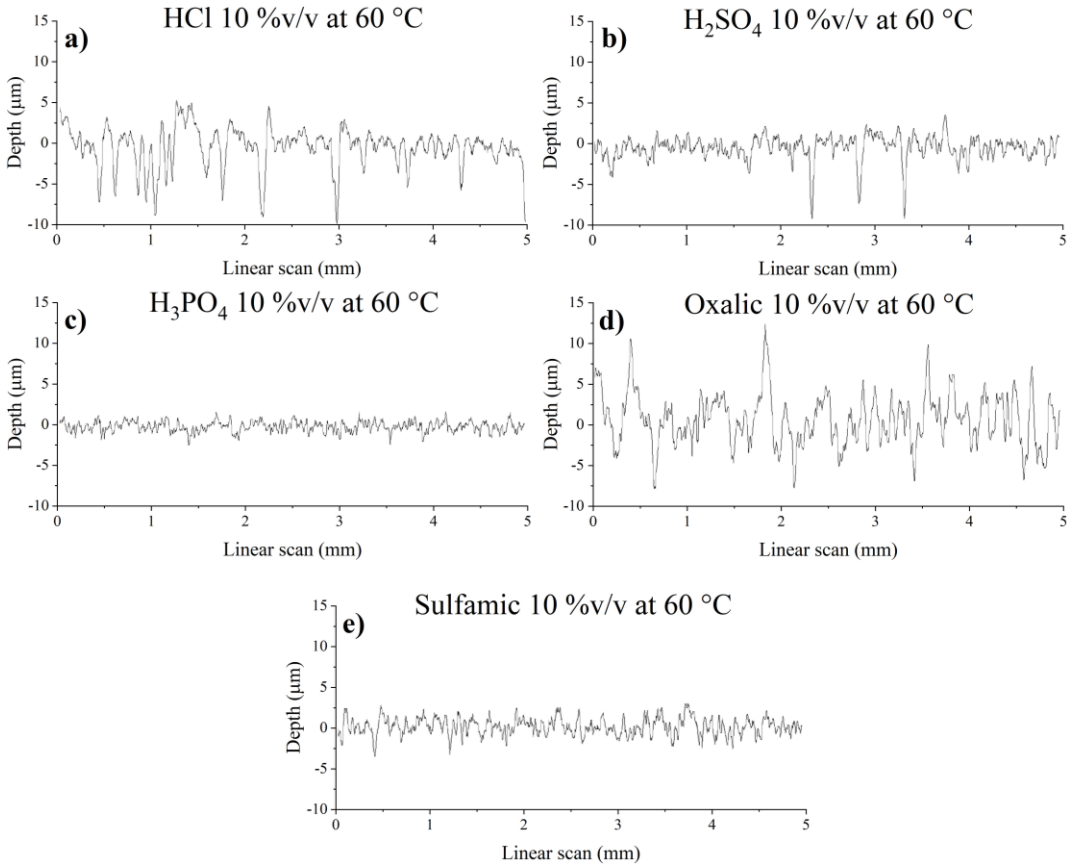

Figure 13: laser profilometry profiles of Ti grade 2 samples immersed in different acids.

Irrespectively of the solution used, an increase in surface inhomogeneity is always noticed by increasing $t_{exposure}$. Numbers confirm HCl to be the corrosion agent inducing deeper craters, especially after 72 h of immersion (sample T_{72}).

By looking at the **roughness profiles**, however, also oxalic acid imprinted a very irregular morphology (see also **Figure 13d**) denoting suitability for those Ti etching procedures with the aim of transferring to the metal a high degree of surface roughness (for example where high adhesion is required like before application of a top coating). On the other hand, H_2SO_4, which favored the highest CR, determined a more uniform attack and no appreciable morphological variations upon different $t_{exposure}$. Profiles related to phosphoric and sulfamic acids confirmed their lower aggressivity towards Ti grade 2. In **Figure 14 cathodic polarization** tests, performed on Ti grade 2 and 7, are shown.

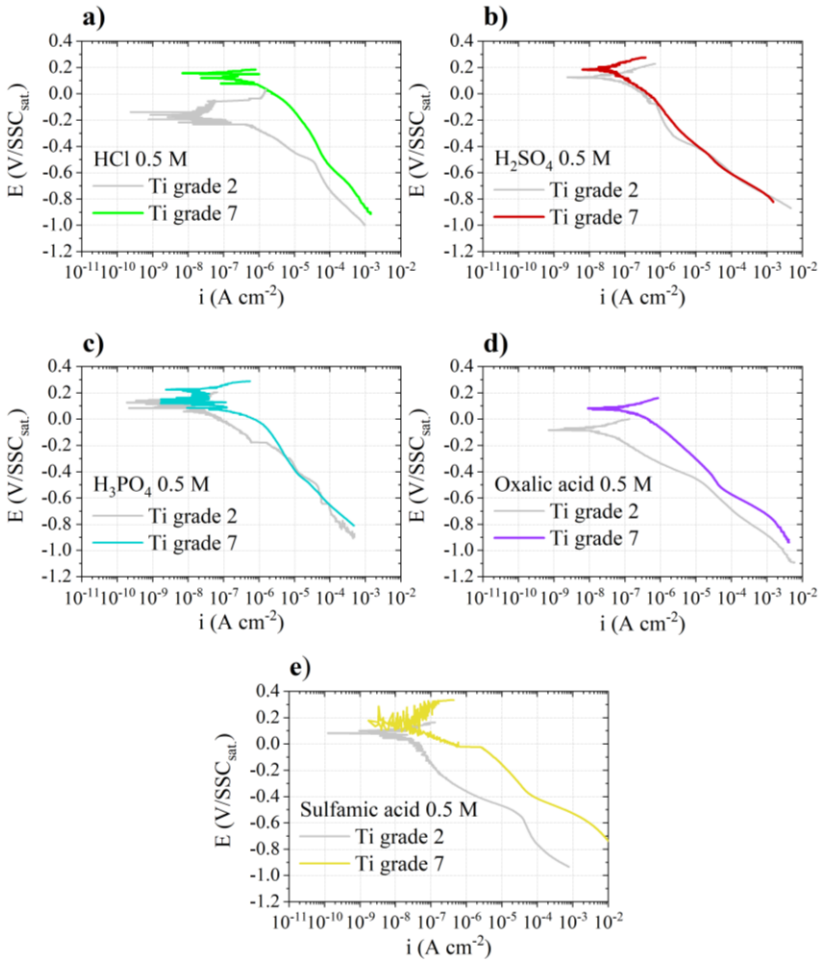

Figure 14: cathodic polarization of Ti grade 2 and 7 samples performed in different acidic solutions.

Regardless the type of acid utilized Ti grade 7 manifested E_{corr} more noble than Ti grade 2 confirming the beneficial action of Pd in moving the reaction potential in the passivation region [96]. The higher current density, generally seen in the present experimental potential window for Ti grade 7, acts as a

demonstration of the catalyzing ability of Pd towards HER. E_{corr} and Tafel slopes, evaluated in correspondence of the low and high overvoltage regions, have been extracted and reported in **Table 11**. Oxygen reduction reaction (ORR) is the only cathodic reaction expected to occur for both electrodes when the potential is only moderately shifted from E_{corr}. However, differences in terms of reduction kinetics (↓ b_c) are manifested for the alloy as the presence of Pd can further enhance even ORR [96,97].

Ti grade 2 shown always lower catalytic properties towards ORR, apart when immersed in HCl where b_c ~ 58 mV·decade^{-1} while in sulfamic acid both metals behaved almost the same in the low overvoltage region.

Table 11: electrochemical parameters of Ti grade 2 and 7 extracted according to cathodic polarization performed in different acidic solutions.

Acid (0.5 M)	Material	E_{corr} (V/$SSC_{sat.}$)	b_c^{low} (mV·decade^{-1})	b_c^{high} (mV·decade^{-1})
HCl	Grade 2	-0.138	58	152
	Grade 7	0.134	20	194
H_2SO_4	Grade 2	0.126	170	136
	Grade 7	0.185	150	239
H_3PO_4	Grade 2	0.125	107	163
	Grade 7	0.152	61	347
Sulfamic	Grade 2	-0.082	86	149
	Grade 7	0.081	85	269
Oxalic	Grade 2	0.081	101	169
	Grade 7	0.179	88	286

Using the equation linking Tafel parameter and transfer coefficient (which can be found elsewhere [96]) and considering higher coverage in the high overvoltage zone ($\alpha = 0.5$), a b_c ~ 118 mV·decade^{-1} was extracted, demonstrating electrochemical desorption to be the rate - determining step for HER on titanium grade 2 at 25 °C in all the acids tested. On the other hand, substantially higher b_c were observed on Ti grade 7 in the high overvoltage region, with b_c ~ 347 mV·decade^{-1} for H_3PO_4.

EIS were performed at E_{corr} for both Ti grade 2 and 7 considering T_{room} and 0.5 M acid concentration. Results are reported in **Figure 15** in the form of Nyquist and Bode representations. Immersion test results were confirmed by looking at EIS finding sulfuric, oxalic, and hydrochloric acids to promote the stronger attacks. Passivity was evidenced by observation of only one broad time constant (- phase angles approaching - 90 °) compatibly with the low acidic concentration (0.5 mol·L^{-1}) [98]. Electrochemical information was extracted according to the use of physically meaningful equivalent circuits. As the system denoted the presence of only one broad time constant, a single R – CPE parallel was used, with the constant phase element (CPE) accounting for surface inhomogeneities [99]. Diffusion phenomena, once present, occurring in the solid - liquid interface (like the electrical double layer) were modelled with a finite space Warburg element (T) [100] as in **Figure 16b**.

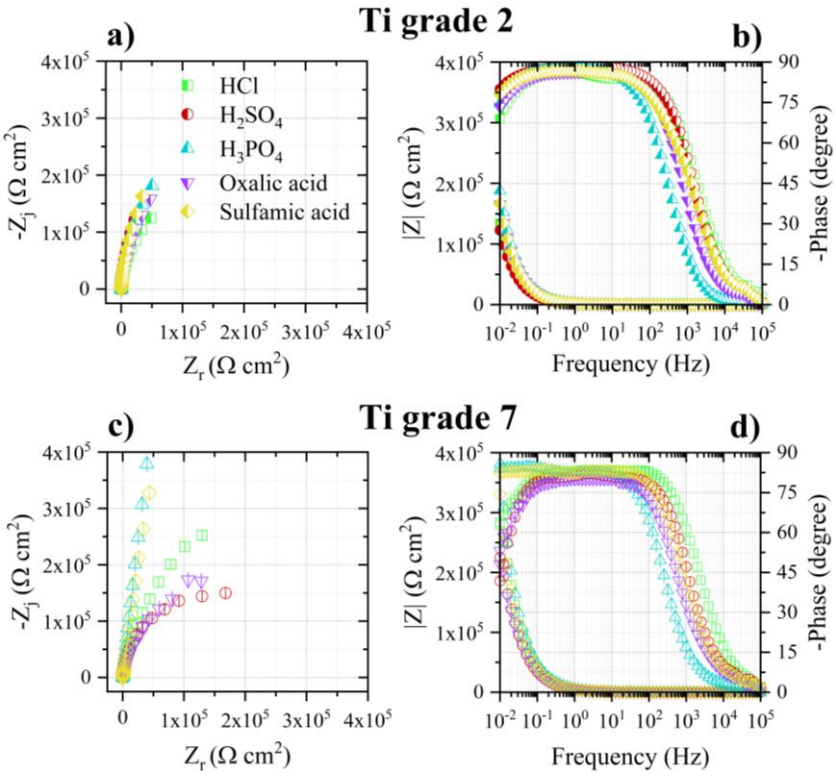

Figure 15: Nyquist (**a** and **c**) and Bode (**b** and **d**) representation of Ti grade 2 and 7 immersed in different acidic solutions.

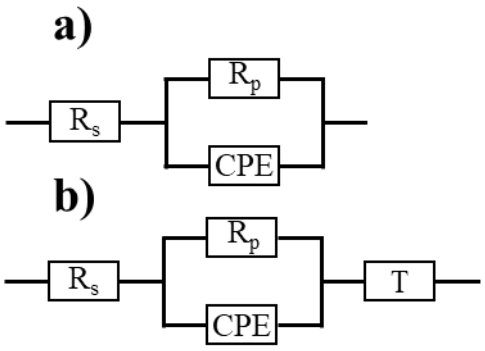

Figure 16: electrochemical equivalent circuits used to fit EIS spectra of Figure 15.

In case of negligible mass transport the circuit reported in **Figure 16a** was considered, as for the case of Ti grade 7 when immersed in less aggressive electrolytes like H_3PO_4 and sulfamic acids, while the circuit in **b** was used for all the other cases. The absence of diffusion related phenomena was indicative of the lower tendency of charges to accumulate inside the EDL as the result of the tendency of Ti grade 7 to behave as a partially blocking electrode. This correlated with the maximum of the –phase angle, observed in **Figure 15d**, maintaining a high value (~ - 85 °) even at the lowest frequency portion of the spectrum ($10^{-2} \div 10^{-1}$ Hz). Fitting parameters of EIS spectra are collected in **Table 12**, where R_p stands for polarization resistance, Yo and n are the admittance and the exponent of the CPE, while R_d is a diffusion resistance. Fitting quality was verified according χ^2 values.

Table 12: parameters extracted according to fitting of EIS data of Ti grade 2 and 7 immersed in different acids.

Acid	Ti	R_p ($\Omega \cdot cm^2$)	Y_O ($S \cdot s^n \cdot cm^{-2}$)	n	R_d ($\Omega \cdot cm^2$)	χ^2
HCl	Grade 2	$4.55 \cdot 10^5$	$9.86 \cdot 10^{-5}$	0.95	31.6	$3.4 \cdot 10^{-3}$
	Grade 7	$9.11 \cdot 10^5$	$4.93 \cdot 10^{-5}$	0.91	99.3	$6.8 \cdot 10^{-3}$
H_2SO_4	Grade 2	$3.08 \cdot 10^5$	$8.81 \cdot 10^{-5}$	0.97	20.8	$7.0 \cdot 10^{-3}$
	Grade 7	$3.67 \cdot 10^5$	$4.34 \cdot 10^{-5}$	0.92	27.0	$5.1 \cdot 10^{-3}$
H_3PO_4	Grade 2	$7.78 \cdot 10^5$	$7.67 \cdot 10^{-5}$	0.97	34.3	$7.1 \cdot 10^{-3}$
	Grade 7	$1.97 \cdot 10^6$	$3.21 \cdot 10^{-5}$	0.93	-	$8.8 \cdot 10^{-3}$
Oxalic	Grade 2	$4.88 \cdot 10^5$	$8.35 \cdot 10^{-5}$	0.96	26.7	$5.2 \cdot 10^{-3}$
	Grade 7	$6.39 \cdot 10^5$	$4.23 \cdot 10^{-5}$	0.89	32.1	$6.2 \cdot 10^{-3}$
Sulfamic	Grade 2	$9.26 \cdot 10^5$	$9.01 \cdot 10^{-5}$	0.96	75.0	$6.6 \cdot 10^{-3}$
	Grade 7	$1.24 \cdot 10^6$	$3.87 \cdot 10^{-5}$	0.91	-	$7.6 \cdot 10^{-3}$

Looking at R_p it is clear how Ti grade 7 shows a higher resistance to ongoing faradaic reactions as compared to Ti grade 2. This is particularly true in case of immersion in H_3PO_4 and sulfamic acids where the capacitive response was preponderant (higher - phase angle) and $R_p \sim 7.78$ and 9.26×10^5 $\Omega \cdot cm^2$. Same conclusions can be drawn by looking at "n" always close to one (see **Table 12**) as a demonstration of the capacitive character of the electrode in all the solutions tested. Only in the case of oxalic acid "n" decreased to 0.89 compatibly with the high surface roughness promoted by its attack (see **Figure 13d**). According to impedance analysis, the use of Ti grade 7 seemed to be particularly advantageous, doubling R_p and R_d, when considering a solution of HCl.

2.3 Summary

As a result of weight - loss and electrochemical investigation, it is possible to draw the following observations:

- Hot concentrated oxalic acid was very aggressive toward unalloyed Ti forming very rough surfaces and CR comparable with H_2SO_4.
- Pd promoted ORR kinetics leading to lower b_c near E_{corr} while in the high overvoltage region it favored film stability resulting in larger b_c.
- EIS results well correlated with previous trend: in particular, Ti grade 7 was found to behave like a blocking electrode when immersed in 0.5 M H_3PO_4 and sulfamic acid.
- Sulfuric acid promoted the highest CR ~ 8 $mm \cdot year^{-1}$ thus deserving the attribute of most corrosive agent, for Ti grade 2, among all the tested solutions in agreement with the progressively increasing solution aggressivity and metal corrodibility.

With a certain degree of confidence, after this analysis, the use of Ti grade 7 when hot concentrated solutions of H_2SO_4, oxalic, and hydrochloric acid are predicted to wet the metal is strongly advised.

Alternatively, a more economic strategy can be the functionalization of the surface with a conversion coating through an anodization process.

Chapter 3 Unipolar PEO

Plasma electrolytic oxidation (PEO) offers the possibility to create metal oxides with peculiar features depending on final applications [101,102]. This is particularly true for PEO on titanium, stimulating a lot of interest in actual research, specifically in the biomedical field, thanks to the possibility to form hydroxyapatite, and in the corrosion sector [79,103–105] thanks to the formation of hard, thick, and adherent oxides. Even if bipolar PEO [106,107] favors a higher oxidation rate [108], leading to thicker and more protective coatings [109], due to the actual global concern for CO_2 emission an upper limit of the energy consumption raises the demand of more environmentally friendly technologies. For this reason research regarding unipolar PEO, involving only the use of anodic polarization, for a controllable amount of time, is still popular. It is well documented [110–112] that *voltage* (*V*) is the more reliable parameter for controlling coating thickness and morphology [113]. For example, Kuromoto *et al.* [114] found higher porosity and larger pore diameters as *V* passed from 50 to 250 V. Similarly Asumpinwong *et al.* [114] observed higher roughness and amount of crystal phase when using higher *V*. *V* control is also important for determining the elemental retention from the electrolyte. In fact, working ~ 100 V [115] limits the deposition of electrolyte species while the opposite holds true when higher *V* (~ 450 V) are employed [51].

Other strategic parameters widely studied with the advent of pulsed anodizing are for sure *frequency* and *duty cycle*. Torres-Cerón *et al.* [116] studied extensively the effect of the former parameter: higher values were found to promote a decrease in crystal size, pore diameters, and higher surface roughness. Concerning duty cycle Williamson *et al.* [117] found benefits in using larger duty cycle (with progressively higher anodic polarization). In fact, this allowed the author to reach the same coating thickness with lower forming voltage with respect to the use of a lower amount of anodic polarization. This effect, manifesting even when too high frequencies are selected, should be related to modifications of the plasma activity developed over the electrode surface [118].

Both alkaline and low pH electrolytes can be used to PEO treat a valve metal. H_2SO_4 with respect to other acids used during PEO of Ti, like H_3PO_4, favors surface porosity, a more homogeneous oxide stoichiometry [119], and the development of rutile [120]. These observation can be related to the particular plasma activity promoted at the electrode surface. For this reason several attempts were done to understand and characterize the different types of plasma developing over the material [71] previously described in *section 1.3.5* and here briefly summarized:

- purely surface sparks produced by water breakdown → *type - A*

- dielectric discharges → *type - B*
- sparks promoted at the bottom of pores filled with gases → *type - C*

Apart from the electrolytic bath even the correct choice of electrical parameters can favor one discharge type with respect to another one. This can considerably widen the degree of functionalization of the coating: for example PEO Ti oxides resistance towards harsh environments containing Br^-, known to promote severe localized attacks, can be easily enhanced by simply increasing the voltage [121–124] beyond the spark limit, thus promoting the formation of thicker and more crystalline oxides. Moreover, as in *section 2* it was shown that Ti can suffer uniform corrosion if strong reducing acids are considered, the oxide prepared in the present section was tested for uniform attacks immersing the metal coupons in sulfuric acid, while localized corrosion resistance was studied according to anodic potentiodynamic scan in a bromides containing solution. Oxides were synthesized in 0.5 M sulfuric acid considering investigation of the following experimental parameters:

- Forming voltage
- Duty cycle
- Frequency

3.1 Materials and methods

Conversion treatments were performed on 10 × 10 × 1.6 mm^3 titanium grade 2 (UNS R50400) with a fully programmable power supply (California Instruments Asterion 751 series AC/DC power source) in potential - controlled regime. The natural oxide was removed, before any treatment, according to mechanical lapping using silicon carbide papers: 100, 320 and 600 grit. After polishing, samples were sonically cleaned in ethanol for 5 min and washed in deionized water.

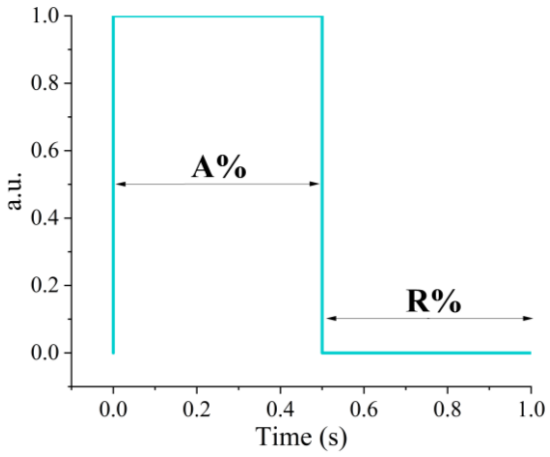

Figure 17: schematic representation of unipolar duty cycle.

Figure 17 allows the reader to be confident with the definition of duty cycle where A% stands for percentage of anodic polarization and R% for percentage of rest time, i.e. no polarization applied at all. The combination of three voltages (120, 160 and 220 V), two frequencies (20 and 1000Hz) and two duty cycles (90 A%–10 R% and 10 A%–90 R%) allowed all the condition highlighted in **Table 13** to be tested. Duty cycle and frequency values were selected as they represent the extreme conditions reproducible by our potentiostat. The final voltage was reached according to a constant voltage ramp with slope: 0.5 $V \cdot s^{-1}$. A Cambridge Stereoscan 360 SEM was used for morphological analysis. A pore recognition macro, developed for ImageJ software, was run over five pictures for each sample allowing to statistically evaluate results in terms of surface porosity and number of pores per image. Structure was investigated thanks to X - ray diffraction (XRD) using a Panalytical Empyrean XRD with Cu $K_{\alpha 1}$ radiation (1.54058 Å) and scanning angle varied between 20 ° and 40 ° to capture the main characteristic peaks of anatase (25.309 ° *PDF 00-064-0863*) and rutile (27.443 ° *PDF 01-089-0553*). Thickness was evaluated according to cross-section observations at SEM: samples were incorporated, via hot pressing, into an epoxy resin and before observation they were mechanically lapped down to ~ 0.8 µm thanks to alumina powder.

Table 13: Unipolar PEO parameters used in the present analysis.

Sample	Voltage (V)	A%	R%	Frequency (Hz)
120-10-20	120	10	90	20
120-10-1000	120	10	90	1000
120-90-20	120	90	10	20
120-90-1000	120	90	10	1000
160-10-20	160	10	90	20
160-10-1000	160	10	90	1000
160-90-20	160	90	10	20
160-90-1000	160	90	10	1000
220-10-20	220	10	90	20
220-10-1000	220	10	90	1000
220-90-20	220	90	10	20
220-90-1000	220	90	10	1000

The electrochemical response was investigated according to the use of potentiodynamic tests in 0.5 M NaBr at 50 °C with a repetition of two per each anodization treatment performed in a standard three - electrode cell [125] with KCl saturated silver/silver chloride ($SSC_{sat.}$) reference electrode and Pt counter electrode. A scan rate of 10 $mV \cdot min^{-1}$ was adopted, starting from 0.1 V below E_{corr} up to 8 V above E_{corr}. The cathodic region was instead investigated in 0.5 M sulfuric acid at 25 °C scanning from 0.1 V to − 1.5 V with respect to E_{corr} using previous scan rate. Immersion tests were conducted in 10 %v/v sulfuric acid with the same test apparatus described in *section 2.1* and the minimum test duration was evaluated as follows [89]:

$$hours = \frac{2000}{CR(mpy)} \quad (14)$$

Experiments conducted in *section 2*, considering previously described solution, allowed to verify a corrosion rate (CR) for untreated titanium grade 2 equal to ~ 8.1 mm·year^{-1} producing a minimum test time of 6.3 h, derived according to **Equation 14**. However, to have a significant and measurable mass loss in the presence of more corrosion resistant films the duration has been extended to 24 h considering a repetition of two samples.

3.2 Results

Anodizing in an oxide dissolving solution forms a porous surface with increasing pore size increasing the *V* from 120 (**Figure 18a**), 160 (**Figure 18b**), and 220 V (**Figure 18c**). **Table 14** lists the number of pores and the surface porosity extracted from ImageJ. A coefficient of variance (CV) was defined as in **Equation 15**:

$$CV = \frac{STDEV}{AVERAGE} \cdot 100 \quad (15)$$

where STDEV stands for standard deviation and AVERAGE for the arithmetic mean. As previously reported, *V* increase favored **surface porosity and roughness**. In particular, at 220 V pores were substituted by interconnected tunnels and large deposits resulting in a less organized oxide growth. Oxides produced at 120 V presented high inhomogeneity in both surface porosity and pores number. Lower porosity (1.52 %) was obtained with condition 120-10-1000, where the use of small duty and high frequency permitted the electrode to be polarized anodically only for 100 µs.

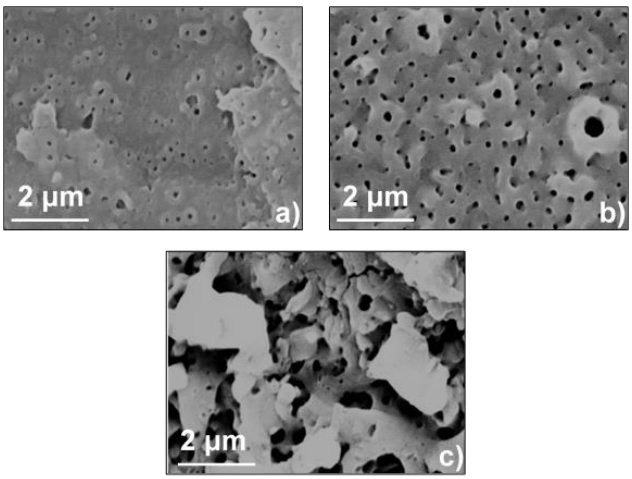

Figure 18: SEM images of sample anodized at **a** 120, **b** 160, and **c** 220 V considering the duty 90 A%-10 R% at 1000 Hz.

Table 14: results of the pore recognition macro applied on PEO treated samples.

Sample	Pores		Porosity	
	n	CV (%)	%	CV (%)
120-DC	207	32.1	4.7	47.6
120-10-20	133	36.8	3.6	23.5
120-10-1000	335	41.3	1.5	36.5
120-90-20	156	30.1	2.7	34.4
120-90-1000	178	23.4	2.3	46.5
160-DC	175	15.2	9.8	18.3
160-10-20	230	11.0	7.7	15.2
160-10-1000	291	4.9	7.1	15.2
160-90-20	216	12.7	11.1	15.0
160-90-1000	278	8.4	7.3	4.9
220-DC	155	21.8	10.7	13.1
220-10-20	175	24.2	15.5	4.0
220-10-1000	219	6.8	13.8	5.6
220-90-20	193	11.4	20.6	13.3
220-90-1000	90	14.2	12.4	15.1

Consequently, the power density used by sparks to locally melt the oxide was strongly reduced [71]. Previous considerations are valid also for the case where higher *V* are employed, allowing to conclude the important role of duty cycle and frequency in controlling the time given to reactions, responsible for local dissolution and porosity formation, to occur. However, even if higher frequency determined a decrease of the overall surface porosity, the total number of pores was increased (pore smaller in diameter) [76]. The reaction leading to porosity formation can be thought as a two-step mechanism, assisted by the high electric field:

– a proton transfer reaction: $TiO_2 + 4H^+ \rightarrow Ti^{4+} + 2H_2O$

– formation of a soluble salt: $Ti^{4+} + 2SO_4^{2-} \rightarrow Ti(SO_4)_2$

Figure 18a highlights a sample anodized at 120 V, showing a smaller number of pores as compared with the other conditions tested using higher forming voltage. This is related to the relatively low potential applied, high enough to favour the formation of pores only in correspondence with defects and small feature sizes amplifying the local electric field. **Figure 18b** presents the surface obtained at 160 V with pores homogeneously distributed over the deposit. In both cases, only small short-living and randomly moving sparks were observed.

The **crystal structure** of the oxides was analyzed by XRD. For sake of comparison, after background removal, the area of the main anatase and rutile peaks was evaluated and collected in histograms shown in **Figure 19a** to **c**.

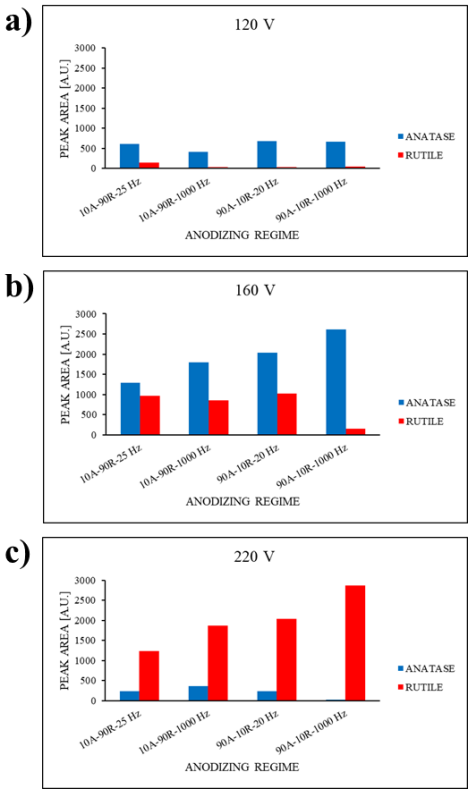

Figure 19: area of the main anatase and rutile peaks, whose values are represented in the form of histograms, for samples anodized at **a** 120 V, **b** 160 V and **c** 220 V.

The increase in voltage determined a strong increase of the rutile phase (red histograms) which however was very low at 120 V (**Figure 19a**) compatibly to the low ΔT involved during the treatment (solution ΔT_{max} = 2). At 160 V (**Figure 19b**) a relatively high anatase quantity combined also with the presence of rutile manifested, in particular the waveform 10 A% – 90 R% at 20 Hz promoted the development of both crystal structures in similar quantity, making the signal appetible for those applications requiring both phases [126].

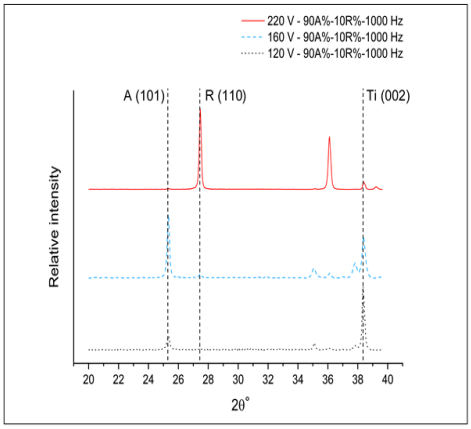

Figure 20: diffractograms of samples produced with the waveform 90 A%–10 R% at 1000 Hz at different voltages.

As previously said, at 220 V (**Figure 19c**), the high heat involved during the process, determining a substantial ΔT_{max} = 41 of the solution, stabilized the formation of rutile. This was particularly true for the waveform 90 A%–10 R% at 1000 Hz which converted the structure almost entirely to rutile thanks to the development of long - lasting orange like sparks. For sake of representation the effect of *V* on the bulk structure of the oxide, produced with the waveform 90 A%–10 R% at 1000 Hz, is displayed in **Figure 20**:

Table 15: results of the thickness analysis performed on PEO treated samples where CV stands for coefficient of variability.

Sample	t_{min} (µm)	t_{max} (µm)	$t_{average}$ (µm)	CV%
120-10-20	0.73	1.35	1.02	18
120-10-1000	0.51	0.85	0.64	25
120-90-20	1.13	1.91	1.52	15
120-90-1000	1.48	2.99	2.19	23
160-10-20	1.25	2.05	1.60	17
160-10-1000	1.27	2.57	1.97	17
160-90-20	1.32	2.24	1.90	14
160-90-1000	1.90	2.89	2.41	14
220-10-20	2.11	3.25	2.64	13
220-10-1000	4.05	7.01	5.45	20
220-90-20	3.12	4.23	3.65	10
220-90-1000	6.93	8.56	7.78	7

As at 120 V the **coating thickness** was considerably lower (~ 2.2 µm) the reflection corresponding to the metallic substrate was enhanced as the x-ray beam experienced an easier penetration towards the substrate. By increasing *V* a raise of the anatase plane (101) is observed, enhanced by the presence of more intense surface sparks, still not powerful enough to promote the heat up of the film – electrolyte system (ΔT = 6 °C) required for the stabilization of the rutile structure [127]. Upon analysis of the upper (continuous red line) diffractogram, it was observed that the anatase peak was substituted by rutile, compatibly with the large electrolyte temperature variation (ΔT = 41 °C). The peak related to metallic Ti was considerably decreased according to the large thickness (~ 8 µm), verified by the following analysis, common for treatments employing large duty cycles (90 A%) and high frequency (1000 Hz).

Minimum, maximum, and average thickness values of the anodized samples are collected in **Table 15**.

The strong dependence of the oxide layer thickness on the forming voltage has been well documented [128]. Unsurprisingly condition 120-10-1000 formed the thinnest coating (~ 0.5 µm) as the time in correspondence of which the electrode was polarized anodically was very low according to the use

of high frequency and small duty cycles. The thickest sample (~ 7.8 μm) resulted by using the signal 220-90-1000, previously found to favor rutile growth (**Figure 21**).

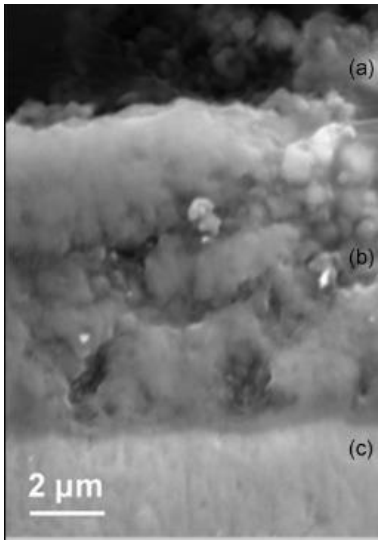

Figure 21: oxide overview of sample anodized with waveform 90 A%–10 R% at 1000 Hz at 220 V.

Apart from condition 120-10-1000 higher frequency always favored higher thickness, as higher currents were involved during oxidation (~ 25 % higher).

After oxide and process characterization **anodic curves** are reported in **Figure 22**, collected according to forming voltage.

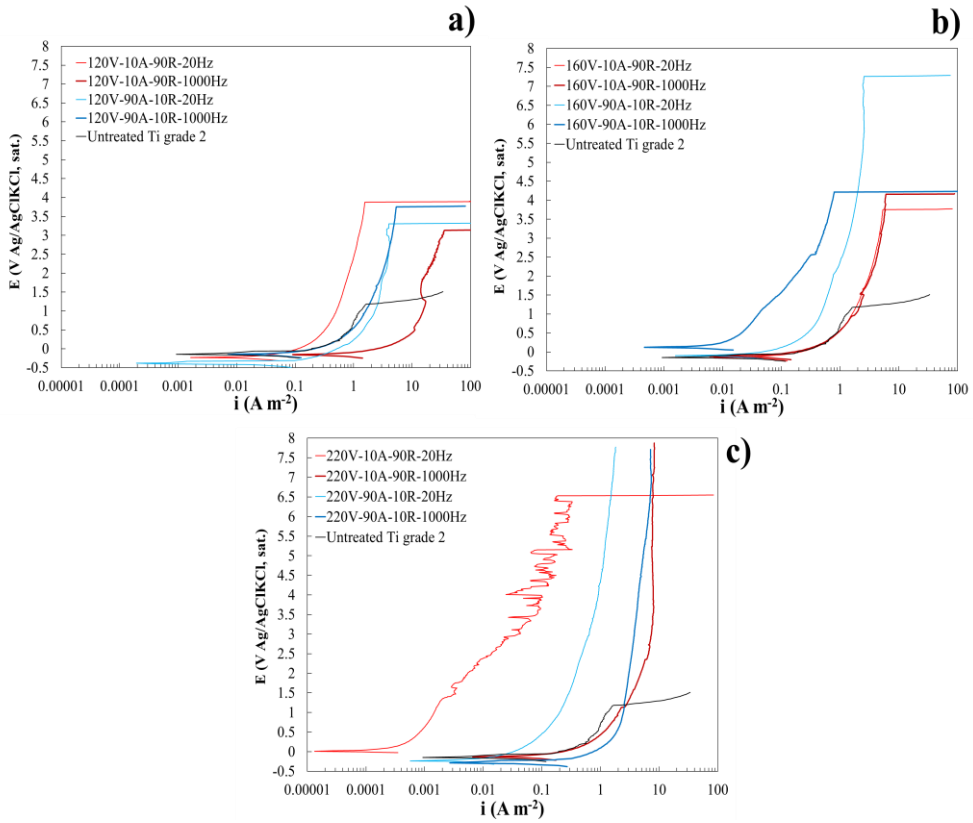

Figure 22: anodic polarization plot for sample treated at **a** 120, **b** 160, and **c** 220 V.

To demonstrate the improvements observed on the treated samples in each *V*-i plot the behavior of pristine titanium grade 2 is reported, showing a breakdown potential (E_{BD}) ~ 1.5 V/$SSC_{sat.}$. Results are grouped in **Table 16** in terms of E_{BD}, corrosion current density (i_{corr}) and anodic current density in correspondence of the passive branch (i_{pass}). Even the less corrosion resistance treatment 120-10-1000 (**Figure 22a**) was able to more than double E_{BD} of titanium grade 2 even if i_{corr} and i_{pass} are slightly larger probably due to the higher electrode crystallinity. This could be related to the smaller thickness but not with surface porosity that was the lowest among all the conversion coatings.

Table 16: electrochemical data extracted from anodic polarization visualized in Figure 22.

Sample	i_{corr} (A m^{-2})	i_{pass} (A m^{-2})	E_{BD} (V/$SSC_{sat.}$)
Ti grade 2	$8.70 \cdot 10^{-3}$	$2.97 \cdot 10^{-1}$	1.20
120-10-20	$1.38 \cdot 10^{-2}$	$2.51 \cdot 10^{-1}$	3.84
120-10-1000	$2.88 \cdot 10^{-1}$	6.47	3.14
120-90-20	$9.70 \cdot 10^{-3}$	$8.37 \cdot 10^{-1}$	3.31
120-90-1000	$2.41 \cdot 10^{-2}$	$6.43 \cdot 10^{-1}$	3.76
160-10-20	$2.62 \cdot 10^{-2}$	$5.93 \cdot 10^{-1}$	3.76
160-10-1000	$4.66 \cdot 10^{-2}$	$5.99 \cdot 10^{-1}$	4.16
160-90-20	$6.10 \cdot 10^{-3}$	$1.82 \cdot 10^{-1}$	7.27
160-90-1000	$3.50 \cdot 10^{-3}$	$7.44 \cdot 10^{-1}$	4.23
220-10-20	$1.32 \cdot 10^{-5}$	$3.00 \cdot 10^{-4}$	6.54
220-10-1000	$6.50 \cdot 10^{-3}$	$6.45 \cdot 10^{-1}$	8
220-90-20	$1.17 \cdot 10^{-2}$	1.21	8
220-90-1000	$3.10 \cdot 10^{-3}$	$5.75 \cdot 10^{-2}$	8

No significant improvements were demonstrated by the anodic scan performed for samples anodized at 160 V (see **Figure 22b**) except for the waveform 160-90-20 presenting E_{BD} = 7.27 V/$SSC_{sat.}$ and lower values of i_{corr} and i_{pass}. **Figure 22c** displays potentiodynamic tests of samples treated at 220 V: an important improvement in terms of E_{BD} was obtained and only sample 220-10-20 faced anodic dissolution. Condition 220-90-1000 performed the best: absence of pitting and improvements in terms of i_{corr} and i_{pass} with respect to pristine titanium grade 2 were the most important features. It is perhaps worth noting that the increase in thickness of the coating determined important improvements with respect to resistance towards localized corrosion [129]. This can be related to the voltage drop occurring inside the oxide layer and proportional to the passive current flowing in the cell. This is not strange as TiO_2 is semiconductive in nature (n-type) thus allowing a residual current to flow even in passive conditions (i_{pass} are not negligible). Keeping this in mind a larger thickness allows to increase the ohmic drop providing a better screening of the effective electric field present at the metallic substrate, applied during potentiodynamic test: this allowed to limit adsorption and diffusion of aggressive anions like Br^- retarding considerably anodic dissolution. The concept can be better visualized in

Figure 23 where the interfacial potential V_i in presence of deep oxide indentation can reach a value V_0 much more similar to the anodic potential experienced by the substrate (V_s), favoring dissolution.

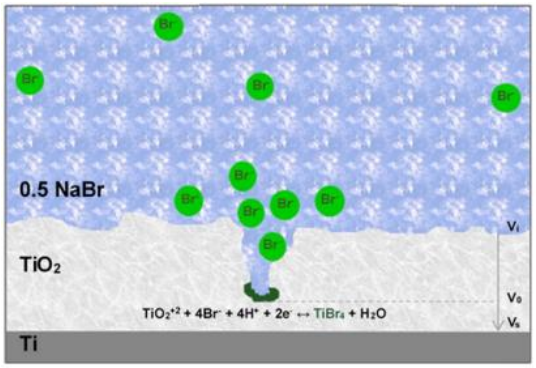

Figure 23: schematic representation of the occurrence of anodic dissolution.

In this high field condition, Br^- chemisorption increased leading to oxygen displacement and formation of the complex $TiBr_4$ [123]. Low E_{BD} and high i_{corr} and i_{pass} were observed on 120-10-1000: thickness measurements clearly indicate a non-homogeneous growth (CV ~ 24.6 %), with high probability of formation of defects and weak spots where preferential adsorption of Br^- can occur, but also a low level of crystallinity (both anatase and rutile concentrations are decreased). The fact that the latter sample manifested the lowest amount of surface porosity is a clear indication of its negligible influence with respect to anodic dissolution. This agreed with observations carried out by others [118] verifying no improvements, in terms of anodic dissolution resistance, when anodizing with "small" duty cycles. If *V* is increased, sample 160-90-20 behaved quite well, presenting a lower CV and improved concentration of rutile phase, increasing E_{BD} to 7.5 V/$SSC_{sat.}$. Apart from condition 220-10-20, with thickness ~ 2.114 μm, the use of 220 V seemed to be beneficial in avoiding anodic dissolution particularly if high frequencies are employed [130,131]. In fact, due to the high thickness, the voltage drop inside the film was high enough to decrease the interfacial potential, thus avoiding excessive accumulation and penetration of Br^{-1}. Surface porosity determined a minor contribution to the overall surface property, making thickness and degree of crystallinity the main factors affecting anodic dissolution resistance.

Weight - losses were converted into CR and collected in **Table 17** where also a percentual improvement, with respect to uncoated Ti grade 2, is proposed:

Final CR values were expressed as the average of both repetition. A sensible reduction of CR ~ 27 % occurred only in case of samples anodized at 220 V, presenting both higher quantity of rutile and thickness. However, the present analysis demonstrates how those treatments are far from the electrochemical response offered by Ti grade 7.

Having assessed the higher protective ability of coatings composed by rutile it is necessary to investigate the plasma regime developed over the electrode, responsible for the stabilization of the latter structure, and its relationship with electrical parameters like: frequency and duty cycle. In fact the different morphologies, encountered in **Figure 18**, suggest different phenomena to occur during the oxide synthesis depending on *V*.

Table 17: results in terms of CR of samples immersed in 10 %v/v H_2SO_4 at 60 °C.

Sample	CR ($mm \cdot year^{-1}$)	ΔCR (%)
Ti grade 2	8.10	-
Ti grade 7	0.21	+97.40
120-10-20	7.99	+1.09
120-10-1000	7.88	+1.09
120-90-20	8.27	-2.29
120-90-1000	7.73	+4.39
160-10-20	8.13	-0.62
160-10-1000	8.95	-10.73
160-90-20	8.38	-3.65
160-90-1000	8.23	-1.79
220-10-20	6.36	+21.26
220-10-1000	6.35	+21.44
220-90-20	6.37	+21.11
220-90-1000	5.91	+26.91

A preliminary understanding about the **process** can be extracted by looking at current – time plot (**Figure 24a** and **b**): several ripples (black arrow in **Figure 24b**) appeared when the voltage was increased from 160 to 220 V only for the signal 90 A%–10 R% at 1000 Hz. Visual observation (**Figure 24c** and **d**) evidenced a transition between randomly moving white sparks, verified at 160 V, and vigorous static discharges characterized by an orange-like hue manifesting at 220 V. The reason why such powerful optical emission verified only for signal 220-90-1000 can be related to the thickness enhancing ability observed when combining proper electrical parameters (like high frequency and large duty cycle). In fact it is well known the strong relation between oxide thickness and dielectric breakdown occurrence. Scanning electron microscopy and energy dispersive X-ray spectroscopy (SEM–EDS) were performed inside the crater left by the discharge to quantify the amount of foreign elements retained from the electrolyte (**Figure 25c** and **d**) and the substrate. SEM images demonstrate that the morphology is very different from a typical titanium oxide synthetized in H_2SO_4 (**Figure 18b**) where a very rough surface mainly composed of droplets, with different sizes and shapes of rapidly condensed oxide [132], developed. Using back - scattered electrons (**Figure 25d**) provided the contrast necessary to see small white spots randomly distributed inside the crater and corresponding to metallic titanium particles. This was the result of substrate evaporation confirming

the presence of *type-B* discharges involving very fast kinetics not allowing complete oxidation of the metal during the ejection process [71].

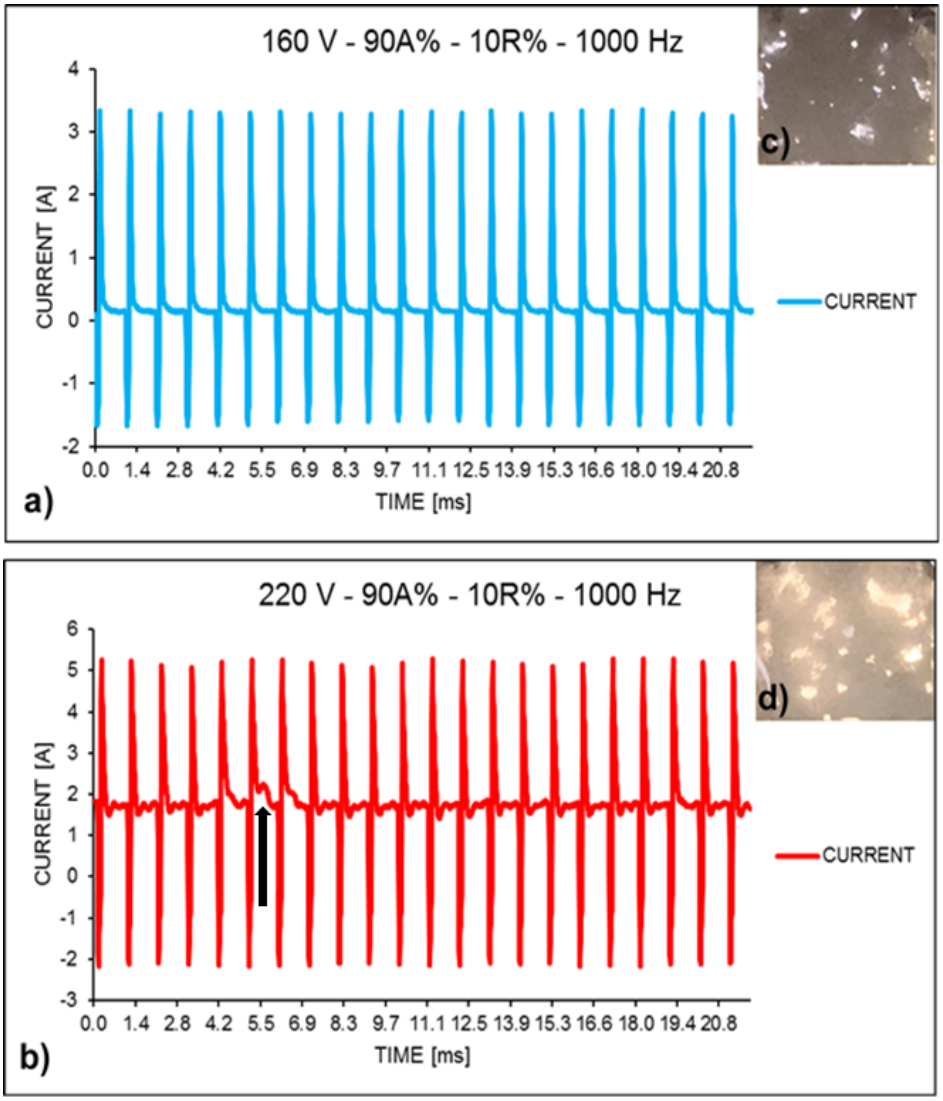

Figure 24: current-time plot of samples anodized with waveform 90 A%–10 R% at 1000 Hz at **a** 160 and **b** 220 V.

As current ripples previously observed generally developed in a time scale of hundreds of µs the static long lasting orange like plasma should be considered a cascade of several single events. To confirm this evidence the sample was cut using a circular diamond saw (**Figure 26**) in correspondence of the crater left by the plasma, measuring a diameter ~ 95 µm [64].

In correspondence of the crater a deep inward oxidation (~ 14.11 µm) occurred and a growth rate of ~ 1.92 µm·min^{-1} in the spark site, higher than typical values obtained outside (~ 1.06 µm·min^{-1}) confirmed the presence of plasma - assisted diffusion phenomena of oxygen species through the metallic substrate enhanced by the anodic polarization [72,133]. From image **Figure 26c** it is possible to better separate the current contribution devoted to plasma occurrence, evaluated ~ 100 µs [134], in correspondence of an anodic contribution lasting 0.9 ms.

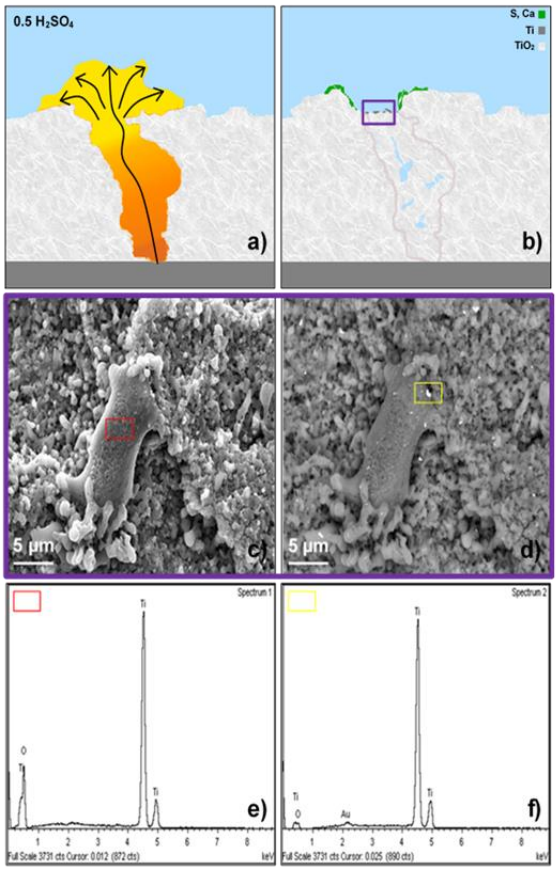

Figure 25: a, **b** schematic representation of a discharge and consequent EDS plot **e**, **f** of the spots highlighted in red and yellow inside the crater **c**, **d**.

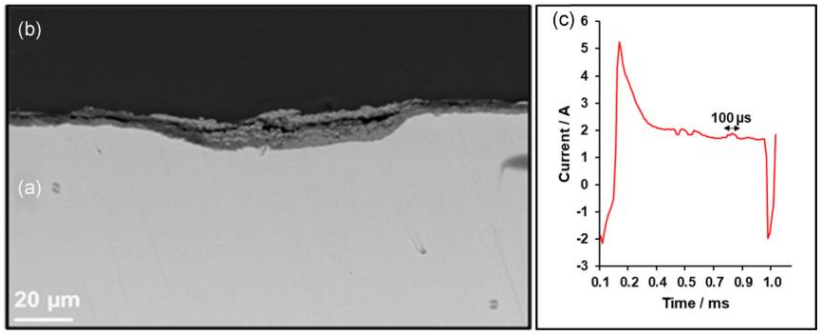

Figure 26: a, **b** cross section of the discharge fingerprint and **c** current-time plot at the ms time scale.

3.3 Discussion

Surface composition evaluated in correspondence of the discharge crater (at%; **Figure 27e**) was as follows: Ti (25.2 %), O (48.8%), S (15.6 %; **Figure 27c**) and Ca (10.4 %; **Figure 27d**) suggesting TiO_2 as the main constituent. S and Ca are mainly deposited along the discharge borders, generally called "nodules" [71,135,136]. Given the high content of S and Ca, retained from the electrolytic bath and the current ripples previously observed, it is reasonable to assume with a certain degree of confidence the concurrent action of *type - A* and *B* plasma.

For sake of summary few steps based on previous observations combined with a schematic representation of the plasma event (**Figure 25a** and **b**) are provided:

- ejection of substrate material → *type - B*;
- partial oxidation of the ejected metal;
- deposition of elements from the electrolyte → *type - A* spark [71,137].

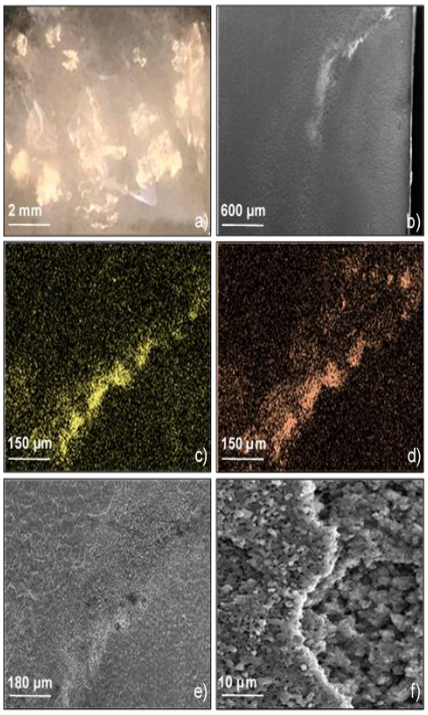

Figure 27: SEM-EDS analysis confined in the crater left by the discharge visible in **a**.

Concerning TiO_2 stability, Pourbaix plots are well known thermodynamic diagrams providing useful preliminary information regarding the possibility of an electrode to undergo dissolution in a certain electrolyte. TiO_2 is generally stable for pH > 0.4 and non - negative potentials with respect to standard hydrogen electrode (SHE). If stronger acidic conditions are employed, or the potential is decreased below 0.2 V/SHE, the overall anodic half reaction becomes:

$$Ti + H_2O \rightarrow TiOH^{2+} + 3e^- + H^+$$

where in presence of dissolved oxygen the cation can oxidize to Ti^{4+} in the form of $TiOH_2^{2+}$. Vaughan *et al.* [92] showed that with sulfates the pH threshold, below which TiO_2 corrodes, is further increased (~ 3.5), leading to the formation of $TiO(SO_4)_2^{2-}$ complexes [92] (a plausible conjecture as no color shift of the solution was observed [138]). According to results previously shown in **Table 17** no significant improvements, apart from coatings synthesized at 220 V, appeared. In fact, sometimes CR larger than untreated Ti were found as the coating acted as a crevice former [139–141]. This was confirmed by looking

at the roughness profile (**Figure 28a** for untreated Ti grade 2) where deep indentations were particularly evident for condition 160-10-1000 (**Figure 28b**), the most corroded one. Roughness parameters are listed in **Table 18** in the form of arithmetic average R_a; root mean square average, R_q; Δ between highest peak and lowest valley, R_t; and the distance between the highest peak and lowest

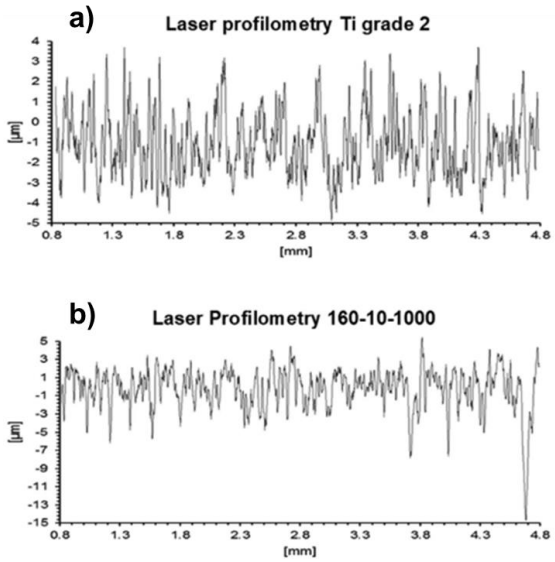

Figure 28: laser profilometry analysis carried out on **a** Ti grade 2 and **b** sample showing the highest CR in sulfuric acid solution.

valley in a sampling length averaged over the five sampling lengths comprising the evaluation length, R_z.

Table 18: roughness parameter extracted according to laser profilometry analysis shown in Figure 28.

Roughness (µm)	Ti grade 2	160-10-1000
R_a	1.337	1.691
R_q	1.666	2.324
R_t	9.234	20.892
R_z	8.586	13.306

In particular the presence of strong localized attacks in sample 160-10-1000 can be evidenced by looking at R_t which was ~ 21 µm.

The best response of coating 220-90-1000 can be related to the relatively low surface porosity ~ 12.4 % and the abundant presence of rutile, demonstrated in other works [142] to be more stable than the amorphous phase. Nonetheless, the high thickness increase promoted by condition 220-90-1000 provided only a rather moderate uniform corrosion improvement (< 30 %). This last observation can find justification again in the particular mechanism of growth, where the high voltage employed contributed to the formation of thick oxides with very rough architecture (**Figure 18c**) but also a low

adherent substrate. The latter hypothesis is demonstrated by the presence of a layer of porosity in correspondence of the oxide - metal interface as in **Figure 29**.

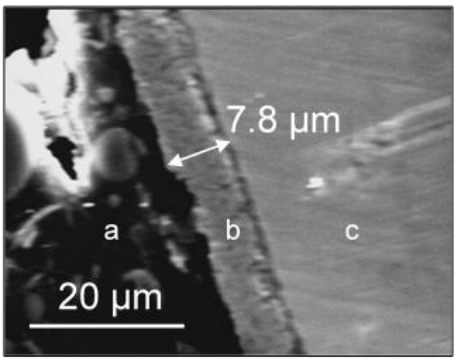

Figure 29: oxide cross-section (220-90-1000) highlighting the porosity band at the oxide - metal interface.

In **Figure 30** the cathodic behavior of sample 220-90-1000 is investigated and compared to the one of Ti grade 2 and 7.

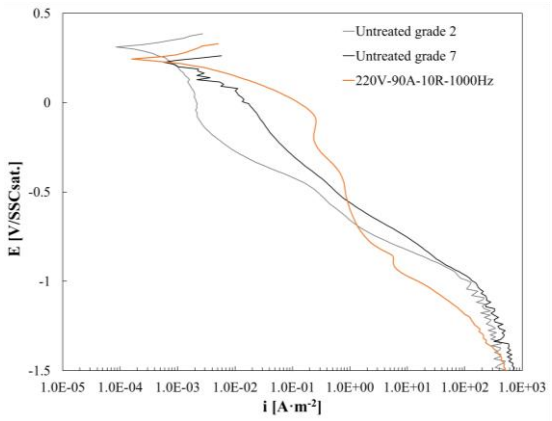

Figure 30: cathodic polarization scan for sample 220-90-1000 (in orange), Ti grade 2 (in gray), and Ti grade 7 (in black).

For the latter metal increasing cathodic current density (i_c) with respect Ti grade 2 are generally observed, in agreement with previous observation according to the presence of Pd [96]. In the first mV below E_{corr} the orange curve, related 220-90-1000, presented higher i_c until a potential ~ − 0.5 $V/SSC_{sat.}$. This could be related to the high content of surface impurities (like SO_4^{2-}) demonstrated according to EDS analysis to favor the development of the reaction SO_4^{2-} / H_2S (feasible at ~ − 0.35 V/SHE at pH = 7 and evaluated according to SO_4^{2-}/HSO_3^- at − 0.52 V/NHE and SO_3^{2-} / H_2S at − 0.17 V/NHE) occurring at a thermodynamic potential similar (~ 6 mV more positive) to proton reduction (− 0.41 at pH = 7). However, as the cathodic potential moved below the stability line of TiH_2 (− 0.6 V/NHE), condition 220-90-1000 showed higher HER polarization with respect to uncoated metals [143].

Pristine Ti grade 2 and anodized titanium showed a diffusion control regime for OER, followed by a Tafel behavior with a slope, in case of anodized titanium, ~ 179 $mV \cdot decade^{-1}$, in accordance with other studies [144,145] while no evident diffusion control region manifested for Ti grade 7 probably masked by the faster kinetics of HER. Apart from that as E_{corr} of the anodic layer, during free corrosion tests, never reached values below − 0.6 $V/SSC_{sat.}$ it is reasonable to assume the high retention of impurities and the rough morphology played a detrimental role in the corrosion resistance in sulfuric acid.

3.4 Summary

According to the present analysis, conducted on titanium oxides synthesized by PEO in unipolar regime, the following conclusions can be drawn:

- Important modifications at the level of morphology, porosity, structure, and thickness where induced by the use of several forming voltages according to the development of different plasma events. In particular, *type - B* discharges developed at 220 V using the signal providing the higher coating growth rate, i.e., 90 A%–10 R%–1000 Hz.
- Localized corrosion resistance was favored by the use of higher *V*, well correlating with thickness, uniformity, and porosity.
- Uniform corrosion, in concentrated H_2SO_4, was improved only for coatings produced at 220 V even if the advantages, in terms of CR, were rather modest. This was attributed to the rough morphology and the high content of S containing impurities, retained during PEO, responsible to modify the electrochemical response of the electrode.

Chapter 4 Bipolar PEO

Despite the research effort spent on unipolar PEO mainly for its interesting opportunity of energy saving, a rather low corrosion resistance enhancement was highlighted particularly when immersing the materials in hot strong reducing acids environments. For this reason the present analysis will be devoted to the investigation of the use of bipolar duty cycles where the combination of anodic and cathodic polarization imparts to the oxide peculiar features, like thickness and crystallinity, greatly enhancing the corrosion resistance towards both in localized and uniform attacks. Particular attention will be paid to the investigation of the effect of electrical parameters, like frequency and duty cycle, the latter intended in this work as the relative amount between anodic and cathodic polarization. Both parameters are responsible to rule the time allowed to the oxide layer to grow and to recover, thus covering an interesting opportunity to control the oxide functionalization. Nominé *et al.* [146] studied in detail their effect on PEO of Al, observing the decrease of the overall plasma using frequency ~ 1500 Hz, a threshold value allowing the anodic half-cycle to be time comparable to the lifetime of a single glow. The author also found a frequency threshold (~ 2500 Hz) in correspondence of which cathodic discharges start to occur: reasons behind this evidence were related to the effect of frequency in modulating the electrophoretic motions of very mobile ions (like Na^+ and K^+) changing the response of the EDL. Parallelly to previous investigation, also Clyne [147] found 1.75 kHz to be a threshold below which only anodic plasma can form. A study mainly focused on the morphological dependences on anodization frequency was carried out by Ishino *et al.* [148] demonstrating a range between 50 and 150 Hz responsible to stimulate film growth and to decrease inter-pore distances, while higher frequency values only promoted HER and consequent coating debonding. Torres-Ceròn *et al.* [116] found lower grain size, pore dimension, and increased surface roughness passing frequency from 1 to 2 kHz on Ti grade 2.

Also cathodic polarization is responsible of important modifications: Takahashi *et al.* [149] reported that during the cathodic half-cycle Al oxide was locally degraded according to two main mechanisms related to HER: 1 mechanical lift of the coating and 2 formation of pits by local pH increase. Other authors [148] found at low voltage (5 – 10 V) the cathodic current (I_c) to favor oxide growth while at higher V if $I_c > I_a$ the oxide grown as the result of the overlapping of several barrier layers. This evidence was related to the simultaneous action of oxidation (during the anodic half-cycle) and exfoliation (during the cathodic one). Other researchers [150] using high frequency (2000 Hz), during PEO of Ti grade 5 with a bipolar signal, increased the amount of rutile and thickness while obtaining a lower surface porosity.

In this section electrochemical impedance spectroscopy (EIS) will be the diagnostic tool selected to assess the electrochemical response of PEO surfaces. EIS is very good in determining coating protectiveness whose interpretation can be achieved extracting information according to the use of electrochemical equivalent circuits. Diamanti *et al.* [151], for example, performed EIS on anodized Ti grade 2 and found a Voigt circuit as a good model relating the high frequency time constant to the response of the EDL and the low frequency one to the presence of the coating. Devilliers *et al.* [152] found that as corrosion advances, a second high frequency time constant manifests attributed to the formation of corrosion products. Other authors [153], performing EIS on TiO_2 grown by micro-arc oxidation (MAO), related the high frequency relaxation (> 50 kHz) to the porous layer, the intermediate (5 Hz to 50 kHz) to the space charge region and the low frequency one (0.01 to 5 Hz) to the EDL. Generally Voigt circuits present C substituted by CPE [154] when describing electrochemical reactions like HER occurring on porous electrodes, attributing the high frequency portion to features like EDL or charge-transfer and the low frequency one to mass transport phenomena like diffusion.

Apart from the EIS a deeper insight, regarding the thermodynamic response of TiO_2 in sulfuric acid, is here provided. Based on well-established coulometric weight - loss and polarographic data [155] Ti was found to corrode in acidic medium as Ti^{3+} for E_{corr} well below a critical potential, E_{crit} , while it dissolves as Ti^{4+} E_{corr} was ~ 100/130 mV nobler than E_{crit} which can therefore be considered as a feasible limit to account for active – passive transition.

As we previously demonstrated in *section 2* the higher aggressiveness of sulfuric acid, this study will be devoted to verify the best amount of cathodic polarization and frequency for Ti corrosion resistance enhancement in the latter acid. Their effects, on film growth, will be rationalized in terms of modification of the EDL. In fact, despite the higher knowledge of PEO treatment on Al or Mg less information is currently available on Ti.

4.1 Materials and Methods

PEO treatments were performed in a solution of 0.5 M H_2SO_4, stirred at 1500 rpm, in a 1 L Pyrex beaker over 10 × 10 × 1.6 mm^3 titanium grade 2 (UNS R50400) samples cut by metal shearing. A cylindrical cathode of activated titanium with a radius of 5 cm was placed around the sample. After PEO, Ti coupons were incorporated into epoxy resin and then mechanically polished with silicon carbide papers according to the following sequence: 100, 320, 600 followed by sonication in ethanol for 5 min and washing in deionized water. PEO treatments were performed thanks to a fully programmable power supply (California Instruments Asterion 751 series AC/DC power source) in a

potential-controlled regime. In order to completely define the signal, 3 main parameters are required and described as in **Figure 31**:

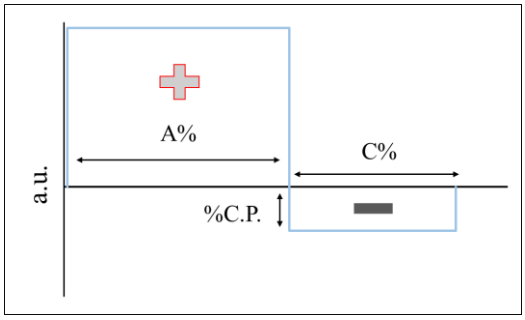

Figure 31: schematic representation of bipolar duty cycle.

- %A: % of anodic polarization

- %C: % of cathodic polarization

- %CP: % of cathodic peak with respect to the anodic one (in **Figure 31** , 20 %)

A forming voltage of 160 V reached in 320 s using a duty cycle 60 A%-40 C% was considered. The amount of cathodic polarization and frequency were varied as in **Table 19**:

Table 19: bipolar PEO anodization conditions.

Sample	CP (%)	Frequency (Hz)
2-1000	2	1000
7-1000	7	1000
20-1000	20	1000
7-20	7	20
7-1000	7	500

Currents and voltages were acquired using a Tektronix TBS-1072B-EDU oscilloscope. Morphology was investigated using a SEM Carl Zeiss EVO 50VP, equipped with an x-ray spectrometer for microanalysis (EDS). Crystal structure was characterized by grazing incidence x-ray diffraction technique (GIXRD) with diffraction angle $\phi = 1$ ° using a Philips PW3020 goniometer with Cu $K_{\alpha 1}$ radiation (1.54058 Å).

A Metrohm Autolab PGSTAT equipped with a FRA32M module for EIS was used for all the electrochemical tests considering a standard 3 electrode cell (ASTM G5 [91]) with a saturated silver/silver chloride ($SSC_{sat.}$) reference electrode and an Amel Pt counter electrode. All tests were repeated three times. EIS tests in deaerated condition were performed after 1 h in N_2 atmosphere with a flux of 25 $ml \cdot s^{-1}$. Anodic polarization curves in a 0.5 M NaBr containing solution were used to evaluate localized corrosion resistance [124], setting T to 50 °C with a Velp Scientifica Arex with VTF digital thermoregulator system.

A potential scan rate of 10 $mV \cdot min^{-1}$ was selected, starting from 0.1 V/E_{corr} to 8 V/E_{corr}. EIS and E_{corr} evolution were studied in a solution of 10 %v/v H_2SO_4 at 60 °C. EIS were evaluated always at E_{corr} , after 1 h of stabilization of the system, at regular intervals of time (1, 4, 20 and 24 h). A sinusoidal perturbation of 10 mV_{rms} was applied between 10 mHz and 100 kHz picking up 10 points per decade of frequency. The software Nova 2.1 was used to fit EIS spectra. As the solution resistance was always below 1 $\Omega \cdot cm^{-2}$, results were not corrected for ohmic drop. The system was checked for mass transfer limitation verifying a negligible variation of Z results (< 3 %).

Uniform corrosion was evaluated by immersion tests considering the same experimental set-up as in *section 3.1*.

4.2 Results

The **cathodic peak** was set to 2, 7, and 20 %. Acquisition of images using a professional camera during the PEO process (**Figure 32 a** to **c**) allowed to distinguish different plasma regimes depending on the electrical parameters selected.

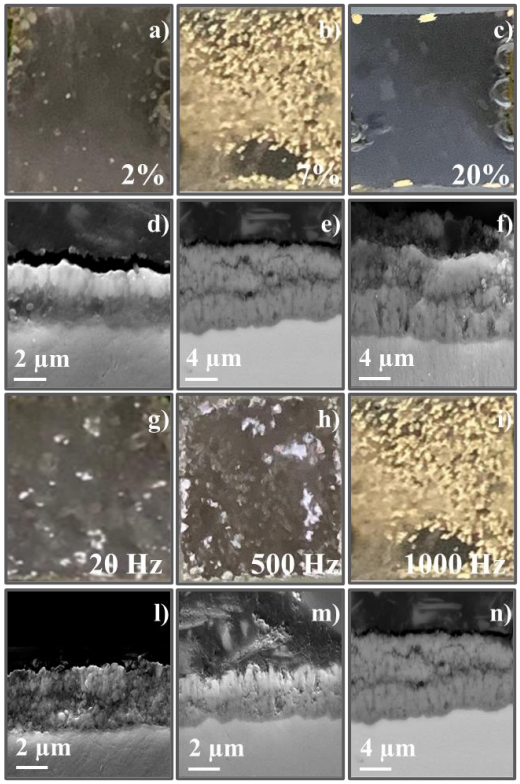

Figure 32: a-b-c images collected at different cathodic polarization; **d-e-f** oxide cross sections acquired by SEM; **g-h-i** images collected at different frequencies and corresponding oxide cross-sections **l-m-n**.

While in **Figure 33** are reported voltage, V , and current, I , trends at the ms time-scale acquired 10 s before the ending of each test.

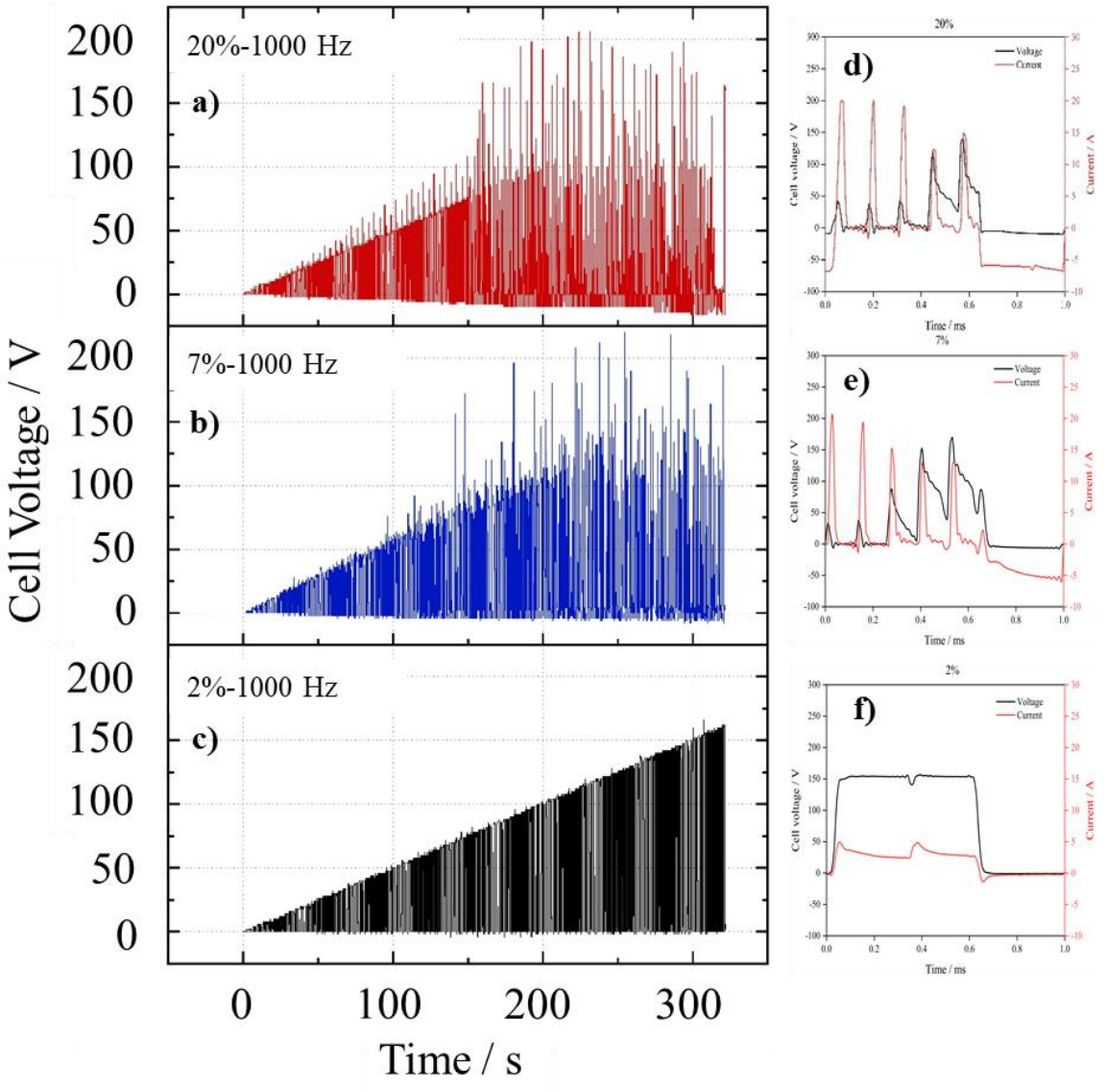

Figure 33: Voltage characteristics for coatings produced at different cathodic peaks **a** 2%, **b** 7% and **c** 20%; current and voltage tendency at the milliseconds time scale **d** 2%; **e** 7%; **f** 20%.

A non - monotonic plasma trend was observed using different cathodic polarization. For example at low level (2 %) only few sparks were observed and the duty cycle was perfectly reproduced (**Figure 33f**), while at 7 % violent yellow sparks, well distributed all over the surface, developed concomitantly with several *V* and *I* abrupt peaks. At 20 % most of the plasma was suppressed but *V* and *I* spikes were still present concluding their relation also to the abundant formation and explosion of gas bubbles. The coating cross-sections, highlighted in **Figure 32d** to **f**, show the effect of the cathodic regime to enhance through-thickness porosity, compatibly with the more intense plasma and higher amount of gas evacuated. All the PEO coatings, apart from sample 7–20, present a characteristic porosity band separating the oxide into an inner and an outer layer, a common features also verified on PEO Al oxides [156]. A columnar morphology , particularly visible in the upper portion of the oxides and similar to the one obtained on annealed TiO_2 [157,158], was observed for all samples

apart from 7 - 20 (**Figure 32l**). This fact is probably related to a condition of growth influenced by the higher T reached when using higher frequencies (ΔT ~ 15 °C higher than when low frequencies are employed). Indeed, sample 7 – 20 (**Figure 32l**) presents a different morphology with prevailing roundly shaped particles, sign that lower frequency provided enough time for Brownian motions to occur and to favor aggregation. Images captured 10 s before the ending of the process (i.e. at 155 V), explaining the influence of **frequency** on plasma, are proposed in **Figure 34g** to **i**. At 20 Hz white slow moving sparks appear over the electrode surface, however their presence was not detected according to *V-I* plots (**Figure 34c**).

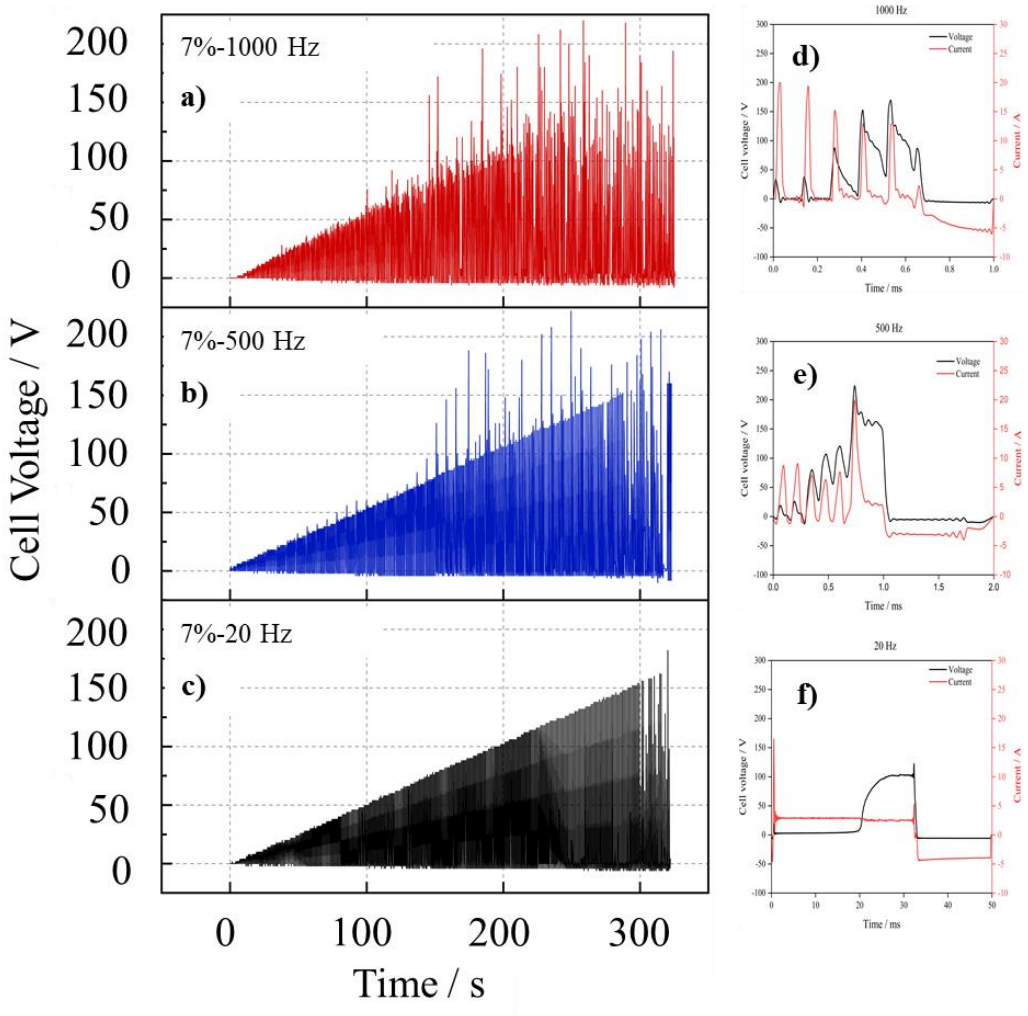

Figure 34: Voltage characteristics for coatings produced at different frequencies **a** 20 Hz, **b** 500 Hz and **c** 10 0 0 Hz; current and voltage tendency at the milliseconds time scale **d** 20 Hz; **e** 500 Hz; **f** 1000 Hz.

This is because they are mostly ignited over the surface, not involving the oxide deeper portions [78] (see the compact morphology in **Figure 32l**). Despite that thickness was enhanced to ~ 4.6 μm. At 500 Hz a thinner (3.3 μm) and less uniform oxide developed presenting higher surface porosity (**Figure 32m**) and surface roughness. The low surface plasma activity is apparently in contrast with both morphological and electrical data: for the latter (see **Figure 34e**), in particular, sharp *V* and *I*

peaks indicate the occurrence of rapid and continuous destruction/reconstruction of the oxide layer. Given the high I_c (~ 3 A) and porous cross-section, sparks probably were ignited below the oxide surface inside pores containing gases like O_2 and H_2 [72,159], a result typically related to *type-C* sparks. At high frequency, 1000 Hz, was observed the same plasma transition verified when increasing the cathodic peak from 2 to 7 % (**Figure 32h** to **i**) and *V* spikes ascribed to *I* values reaching the highest limit sustained by the instrument (20 A) for a limited amount of time.

4.3 Discussion

Observation of V_c (**Figure 35**) allowed to verify higher V_c when using 1000 Hz sustained by the larger I_c [147]. Higher *I* can be obtained using larger frequency as certain slow time scale electrochemical phenomena, like diffusion and adsorption, could be by-passed.

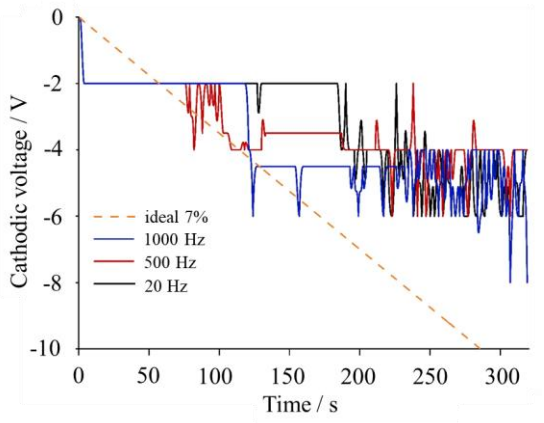

Figure 35: V_c evolution in time, for coating produced at different frequencies.

In the following paragraphs it will be shown how the variation of the cathodic polarization can influence the conductive state of the electrode and so the amount of plasma developed. According to that the area under I_a and I_c profiles was calculated from **Figure 33d** to **f** and shown in **Table 20**:

Table 20: evaluation of anodic, cathodic charges and their ratio (R) at 310 s for different cathodic peaks.

C.P. %	Q_A (10^{-3} C)	Q_C (10^{-3} C)	R (= $\frac{Q_C}{Q_A}$)
2	1.87	0.13	0.07
7	1.77	1.39	0.78
20	1.92	2.15	1.12

defining $R = \frac{Q_C}{Q_A}$ as a parameter of control to account for possible plasma regime transitions [160]. Because of the transient nature of the experiment, calculations were repeated at three different time intervals. However, since the trend was always respected only values collected at 310 s were provided. Using 20 % cathodic peak determined $I_c > I_a$. This implied plasma suppression, a higher

thickness and so a sensibly higher corrosion resistance [161]. In these conditions, the V_a diminished at ~ 100 V, a result which will be justified here in after.

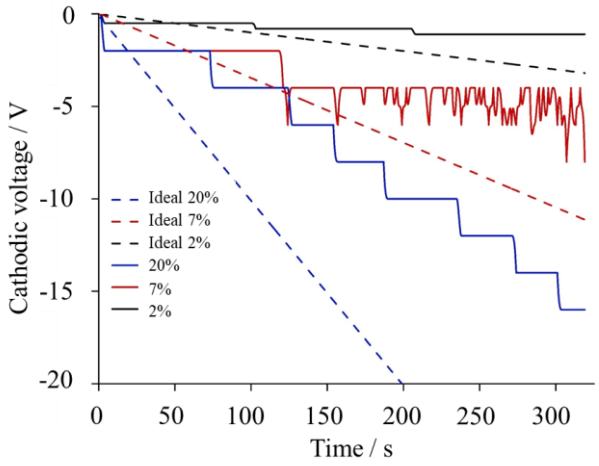

Figure 36: V_c trend for PEO treatments performed at different cathodic polarization.

This particular V trend is generally caused by the formation of surface charge leading to a non-barrier like oxide growth [137,162,163], requiring higher amount of I_c to be transmitted to the sample. The latter observation can be better demonstrated by looking at the evolution of V_c as in **Figure 36.** When passing from 2 % to 7 %, V_c evolved from 1 V to 6 V entirely sustained by I_c (~ 6 A) (**Figure 33e**), demonstrating the electrode to be in a fully conductive state with respect to cathodic reactions. However, at 20 %CP V_c rose up to 8 V (I_c = 7 A) at ~ 150 s then even reaching 16 V ~ 20 s before the end. Based on that a strong influence of the cathodic conductivity of the electrode on plasma formation should be considered. However not only conductivity, but also surface charge rules plasma formation. Surface charge can be assumed to develop over the electrode depending on the technological parameters used and also according to the nature of the material in contact with the solution. Considering PEO coatings as mainly constituted by anatase and rutile but also reach in sulfates, it is possible to assume an isoelectric point (IEP) ~ 5.2 to 6.8 [164–167]. During cathodic conduction with high I_c (cathodic peak = 7 %) HER was responsible for strong local alkalization of the electrode [168], exceeding for sure the IEP of the material, thus inducing a negative charge over the electrode. This contributed to the formation of a potential barrier, responsible to make more impervious ions motion (whose magnitude can be estimated through Nernst equation [133,169]), enhancing anodic breakdown. In fact, as the Debye-Huckle length, describing the EDL thickness, is ~ tens of nanometers, the electric field developed on it can reach very high values (100 – 200 kV·cm^{-1}, i.e., several orders of magnitude larger than the external field provided by the potentiostat, tens of V·cm^{-1}). The enabling condition was only verified when using a 7 % cathodic peak, since at 2 % HER was not enough powerful to increase the pH and to promote the required negative surface charge (V_c < 1 V).

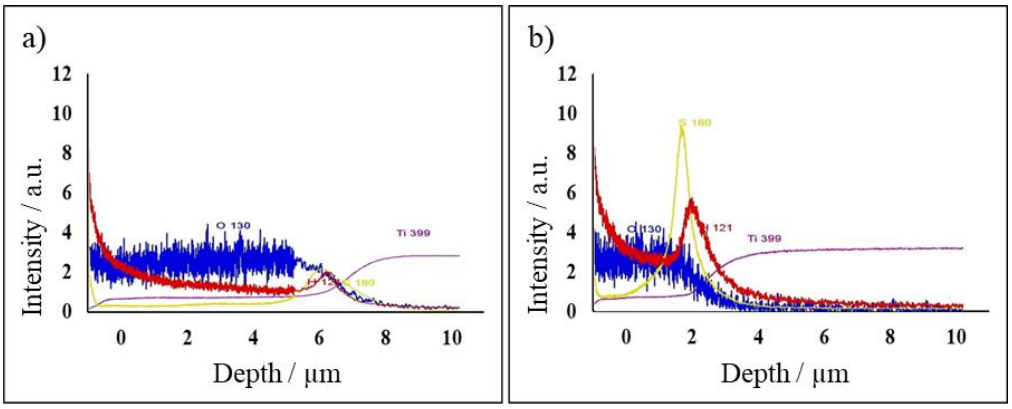

Figure 37: a GD - OES chemical profiling of sample anodized using a cathodic peak of 20%; **b** and 2%.

Thanks to GD - OES analysis it was possible to see that using higher cathodic peak (20 %) allowed to limit the amount of substances retained from the electrolyte (H in red, S in yellow) [170,171]. GD - OES analyses also allowed to confirm oxide thickness which was the highest for sample 20–1000 (~ 7 µm) quite in agreement with SEM (~ 7.8 µm) indicating a growth rate of 1.46 $\mu m \cdot min^{-1}$ versus 1.12 $\mu m \cdot min^{-1}$ obtained when using a lower cathodic peak. Based on previous results [172] it is possible to assume that the increase in thickness and the higher defectiveness, promoted when using higher cathodic peaks (**Figure 32f**), favored the polarization of HER. Consequently, acidification and variation of the oxide zeta potential induced the formation of a positive surface charge favoring the decrease of the potential barrier generated by the EDL: this was in turn the strategy found to be effective in lowering the plasma formation [146,169]. Similar results were not verified for sample 2–1000 whose thickness and defectiveness were not enough to polarize HER which instead was particularly enhanced by the high crystallinity of the oxide, causing strong alkalization [173].

To conclude, it was discovered how the use of the cathodic peak can modify the local pH near the electrode leading to a decrease in surface potential below water breakdown (~ 1 $MV \cdot cm^{-1}$). This permitted to tune the plasma emission sometimes even causing its total suppression [174].

Frequency modulation allows to tune the migration of charged species in correspondence of the EDL. This can result in the formation/suppression of a potential barrier limiting/favoring electrochemical reactions at the electrode. According to that it is not surprising to use frequency, in the same way as we previously did with cathodic polarization, to control the plasma activity amplifying or even limiting sparks and their effect on film growth [146]. For sake of quantification the Debye - Huckel theory was used to evaluate the relative positions of the main ions present in solution with respect to the growing oxide layer and depending on the applied polarization. According to that **Equation 15** was used to calculate the EDL thickness (stern + diffuse layer):

$$t_{D-H} = EDL\ thickness = \left(\frac{\varepsilon_0 \varepsilon_w N_A k_B T}{2F^2 I}\right)^{\frac{1}{2}} \quad (15)$$

$$I = \frac{1}{2}\sum_{i=1}^{n} c_i z_i^2 \quad (16)$$

$$v_i = \mu_i E \quad (17)$$

where ε_0 is the dielectric permittivity of vacuum, ε_w the permittivity of H_2O, N_A = Avogadro's number, k_B = Boltzmann's constant, T = temperature, F = Faraday's constant and I is the ionic strength of the electrolyte calculated according to **Equation 16**. The velocity of charge carriers migration v_i (**Equation 17**) can be evaluated according to the knowledge of the external electric field multiplied by the mobility of the *i* - th ion, while the distance (**Equation 18**) travelled as:

$$d_i = v_i t \quad (18)$$

with t the time corresponding to the anodic/cathodic half-cycle strictly related to duty cycle and frequency. In particular, at high frequency the amount of time at which a certain polarization was held decreases, thus avoiding the complete local depletion of the reactants necessary for a certain process to occur. Electric fields generated during anodic and cathodic half - cycles, used in **Equation 17**, are the one extracted in correspondence of the spark voltage. To extract this value precisely, the acquisition system was triggered to acquire the waveform once an abrupt *V* change, involving a rise front with a slope > 0.5 $V \cdot s^{-1}$ (the prescribed voltage ramp), occurred. Voltages extracted were collected in **Table 21** while mobility of ions in water were taken from Atkins' Physical chemistry 8th edition [175]:

- $\mu_{H^+}\ [\frac{m^2}{V \cdot s}] = 3.623 \cdot 10^{-7}$
- $\mu_{OH^-}[\frac{m^2}{V \cdot s}] = 2.064 \cdot 10^{-7}$
- $\mu_{SO_4^{2-}}[\frac{m^2}{V \cdot s}] = 8.290 \cdot 10^{-8}$

The analysis was restricted to common ions present in 0.5 M H_2SO_4 water based solution, i.e., H^+, SO_4^{2-} and OH^-, the latter produced at the cathode according to **Equation 19** [176]:

$$H_2O + e^- \rightarrow \frac{1}{2}H_2 + OH^- \quad (19)$$

The Debye-Huckle length was evaluated as $7.986 \cdot 10^{-9}$ m, considering 1 M of H^+ and 0.5 M of SO_4^{2-} ions, being negligible the amount of OH^- contained in an acid (apart from those OH^- produced at the cathode according to **Equation 19** which are however difficult to quantify). The bisulfate ion was

assumed to be deprotonated [177] according to the high electric field experienced at the electrode and thanks to the reaction displayed in **Equation 20** to give H_2O:

$$HSO_4^- + OH^- \rightarrow SO_4^{2-} + H_2O \quad (20)$$

Table 21: list of parameters used for calculations in the Debye - Huckel theory.

Cathodic peak	20 Hz	500 Hz	1000 Hz
V_a [V]	84	84	84
V_c [V]	3	3.2	4.5
t_a [s]	0.03	0.0012	0.0006
t_c [s]	0.02	0.0008	0.0004

At 1000 Hz, OH^- and SO_4^{2-} accumulated inside the EDL (see **Figure 38**) thus inducing higher amount of negatively charged ions adsorbed on the oxide surface.

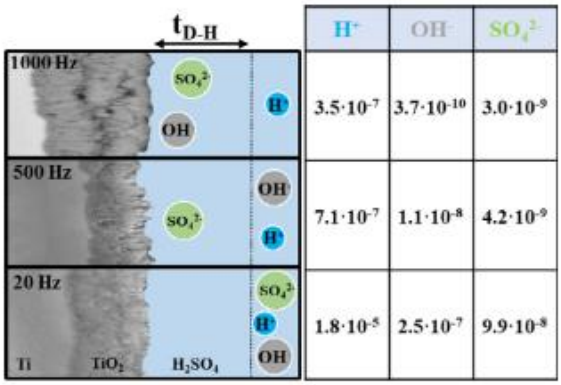

Figure 38: graphical outcome of the Debye - Huckel theory.

As a consequence, the local alkalization combined with the acidic IEP gave rise to a potential barrier favoring sparks occurrence [146,160,169]. Differently as frequency was decreased less anions were retained inside the EDL and in fact a lower plasma was observed according to **Figure 32**. For sake of summary, a brief literature survey regarding the effect of frequency and cathodic current is presented in **Table 22**. It is evident how the lack of notions regarding PEO on Ti justifies the present analysis.

Previously described samples are now investigated for localized corrosion: potentiodynamic tests (see **Figure 39**) were performed on all PEO oxides, plus untreated Ti grade 2 and 7 as in **Table 23**, reporting all the electrochemical parameters extracted like E_{corr} , i_{corr}, oxide breakdown potential E_{BD} (if present) and current in correspondence of the passive anodic branch, i_{pass}. Apart from sample 7 - 500, presenting lower thickness (~ 3.3 μm) higher porosity and roughness [123,129], no anodic dissolution was observed for all the other coatings. In fact, they reached the highest cap (8 V) of the testing apparatus even if in correspondence of high anodic overvoltages some metastable pits formed, leading to sharp increases in "i" followed by repassivation.

Table 22: Comparison among literature and results obtained in the present study, where R stands for the cathodic to anodic charge ratio transferred after a single duty cycle.

Reference	Effect of cathodic polarization (CP) and frequency (F)	R (= $\frac{Q_C}{Q_A}$)
Present study	F: ↑ frequency favors accumulation of negative surface charge and alkalization → plasma formation	/
Present study	CP: strong alkalization → plasma formation → rutile stabilization, ↑ growth rate and porosity: maximum corrosion resistance in reducing acid environments	0.78
Present study	CP: electrode polarization towards her → acidification → plasma suppression: ↑ growth rate and corrosion resistance	1.12
[146]	F: ↑ frequency (2000÷2500 Hz) → surface charge accumulation → cathodic breakdown	/
[178,179]	F: ↑ frequency favors pores branching, microhardness and growth rate	/
[50]	F: ↑ frequency favors homogeneity and growth rate as spark density, size, and lifetime ↓	/
[76]	F: ↑ frequency: smaller but higher number of discharge channels. Corrosion resistance is increased when working at 1000 Hz	/
[150]	CP: favors formation of rutile and higher coating density. Thickness ↓	0.2; 0.5
[176]	CP: ↑ oxide conductivity → local pH modification → subsequent anodic cycle is favored	1.045
[180]	CP: Discharges are delayed, smaller in size and lifetime, thickness ↑ and porosity ↓	1.11
[181]	CP: ↑ growth rate, uniformity and ↓ defectiveness	1.25
[182]	CP: ↑ thickness and uniformity and ↓ number of large discharge channels	1.12
[183]	CP: I_c modifies the oxide structure and allows precipitation of foreign elements thus determining "soft sparking" and a rougher surface	1.25
[184]	CP: ↑ coating adhesion, corrosion resistance, hardness, compactness, thickness	/
[185]	CP: I_c favors crystallization by promoting resistive heating	/
[186]	CP: ↓ oxide space charge → ↑ oxide conductivity → ↑ crystallization and growth rate	/

Table 23: electrochemical parameters extracted according to anodic polarization performed in Figure 39.

Sample	$i_{corr}\cdot10^{-7}$ (A m^{-2})	$i_{pass}\cdot10^{-5}$ (A m^{-2})	E_{corr} (V/$SSC_{sat.}$)	E_{BD} (V/$SSC_{sat.}$)
Ti grade 2	3.12	16.10	-0.232	1.08/1.31
Ti grade 2	2.45	3.60	-0.294	1.90/1.74
2-1000	0.08	0.16	+0.348	/
7-1000	2.14	91.30	-0.197	/
20-1000	10.50	31.80	-0.202	/
7-20	0.02	0.19	+0.367	/
7-500	47.90	345.00	-0.210	6.23/6.48

The compact morphology observed for samples 2 - 1000 and 7 - 20 (**Figure 32**) determined a nobler E_{corr} and lower i_{corr}, i_{pass}. On the other hand when producing thicker coatings, by increasing frequency or cathodic potential, the loss in compactness favored higher i_{corr} and i_{pass} even if the passive branches did not manifest any sign of instability.

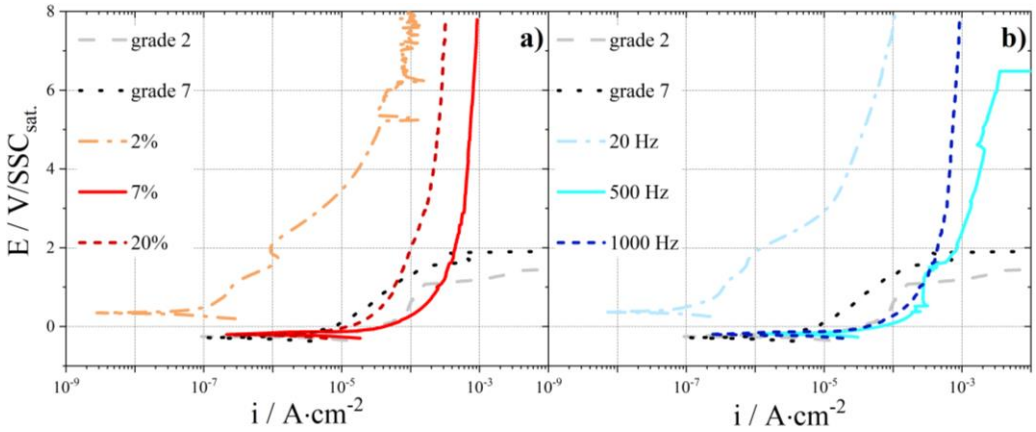

Figure 39: anodic polarization scan performed on sample anodized with **a** different cathodic polarization and **b** using different frequencies.

Concerning uniform corrosion, **Table 24** summarizes results, in terms of CR, related to previous samples (immersed in 10 %v/v H_2SO_4 at 60 °C) and the improvement defined by **Equation 21** [123] related to untreated Ti grade 2 whose CR was defined in *section 2.1*:

$$Improv.\% = \frac{CR(Ti\ grade\ 2) - CR(Ti\ anodized)}{CR(Ti\ grade\ 2)} \cdot 100 \quad (21)$$

Table 24: immersion tests results in terms of CR (mm·year^{-1}) and improvement parameter (%) with respect to untreated Ti grade 2.

Condition	C.R. (mm·year^{-1})	Improv. %
2-1000	6.04 ± 7%	21.5
7-1000	0.03 ± 31%	99.6
20-1000	0.36 ± 22%	95.4
7-20	6.02 ± 9%	21.7
7-500	8.03 ± 12%	/

Important benefit were achieved when using high cathodic potential: condition 7 – 1000 outperformed titanium grade 7 (CR ~ 0.12 mm·year^{-1}) with a CR averaged over the 24 h ~ 0.03 mm·year^{-1}. Also 20 – 1000 gave excellent performances, decreasing corrosion rate below 1 mm·year^{-1} and not showing oxide debonding, a condition verified for all the other oxides after few hours of immersion.

Before electrochemical characterization a brief crystalline structure survey (**Figure 40**) is here provided based on XRD results of conditions 7 - 500 and 7 - 1000, i.e., the one leading to worst and best behaviour in the low pH solution. As observed in *section 3.2* the intensity of the reflections related to the metallic substrate were highly dependent on oxide thickness. For this reason they appear

more intense for sample 7 - 500 (~ 3.3 µm) than 7 - 1000 (~ 6 µm). Moreover, a phase inversion occurred, with the coating produced at 1000 Hz showing rutile as the dominant structure. Relative amount of both phases (anatase and rutile) was calculated applying the Spurr-Myers equations (**Equation 22** and **23**) [187] on the more intense peaks for anatase (2θ = 25.316 °) and rutile (2θ = 27.434 °).

$$X_A\% = \frac{100}{\left(1+1.265\frac{I_R}{I_A}\right)} \quad (22)$$

$$X_R\% = \frac{100}{\left(1+0.8\frac{I_A}{I_R}\right)} \quad (23)$$

where the weight fraction (X_A and X_R) of anatase and rutile were extracted from the peak intensities I_A and I_R:

- 7-500: A = 59.4 %; R = 40.6 %
- 7-1000: A = 35.9 %; R = 64.1 %

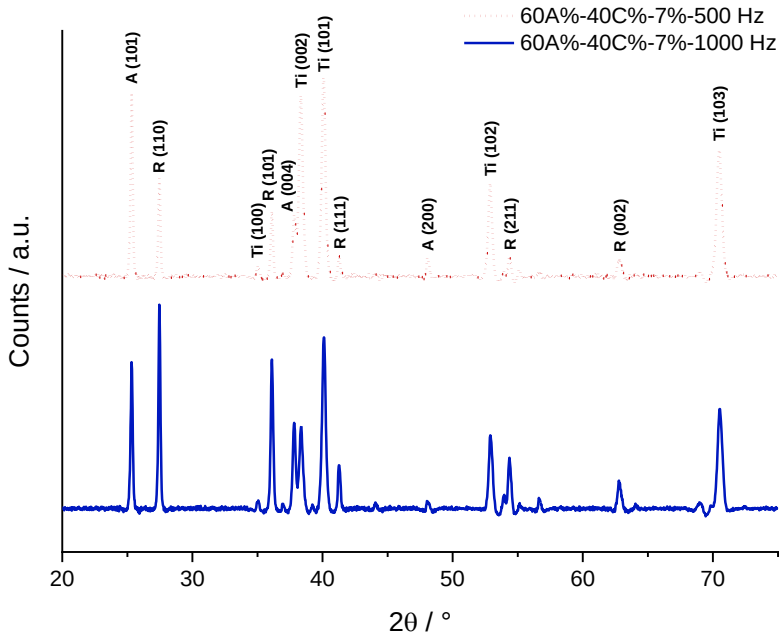

Figure 40: XRD diffractograms of sample presenting worst (dashed red) and best (blue) corrosion response in sulfuric acid.

As a first step E_{corr} evolution was investigated for both 7-500 and 7-1000, i.e. worst and best oxides in free corrosion. According to Evans, in fact, important information can be extracted observing E_{corr} trend. For sake of comparison also untreated Ti grade 2 was included in the analysis (**Figure 41**).

Initially all the electrode presented E_{corr} in the passive region, however after an incubation period dependent on the quality of the surface treatment, two potential drops occurred:

- 1st drop: from E_{corr} > 0 to ~ - 0.48 V/$SSC_{sat.}$ (passive to mixed active-passive state);

- 2nd drop: from ~ - 0.48 V/$SSC_{sat.}$ to a stable active state (~ − 0.65 V/$SSC_{sat.}$) with evident HER.

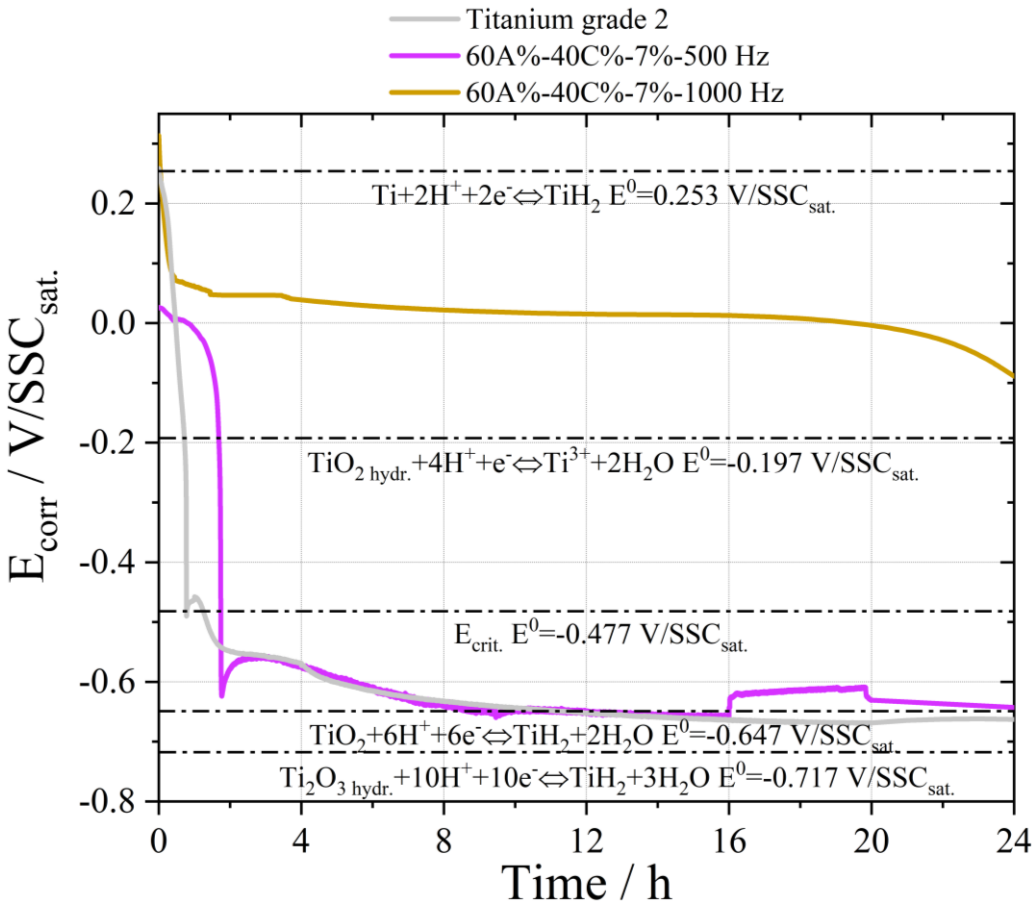

Figure 41: E_{corr} evolution of Ti grade 2 (in gray) and samples presenting worst (in purple), and best (in orange) corrosion behavior in sulfuric acid.

Such intermediate potential (~ - 0.48 V/$SSC_{sat.}$) corresponds to a critical value ($E_{crit.}$) below which Ti is considered completely active [155]. For potential more cathodic than $E_{crit.}$ it is reasonable to assume the electrode as covered by a monolayer of adsorbed species or by a reduced form of TiO_2 like Ti_2O_3 [145]. Sample 7 – 500 presented a similar behavior confirming no substantial improvements with respect to uncoated Ti. On the other hand, sample 7 - 1000 held passivity for all the 24 h of immersion. To better investigate the reasons behind these trends EIS will be applied on all samples and results highlighted in the form on Nyquist and Bode representations.

Starting from Ti grade 2 data were collected at 1, 4, 20 and 24 h of immersion in sulfuric acid (**Figure 42**) and two time constants were always observed, one at low (~ 10^{-1} Hz) and the other at high frequency (~ 10^{2} Hz) suggesting the occurrence of a reaction ruled by two activation energies.

As E_{corr} was always in the active region and provided the abundant amount of gas developed over the electrode surface it is reasonable to relate the two time constants to the development of a multi - step

faradaic reaction with adsorption intermediates like HER. In particular the high frequency portion of the EIS spectrum should be related to charge transfer while the low frequency one to adsorption/desorption [188–191].

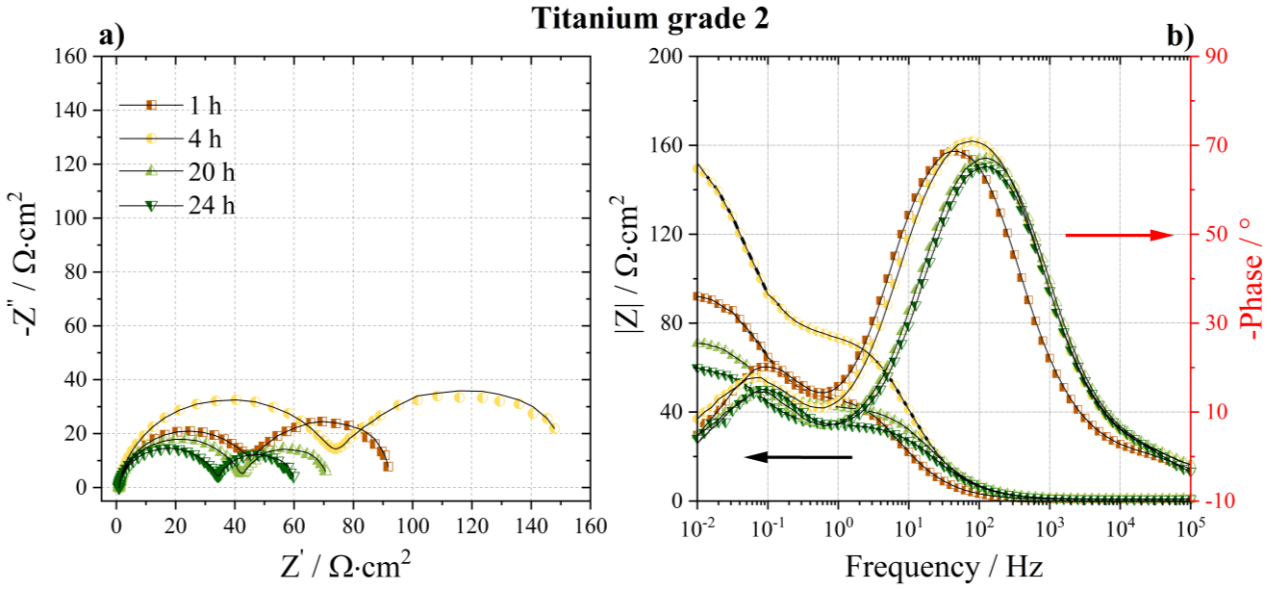

Figure 42: a Nyquist and **b** Bode plot for non-anodized Ti.

According to the corrosion process as immersion time increases both semicircles decrease their diameters and interestingly, data collected after 1 h of immersion were smaller than Z collected after 4 h, correlating with the position of E_{corr} which after 1 h immersion was much more similar to $E_{crit.}$. Comparison of Nyquist plots in **Figure 42a** allowed to understand that the cathodic reaction was initially controlled by the adsorption/desorption step (higher diameter of the low frequency semicircle) but at high immersion time the process switched to charge transfer control, as a consequence of the complete reduction of the native TiO_2 layer. A more complex behavior was found for sample 7 – 500 (**Figure 43**), where the initially larger semicircle diameters agree with the presence of the anodic film. Only one time constant appeared in the 1st h of immersion, corroborating the passivity of the electrode. After only 2 h of immersion, the drop of E_{corr} and visual observation confirmed coating debonding: consequently a third time constant appeared at intermediate frequency (in between $10^0 \div 10^1$ Hz). However, after an immersion time more or less coincident with the complete removal of the oxide layer impedance data saturated towards the ones of untreated Ti grade 2. A simpler electrochemical response was observed in case of sample 7 – 1000 (**Figure 44**) denoting the maintenance of a passive behavior for all the immersion period.

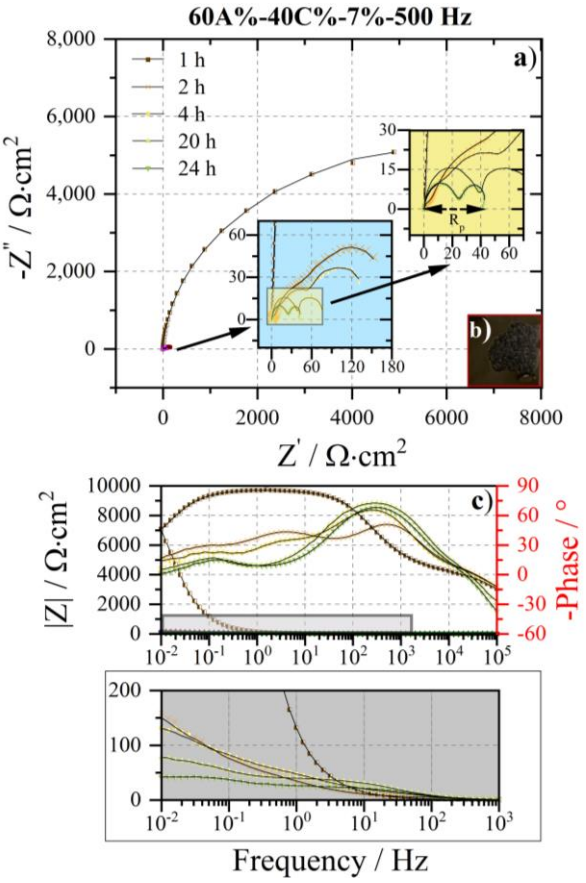

Figure 43: a Nyquist plot **b** highlight of delaminated 7 – 500 oxide and **c** consequent Bode plot of sample 7–500 immersed in 10% v/v H_2SO_4 at 60 °C in aerated environment.

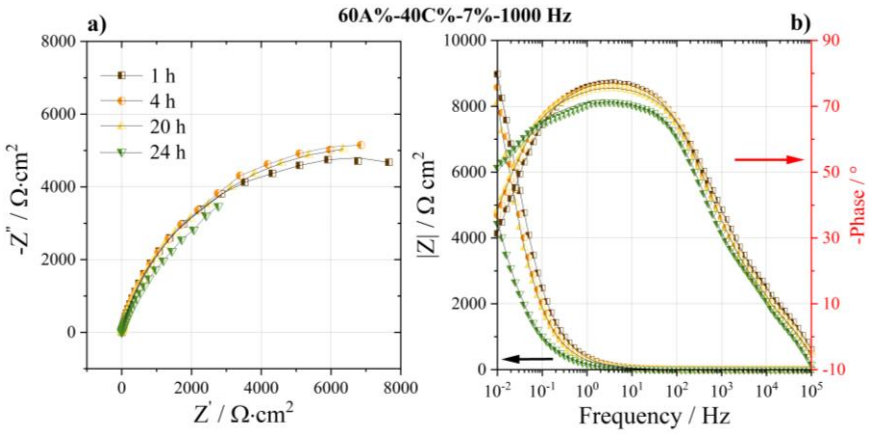

Figure 44: a Nyquist and **b** Bode plot of sample 7 – 1000 immersed in 10% v/v H_2SO_4 at 60 °C in aerated environment.

Apart from qualitative information extracted simply by simple inspection of the Nyquist representations circuit fitting analysis, using a Voigt model modified by the addition of an inductance L to account the high frequency set-up related features (**Figure 45c**), was used.

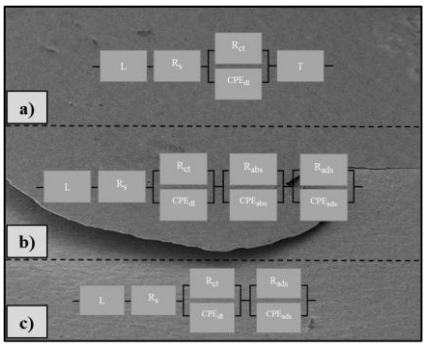

Figure 45: Circuit models used to describe Ti **a** in passive state, **b** with a delaminated oxide and **c** in active state.

Results regarding untreated Ti grade 2 are collected in **Table 25**:

Table 25: Electrochemical parameters obtained from EIS tests carried out on Ti grade 2 immersed in 10 %v/v H_2SO_4 at 60 °C. R_p refers to LPR test carried out immediately after the corresponding EIS.

Time (h)	E_{corr} (V/SSC$_{sat.}$)	R_{ct} ($\Omega \cdot cm^2$)	C_{edl} ($\mu F \cdot cm^{-2}$)	R_{ads} ($\Omega \cdot cm^2$)	C_{ads} ($mF \cdot cm^{-2}$)	R_p ($\Omega \cdot cm^2$)	χ^2
1	-0.459	44.7	480	50.9	36.4	96.8	$1.31 \cdot 10^{-3}$
4	-0.573	72.5	213	85.1	24.2	132.1	$2.63 \cdot 10^{-3}$
20	-0.669	41.3	190	30.9	69.6	70.5	$6.38 \cdot 10^{-3}$
24	-0.643	33.3	210	26.5	71.1	59.4	$5.44 \cdot 10^{-3}$

Given the good reproducibility only average values are presented. CPE where converted into effective capacitances according to Brug's equation (**Equation 24** [99]):

$$C_{eff} = Y_O^{\frac{1}{n}} \left(\frac{1}{R_s} + \frac{1}{R_M} \right)^{\frac{n-1}{1}} \quad (24)$$

Generally obtained values were > than typical C_{edl} (10 ÷ 60 $\mu F \cdot cm^{-2}$) evaluated on metal oxide systems immersed in conducting media [151,192,193]. This is particularly true if considering C_{ads} extracted from the low frequency portion of the spectrum, whose high value ($mF \cdot cm^{-2}$) is similar to pseudocapacitances arising from faradaic reactions validating the hypothesis of adsorption/desorption of electroactive species like H^+. On the other hand, values extracted from the high frequency portion C_{edl} very well agreed with literature data of experiments performed in similar conditions [155]. To confirm the results linear polarization resistance (LPR) tests were immediately performed after EIS allowing the estimation of R_p as in **Table 25** and whose value was found to precisely correspond to $R_{ct} + R_{ads}$, i.e., the faradic impedance at $\omega \rightarrow 0$ in presence of hydrogen adsorption limitations coupled with evolution (no diffusion or absorption controlling the process) [194]. As a further prove of the quality of the result a corrosion current i_{corr}^{WL} was extracted from weight - losses and compared with the evolution in time of both $R_{\omega \rightarrow 0}$ and the resistance associated with the largest loop diameter, assumed

to account for the rate determining step, R_{rds} (**Figure 42a**) of the cathodic reaction responsible for the corrosion of the electrode.

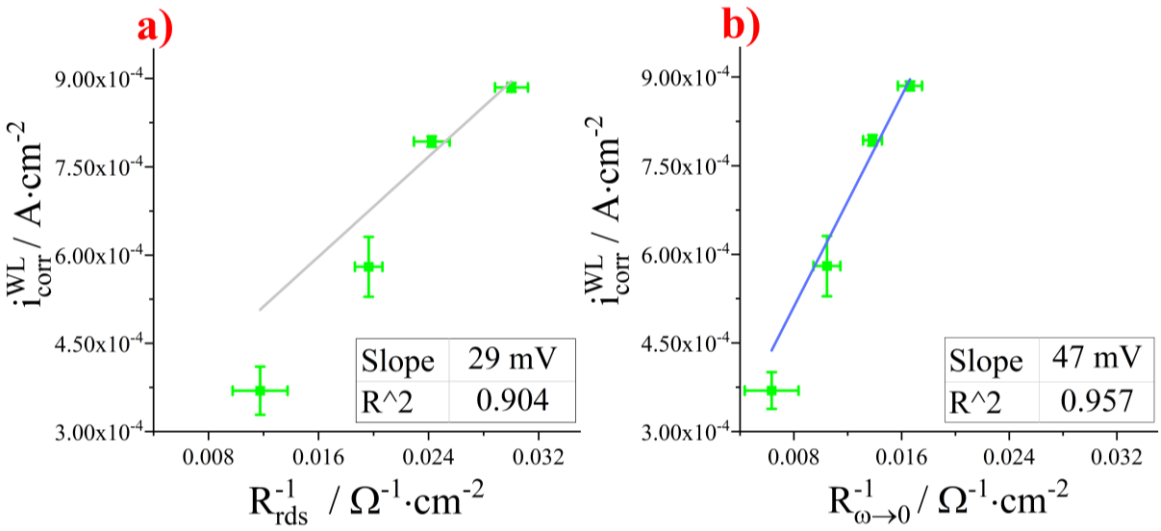

Figure 46: Linear fit of i_{corr} WL with **a** R_{rds} and **b** $R_{\omega \to 0}$ extracted from EIS at different time intervals.

Figure 46 demonstrates an interesting linearity between i_{corr}^{WL} and both $R_{\omega \to 0}$ and R_{rds} obtained from EIS. Consequently an equivalent Stern-Geary coefficient $B_{Eq.}$ was extracted from the slope. With the aim of obtaining anodic Taffel coefficients from $B_{Eq.}$ the cathodic Tafel slopes b_c were extracted according to investigation of the high over-voltage region: for sake of briefness only results related to Ti grade 2 in a solution of 10% v/v H_2SO_4 at 60°C are presented and the linear fit of the region of interest was selected according to the following simple rules:

- $\eta > 120$ mV.
- Linearity should be verified at least on one decade of "i".

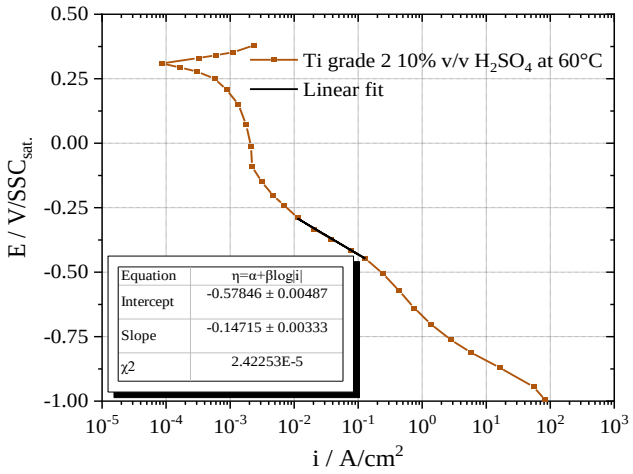

Figure 47: cathodic polarization of Ti grade 2 in sulfuric acid and linear fitting of the high overvoltage region for Tafel parameter extraction.

Polarization curve was plotted in **Figure 47** after 15 min of E_{corr} stabilization. Origin software was used to perform the linear regression and results highlighted in the insert of **Figure 47**. Here the "i" range adopted for b_c estimation was:

$$0.011\ A\cdot cm^{-2} < |i| > 0.1247\ A\cdot cm^{-2} \rightarrow \eta = -0.57 - 0.147 \log|i|$$

b_c values and related anodic parameters (b_a) are collected in **Table 26**.

Table 26: CR and collection of electrochemical parameters.

Time h	CR^{WL} $mm\cdot year^{-1}$	CR^{EIS} $mm\cdot year^{-1}$	b_c $mV\cdot dec^{-1}$	$b_a^{\omega\rightarrow 0}$ $mV\cdot dec^{-1}$	b_a^{rds} $mV\cdot dec^{-1}$
1	5.04	4.90	0.147	408	122
4	3.03	2.93	0.143	442	125
20	6.21	6.04	0.145	424	123
24	7.69	7.48	0.149	393	120

Interestingly, considering $B_{Eq.}^{rds}$ a value of b_a near 120 $mV\cdot dec^{-1}$ was found, compatibly with the monovalence of HER and the nature of the metal while calculations associated to $B_{Eq.}^{\omega \rightarrow 0}$ gave inacceptable results. Since titanium is a metal generally not showing a Tafel kinetics in the anodic direction [195] b_a values should be considered only as a demonstration of the quality of the procedure but other routines must be adopted for CR extraction avoiding the use of Tafel parameters. With this aim, considering the low overvoltages applied during EIS, the Butler - Volmer relation was expanded at the 1st order to obtain the exchange current density corresponding, for a corrosion process, to i_{corr} **Equation 25** [97]:

$$i_{corr} = \frac{R_G T}{zRF} \qquad (25)$$

Posing $R = R_{rds}$ and considering an equivalence of 1 e^- (according to the monovalence of HER) values collected in **Table 26** were obtained. It is possible to see that the procedure well approximated CR^{WL} calculated from i_{corr}^{WL}. Further EIS tests were conducted purging the solution with N_2 (**Figure 48**) to demonstrate the assumption previously attributed to the nature of the two capacitive loops. After 45 min of immersion, the two loop diameters were considerably lowered with respect to the corresponding aerated condition. This was attributed to inhibition of the Ti tendency to passivate, making the process charge transfer controlled. Surprisingly, in an extreme way the disappearance of the low frequency loop occurred after ~ 90 min of immersion. In this condition b_c = 124 $mV\cdot decade^{-1}$ and $E_{corr} = -0.516$ V/$SSC_{sat.}$, according to typical HER, as a result of the lower tendency of TiO_2 or other lower valence oxides to form. Furthermore hydrides instability, observed once E_{corr} approached $E_{crit.}$ [196], should contribute to the observed behavior, thus favoring H^+ adsorption with R_{ct} saturating to ~ 20 $\Omega\cdot cm^2$.

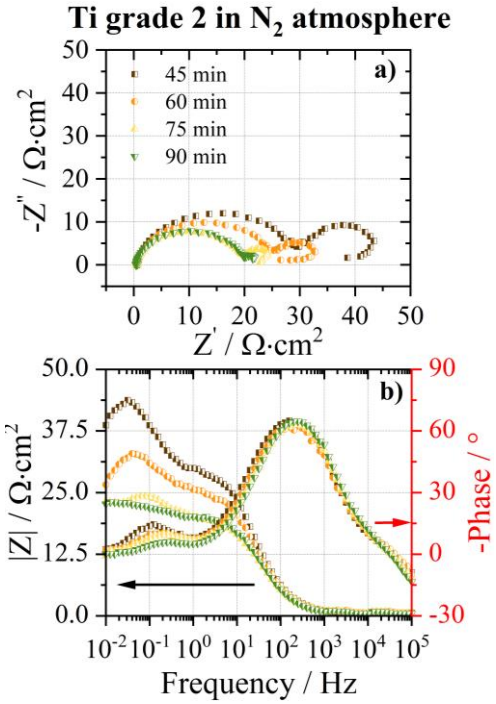

Figure 48: a Nyquist and **b** Bode spectra of Ti immersed in 10% v/v H_2SO_4 at 60 °C in deaerated environment.

The increase in conductivity enhanced by the extensive adsorption of electroactive species, combined with the high corrosion rate as a consequence of deaeration (evaluated by weight - loss to be 15.01 mm·year^{-1}) favored the development of a maximum in the |Z| plot at low frequency. **Table 27** collects parameters extracted from circuit fitting of spectra related to sample 7-500:

Table 27: Electrochemical parameters obtained from EIS tests carried out on sample 7 – 500 immersed in 10 %v/v H_2SO_4 at 60 °C. R_p was estimated from LPR tests carried out immediately after the corresponding EIS.

Time h	**E_{corr}** V/$SSC_{sat.}$	**CR^{WL}** mm·year^{-1}	**CR^{EIS}** mm·year^{-1}	**R_{ct}** Ω·cm^2	**C_{dl}** µF·cm^{-2}	**R_{MF}** Ω·cm^2	**C_{eff}^{MF}** µF·cm^{-2}	**R_{ads}** Ω·cm^2	**C_{ads}** mF·cm^{-2}	R_p Ω·cm^2	$\chi^2 \cdot 10^{-3}$
1	-0.173	/	0.03	/	/	7954	1047	/	/	7542	2.36
2	-0.627	/	1.88	3.44	256	47.8	755	132.3	11.6	147.2	5.83
4	-0.578	/	2.56	11.4	285	40.7	797	97.4	9.0	139.3	5.11
20	-0.678	5.12	5.77	36.5	142	/	/	43.2	18.5	75.7	3.84
24	-0.618	8.02	10.84	23.0	149	/	/	20.9	25.0	48.4	2.15

It is possible to see that R_p dropped by almost two orders of magnitude as the coating started to detach from the substrate. Consequently common phenomena related to HER, like charge transfer and H^+ adsorption, developed. The 3rd time constant, observed at middle frequency, was attributed by Lasia *et al.* [190] to proton absorption. Consequently this further potential - dependent process required an additional R-CPE parallel added in series with respect to the previous circuit (as in **Figure 45b**). However, as this loop disappeared once the coating fully detached from the metal and more cathodic E_{corr} established the spectra overlapped to the one of pristine Ti where absorption was so fast to make the third time constant no more discernable. CR were evaluated again from weight - losses, but only

values picked up at 20 and 24 h were considered compatibly to the resolution of the apparatus. Slight deviations between CR^{EIS} and CR^{WL} were observed at 20 h probably caused by the initial presence of the coating while in the last 4 h of immersion the rapid increase of CR^{WL} was probably determined by the action of the residual coating acting as a crevice former [108]. This further evidence allows to say that PEO coatings if not properly done can detrimentally affect the final behavior of the electrode. **Table 28**, referred to sample 7 - 1000, demonstrated smaller values of capacitance compared to other samples, compatibly with the lower amount of faradaic reactions, like oxide reduction, occurring on it. This can be related to the abundant presence of the more stable rutile phase, well known to be characterized by a smaller crystal lattice volume probably offering a better protection towards H^+ intercalation [197].

Table 28: Electrochemical parameters obtained from EIS carried out on sample 7 – 1000 immersed in 10 %v/v H_2SO_4 at 60 °C. R_p was estimated from LPR tests carried out immediately after the corresponding EIS.

Time h	**E_{corr}** $V/SSC_{sat.}$	**CR^{WL}** $mm \cdot year^{-1}$	**R_{ct}** $\Omega \cdot cm^2$	**C_{dl}** $\mu F \cdot cm^{-2}$	R_p $\Omega \cdot cm^2$	χ^2
1	+0.059	/	9145	216	8887	$5.25 \cdot 10^{-3}$
4	+0.057	/	9410	225	9274	$3.03 \cdot 10^{-3}$
20	+0.021	/	8766	222	8543	$5.08 \cdot 10^{-3}$
24	-0.112	0.032	4031	240	4191	$2.02 \cdot 10^{-3}$

When the sample was passive the electrochemistry was described according to the circuit highlighted in **Figure 45a** including a Finite Space Warburg element (T), in series to an R-CPE parallel, accounting for diffusion related phenomena [100]. This choice is common when dealing with reflecting boundaries showing – phase angles > - 45 °. However, in the initial hours of immersion this should not be the case as – phase angles were less negative than - 45 °. Only after 24 h of permanence in the acidic solution it assumed values more negative than - 45 °, sign that the diffusing charges started to feel a reflecting boundary. Despite that, the use of a Finite Length Warburg (FLW), used in case of absorbing/transmitting boundaries (and so – phase angle < 45 °), did not allow convergence of the fitting process hence the use of FSW was proposed according to the fact that the finite diffusion process developed with a characteristic frequency ω_D (for sample 7 - 1000 corresponding to ~ 2-3 Hz) too low for allowing a complete detection by EIS. In fact, with respect to ω_D only two additional frequency decades were provided by the test to detect the presence of a reflective condition, making the use of a wider frequency window necessary. Accordingly, as after 24 h ω_D became ~ 187 Hz the phase angle at 10^{-2} Hz overcame – 45 ° making consistent the previous hypothesis. **Equation (26)**

offers the opportunity to extract diffusion related parameters, collected in **Table 29**, like R_D corresponding to a low frequency diffusion related resistance

$$Z_o = R_D \frac{coth\left(\sqrt{\frac{j\omega}{\omega_D}}\right)}{\sqrt{\frac{j\omega}{\omega_D}}} \quad (26)$$

and the already defined ω_D used to separate a pure Warburg diffusion process (for $\omega > \omega_D$) from finite diffusion (for $\omega < \omega_D$).

Table 29: Diffusion parameters for electrodes in passive state.

Time h	**E_{corr}** V/$SSC_{sat.}$	**L_D** µm	**R_D** Ω·cm^2	**C_D** mF·cm^{-2}
7-500 1 h	-0.173	7.6	6.56	0.855
7-1000 1 h	+0.059	57.1	49.15	6.363
7-1000 4 h	+0.031	33.5	31.12	3.473
7-1000 20 h	+0.021	24.7	26.11	2.259
7-1000 24 h	-0.112	7.4	10.13	0.525

L_D is the diffusion length, i.e., the distance from the oxide surface where the concentration of reactants decreases by a factor 1/e, calculated using **Equation 27**:

$$L_D = \sqrt{\frac{D}{\omega_D}} \quad (27)$$

being E_{corr} always > the redox couple Ti^{3+}/Ti^{4+}, which is the thermodynamic condition for H^+ intercalation to start, it is reasonable to assume the diffusion as a process occurring in the liquid phase. Accordingly Einstein equation can be used to calculate the diffusion coefficient D of H^+ [175], finding a value of 10^{-8} m^2·s^{-1} at 60 °C. As immersion time increased the diffusion length shortened compatibly with the concentration gradient established at higher coating permeation levels. Consequently, R_D decreased and as less H^+ were involved in the diffusion process, C_D changed accordingly. These parameters can be used to show that sample 7 - 500 presented, only after 1 h of immersion, similar values of permeation of sample 7 - 1000 after a prolonged immersion of 24 h.

4.4 Summary

The information collected in this research, focused on bipolar PEO applied on titanium grade 2, allowed the following conclusions to be drawn:

- *Corrosion resistant coatings were obtained*: when promoting high thickness (3/4 µm) and low porosity i_{corr} and i_{pass} were lowered and anodic dissolution avoided. On the other hand, if the

material should be utilized in low pH environments high thickness and high quantity of rutile play a major role with respect to compactness.

- *Cathodic polarization ruled PEO regime transitions*: when the cathodic potential was set to allow high I_c, strong alkalization and development of a negative surface charge enhanced plasma formation. Once the electrode started to be polarized with respect to HER, acidity restored the conditions necessary to suppress the plasma resulting in a non - barrier like growth leading to thicker oxides with less impurity retained from the electrolyte.
- *Frequency also altered PEO regime*: the strong accumulation of SO_4^{2-} and OH^- inside the diffuse layer when using high frequency amplified the plasma regime according to the formation of a potential barrier making more impervious the migration of ionic species.
- *EIS analyses gave important mechanistic insights*: this allowed to conclude that the corrosion process, initially adsorption controlled, became charge transferred controlled at prolonged immersion time. Moreover EIS allowed to understand that, if not properly done, a PEO coating can dramatically compromise corrosion performances of titanium exposed in hot low pH solutions.

Chapter 5 PEO oxide characterization

Until now only few authors [198] used the outstanding power of transmission electron microscopy (TEM) to extract local structural and morphological information from Ti oxides grown by PEO. A first attempt was done by Mortazavi *et al*. [199] studying the effect of different amount of current density on the anodic growth of Ti oxides produced in alkaline electrolyte (pH ~ 12). Coating substrate interface was characterized by the presence of nano-crystalline domains and nano-pores while the upper coating portion by a mainly amorphous layer. However, despite the long treatment time (> 1000 s) only modest thicknesses (< 3 μm) were reached, also justifying the quantity of amorphous material present according to the development of a not so intense plasma regime.

Apart from the opportunity to obtain high resolution images down to the atomic scale the outstanding lateral resolution of TEM can be exploited according to the use of electron energy loss spectroscopy (EELS). This technique allows to measure energy losses arising from inelastic scattering events between the analyzed material and the TEM e^- beam passing through it. This causes core level electronic transitions of the material under investigation making possible the extraction of chemical and solid-state information in a very competitive approach with respect to other techniques such as X-ray absorption near edge spectroscopy (XANES), down to a spatial resolution < 1 nm and an energy resolution even < 0.2 eV. Application of EELS on Ti requires a profound knowledge of the shape of the $L_{2,3}$ edges, corresponding to energy losses in correspondence of $2p \rightarrow 3d$ electronic transitions. By direct comparison of the obtained spectra with the ones present in databases it is possible to extract crystal structure information and the actual chemical bonding environment of the cation under study. In this way it is possible to discriminate among all the TiO_2 polymorphs in a very confident manner.

The EELS work was carried out at the Canadian Centre for Electron Microscopy, a facility supported by the Canada Foundation for Innovation under the Major Science Initiatives program, NSERC and McMaster University. It was decided to apply such powerful technique to study the effect of two main electrical parameters widely studied until now in the present dissertation, i.e.:

- Frequency
- Duty cycle

and how they modify crystalline and microstructure. The analysis will be approached considering the two main morphological features characterizing a PEO coating, i.e., barrier and porous layer. An innovative approach for data analysis and visualization will be applied on EELS images with the aim of constructing colored structural component maps, with each component corresponding to a

particular crystal structure. This allowed to extract thousands of spectra, from each pixel composing an EELS image, according to an homemade script written in Python language exploiting built in functions provided by the Hyperspy [200] package. According to this competitive strategy it was possible to link local structural information to the effect of previously defined macroscopic technological parameters thanks to the visualization of maps representing relevant oxide portion on the micrometers length scale.

5.1 Materials and Methods

Three electrical regimes were considered with the purpose of studying different conditions, i.e., direct current (DC), unipolar and hybrid where for hybrid it is intended the conjunction use of anodic (A%) and cathodic (C%) polarization separated by a rest period (R%) as in **Figure 49**. Following previous studies a solution of 0.5 M H_2SO_4 was placed in a 1 L Pyrex beaker for the conversion of titanium grade 2 (UNS R50400) coupons cut by metal sharing and presenting a volume of 10 x 10 x 1.6 mm^3. After incorporation into an epoxy resin samples were mechanically lapped with emery papers: 100, 320, 600, 800, 1200, 2400/4000 and alumina particles to obtain a mirror like surface with roughness down to 0.8 µm followed by sonication in ethanol for 5 minutes and washing in deionized water. The electrochemical cell was composed by a cylindrical activated Ti cathode with radius of 50 mm and magnetic stirring (1500 rpm) for solution homogenization.

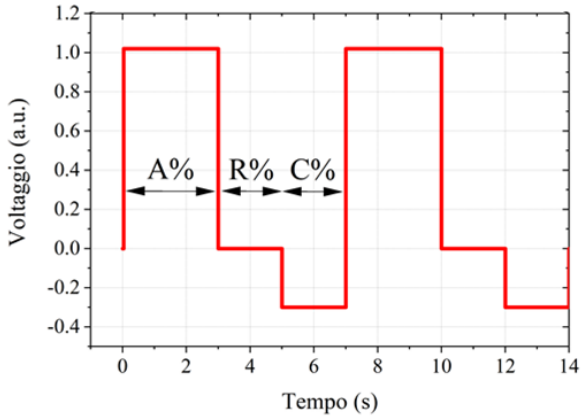

Figure 49: schematic representation of hybrid duty cycle.

The anodization signal was designed according to the fully programmable California Instruments Asterion 751 series AC/DC power source in a potential-controlled regime with forming voltage of 160 V reached though a constant voltage ramp of 0.5 $V \cdot s^{-1}$ (i.e. total treatment time = 320 s).

Table 30 summarizes all conditions tested and related sample labels. Current (*I*) and voltage (*V*) curves were acquired using a Tektronix TBS-1072B-EDU oscilloscope.

Table 30: list of anodization conditions employed in the present analysis.

Sample identifier	Duty cycle	Cathodic peak (%)	Frequency (Hz)
DC	DC	/	/
25-75-20	25A-75R (unipolar)	/	20
25-75-1000	25A-75R (unipolar)	/	1000
25-25-20	25A-25C-50R (hybrid)	5	20
25-25-1000	25A-25C-50R (hybrid)	5	1000

Focused Ion Beam (FIB) Zeiss NVision 40 was used to mill and extract an electron transparent lamella (~ 100 nm thickness) for TEM. Given the sample preparation with a protective top layer on the coating, with final thinning carried out at low energies, we expect the damage, induced by FIB operations, confined to few nm and uniform across the section. This can be considered as a reasonable confirmation of the absence of structural gradients through the lamella thickness. The sample was positioned onto a supporting grid and attached via electron beam deposition of a precursor gas, then stored into a double membrane layer. The bulk structure was firstly investigated by X-ray diffraction using a Bruker D8 Discover Vantec500 Co 2D and the diffractograms refined by Rietveld using GSAS II software. Then, the phase distribution was investigated with EELS exploiting a FEI Titan 80-300 TEM working at 300 keV with a field emission electron source equipped with an electron monochromator, allowing to improve the energy resolution to ~ 0.11 eV. As previously said EELS spectra were extracted according to a home-made script developed in Python environment, with the help of Hyperspy [200] where each spectrum was identified according to a rigorous investigation of the titanium oxide related EELS spectra, comparing reference data in the literature. The crystal structure was also confirmed according to selected area electron diffraction (SAED). Elemental composition of the coating was also studied according to glow discharge optical emission spectroscopy (GD - OES) using a SpectrumA ANALYTIK GDA 750 HR analyzer. Plasma activity, developed during PEO, was characterized by in situ optical emission spectroscopy (OES) with an Ocean Optics S2000 spectrometer equipped with a fiber optics P400-1-UV-VIS, capable of an overall spectral resolution ~ 0.3 nm in a window of 300-1100 nm.

5.2 Results

I and ***V*** waveforms at the ms time scale were collected always five seconds before the end of the four different treatments carried out in pulsed regime. Capacitive effects, like charging/discharging of the EDL, determined the presence of a *I* peak as the result of the voltage rise front, particularly accentuated when working at 20 Hz (**Figure 50a** and **c**). At 1000 Hz current damping was more consistent, probably because of the PEO frequency interfered a little bit more with the time scale

responsible for the EDL relaxation [201]. The lower *I* observed for sample 25-75-20, compared to 25-75-1000, is related to the higher resistivity provide by the growing coating.

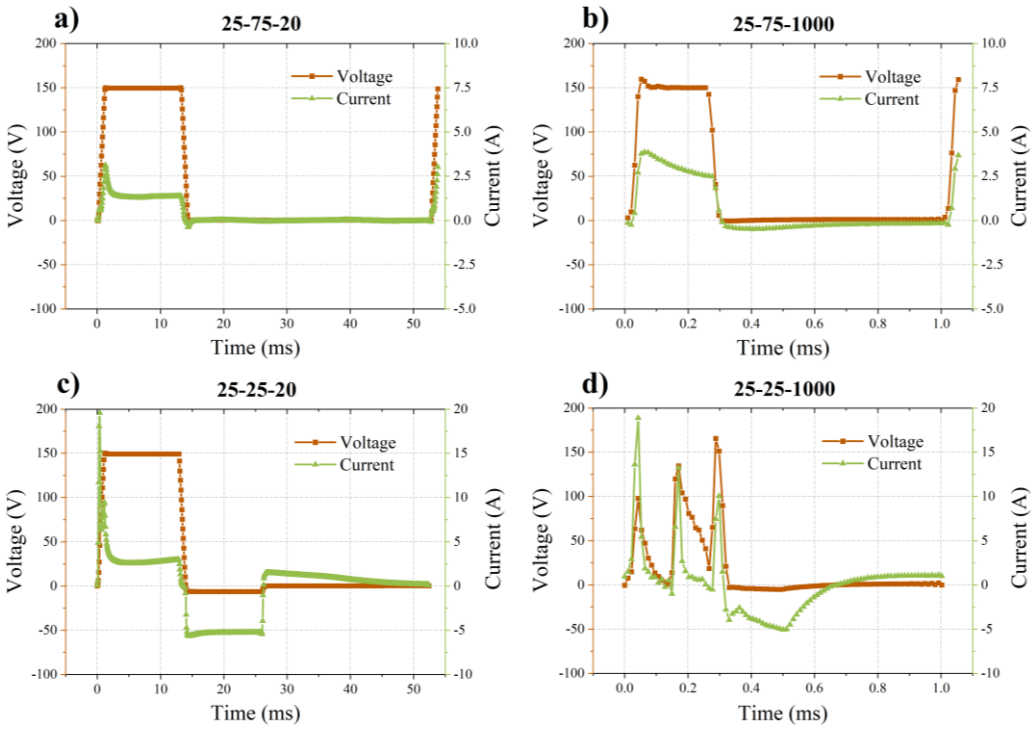

Figure 50: Current-voltage trend for pulsed anodized samples.

It was already shown in *section 4.3* the importance of collecting the charged passed during each half-cycle permitting to make hypothesis about the plasma regime developed over the electrode. In particular, making the ratio between cathodic and anodic charge and defining the usual parameter $R = \frac{Q_C}{Q_A}$ it appears evident how using different frequency keeping constant the duty-cycle (25-25-20 and 25-25-1000) promoted different R values, affecting the relative intensity between anodic and cathodic reactions. In fact, at 1000 Hz R = 0.84 while at 20 Hz a $I_c > I_a$ determined R = 1.01 demonstrating frequency to strongly modulates the transfer of charges [108]. However, the smooth *I* and *V* shape presented by sample 25-75-1000 (**Figure 50b**) indicated that frequency alone cannot be considered the only responsible of the different plasma regime encountered, indicating the need of other physical parameters, influencing the electrochemical environment, to be considered.

Bulk structural information extracted according to XRD, and collected in **Figure 51** in the form of diffractograms, indicates all the PEO coating to be mainly crystalline.

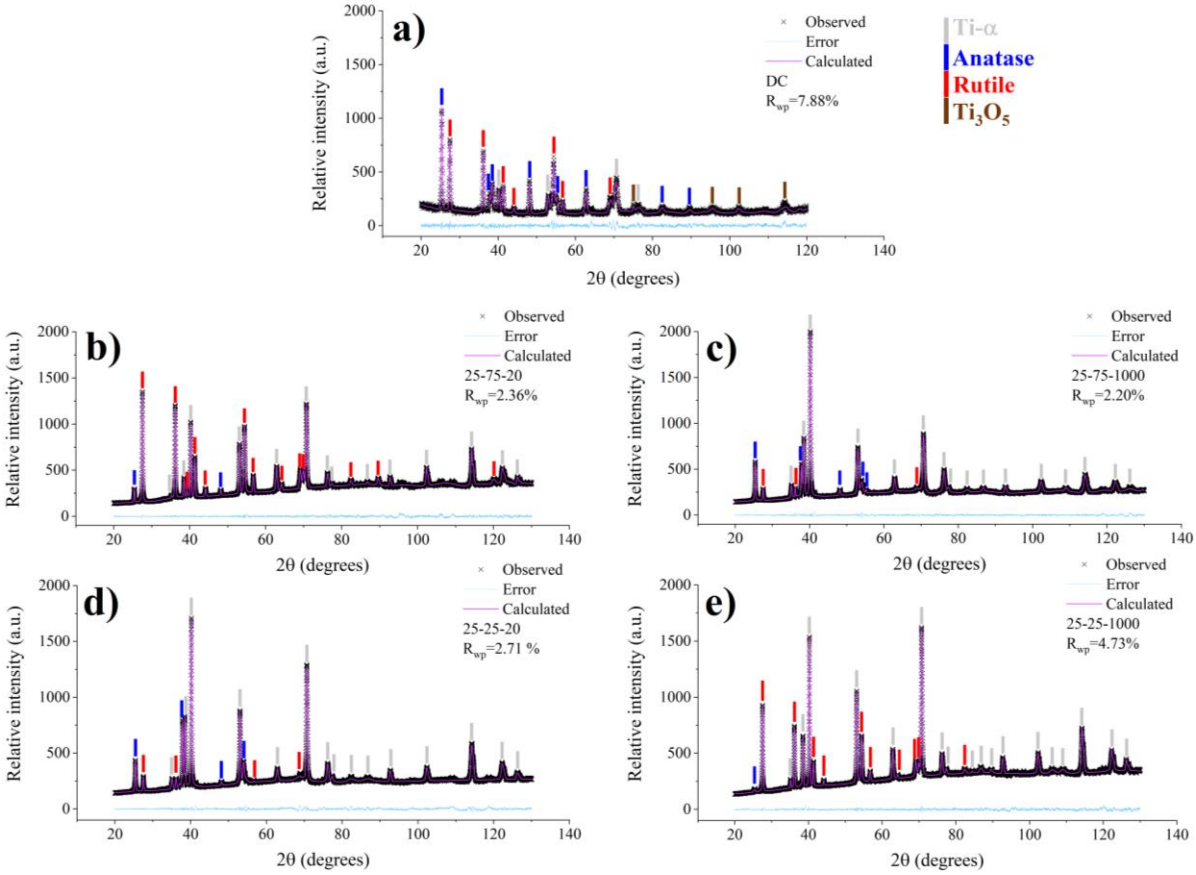

Figure 51: Rietveld refined XRD diffractograms of all anodized samples.

In particular, the condition 25-75-1000 (**Figure 51c**) provided the higher peak intensity related to metalic Ti compatibly with a lower coating thickness. Rietveld refinement was applied to extract additional knoledge: data were represented by black dots, while calculated and error values as purple and light blue lines. The following phases were identified: titanium, anatase, rutile and Ti_3O_5 and details of the crystalline structures collected in **Table 31**. As Ti_3O_5 peak intensities were too low to provide meaningful numbers, this phase will not be considered for quantification. DC PEO (**Figure 51a**) promoted higher quantity of anatase (~ 77.7%) leaving the rest mainly constituted by rutile. According to pulsed PEO, and confirmed by this analysis, it is possible to use duty cycle and frequency to modulate the relative amount of crystalline phases. In particular, if low frequency is employed in unipolar regime, the coating was mainly composed by ~ 94 % of rutile, while switching to high frequency (1000 Hz) anatase formation was favored (~ 72 %). This is in agreement with *I-V* plots of **Figure 50**: the lower *I* promoted for sample 25-75-20 suggests lower electronic contribution responsible for micro-arc proliferation and subsequent rutile stabilization [202]. An opposite trend is verified using a hybrid signal: in this case working at 20 Hz determined a structure mainly composed by anatase (~ 75 %) correlating with a similar *I* trend previously observed in sample 25-75-1000. The most interesting modifications were observed when increasing frequency with a hybrid duty cycle where abrupt *V* and *I* peaks, gas evolution, and violent light emissions strengthen the hypothesis of

type-B discharges to occur. As a result the coating was composed by ~ 92 % of rutile. Williamson-Hall analysis was performed separating the contribution of the two phases composing all the conditions tested (anatase and rutile) allowing to quantify the compressive residual deformation and the average crystallite size collected in **Table 31**.

Table 31: Williamson-Hall analysis result, D stands for crystallite size (nm) while ε indicates the lattice strain.

Condition	Anatase (%)	Rutile (%)	D_A (nm)	ε_A	D_R (nm)	ε_R
DC	77.7	22.3	20	$-8.12\cdot10^{-4}$	16	$-1.62\cdot10^{-3}$
25-75-20	94	6	18	$-1.82\cdot10^{-3}$	16	$-1.78\cdot10^{-3}$
25-75-1000	72	28	19	$-1.15\cdot10^{-3}$	18	$-1.37\cdot10^{-3}$
25-25-20	75	25	23	$-5.88\cdot10^{-4}$	21	$-6.94\cdot10^{-4}$
25-25-1000	92	8	/	/	18	$-1.38\cdot10^{-3}$

For sake of briefness only W-H plot of condition 25-75-1000 is shown in **Figure 52**:

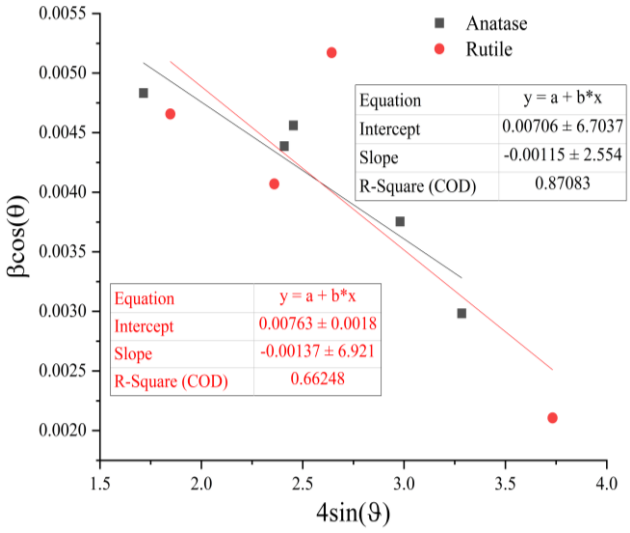

Figure 52: Williamson-Hall plot of sample 25-75-1000.

The presence of compressive stresses is a direct consequence of the high Ti/TiO_2 Pilling and Bedworth ratio [203]. Generally the choice of the electrical regime seems not to influence the dimension of the diffracting domains as only few deviations from average crystallite size were recorded for sample 25-25-20 responsible also for a lower residual deformation.

Having clarified the main phases involved in the bulk material, it is now the time to extract high-resolution structural information through the analysis of **electron energy loss near-edge structures**. The absolute energy position of the spectral features depends on the correct calibration of the zero loss peak. For this reason a more reliable approach is to consider the relative positions among the main peaks. Nonetheless, for sake of comparison with other studies, here we provide the absolute E position of Ti L_3 and L_2 edges observed at 457 eV and 462.5 eV [203,204], in comparison to

Stoyanov [205]: L_3 at 456 eV and L_2 at 462 eV. This small deviation is due to a relative calibration of the spectra without affecting the energy differences between the series of spectra and the Ti metal edges.

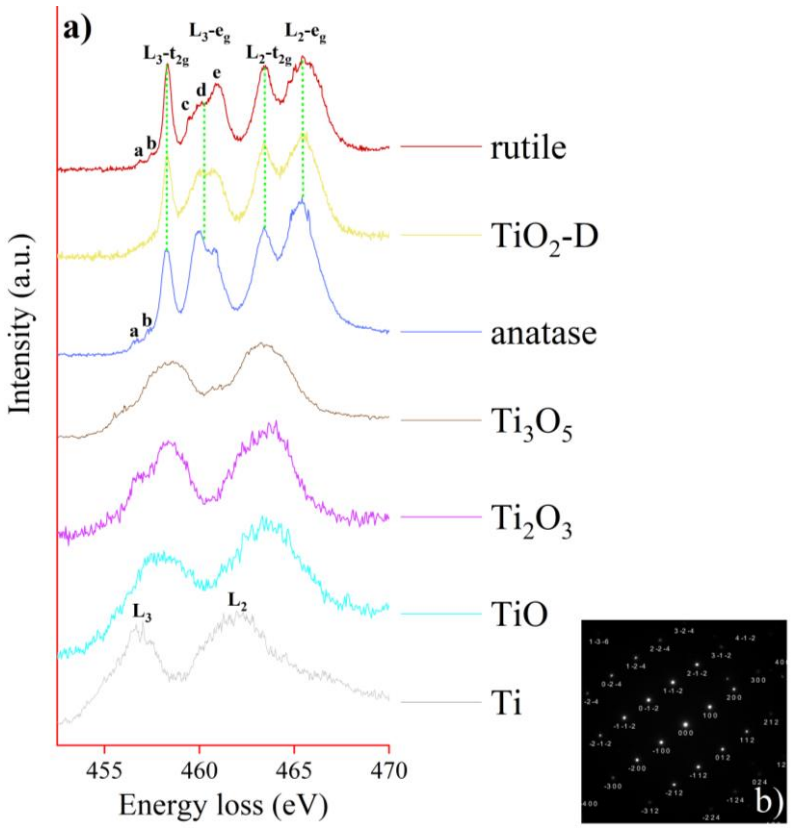

Figure 53: a EEL spectra of the main phases encountered in the present samples: **b** insert is the selected area diffraction pattern of metallic Ti.

A selected area diffraction pattern (SAED) was acquired from the same spot used to acquire EELS spectra on the Ti metal, reported in **Figure 53** in gray, confirming the Ti hcp structure of the substrate. Spectral intensities, related to the probability of a certain electronic transition to occur, were normalized with respect to the L_3 edge of Ti. This work found good agreement with the fine structures observed by Cheynet [206] working with an experimental apparatus able to provide a similar energy resolution (~ 0.11 eV evaluated at the FWHM of the zero loss peak). As the main peaks of the Ti L_3 and L_2 edges arise from e^- transitions between 2p orbitals and 3d unoccupied states EELS can be used to extract, in a very reliable manner, the oxidation state of the metal cation and information of the surrounding environment. As a consequence specific spectral features can be related to bonding symmetry, crystal field effects and degeneracy. Those concept can be clarified if looking at the spectral modifications arising from the shift (see **Figure 53**) from metallic Ti to oxide phases, characterized by the presence of Ti^{4+}, where the occurrence of a strong splitting of the $L_{3\text{-}2}$ doublet (each one splitting into t_{2g} and e_g peaks), attributed to crystal field effects occurred. Particularly informative of the state of the Ti-O bond is the L_3-e_g peak as the Ti 3d e_g orbitals point directly

towards the ligand. This can easily differentiate anatase to rutile where the former presents a peak followed by a shoulder at higher energies and the latter polymorph two spread-out shoulders labelled "c" and "d" before the main feature ("e") (see **Figure 53a**). These differences were recognized also by other researchers [206] and attributed to the effect of long range band structure interactions permitting an easy discrimination of both crystal phases according to comparison with reference spectra of pure compounds. Other features are present before the L_3 t_{2g} labelled as "a" and "b", coming from atomic multiplets, consistent with simulations based on atomic theory [207] of Ti^{4+} in octahedral environment. Several other phases were found with valence in between metallic Ti and Ti^{4+} oxides presenting intermediate features along the energy loss diagram. The spectrum of TiO, presenting Ti^{2+} valence, was very similar to metallic Ti even if features are considerably broadened. The absence of crystal field splitting for TiO arises from the presence of two electrons populating the d-orbitals of the cation imparting to the material a metallic conductivity. Upon evaluation of 234 spectra a spin orbit splitting ~ 5.12 eV (stdev = 0.09) was found in good agreement with the one observed by Stoyanov *et al.* [205]: 5.19 eV. As the cation loses one d-electron, two shoulders, pointing towards lower energy, appeared concomitantly with a rightwards energy shift of ~ 0.2 eV of the whole spectrum. Radtke *et al.* [208] on Ba_2TiNbO_6 and Muller *et al.* [209,210] with $LaTiO_3$ found the same spectrum, clearly indicating without uncertainty the presence of Ti^{3+}. When the Ti^{4+}/Ti^{3+} ratio approached 1:2, the Ti_3O_5 spectrum presented features related to spin orbit splitting with energy separation ~ 5.43 eV, consistent with Stoyanov *et al.* [205] (309 spectra and stdev = 0.12) and two lower-energy and low-intensity shoulders.

At first glance the spectrum drawn in yellow color, of **Figure 53**, could be related to brookite [211,212] however this should not be the case as despite its abundancy, verified by EELS, no evidence was accounted according to bulk XRD analysis. A possible explanation could be related to the superposition of the L_3-e_g features of anatase and rutile, leading to a single broad and smooth peak however this fine structure manifested even when only one phase was present. A similar feature was observed also in the following materials:

- Sr and Ba titanates [213]: showing an octahedral geometry sharing corners instead of edges.
- Nanotubular geometries [214] where a lowering or even elimination of the e_g peak splitting occurs as a consequence of the lower crystal field effects.

As the broadening of a fine structure feature corresponds to a higher degree of hybridization between antibonding Ti e_g orbitals with the one of the ligand [215] a weaker Ti-O bond is expected [216]. This features will be particularly present in oxides with non-homogeneous structures, only partially

converted to rutile, or when a considerable quantity of impurities affects the crystal lattice, like in correspondence of the barrier region.

Based on spectral analysis of the main edges, a script for automatic crystal structure discrimination was developed in the Hyperspy data processing environment [200]. This allowed to extract much information from a single spectrum, such as the degree of oxidation of the metal cation, but also to average the results over thousands of similar spectra, making the output statistically consistent. An example of fine structures used as a marker to extract the degree of cation oxidation [216,217] is the intensity ratio between L_3-t_{2g} and L_3-e_g peaks and the crystal splitting occurring at the L_3 feature. In fact, a higher intensity of the L_3-t_{2g} peak indicates stronger hybridization between O 2pπ and Ti 3d orbitals. For example, as the metal cation valence passes from 4+ to 3+ (3d orbitals partially filled) it can be seen a sensible decrease of the t_{2g} intensity, as antibonding orbitals are populated. Accordingly **Equation 28**, defined here in after, will be used to assess an oxidation-level based on previous fine structures (labeled as O_x). A similar interpretation was provided by Bertoni *et al.* [218] to discriminate between amorphous and crystalline phases. However, Tian *et al.* [219] advanced doubts regarding this procedure as even amorphous structures showing crystal field splitting and crystalline phases not showing it can exist (e.g. cubic TiO [205]). As in our research, supported by a huge amount of data, a rigorous agreement with L_3 crystal field splitting will be demonstrated (known to be very indicative of the cation valence) we believe this parameter to be more indicative of the valence state of the metal. For a better interpretation of **Equation 28**, **Figure 54** shows three different EEL spectra with a different level of Ti valence and good correlation between O_x and ΔL_3.

$$O_x = \frac{I_{L_3}^{t_{2g}} - I_0}{I_{L_3}^{t_{2g}}} \cdot 100 \qquad (28)$$

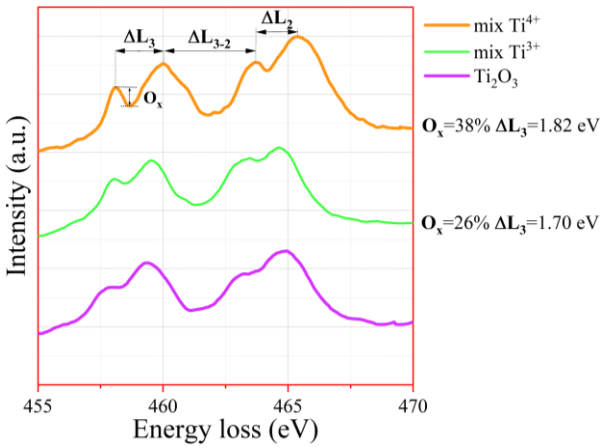

Figure 54: Representation of the parameters used to discriminate the degree of oxidation (O_x) and crystal field parameters applied on Ti_2O_3 (in purple), on a phase containing both Ti^{3+} - Ti^{4+} character (in green) and a phase showing stronger Ti^{4+} component (in orange).

The O_x parameter assumes a zero value in case of pure Ti^{3+} bearing phase like in the purple spectrum where pre-peak features are converted to shoulders. Since systematic variations of the O_x parameter were detected inside precise range of values different colors will be assigned to structures showing a different level of oxidation. For example, the material identified as "mix Ti^{3+}", drawn in green, was indicative of a mixed Ti 3+/4+ character (with prevalence of the former) showing a $21 < O_x < 27$. If a higher level of crystal field was present, with $\Delta L_3 \sim 1.82$ eV and $31 < O_x < 39$ indicative of a higher level of oxidation ("mix Ti^{4+}"), orange was used. Higher values of the O_x parameter were detected for the all TiO_2 polymorphs: in case of TiO_2-D, anatase and rutile in fact, it was comprised in between $44 < O_x < 73$. Another confirmation of the O_x parameter pertinence is its strict relation with the position of the main spectral feature along the energy loss scale. In fact, as the valence of the metal increases peaks undergo an energy shift towards higher energy losses. This was verified for "mix Ti^{4+}" where a shift of 0.36 eV towards higher energies occurred confirming higher oxidation of the cation. Furthermore, we provide here a collection of the splitting values between all the peaks encountered in the present analysis, (**Table 32** for barrier and **Table 33** for porous layer) as the outcome of several thousands of spectra, making the output statistically consistent. This in turns allowed to distinguish the principle structures composing the coatings presented in the following according to colored maps.

Table 32: relative position of the main edges extracted according to automatic procedure from the barrier layer.

Condition	Ti	TiO	Ti_3O_5	mix $Ti^{+3/+4}$	mix $Ti^{+4/+3}$	TiO_2-D	Anatase (%)	Rutile(%)
DC								
ΔL_3	-	-	-	1.68-0.05	1.78-0.03	1.82-0.10	-	-
ΔL_2	-	-	-	1.63-0.08	1.60-0.03	1.85-0.09	-	-
$\Delta L_{3\text{-}2}$	5.83-0.1	5.11-0.04	5.43-0.12	3.84-0.08	3.88-0.05	3.59-0.07	-	-
25-75-20								
ΔL_3	-	-	-	1.78-0.06	1.87-0.09	2.24-0.25	1.95-0.08	2.68-0.11
ΔL_2	-	-	-	1.66-0.08	1.82-0.13	2.08-0.11	2.00-0.09	2.26-0.09
$\Delta L_{3\text{-}2}$	5.76-0.11	-	5.65-0.25	3.80-0.08	3.67-0.13	3.24-0.25	3.53-0.09	2.81-0.11
25-75-1000								
ΔL_3	-	-	-	1.70-0.05	1.82-0.05	1.84-0.10	1.84-0.05	-
ΔL_2	-	-	-	1.60-0.11	1.85-0.11	1.88-0.10	1.89-0.07	-
$\Delta L_{3\text{-}2}$	5.89-0.12	-	5.58-0.35	3.93-0.09	3.71-0.09	3.67-0.12	3.67-0.06	-
25-25-20								
ΔL_3	-	-	-	1.72-0.12	1.81-0.08	2.08-0.39	1.81-0.08	2.65-0.28
ΔL_2	-	-	-	1.71-0.09	1.73-0.08	1.98-0.21	1.91-0.13	2.14-0.17
$\Delta L_{3\text{-}2}$	5.64-0.37	-	5.57-0.29	3.82-0.13	3.89-0.08	3.43-0.40	3.69-0.14	2.81-0.26
25-25-1000								
ΔL_3	-	-	-	1.75-0.09	1.83-0.07	2.05-0.31	1.86-0.08	2.76-0.08
ΔL_2	-	-	-	1.65-0.38	1.81-0.13	2.00-0.14	1.98-0.11	2.30-0.08
$\Delta L_{3\text{-}2}$	5.76-0.18	-	5.55-0.48	3.78-0.48	3.71-0.13	3.43-0.32	3.60-0.09	2.71-0.08

Table 33: relative position of the main edges extracted according to automatic procedure from the porous layer.

Condition	Ti	TiO	Ti_3O_5	mix $Ti^{+3/+4}$	mix $Ti^{+4/+3}$	TiO_2-D	Anatase (%)	Rutile(%)
DC								
ΔL_3	-	-	-	1.73-0.07	1.81-0.09	2.11-0.45	1.73-0.05	2.71-0.07
ΔL_2	-	-	-	1.62-0.09	1.68-0.14	2.06-0.20	2.01-0.09	2.25-0.08
ΔL_{3-2}	5.71-0.19	5.12-0.09	5.43-0.06	3.86-0.09	3.80-0.10	3.20-0.58	3.67-0.09	2.64-0.07
25-75-20								
ΔL_3	-	-	-	1.71-0.08	1.76-0.17	2.11-0.37	1.84-0.05	2.73-0.05
ΔL_2	-	-	-	1.59-0.08	1.81-0.07	2.05-0.14	1.97-0.06	2.28-0.09
ΔL_{3-2}	5.84-0.23	-	5.47-0.08	3.89-0.07	3.77-0.14	3.39-0.37	3.65-0.06	2.78-0.06
25-75-1000								
ΔL_3	-	-	-	1.66-0.04	1.85-0.04	1.93-0.24	1.84-0.05	2.68-0.05
ΔL_2	-	-	-	1.59-0.08	1.90-0.08	1.93-0.12	1.90-0.10	2.21-0.07
ΔL_{3-2}	5.71-0.20	-	5.45-0.58	3.89-0.11	3.64-0.06	3.55-0.24	3.64-0.08	2.80-0.05
25-25-20								
ΔL_3	-	-	-	1.65-0.06	1.80-0.04	2.23-0.41	1.83-0.04	2.74-0.04
ΔL_2	-	-	-	1.64-0.02	1.90-0.07	2.09-0.16	1.99-0.08	2.30-0.07
ΔL_{3-2}	5.68-0.50	-	5.42-0.34	3.63-0.12	3.69-0.06	3.26-0.41	3.64-0.07	2.75-0.05
25-25-1000								
ΔL_3	-	-	-	1.71-0.07	1.74-0.06	2.32-0.55	1.81-0.08	2.77-0.04
ΔL_2	-	-	-	1.57-0.08	1.70-0.12	2.07-0.25	1.93-0.24	2.33-0.07
ΔL_{3-2}	5.73-0.17	-	5.39-0.24	3.87-0.11	3.82-0.11	3.16-0.47	3.65-0.20	2.68-0.04

In **Figure 55** all the oxide lamella, which will be analyzed by EELS, are presented to understand the overall morphological differences.

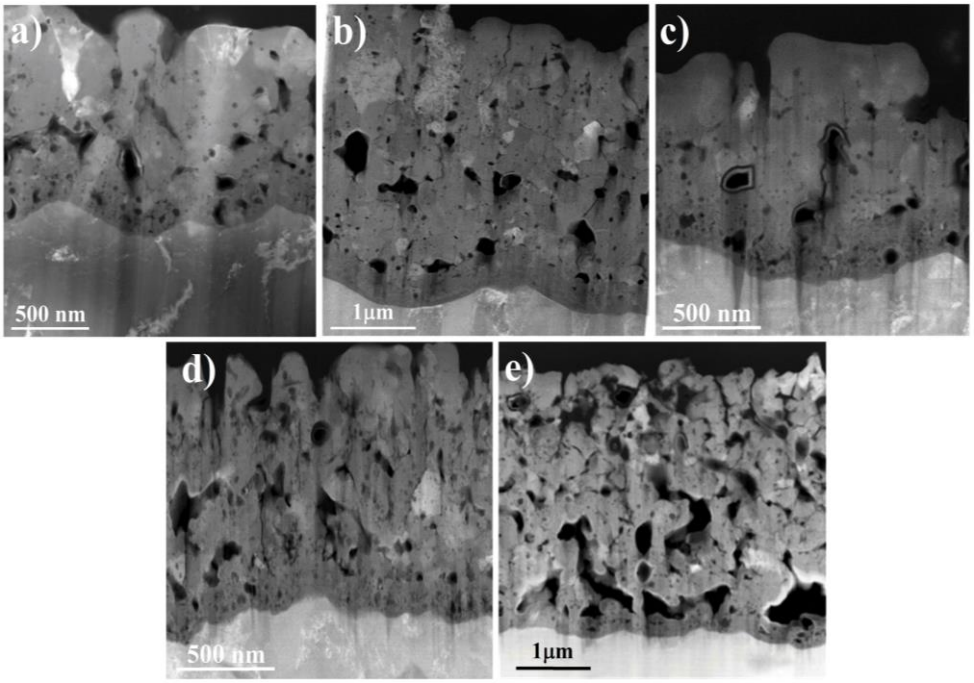

Figure 55: Oxide cross-section of sample **a** dc, **b** 25–75-20, **c** 25–75-1000, **d** 25–25-20 and **e** 25–25-1000.

As the different electrical parameters used in the present analysis strongly affected the few layers immediately in contact with the substrate (a region generally referred as **barrier layer**), a first attempt to clarify their structure is here provided, starting with **Figure 56** reporting results for sample "DC" where the components are discriminated based on the shape of the spectra color coded.

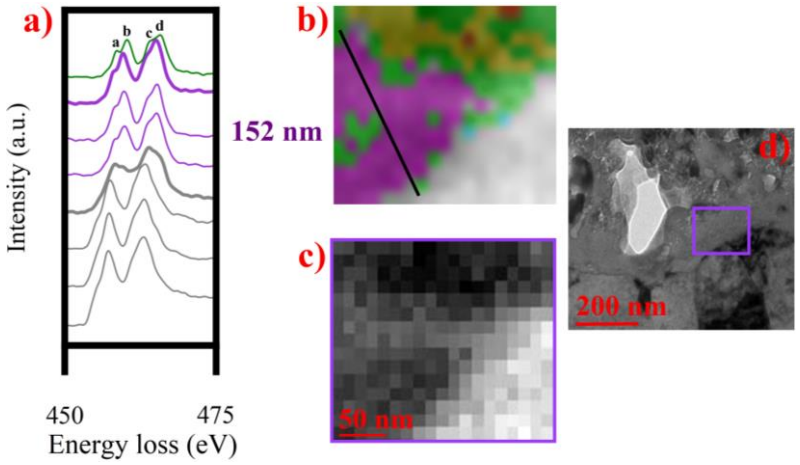

Figure 56: a EEL spectra of phases encountered during analysis of the DC oxide barrier layer; **b** EELS component map based on the spectra identified with a color in a) where gray corresponds to metallic Ti, green to mix-Ti^{3+}, purple to Ti_2O_3 and yellow to TiO_2-D; **c** Ti integrated signal map and **d** bright-field image of the DC coating interface with the identified region of interest for the EELS acquisition.

The use of DC field favored the formation of clusters of Ti_2O_3 (~ 152 nm thick in purple) alternated by "mix Ti^{3+}" (in green) and the presence of TiO crystals (in light blue) and TiO_2-D (in yellow). The slightly lower oxidation state of Ti_2O_3 with respect to "mix Ti^{3+}" is demonstrated by the presence of an energy shift ~ 0.48 eV. Calvert *et al.* [220] verified a similar structure in correspondence of grain boundaries in $CaCu_3Ti_4O_{12}$ (CCTO). Automatic discrimination was relatively easy between Ti_2O_3 and "mix Ti^{3+}": in fact the former phase was characterized by only two peaks with spin orbit splitting ~ 5.47 eV (stdev = 0.06 over 432 spectra) but with considerably finer features with respect to metallic Ti. The presence of small nanocrystals, in the barrier region, seems to be confirmed by the bright field image of **Figure 56d** even if not clearly resolvable in the first oxide layers in contact with the metal. Two layers stacked with respect to each other formed when a unipolar regime at low frequency was used (25-75-20). The first 65 nm were composed by an oxide with Ti^{3+} and Ti^{4+} character, indicating a partially higher oxidation state of the metallic cation with respect to sample anodized with DC field. Then a layer ~ 396 nm thick, largely composed by TiO_2-D, formed comprising also some traces of rutile (in red) and anatase (in blue). Prior two sublayers can be distinguished even looking at morphological features whose contrast can be enhanced according to dark-field analysis shown in **Figure 57d** where the 1st layer appears to be mainly composed of nano-domains while the 2nd clearly demonstrates the presence of grains with diameters of even hundreds of nm.

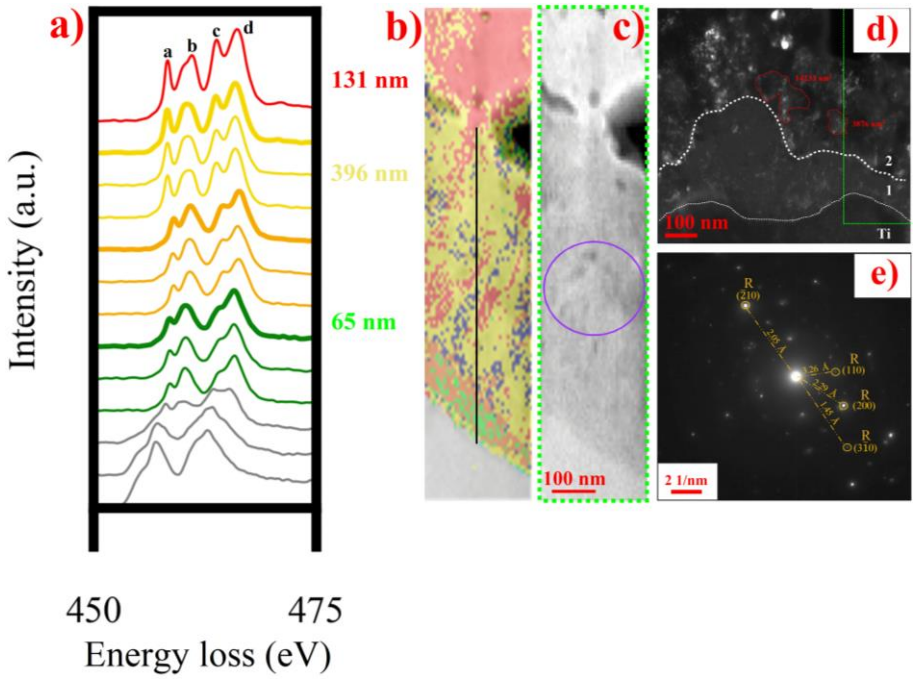

Figure 57: a EEL spectra of phases encountered during analysis of the 25–75-20 oxide barrier layer; **b** EELS component map based on the spectra identified with a color in a) where gray corresponds to metallic Ti, green to mix-$Ti^{3+,}$ orange to mix-Ti^{4+}, red to rutile, blue to anatase and yellow to TiO_2-D; **c** Ti integrated signal map; **d** dark-field image with the area identified for the EELS acquisition and **e** SAED pattern confined in the second layer.

The SAED pattern (**Figure 57e**) extracted in correspondence of the violet ROI, present in the 2nd layer of **Figure 57c**, indicates intermediate mono and polycrystalline features. Rutile planes, (110), (200), with satellites and streaks near the main diffraction spots are the most important features indicating the prevalence of a distorterted octahedral arrangement. As satellites near the main diffraction spots are attributed to crystal lattice distortions by the presence of foreign elements [221] GD - OES analysis, as in **Figure 58**, was carried out:

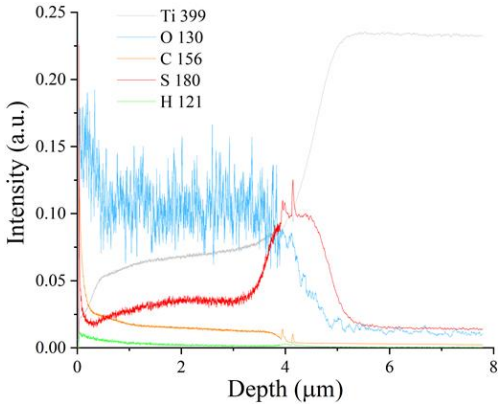

Figure 58: GD - OES profile of sample 25-75-20.

It is possible to notice a large accumulation of foreign elements, mainly retained from the electrolytic bath, like S, C, and H. As those elements generally tend to segregate inside octahedral sites, the bonding environment would be altered in accordance with the broadening of the L_3-e_g feature observed in the TiO_2-D spectrum.

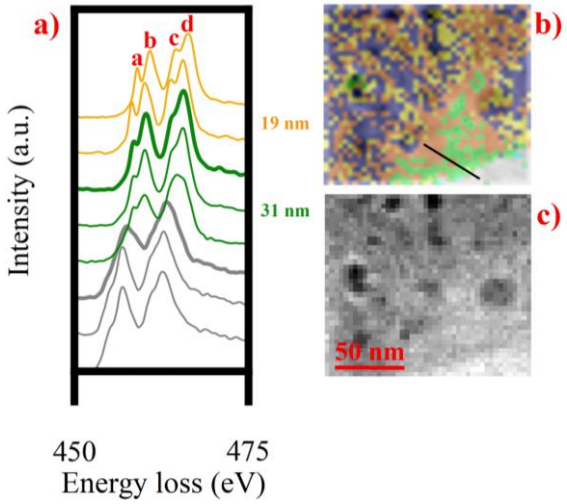

Figure 59: a EEL spectra of phases encountered during analysis of the 25–75-1000 oxide barrier layer; **b** EELS component map based on the spectra identified with a color in a) where gray corresponds to metallic Ti, green to mix-Ti^{3+}, orange to mix-Ti^{4+}, blue to anatase and yellow to TiO_2-D and **c** Ti integrated signal map.

Using a unipolar regime at high frequency (**Figure 59**) allowed to establish an oxide with mixed valence states where the first 31 nm, depicted in green, were characterized by prevalence of Ti^{3+} fingerprint. However, after ~ 19 nm thickness of "mix Ti^{4+}", the structure stabilized towards anatase (in blue) and randomly dispersed agglomerates of TiO_2-D (in yellow).

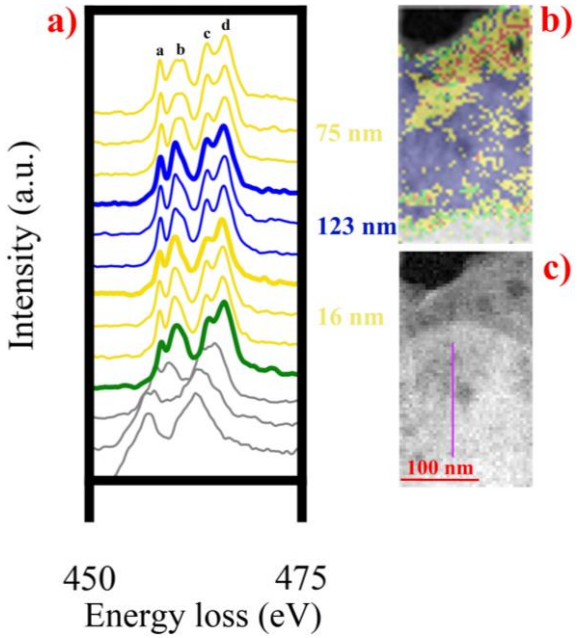

Figure 60: a EEL spectra of phases encountered during analysis of the 25–25-20 oxide barrier layer; **b** EELS component map where gray corresponds to metallic Ti, green to mix-Ti^{3+}, red to rutile, blue to anatase and yellow to TiO_2-D and **c** Ti integrated intensity map.

Differences were accounted when a hybrid duty, comprising cathodic polarization, was used. In fact, the valence transition leading to the establishment of Ti^{4+} bearing oxides seemed accelerated. In particular, when working at 20 Hz, immediately in contact with the metallic substrate, a 16 nm thick layer of "mix-Ti^{3+}" and TiO_2-D formed (**Figure 60b**). Then, the formation of ~ 123 nm of anatase (in blue), allows to speculate the idea that cathodic current can effectively favor coating oxidation.

Then, as the hole present in the upper portion of **Figure 60b** is approached, the same structural evolution seen before established, with "mix Ti^{3+}" material followed by a thick portion of defected TiO_2. A rather thick and variegated interface was observed when working with condition 25-25-1000. Differently from previous results this barrier region (see **Figure 61b**) was characterized by phases presenting only Ti^{4+} valence even in contact with the metallic substrate (~ 62 nm in orange). The first layers of material in contact with the holes left by plasma and gas bubble explosions is characterized by "mix Ti^{3+}" as the result of the de-oxidative condition promoted by high T and the presence of a slightly reducing atmosphere. In between the main phase constituting the present coating (i.e. rutile) ~ 258 nm of TiO_2-D developed also presenting some traces of anatase.

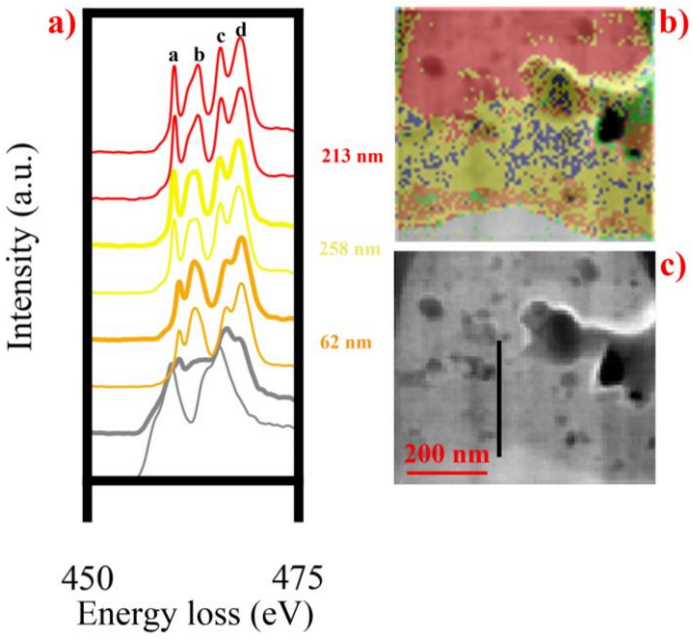

Figure 61: a EEL spectra of phases encountered during analysis of the 25–25- 1000 oxide barrier layer; **b** EELS component map based on the spectra identified with a color in a) where gray corresponds to metallic Ti, green to mix-Ti^{3+}, orange to mix-Ti^{4+}, red to rutile, blue to anatase and yellow to TiO_2-D; **c** Ti integrated intensity map.

Having characterized all the barrier regions of the coatings analyzed in the present research, in **Figure 62b** a first bright-field survey of the DC oxide, to highlight the **porous layer** features, is shown.

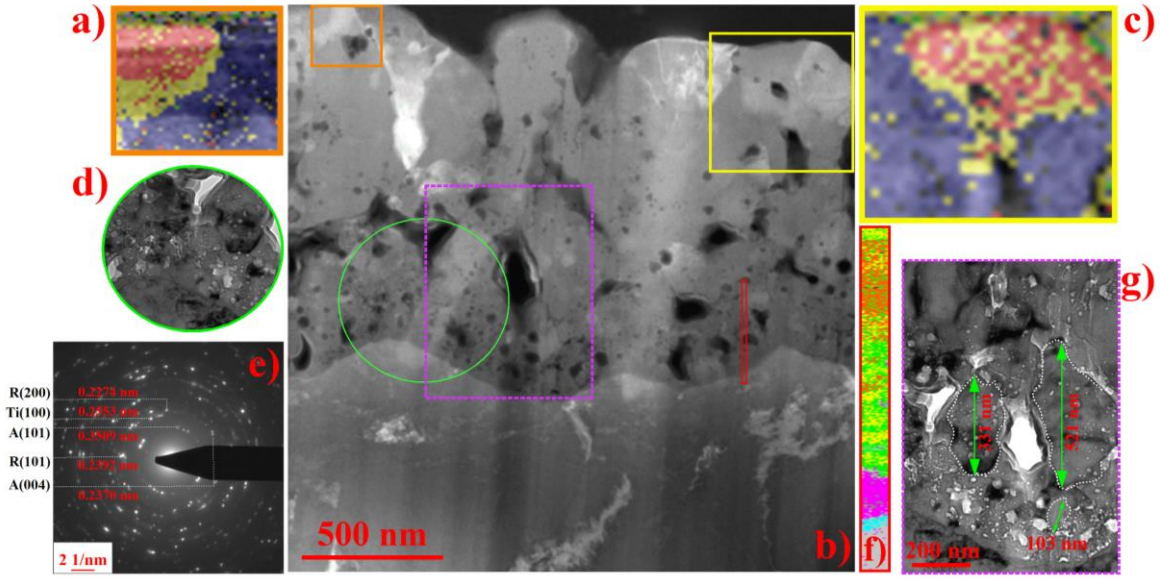

Figure 62: a, and **c** EEL component maps of the upper layer of the DC sample (anatase in blue, rutile in red and TiO_2-D in yellow); **b** bright-field overview; **d** detailed view of the area identified in green in Figure 62b from which the selected area patter shown in e) is taken, **e** SAED pattern collected in the barrier-porous region shown in d); **f** EEL component map highlighting structural evolution at the barrier-porous region (mix Ti^{4+} in orange, mix Ti^{3+} in green, Ti_2O_3 in purple and TiO in light blue); **g** bright-field magnified view of the barrier region to highlight grains.

The overall structure seems to be three layers in nature: a compact barrier, a porous intermediate and a relatively compact upper layer. Structures found by XRD analysis are confirmed according to EELS confined in the upper oxide portion where large clusters of rutile and anatase are alternated through the formation of layers of TiO_2-D ~ 24 nm thick. A high density of TiO_2-D particles can be seen, particularly inside rutile grains, while the anatase cluster appears more uniform. As the main phase detected by XRD was anatase, it is reasonable to say that the latter polymorph resulted in an incomplete thermodynamic transition to the more stable rutile, constituted by a final distorted crystal structure. A SAED pattern collected from the area identified with the green circle revealed that the intermediate oxide region was polycrystalline in fact, as can be seen in **Figure 62e** the electron diffraction contribution came from several small grains, denoting the presence of even Ti planes while the image in **Figure 62d** shows small bubbles of entrapped O_2 and H_2 gas [118,136]. A comparison of the interplanar distances, extracted from SAED and d-spacings evaluated according to XRD (card PDF 01-089-0553), are in good agreement apart from the rutile plane (101) conserving a deviation ~ 3.74 % due to compressive stresses arising from the high Pilling-Bedworth ratio (1.95 [222]) encountered in Ti-TiO_2 system, as previously demonstrated according to Williamson-Hall analysis. In **Figure 62f** an interesting structural gradient, with prevalence of TiO (light blue region ~ 8.5 nm thick) in contact with the metal established, similarly to what previously observed in **Figure 56b**. As the surface is approached the cation valence increases with ~ 50 nm of Ti_2O_3 (Ti^{3+} in purple) and 144 nm of "mix Ti^{3+}" (in green) also confirming the good spatial structural uniformity imparted by the treatment to

the growing oxide layer. The intermediate layer, characterized by a porosity band (generated by the abundant gas evolution) and a columnar structure with grains spanning from 100 (in contact with the barrier layer) to 500 nm (in the upper zone) presented a higher level of oxidation, described by an orange like color (orange layer ~ 103 nm thick) representing the "mix Ti^{4+}" phase.

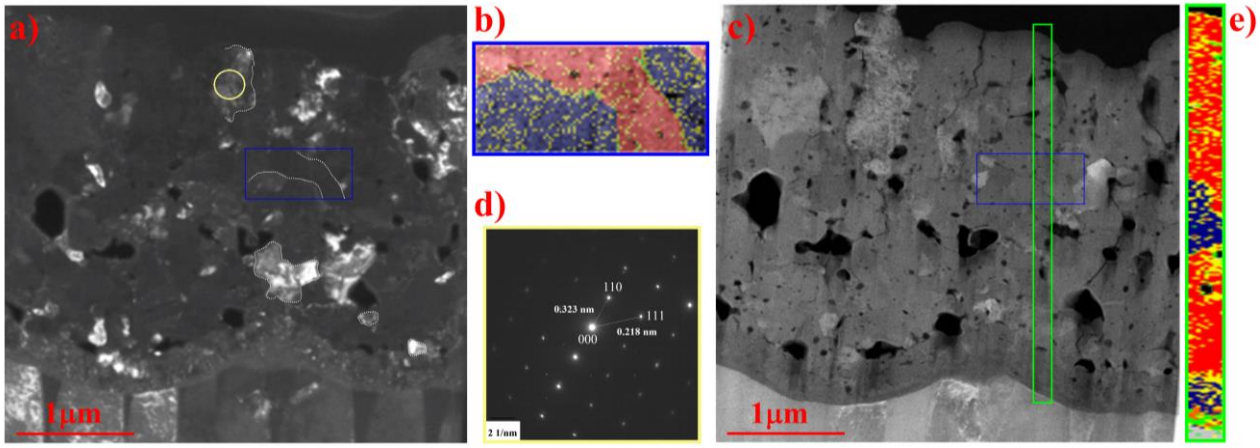

Figure 63: a dark-field image of sample 25–75-20; **b** EELS component map collected in the porous-upper region (anatase in blue, rutile in red and TiO_2-D in yellow); **c** bright-field oxide overview; **d** SAED pattern collected in the single grain located on top layer; **e** EELS component map highlighting structural evolution along all the coating thickness.

Oxide growth was favored if using the signal 25-75-20 enhancing thickness (see **Figure 63c**) to ~ 3.2 µm. EELS map shown in **Figure 63e** collected from the green ROI indicates the vast presence of rutile (in red, demonstrated by XRD to be the dominant phase) with even some traces of anatase. With respect to DC condition a sensible temperature variation of the electrolyte (~ 31 °C), during the oxide synthesis, demonstrates the development of a large amount of heat used to convert the structure to the most thermodynamically stable form of TiO_2 (i.e. rutile). Consequently, differently from what it was notice before, now a lower density of TiO_2-D grains is observed in correspondence of anatase clusters sign that now the thermodynamic equilibrium was shifted towards the stabilization of rutile. SAED collected on the top surface layer in **Figure 63d** allowed to understand the presence of large single rutile crystals with lattice parameters perfectly in agreement with the ones extracted from XRD analysis.

The huge amount of rutile found in the upper portion of the oxide (demonstrated thanks to SAED and EELS) is the reason why according to XRD a very small portion of anatase was found. According to EELS component maps of **Figure 63b** and **e** anatase is relatively abundant in intermediate regions where the x-ray signal can be subjected to a partial screening due to a sort of encapsulation effect [26]. In fact, this can strongly alter the XRD reflection intensities affecting the accuracy of the quantitative phase assessment [31,223]. According to the relatively compact morphology and the abundant presence of rutile in the upper portion of the oxide, plasma mainly developed on the surface without

compromising the inner integrity of the oxide. This affected considerably the grain size distribution, ~ 50 nm immediately above the barrier region to ~ 500 - 600 nm in the middle-upper portion, similarly to what previously observed when using a DC field.

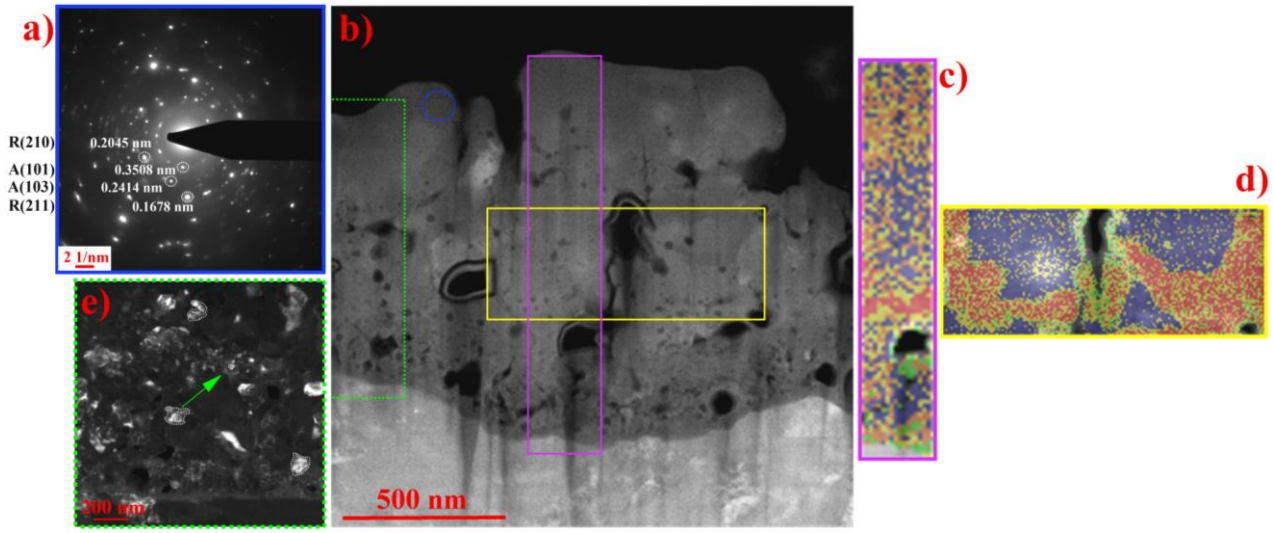

Figure 64: a SAED pattern collected in the upper layer; **b** bright-field image of sample 25–75-1000; **c** EELS component map collected along the coating thickness and **d** in the porous region (anatase in blue, rutile in red, mix Ti^{3+} in green and TiO_2-D in yellow); **e** dark-field image overview.

Using high frequency in unipolar regime (condition 25-75-1000) did not favor oxide growth, as only ~ 1.03 µm formed (**Figure 64b**). Structural investigation correlates with the relatively small thickness encountered. In fact the huge amount of TiO_2-D, particularly concentrated inside rutile grains, is a demonstration of the mild plasma activity developed. Both anatase and rutile planes resulted from SAED analysis confined in the blue region in proximity of the oxide surface showing polycrystalline features and lattice parameters in very good agreement with d-spacings extracted from XRD. Dark-field overview of **Figure 64e** highlights the presence of small nanograins (between 7 to 13 nm in diameter) with consequent arrangement of a chaotic phase distribution (see **Figure 64c**) alternating "mix Ti^{3+}" and "TiO_2-D". However, apart from this oxide portion, mainly confined in the upper region, the grain size remained quite constant throughout the thickness, with average size ~ 100 nm, considerably smaller with respect to previous cases.

Looking at **Figure 64d** it can be seen that holes are generally linked by elongated rutile grains demonstrating the phenomena causing voids formation as the main actor in favoring the production of heat and consequent phase transition. The microstructure was not altered if using a hybrid duty at low frequency confirming rutile nucleation to start in regions near the porosity band (see **Figure 65a**, **d** and **g**). A more ordered microstructure developed according to the lower TiO_2-D density and larger grains resulting in (~ 217 nm in the middle portion to ~ 414 nm on the topmost region) a lower density of grain boundaries. SAED analysis (**Figure 65e**) was used to confirm the phase mapping performed

by EELS: this allowed to verify a polycrystalline sample where the presence of multiple diffraction spots resulted from the comparable size between diffracting domains and SAED aperture diameter (~ 180 nm) whose lattice parameter generally agreed with d-spacing extracted from XRD (only for rutile plane (210) a significant deviation due to compressive stress arose ~ 1.99 %).

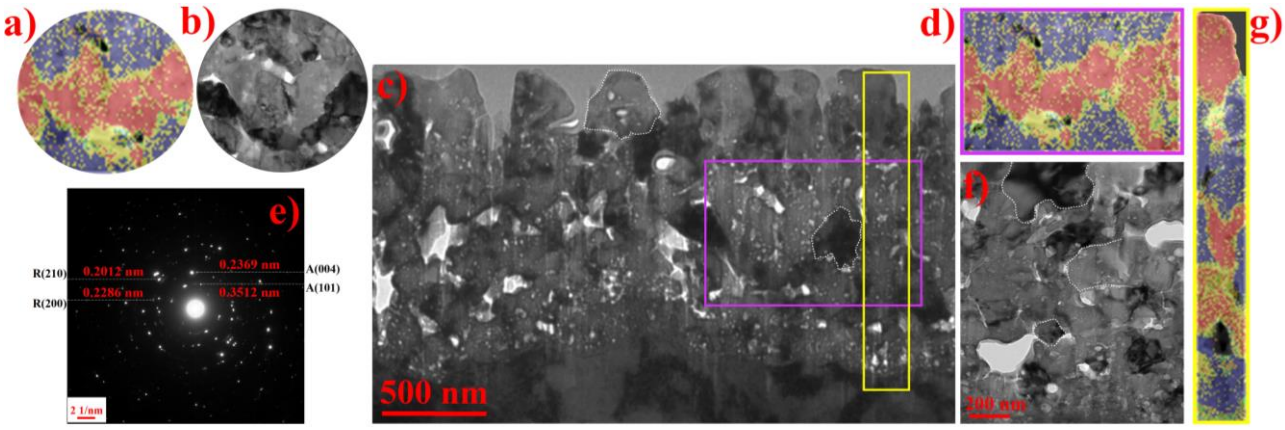

Figure 65: a, **b**, **e** SAED pattern located in the porous layer of coating 25–25-20; **c** bright-field overview; **d**, **g** EELS component map collected along coating thickness and porous layer (anatase in blue, rutile in red and TiO_2-D in yellow); **f** bright-field magnified view of the upper layer.

The presence of larger grains even reaching ~ 480 nm demonstrated frequency as the dominant factor in controlling the kinetics of growth of the oxide, which generally seemed not to be particularly enhanced considering the low oxide thickness (~ 1.4 µm) obtained using such technological parameters.

Condition 25-25-1000 permitted the growth of a very different morphology and structure, the latter verified according to EELS to be mainly composed of rutile in accordance with XRD results. The few layers of oxide immediately in contact with the holes present was constituted mainly by "mix Ti^{3+}" ~ 30 to ~ 60 nm thick. The presence of a high density of holes, the vast amount of rutile, and the low content of TiO_2-D served as an indication that there must be high temperatures developed during the process. SAED analysis, confined in the purple ROI, confirmed polycrystallinity and the only presence of rutile planes with d-spacing perfectly in agreement with card PDF 01-089-0553. The near surface high magnification bright field image highlighted in **Figure 66a** indicated the presence of grains ranging from ~ 170 to 254 nm, considerably smaller than the one observed if working at low frequency or in DC regime. As a general remark one can argue that sometimes grains smaller than the ~ 100 nm e^- transparent sample thickness could lead to projection mixing of different phases encountered along the TEM lamella scanned by the e^- beam path. However, the changes observed are generally over larger length scales than 100 nm with clear indications that the fraction of mixing (if any), due to overlapping grains of different titanium oxide phases, still occurs and is the reason why

it is not due to the projection and overlap. While the overlap could not be excluded in individual spectra or within small regions, overall, the maps clearly show trends in changes of relative fraction of the phases over the thickness of the coating.

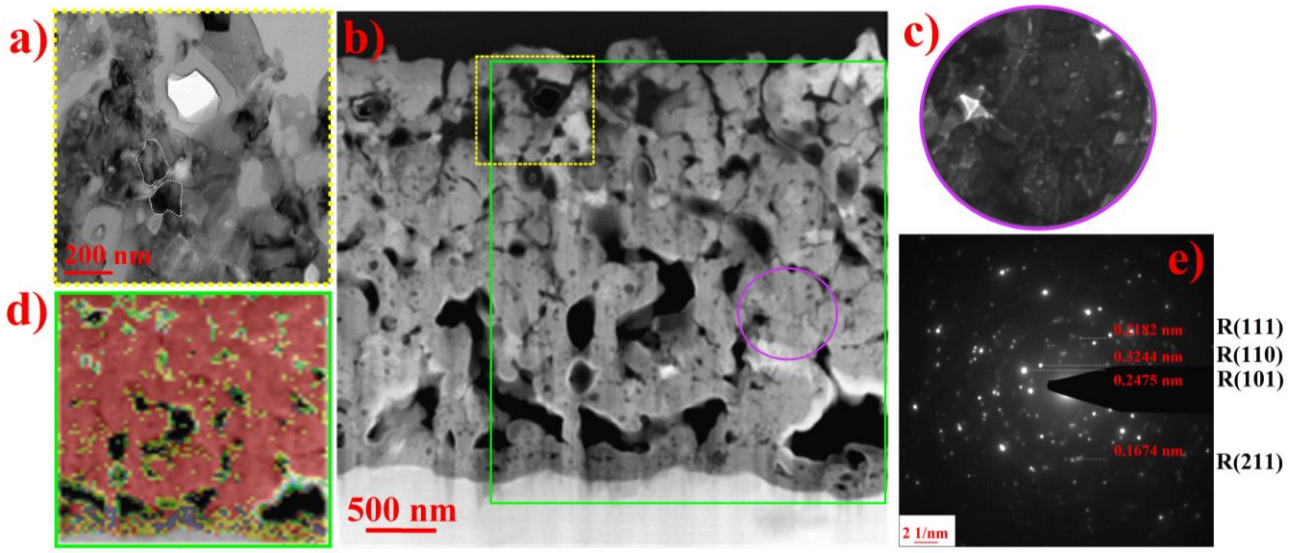

Figure 66: a magnified view of the upper layer of sample 25–25-1000; **b** bright-field overview; **c**, **e** SAED pattern collected in the porous region; **d** EELS component map (anatase in blue, rutile in red, mix Ti^{3+} in green, mix Ti^{4+} in orange and TiO_2-D in yellow).

5.3 Discussion

According to results presented so far the following anodizing mechanisms can be drawn: a three layers structure resulted from PEO carried out in DC regime with a barrier layer marked by the presence of Ti in 3+ (Ti_2O_3) and 2+ (TiO) valence, a well-organized upper layer in contact with the environment separated from the previous region by an intermediate porosity band. EELS mapping and evolution of the O_x parameter (**Figure 67**) allowed to discover the DC oxide to be characterized by an important structural gradient along the coating thickness where the lower degree of oxidation, seen in the first 200 nm oxide portion in contact with Ti resulted from an oxygen deficient atmosphere established during the oxide growth. In fact, a dynamic equilibrium between inward migration of oxygen anions and outward movement of Ti cations occurred, where the spatial arrangement of the reaction environment disposed according to transport numbers ~ 0.4 for Ti^{4+} and ~ 0.6 for O^{2-} [224,225] of the species responsible for the formation of TiO_2. This led to stabilize the reaction region roughly around the middle of the oxide thickness where the abundant heat, developed during the oxidation process, favored the formation of crystalline domains contributing to a considerable amount of parasitic currents, devoted to oxygen evolution, and consequent voids formation producing the peculiar intermediate porosity band. As the electric field responsible for ionic migration inside the oxide is inversely proportional to the coating thickness, after a while it is reasonable to assume less

O^{2-} to arrive with sufficient rate at the barrier region favoring the formation of an oxygen deficient environment. Accordingly a transition region, ~ 300 nm thick, along which the cation valence adjusted from 2+ (in contact with the metallic substrate) to 4+ (in the bulk region) occurred. Observation of the O_x parameter in **Figure 67** and the lower ΔL_3 splitting seen in **Table 32** supported this hypothesis.

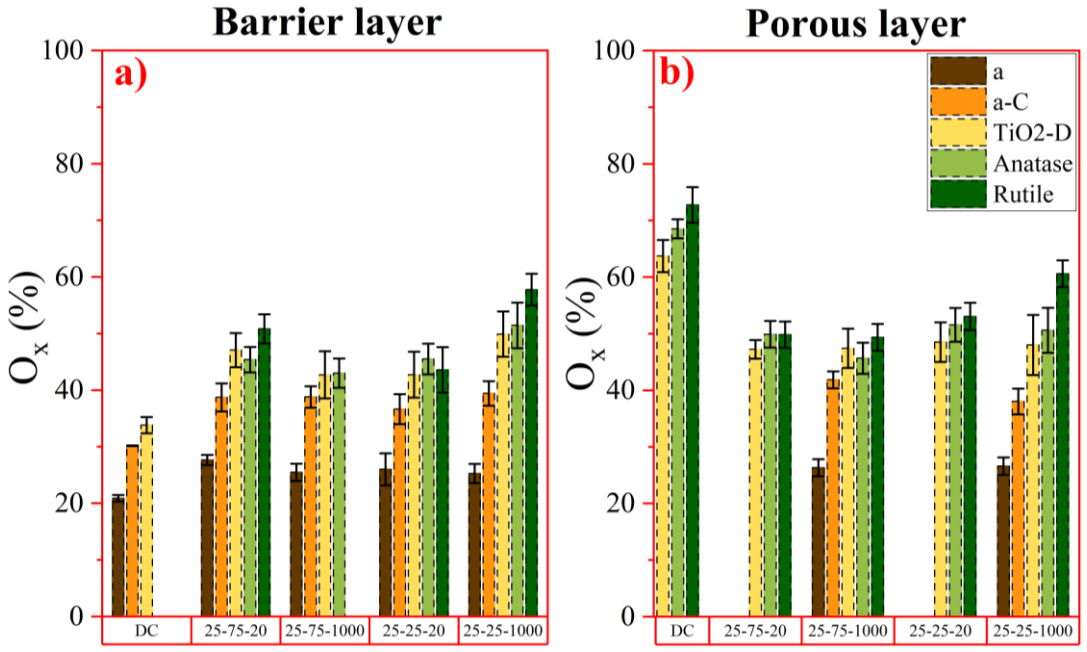

Figure 67: Collection of oxidation parameter (Ox) for barrier **a** and porous layer **b**.

The upper coating region appeared sensibly different thanks to the higher O^{2-} availability and plasma - induced local heating which favored the stabilization of rutile and the formation of large grains (~ 500 - 600 nm) as a demonstration of a faster kinetics of growth with respect to nucleation. Despite the lower degree of oxidation, interesting the barrier region of the DC coating, the upper layer appeared characterized by a high oxygen content, an observation supported also by the finer L_3-t_{2g} feature indicative of a higher degree of crystallization.

Pulsed anodizing, performed in certain conditions (as for the cycle based on 25 % of anodic peak, 75 % rest potential, frequency 20 Hz), favors the so called "recovery effect" [226] determining the growth of a relatively compact and thick layer (~ 3.2 µm). In this case the application of 12.5 ms of anodic *I* determined enough Joule heating necessary for rutile stabilization showing elongated clusters of rutile prevalently found near the surface, due to plasma activity, and the intermediate porosity band due to defects enhanced stabilization [26]. In fact, as the anatase to rutile transformation is a nucleation and growth process defect - assisted heterogeneous nucleation can be effective in that region. This allowed to think the crystallization process in TiO_2 as self-sustaining in fact other authors [173] found the

formation of a nano-crystals to be generally accompanied with the delivery of an oxygen bubbles promoting another defect responsible to sustain further crystal structure modifications.

Morphology, structure, and electrical characteristics demonstrated the importance of using a signal with pulse duration different from the time scale required for the EDL relaxation. This allowed the formation of smaller grains (~ 100 nm), a prevalent distribution of anatase and a small thickness. The abundant presence of "mix Ti^{4+}", denoted the impossibility of the structure to stabilize to a TiO_2 polymorph in accordance with a less developed PEO process. EELS components maps and dark-field image shown in **Figure 64** agreed with this idea showing a non-homogeneous material with prevalence of nucleation with respect to grain growth.

The porosity band was considerably enlarged using hybrid duty cycles as an evidence of the abundant gas evolution developed. The higher content of Ti^{4+} bearing phases in the barrier region (anatase and TiO_2-D for sample anodized at 20 Hz and rutile and TiO_2-D for sample grown at 1000 Hz) came from the high resistive heating induced by the use of cathodic *I*. Sample 25-25-20 demonstrated a similar phase distribution, in the porous region, as previous coatings with prevalence of rutile in the upper portion and in correspondence of the porosity band. However this is not the case if looking at sample 25-25-1000 where the presence of large pores, in contact with the barrier region, denoted the occurrence of intense phenomena like gas evolution and plasma activity. This is not strange as the conjunction of anodic and cathodic polarization followed by a rest period permitted gas evolution to be completed as in the case of O^{2-} generated from water dissociation whose reaction according to **Equation 29** [227] can stimulate the formation of nano-bubbles:

$$2O^{2-} \rightarrow O_2 + 4e^- \quad (29)$$

In particular, this process was very effective if using high frequencies where the gas found no time for an efficient evacuation according to the fast kinetics: this at least resulted in an enhanced ignition probability of powerful discharges. In fact, dielectric strength of a gas (air ~ 3 $MV \cdot m^{-1}$ [228]) is considerably lower than the one of an aqueous electrolyte (water ~ 65-70 $MV \cdot m^{-1}$ [229]). To confirm this hypothesis **optical emission spectroscopy** (OES) was used to collect the optical transition emitted during the PEO process. This allowed plasma characterization and the calculation of useful plasma parameters like plasma temperature T_e and the collection of the intensity lines of the major elements involved. Results are highlighted in **Figure 69a** for sample 25-25-1000 and a typical OES spectrum displayed here in **Figure 68**.

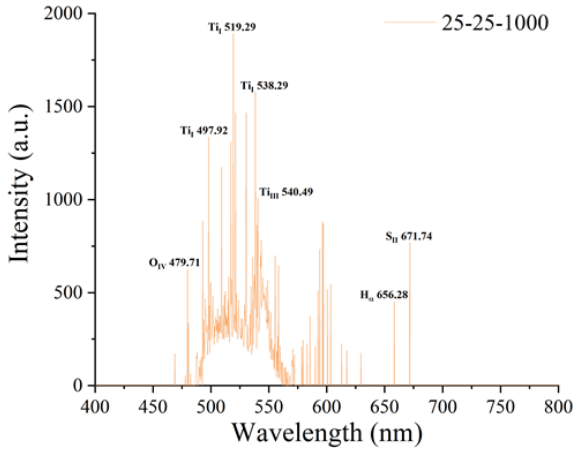

Figure 68: example of OES spectrum collected during PEO of sample 25-25-1000.

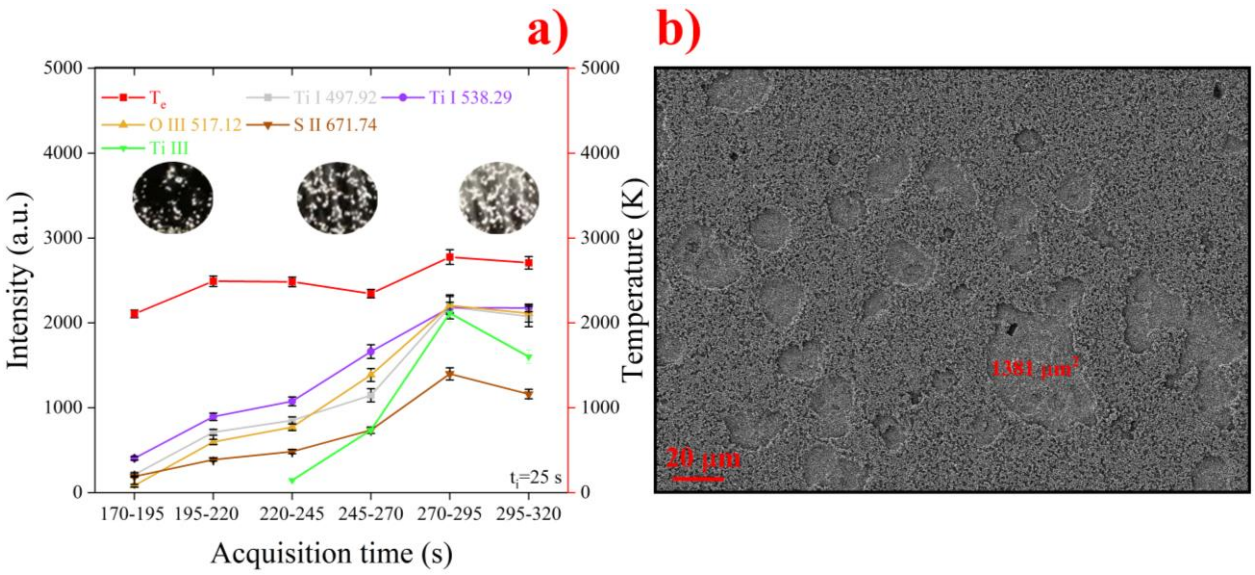

Figure 69: a Temporal evolution of the main reflections encountered during OES performed on sample 25–25-1000; **b** SEM overview of sample 25–25-1000 to highlight discharge craters.

According to visual observation of the sample surface undergoing PEO (presented in the insert of **Figure 69a**) an active area in between 0.2 ÷ 0.4 mm^2 can be defined while the absence of color variation of the plasma during the treatment indicated the optical emission to keep constant features along the process evolution, even if they underwent a marked increase in size, passing from ~ 64 μm^2 to ~ 2.59 10^{-3} mm^2.

As those values strongly differ from the fingerprint (~ 1.38 10^{-3} mm^2) observed by SEM image shown in **Figure 69b** those events should be interpreted as the sum of collective phenomena. The plasma process was characterized performing six acquisitions, during the last 150 s, with the aim of obtaining a meaningful average description considering the spatial and time random nature of the event. An integration time of 25 s was used and the first luminescence collected ~ 170 s. A fully developed spectrum, as in **Figure 68** developed only after ~ 245 s (~ 120 V). After background subtraction, the temporal variations of the major emission lines [230] in common to almost all the steps of the treatment,

i.e. Ti I 497.92 nm, Ti I 538.29 nm, Ti III (540.49 nm), O III 517.12, S II (671.74 nm) were collected and reported in **Figure 69a**. From 220 - 254 s other signals both coming from elements contained in the substrate material and electrolyte developed in the form of the following emission lines: Ti II (600.58 nm), O I (555.48 nm), O II (558.32 nm), O IV (479.72 nm), S I (537.58 nm), S III (480.43 nm), H_α (656.28 nm).

Equation 30 can be used to calculate the plasma electron temperature T_e and its time evolution during the treatment upon the selection of Ti I reflections.

$$T_e = \frac{E^2_{TiI} - E^1_{TiI}}{k_B \ln\left(\frac{I_1 A_2 g_2 \lambda_1}{I_2 A_1 g_1 \lambda_2}\right)} \quad (30)$$

According to that the lines peaked at 497.92 nm and 538.29 nm were used, considering the details about electronic transitions as in **Table 34**:

Table 34: List of the Ti I lines used for the calculation of plasma temperature T_e: λ-wavelength; g_k-statistical weight of upper energy level; A_{ik}-transition probability.

Reflection	λ (nm)	Transition	Energy (eV)	A_{ki} (10^6 s^{-1})	g_k
Ti I	497.92	$3d^3(^2D2)4s$-$3d^3(^2G)4p$	4.664	1	9
Ti I	538.29	$3d^3(^2G)4s$-$3d^3(^4F)4p$	4.175	0.18	7

Those lines were selected in accordance with other authors [231] suggesting better reliability to perform spectral line shape analysis. Initially, as the PEO process was just ignited (~ 170 - 195 s), and the plasma non uniformly distributed T_e arranged ~ 2253 K, while as the process fully developed (in between 270 - 295 s) ~ 2777 K were reached in good accordance with PEO on Ti results carried out by others [232]. In order to investigate how the plasma affected the oxide morphology and structure, a TEM lamella was extracted from the crater region. Large holes were left in correspondence of the substrate - oxide region as it is possible to see in **Figure 70**, were the deep inward indentation in the metallic substrate were identified as an artefact induced by the excessive milling during FIB preparation. Based on previous observations and keeping in mind the peculiar shape of the *I-V* curve (**Figure 50d)**, it is possible to draw the following discharge mechanism by comparing information extracted from: OES, *I-V* plot, and EELS. First emission signal extracted from OES (170 - 195 s) allowed to hypothesize a breakdown voltage in the range ~ 85 ÷ 97.5 V where the presence of Ti I lines suggests the involvement of substrate melting.

This found a very good agreement by looking at **Figure 70** where considering a breakdown field for titanium dioxide ~ 3.6 $MV \cdot cm^{-1}$ [233] a barrier layer thickness of ~ 250 nm was derived from

calculations. The use of cathodic *I*, and consequent delivery of resistive heating, enhanced the oxide crystallization at the early stages of the treatment resulting in abundant gas formation [176,234]. As a result of the EELS fine structure analysis, a larger O_x parameter was verified for this coating, indicating a rather lower presence of oxygen vacancies. This can make ions migration less favorable leading to the development of higher electric field inside the lattice. This in turns can rise the holes' formation probability, promoting e^- from valence to conduction band, favoring oxidation of O^{2-} and abundant oxygen evolution in correspondence of the oxide-metal interface were strong *type-B* discharges were ignited.

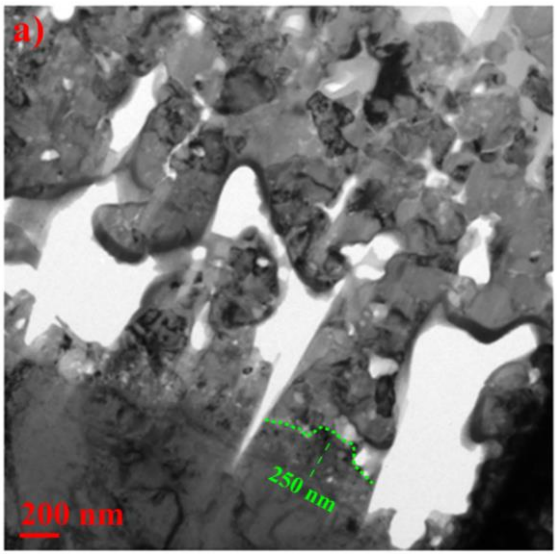

Figure 70: Bright-field view of sample 25–25-1000 with large holes due to type- B discharge.

Upon failure of the barrier layer, the discharge found an easy path to propagate through the gas phase so T increased even beyond the TiO_2 evaporation threshold (corresponding to ~ 2500 K for the Ti-O-H system) and the oxide was found to evaporate as TiO molecules [235]. Upon contact with the cold solution the evaporated material rapidly condensed to Ti_2O_3, Ti_3O_5 or even TiO_2 depending on complex plasma-chemical reactions, T, and oxygen availability.

This intuition was justified by the presence of the Ti III emission line (corresponding to Ti^{2+} related optical transitions) manifesting (195 - 220 s) when T_e (~ 2492 K) approached TiO_2 evaporation T. This caused the material immediately in contact with the plasma core to vaporize leaving behind holes with size ~ 0.4 μm^2. **Figure 71** presents EELS mapping performed on the few oxide layers affected by the interaction with the plasma.

The stoichiometric evolution, represented by the color gradient of **Figure 71** satisfies common binary Ti-O diagrams [236,237] where the first ~ 18 nm in contact with the hole were constituted by oxide with

prevalence of Ti^{3+} valence, as the result of the rapid quenching summed to the presence of a slightly reducing atmosphere, and the formation of a Magneli phase Ti_3O_5 with few particles of Ti_2O_3. Before rutile, which was the dominant component found in this system, it was observed a transition region ~ 12 nm denoted as "T" with intermediate features between Ti_3O_5 and subsequent TiO_2-D layer ~ 13 nm thick.

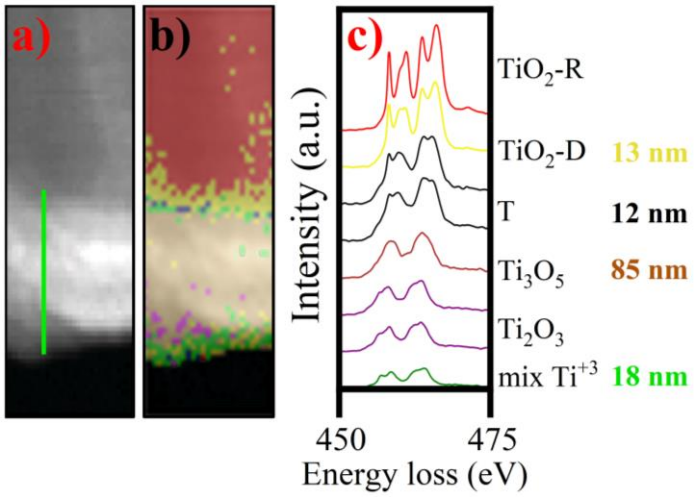

Figure 71: a Ti integrated intensity map used to perform EELS component map **b** (rutile in red, mix Ti^{3+} in green Ti_3O_5 in brown, Ti_2O_3 in purple and TiO_2-D in yellow) collected at the boundary of the hole left by a discharge and relative EEL spectra **c** where T stands for transition region.

The following analysis has the aim in demonstrating that by comparing electrical characteristics like *I* and *V* with structural information it is possible to model the discharge event inducing the thermal gradient responsible for the structural evolution highlighted in **Figure 71**. Keeping this in mind, **Equation 31** and **32** were used to evaluate the resistive heating generated by a discharge event relating the thermal gradient, induced inside the oxide, to current density affecting the overall crater left by the collective phenomenon. Details and physical parameters related to TiO_2, necessary for this theoretical treatment, are collected in **Table 35**:

Table 35: physical parameters of TiO_2.

Property	Symbol	Value
Specific resistance (Ω·m) at 1387 K [238]	ρ	10^{-2}
Density ($Kg \cdot m^{-3}$)	d	4250
Heat conduction ($W \cdot m^{-1} \cdot K^{-1}$) [239]	λ	8.5
Molar heat capacity ($j \cdot mol^{-1} \cdot K^{-1}$) [240]	$c_p = 17.14 + 0.00098T - \frac{350000}{T^2}$ at 2300 K	80.88
Molar weight ($Kg \cdot mol^{-1}$) [240]	M	0.07987
Specific heat capacity ($j \cdot Kg^{-1} \cdot K^{-1}$)	$C=\frac{c_p}{M}$	1012.64
Thermal diffusivity ($m^2 \cdot s^{-1}$)	$\chi = \frac{\lambda}{dC}$	$2.06\ 10^{-6}$

$$q = i^2 \rho \tau_i \quad (31)$$

$$\Delta T = q \frac{\chi}{\lambda V_i} \quad (32)$$

where i is the current density, ρ the specific resistance and τ_i the duration of the discharge event. According to phase diagrams of the Ti-O-H system, TiO_2 should be reduced to Ti_3O_5 only above ~ 1400 K. Considering this T as the lower bound and accounting for an average discharge duration ~ 15.5 µs (extracted from the FWHM thickness of *I* peaks observed in **Figure 50d**) a current density ~ 304 $kA \cdot m^{-2}$ is obtained as the output of **Equation 31** and **32**. At this point considering an average *I* peak ~ 14 A (see **Figure 50d**) an active surface ~ $4.59 \cdot 10^7$ μm^2 was derived. This result demonstrates a good correlation with the average total area deduced by looking at **Figure 69b** were the sum of all fingerprints left by discharges (occupying ~ 17 % of the total surface of the SEM image) was ~ $3.35 \cdot 10^7$ μm^2. Deviation between the two values can be manly related to the assumption of homogeneous presence of craters outside the SEM image.

5.4 Summary

After this conclusive analysis it was clearly adduced a correlation between electrical parameters, which could be monitored by simple investigation of the *I* and *V* plot, and structural features requiring a nanoscopic investigation made possible according to EELS. Moreover, the improved data visualization, guaranteed according to the design of an algorithm for automatic EEL spectra discrimination, further enhanced the quality of the information extracted from a local technique like EELS. This allowed to find PEO oxides as characterized by three layers: a metal-oxide interface called "barrier layer", an intermediate porosity band and an upper layer whose features appeared strongly dependent on the plasma involved during the treatment. The structural evolution highlighted in previous regions were found to be strongly related to the technological parameters selected, particularly if considering crystallinity and degree of oxidation, the latter expressed according to the definition of an oxidation parameter O_x. In summary the following important points can be drawn:

- preliminary XRD analysis found anatase, rutile and Ti_3O_5 to be the main phases composing the coatings appearing all subjected to compressive stresses as demonstrated by Williamson - Hall analysis, and d - spaces extracted from SAED patterns. Crystallite size was found to be nearly independent on anodizing conditions.
- *The few layers immediately in contact with the substrate were found to be slightly reduced to* Ti^{3+} *or lower valences:* this was particularly true in case of PEO performed in DC where clusters of Ti_2O_3 ~ 152 nm thick, showing almost no crystal field splitting, manifested. As the use of a DC

field did not favor barrier layer recovery and oxidation, a coating characterized by strong inhomogeneity between lower and upper portion resulted. This feature can be smoothed using a pulsed signal with hybrid duty cycle, where the improved oxygen availability and the abundant resistive heating favored crystallization and degree of oxidation. As the intermediate porosity band is approached, a structural gradient (showing progressively increasing cation valency) established with presence of Ti^{4+} component and grain size ~ 521 nm in correspondence of the upper portion. A steeper low Ti valence - Ti^{4+} transition occurred using pulsed anodizing, particularly if using cathodic *I* responsible to favor crystallinity and an oxidizing environment. Furthermore, in order to accommodate the lattice strain, caused by the contact between different phases, a layer of TiO_2-D was always present.

- *The microstructure was largely affected by frequency:* in fact, the DC regime or using low frequencies favored large surface grains (~ 500 nm) while the deeper oxide microstructure was considerably finer (grain size ~ 100 nm). On the other hand, using 1000 Hz homogenized the microstructure creating no difference between inner and outer coating regions.
- *Rutile presence was high in correspondence of the upper oxide portion and the porosity intermediate region:* this was due to plasma formation, above the electrode surface, and gas evolution at the reaction zone. During anatase – rutile phase transition TiO_2-D was found to be particularly abundant in correspondence of anatase grains once the thermodynamic equilibrium propended towards rutile formation.
- *Type-B discharges where ignited according to the use of high frequency (1000 Hz) and cathodic polarization:* direct comparison of *I, V* curves with local structural information demonstrated *I* peaks as the summation of several thousands of discharges ignited at the oxide - substrate interface. The oxide in contact with the emission phenomenon evaporated: then rapid quenching and condensation allowed ~ 18 nm of oxide with strong Ti^{3+} valence and the formation of ~ 85 nm of Ti_3O_5 in agreement with phase diagram predictions. As T decreased the structure rearranged through a transition region ~ 12 nm plus ~ 13 nm of TiO_2-D to rutile.
- *TiO_2 vaporized in the form of TiO molecules during direct contact with the plasma:* this was assessed according to detection of Ti III (Ti^{2+}) lines collected by OES in treatments combining 1000 Hz and a hybrid duty cycle.

Chapter 6 PEO oxide debonding

Oxide debonding is the main form of degradation when an anodic coating is exposed to a low pH environment [241]. Several intermediate steps are responsible for the degradation process, like oxide reduction involving the diffusion of charged species through the material, a process generally highly dependent on oxide thickness, structure, and morphology. When hydrogen makes its way into Ti criticisms arise from TiH_x formation, causing ductility losses and component failure [242]. This can be easily verified if the metal is employed in cathodically protected structures like heat exchangers, present in desalination plants, where the formation of scales like $Mg(OH)_2$ and $CaCO_3$ can affect the heat transfer coefficient prejudicing the overall rated capacity of the plant. To restore the operating condition sulfuric acid is generally employed as a descaling agent [243,244] even if several literature contributions [108,244–246] demonstrate the high susceptibility of unalloyed Ti to low pH environments containing sulfates. In fact, corrosion rates (CR) ~ 8 mm·year^{-1} [245] for pristine Ti grade 2 immersed in 10 %v/v H_2SO_4 at 60 °C are generally observed. According to a relevant industrial interest Ti corrosion in sulfuric acid has been well investigated and according to coulometric weight-loss and polarographic analyses [196] it was established that Ti generally goes in solution as Ti^{3+} when the electrode is active (i.e. corrosion potential E_{corr} < ~ 620 mV/$SSC_{sat.}$ for Ti in 2 M H_2SO_4) while it corrodes as Ti^{4+} if E_{corr} rises ~ 100/130 mV above a certain threshold, identified as the critical potential (E_{crit}) verified ~ -477 mV/$SSC_{sat.}$ (for Ti in 2 M H_2SO_4) [196,247]. It is well - admitted that provided E_{corr} is sufficiently cathodic and the pH low enough (in this analysis pH << 2) H^+ can not only be adsorbed, contributing to charge accumulation in the EDL, but also to intercalate within TiO_2 according to reduction described by **Equation (33)** [152,248,249]

$$Ti^{4+}O_2 + H_3O^+ + e^- \leftrightarrow Ti^{3+}(O)(OH) + H_2O \quad (33)$$

becoming feasible for E_{corr} < 197 mV_{SSC} [108] in present experimental conditions. During this reduction reaction H^+ intercalate according to local charge compensation by formation of Ti^{3+} centers. Before electrochemical reduction, Blackwood *et al.* [250,251] hypothesized a chemical dissolution mechanism with reaction rate first order with proton concentration, a mechanism probably responsible for the cathodic shift of E_{corr} till values required for electroreduction to start. Based on previous analysis and information present in literature [52,79,161] typical PEO oxides are known to be constituted by a porous outer layer, imparting to the coating a rather high thickness, and a barrier layer, immediately in contact with the metallic substrate, responsible for corrosion protection. Until now, few papers analyzed morphology [132,252] and microstructure [253,254] of Ti PEO oxides however without providing exhaustive

stoichiometric details about the barrier layer and its influence of the corrosion response in acidic environment.

It is expected, in fact, stoichiometry to exert a preponderant function ruling the mechanism leading to corrosion of electrodes immersed in low pH where the transport of H^+ generally requires low activation energy thanks to combination of small dimension and the absence of an electron cloud. Different models can be used to account for H^+ conduction at low T and in nanometric oxides [255]: 1) *solid state diffusion through the crystal lattice* 2) *within an adsorbed H_2O layer* 3) *within grain boundaries* and 4) *beneath the space charge region formed at the water/oxide interface*. The presence of oxygen vacancies seems to be particular advantageous for H^+ conduction in perovskites [256] where H_2O molecules can find an easy path to dissociate into OH^- and H^+, the former incorporated inside the oxygen vacancy while the latter forming a bond with a lattice oxygen [257]. As the present electrochemical investigation is limited to almost compact barrier regions, it is reasonable to hypothesize mass transport to occur in the bulk either through the lattice or within grain boundaries. As a consequence, after H^+ adsorption, solid-state diffusion can be described according to 1) *a fast rotation around the host oxygen ion* followed by 2*) transfer to another oxygen ion* through an hopping process [258].

Using results collected in *section 5* here we demonstrate how the use of a pulsed regime, favoring the growth of a barrier layer mainly constituted by Ti^{4+}, and containing a low level of S, results in enhanced protection of the metallic substrate by limiting H recombination at the oxide - metal interface. This retarded coating debonding preventing Ti corrosion from 24 h immersion in 10 %v/v sulfuric acid at 60 °C, a common environment adopted during metal pickling operations [259].

6.1 Materials and Methods

Two PEO treatments were analyzed in this research, deeply characterized in *section 5*: a DC process, further on referred as "PEO-DC", and a pulsed signal with a hybrid duty cycle: 25 A%-25 C%-50 R%-5 CP% repeated at 1000 Hz called "PEO-H-25" with "A", "C", "R", and "CP" having the usual meaning.

All the electrochemical tests were performed using a Metrohm Autolab PGSTAT equipped with a FRA32M module for EIS using a standard 3 electrode cell (ASTM G5 [91]) with a KCl saturated silver/silver chloride ($SSC_{sat.}$) reference electrode and an Amel Pt counter electrode. All the tests were repeated three times in 1 liter solution. EIS and E_{corr} evolution, upon immersion, were studied in 10 %v/v H_2SO_4 at 60 °C using a Velp Scientifica Arex with VTF digital thermoregulator system. The impedance was evaluated cyclically at E_{corr} after 30 min of stabilization, until complete electrode

activation, considering a frequency window between 10^{-2} to 10^{5} Hz and collecting 10 points per decade with a voltage amplitude, of the sinusoidal perturbation, of 10 mV_{rms}. Salt bridge, composed by Agar-Agar and KCl were used to not expose the reference electrode directly to the aggressive solution. EIS spectra were analyzed according to the software Nova 2.1. Potential step chronometric responses were evaluated, in the above solution, considering a polarization of -1 $V/SSC_{sat.}$ held: 30, 45 and 90 s respectively monitoring the resulting *I* transient. Details regarding the corrosion rate evaluation can be found in *section 2.1*. Glow discharge optical emission spectroscopy (GD - OES) was performed according to a SpectrumA ANALYTIK GDA 750 HR analyzer considering an anode diameter of 2.5 mm, an operating voltage of 700 V with internal Ar pressure of 2.3 hPa in RF regime.

6.2 Results

As a preliminary step samples were immersed 24 h in 10 %v/v H_2SO_4 and investigated for weight-losses and E_{corr} (see **Figure 72**). A corrosion rate of 6.2 mm·$year^{-1}$ was verified on coating PEO-DC while PEO-H-25 was found to be very resistant towards the aggressive solution with only ~ 0.03 mm·$year^{-1}$. E_{corr} Vs time indicated that PEO-DC oxide degraded after few hours passing from a passive condition (region 1) to an active state (region 3). In region 2, denoted as an active-passive transition zone, all the major processes resulting in oxide detachment occurred. For sake of clarity, some relevant redox reactions are indicated by black dashed horizontal lines, corrected according to the present experimental conditions.

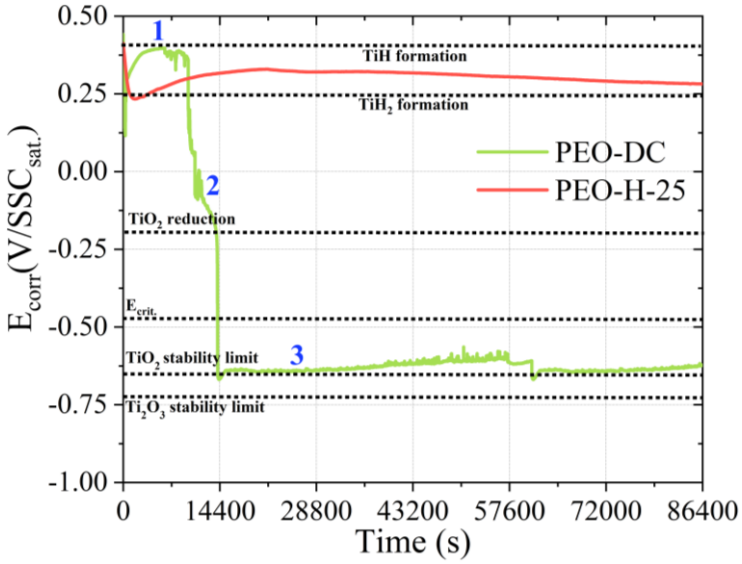

Figure 72: E_{corr} evolution for sample PEO-DC (in green) and PEO-H-25 (in red).

A first GD - OES analysis was done, on both samples, to extract the total thickness and for elemental quantification purpose, allowing to define the profile of **Figure 73**:

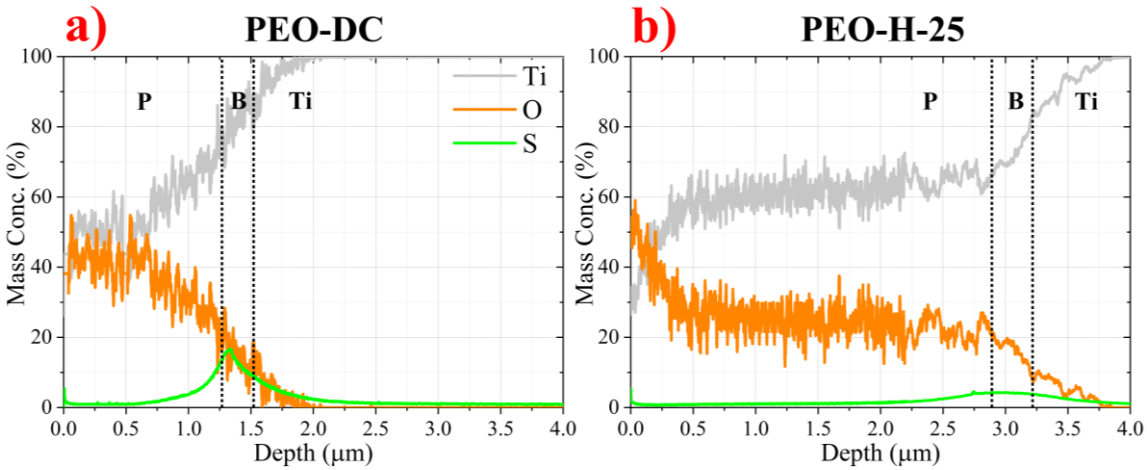

Figure 73: GD - OES profiles of sample **a** PEO-DC and **b** PEO-H-25.

thickness values very well agreed with data extracted from bright-field images of *section 5* denoting the presence of a high accumulation of S in correspondence of the barrier layer [260] (denote as "B"). According to that, a second run was performed removing only the porous layer ("P") leaving metallic Ti and a residual thickness corresponding to the barrier region (according to TEM ~ 190 nm for PEO-DC and 320 nm for PEO-H-25). Ar etching parameters were optimized to reduce as much as possible roughness and indentations (see **Figure 74)**:

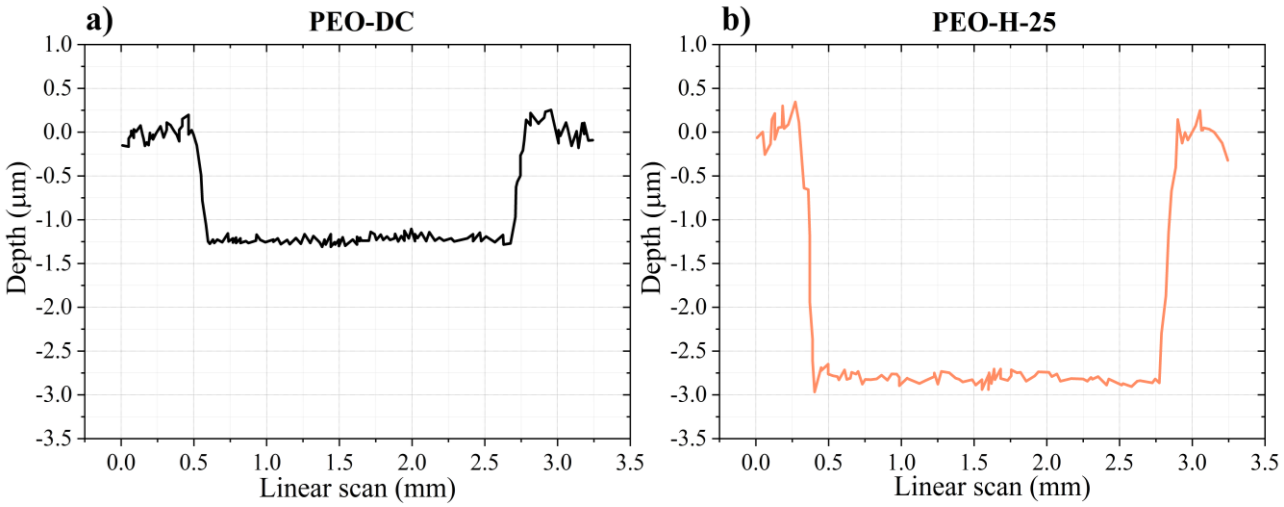

Figure 74: laser profilometry analysis over the crater left after Ar sputtering of sample **a** PEO-DC and **b** PEO-H-25.

Arithmetical roughness (R_a) was evaluated for both craters ~ 93 nm and ~ 138 nm for PEO-DC and PEO-H-25 and the values used as a "safety" tolerance to anticipate the shut - down of the sputtering procedure. In this way the oxide portion relevant for further analysis can be assumed to be almost preserved from indentations and other residual stoichiometric alterations (if any considering the robust nature of titanium oxides) imparted by scattering with the energetic particles.

As the trend was respected for both coatings only EIS results carried out on PEO-DC are presented in **Figure 75** in the form of Nyquist and Bode representation.

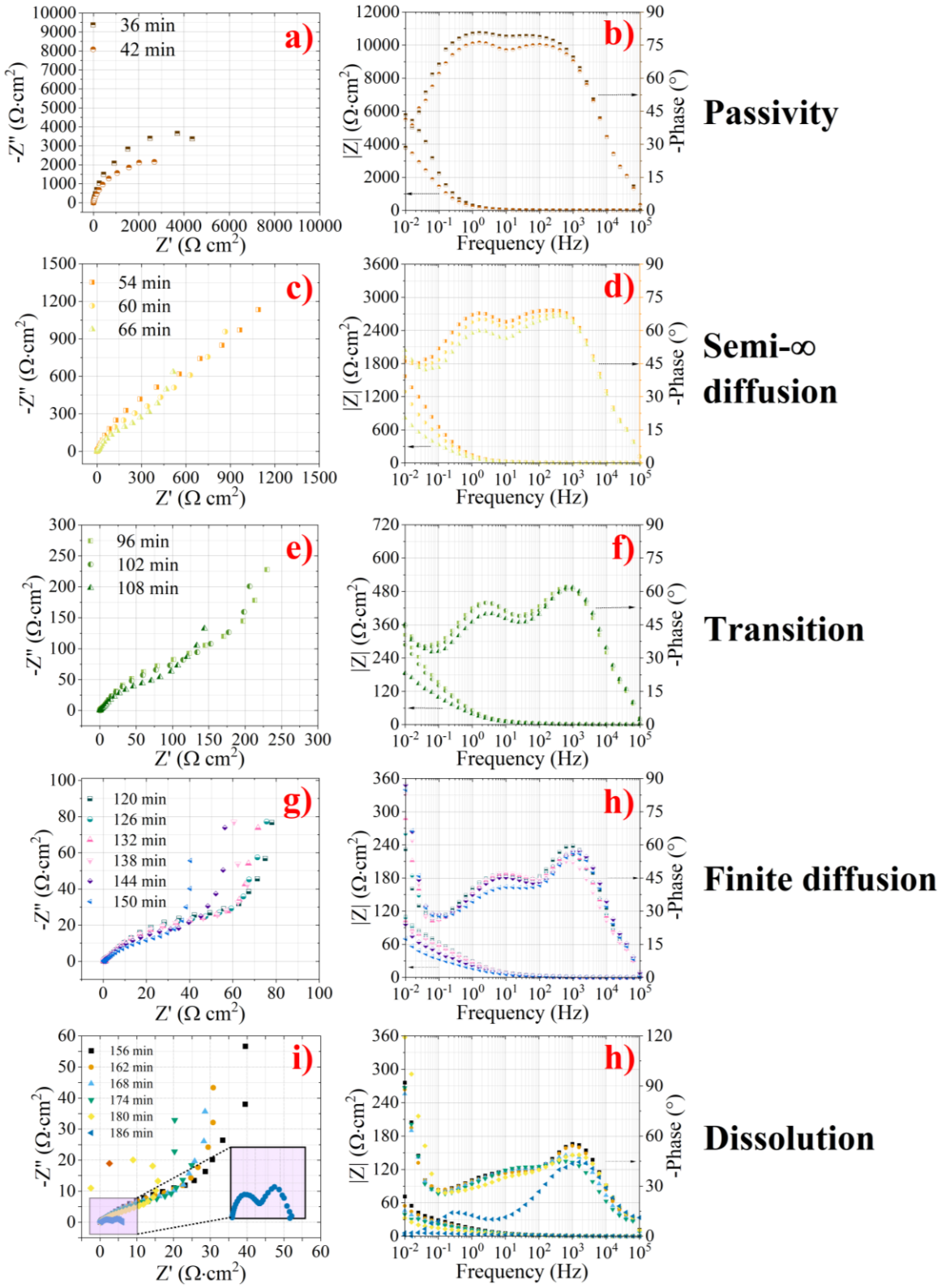

Figure 75: Nyquist and Bode representation of PEO-DC immersed in sulfuric acid.

According to the spectra the residual barrier layer held passivity for the first few minutes of immersion according to E_{corr} measured on the complete coating (i.e. also considering the presence of the porous layer), demonstrating the relevant role covered by the barrier region in determining the corrosion resistance of the coating. As the electrode was still passive only a single depressed semicircle was present in the Nyquist representation. Time constants distribution became more evident at progressively higher immersion time, where the depression in – phase angle, evidenced ~ 10 Hz and more marked as the immersion time proceeds, determined the appearance of two peaks. The imaginary impedance can be used as a reliable tool to get insight about the time scale governing the electrochemical process, as it is unaffected by the solution resistance contribution. Accordingly imaginary impedances were plotted for both coatings in **Figure 76**.

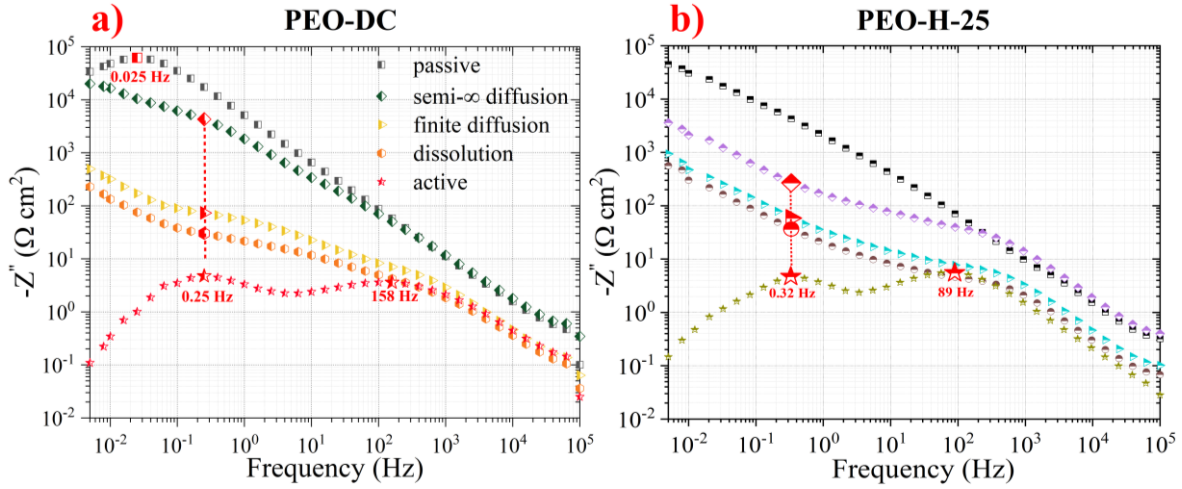

Figure 76: imaginary impedance of sample **a** PEO-DC and **b** PEO-H-25.

Initially, as passivity was held, a single peak in -Z'' established ~ 0.025 Hz for sample PEO-DC, indicating a corrosion mechanism prevalently diffusion controlled. As immersion time increases charged species diffused through the compact oxide lattice in a semi-∞ manner according to the appearance of a straight line with slope = 1 as in **Fig 75c** (- phase angle → 45 °). A change of slope - Z'' in correspondence of 0.25 Hz (for PEO-DC) and 0.32 Hz (for PEO-H-25) was indicative of the presence of concomitant reactions occurring with different time scales, as in mixed diffusion-charge transfer control reactions. The same relaxation frequency (0.25 Hz or 0.32 Hz) was verified for the electrode in the active state where such a peak is generally related to electrochemical H^+ desorption (Heyrovsky step) [108,145,190]. In case of electrode activity an additional feature in the middle frequency range revealed (158 Hz for PEO-DC and 89 Hz for PEO-H-25) describing H^+ discharge reaction (Volmer step), previously hindered by the prominent capacitive reactance of the protecting film. Similar conclusions can be drawn for sample PEO-H-25 apart from the absence of the low frequency diffusion related time constant.

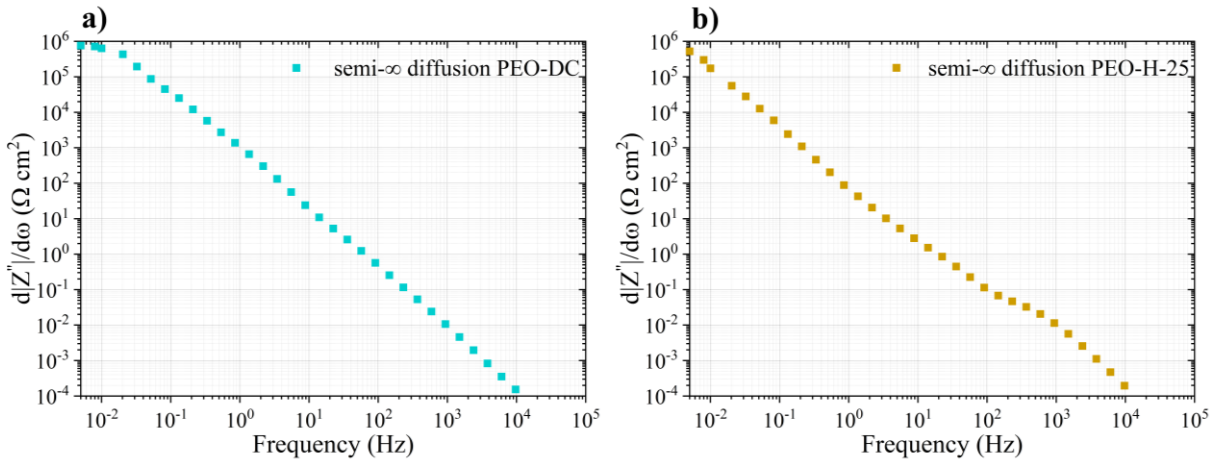

Figure 77: first derivative of the imaginary impedance plotted for sample **a** PEO-DC and **b** PEO-H-25.

This agrees, as it will be demonstrated, with the decreased diffusion coefficient of charged species inside the latter coating, thus corroborating the occurrence of mass transport in a time interval not detectable according to the experimental frequency window used in the present analysis (even in case of lower bound decreased to 5 mHz). Deeper knowledge of the corrosion mechanism can be extracted according to the first derivative of -Z" as in **Figure 77** where a regime of semi-∞ diffusion was detected. Despite the similar E_{corr} (~ -160 mV/$SSC_{sat.}$) it is evident the presence of a high frequency shoulder, manifesting in between $10^2 \div 10^3$ Hz, related to the occurrence of a potential dependent relaxation process (HER).

By looking at **Figure 75c**, **e**, **g** and **i** formation of a vertical line, in the low frequency portion of the Nyquist representation, reflects the transition between semi-∞ to finite diffusion. This can occur if charged species, involved in the diffusion process, approach a reflecting boundary or in case the charge saturation limit of the material is reached. As a result -Z" values, confined in the low frequency tail of the Nyquist plot, can be fitted by a vertical line with slope shifting from 1 (- phase angle = 45 ° typical of semi - ∞ diffusion regime) to almost ∞ (- phase = 90 °). The process can be better visualized graphically in **Figure 78** where a transition frequency (ω_{trans} ~ 39.1 mHz for PEO-DC), between semi-∞ to finite diffusion and embedded by a red ellipses, can be extracted. As the corrosion process advanced ω_{trans} shifted towards higher values passing from 0.025 Hz, after 102 min of immersion, to 0.1 Hz for 180 min immersion. From **Equation 34** it is clear that $\Delta\omega_{trans}$ can be related to modification of the finite diffusion length (probably reduced by material dissolution) or variation of the diffusion coefficient according to a different state of charge of the electrode.

$$\omega_{trans} \propto \frac{D^{H^+}}{l^2} \qquad (34)$$

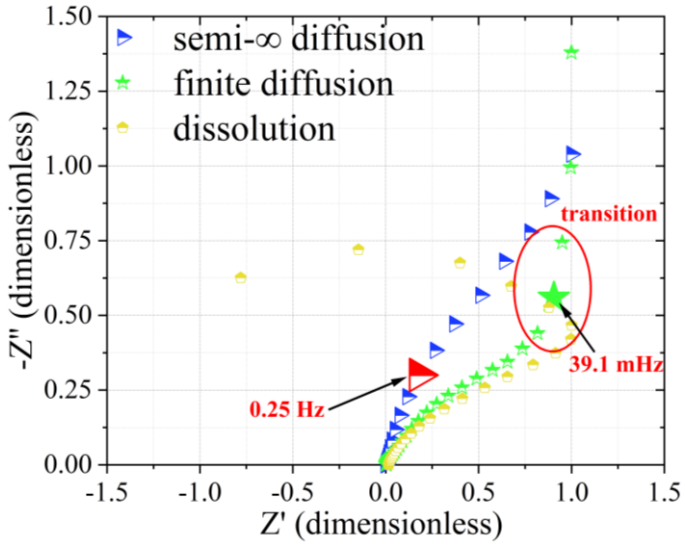

Figure 78: normalized Nyquist representation for diffusion transition understanding.

After the blocking condition was reached oxide debonding occurred as a result of the complete dissolution of the barrier layer loosing completely its protectiveness. This event can be related to the formation of a low frequency capacitive loop with negative real impedance, describing the release of charges accumulated in the redox capacitance (C_{redox}) of the material during immersion in the low pH solution. The necessary condition for such phenomena to occur is E_{corr} to become cathodic with respect to the conduction band edge of TiO_2 found to be ~ - 166 mV/$SSC_{sat.}$ [261,262] according to its Nernstian dependence on pH. After that the electrode can be considered as almost fully H^+ transparent.

6.3 Discussion

Immediately after immersion a strong concentration gradient favored H^+ diffusion inside the porosity of the oxide filling all the active surface in contact with the acid. Proton reduction, at the oxide interface, was highly enhanced by the almost free e^- provided by the presence of donor defects (n-type in nature) like oxygen vacancies. As a consequence surface adsorption and oxide reduction, according to **Equation 33**, occurred. As the E_{corr} in the first period of immersion was very anodic no HER was observed concomitantly to H^+ intercalation, thus only a low frequency relaxation (0.025 Hz) was detected and attributed to mass transport. As HER became feasible a time constant coincident with the Heyrovsky step, generally well discernable on active Ti, appeared ~ 0.25 Hz while the Volmer discharge reaction remained hindered by the capacitive reactance of the still present oxide coating until the metallic substrate was exposed to the aggressive solution.

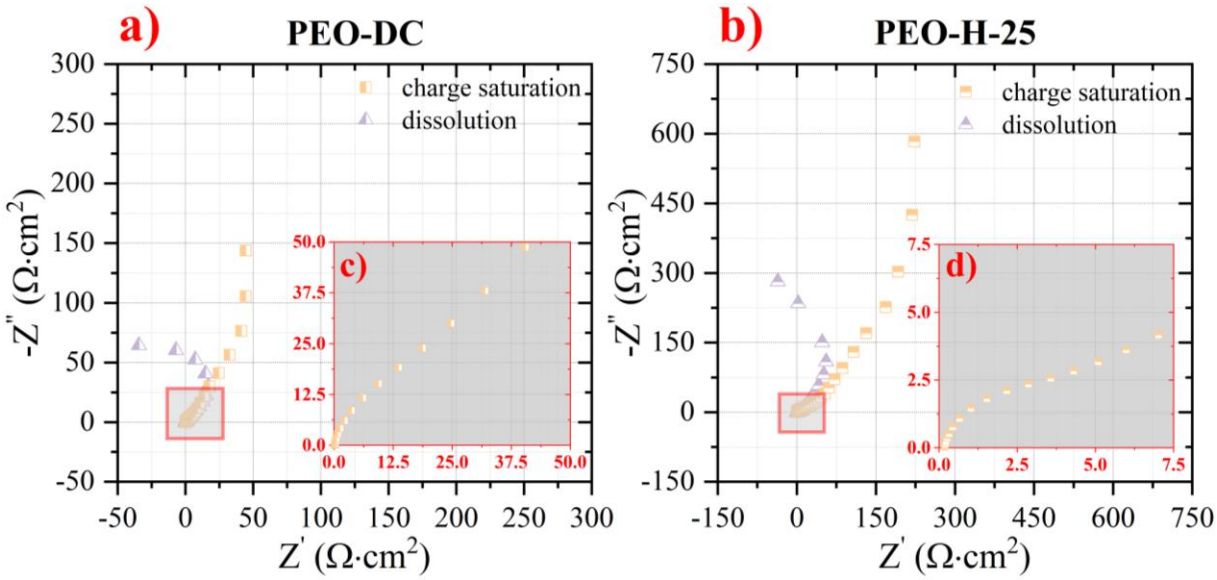

Figure 79: Nyquist representation of **a** PEO-DC and **b** PEO-H-25 in correspondence of charge saturation and coating debonding.

At progressively increasing immersion time semi-∞ diffusion shifted towards finite diffusion due to charge saturation of the oxide layer. So, according to previous observations, where a slightly different electrochemistry characterized the very different corrosion behavior of both coatings, a procedure based on EIS [263,264] will be adopted to extract diffusion parameters. Accordingly the oxide redox capacitance (C_{redox}) was extracted by fitting the low frequency portion of the Nyquist plot in **Figure 79** according to the definition of capacitive reactance (**Equation 35**):

$$Z'' = \frac{1}{2\pi C \omega} \tag{35}$$

and the slope, extrapolated by linear regression of data shown in **Figure 80**, used to estimate C_{redox} arising from e^- coupled H^+ intercalation.

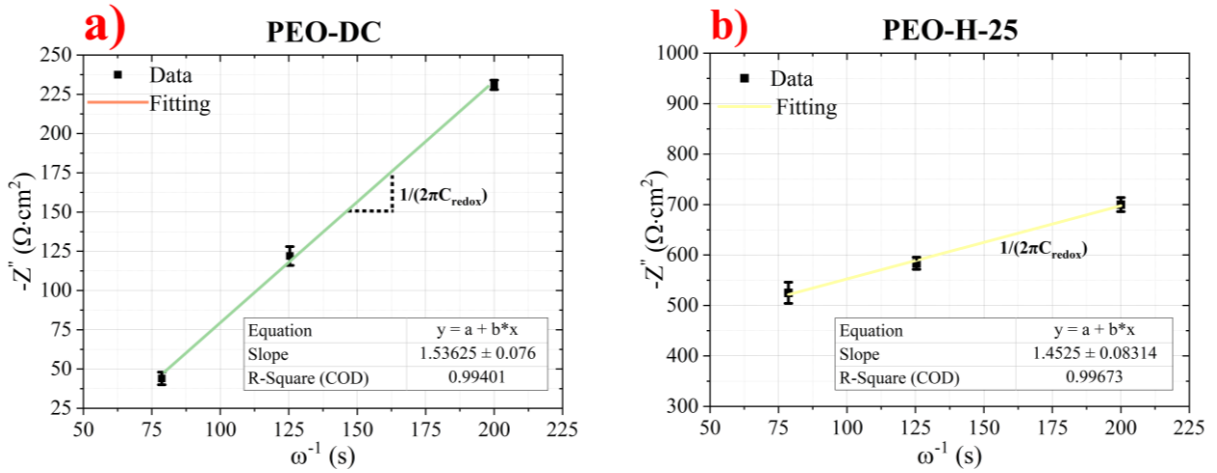

Figure 80: graphical procedure for extrapolation of Credox of sample **a** PEO-DC and **b** PEO-H-25.

By inserting C_{redox} inside **Equation 36** and using the low frequency resistance (R) as the intersection between a virtual vertical line, fitting data in the charge saturation regime, and the real impedance axis it is possible to evaluate proton diffusion coefficient describing the percolation process inside the barrier layer of length "l".

$$D^{H^+} = \frac{l^2}{3C_{redox}R} \tag{36}$$

Slightly different values were observed for the procedure applied on both electrodes:

- $D^{EIS}_{PEO-DC} = 2.61 \pm 0.31 \cdot 10^{-11}\ cm^2 \cdot s^{-1}$
- $D^{EIS}_{PEO-H-25} = 8.51 \pm 0.87 \cdot 10^{-12}\ cm^2 \cdot s^{-1}$

It was reasonable to apply this strategy only when E_{corr} was such that to allow charge percolation i.e. in correspondence of the active-passive transition region highlighted in **Figure 72**. Same tests were carried out considering solution stirring to confirm the prevalence solid-state nature of the diffusion process and only small deviations inside the experimental error were obtained.

From the value of C_{redox}, evaluated immediately before oxide debonding, it is possible to quantify the number of charges accumulated during oxide reduction. With the purpose of doing that, considering 10 mV_{rms} as the potential used to fill the C_{redox} of the oxides $1.66 \cdot 10^{15}$ and $3.412 \cdot 10^{16}$ H^+ intercalated inside PEO-DC and PEO-H-25. It is possible to compare those values with the amount of Ti^{4+} centers reduced during immersion assuming PEO-H-25 barrier region to have ~ crystal cell parameters of rutile. So, accounting for a cell volume of ~ $6.235 \cdot 10^{-23}$ cm^3 and the presence of two Ti atoms per cell, a total of ~ $4.62 \cdot 10^{16}$ atoms can be assumed in an oxide volume of ~ $1.44 \cdot 10^{-6}$ cm^3 (320 nm barrier layer thickness and exposed surface area of 0.045 cm^2) affected by the intercalation process. According to this analysis, oxide debonding occurred after the reduction of ~ 85 % ± 9 % of total Ti^{4+} sites, as the result of an immersion period of 28 h ± 2 h. The smaller number of charges involved in the diffusion process, before debonding occurred, correlated with the lower content of Ti^{4+} present in PEO-DC (no chance to quantify according to structure highlighted in *section 5*) and time required for the oxide to lose protectiveness (< 3 h).

Current transients, upon applications of potential steps, were monitored to confirm previous results. In this way it was selected a sufficiently cathodic potential of -1 $V/SSC_{sat.}$ held for 30, 45 and 90 s such that to determine H^+ intercalation. In any case the polarization times were sufficiently small to assume semi-∞ diffusion of protons, so justifying the adoption of the Cottrell equation (**Equation 37**) for D^{H^+} quantification:

$$i = \frac{D^{\frac{1}{2}}\Delta Q}{\pi^{\frac{1}{2}} l} \cdot \frac{1}{t^{\frac{1}{2}}} \quad (37)$$

and used to fit of the linear portion of the i - $t^{\frac{1}{2}}$ trend. **Table 36** presents results in terms of D^{H^+}, demonstrating the decrease of the diffusion coefficient by increasing the polarization time to 90 s where values found in saturation regime were measured: $8.6 \pm 0.23 \cdot 10^{-11}$ and $7.51 \pm 0.41 \cdot 10^{-12}$ $cm^2 \cdot s^{-1}$ for PEO-DC and PEO-H-25 respectively. Numbers extracted from PEO-H-25 agreed with the one obtained by the theoretical model used by Hupfer *et al.* [265] based on **Equation 38** applied in case of protons diffusion in a rutile crystal along the c-axis.

$$D^{H^+} = 9.4 \cdot 10^{-4} \exp\left(\frac{-0.541}{k_b T}\right) = 6.15 \cdot 10^{-12}\ cm^2 \cdot s^{-1} \quad (38)$$

As a slightly lower diffusion coefficient was verified with both electrochemical techniques for sample PEO-H-25, it was confirmed the slower diffusivity occurring in oxygen rich oxides providing a more efficient barrier against proton diffusion with respect to oxygen deficient materials like TiO (~ 12 nm) and Ti_2O_3 (~ 47 nm).

Table 36: electrochemical parameters extracted according to fitting of the current transient response highlighted in Figure 81.

	30 s		**45 s**		**90 s**	
Parameters	DC	25	DC	25	DC	25
R_s ($\Omega \cdot cm^2$)	1.62±0.1	1.73±0.1	1.55±0.1	1.63±0.2	1.75±0.14	2.06±0.11
C_{edl} ($F \cdot cm^{-2} \cdot 10^{-4}$)	2.77±0.2	1.38±0.1	2.78±0.1	2.00±0.1	2.92±0.31	2.49±0.27
B (10^{-3})	16.3±1.8	39.1±2.7	11.9±0.9	5.76±0.7	1.85±0.08	0.58±0.42
F ($A \cdot cm^{-2} \cdot 10^{-2}$)	1.67±0.1	0.88±0.0	1.60±0.1	2.25±0.1	1.43±0.06	3.79±0.12
D^{H+} ($cm^2 \cdot s^{-1} \cdot 10^{-9}$)	3.86±0.2	5.00±0.3	2.07±0.1	0.47±0.03	0.086±0.004	0.0075±0.00026

Such a deduction was previously highlighted by Yen *et al.* [266], emphasizing the importance of oxygen content with respect to thickness of titanium oxides synthesized by thermal routes. It was also verified in other systems, like WO_3 [267], the role covered by oxygen vacancies in promoting H_{ads} eventually leading to substantial alterations of the corrosion mechanism, particularly when HER is involved.

Another model (which can be found elsewhere [268]) can be applied to describe *I* transients contributions coming from the EDL, mass transport, and residual ongoing faradaic reactions using **Equation 39**.

$$i_T = \frac{V}{R} \exp\left(-\frac{t}{RC_{edl}}\right) + \frac{B}{t^{\frac{1}{2}}} + F \quad (39)$$

V is the applied potential, C_{edl}, R, B and F are fitting parameters evaluated according to non-linear least square regression performed in SciPy [269] environment.

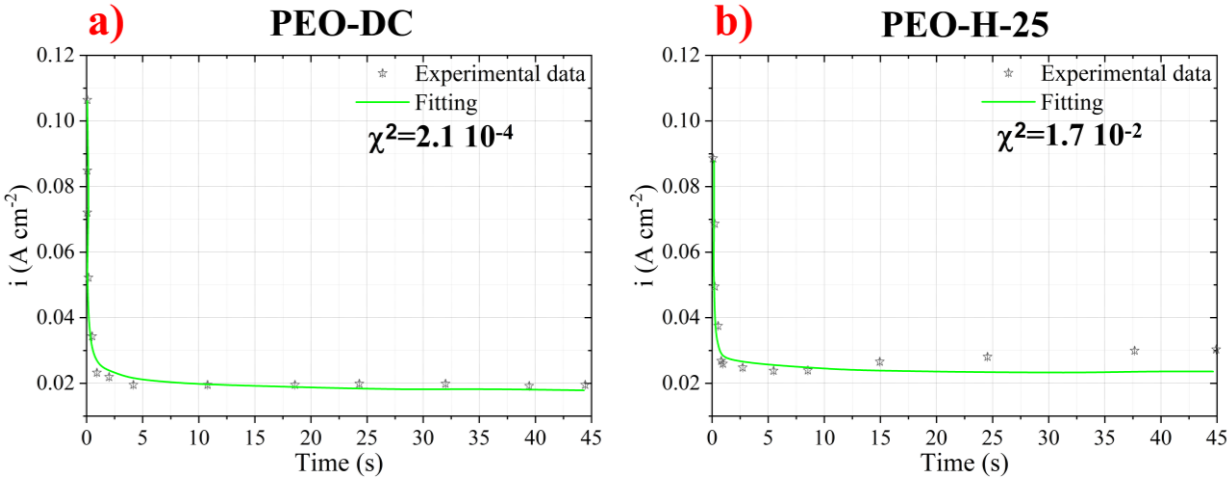

Figure 81: Experimental data and fitting of the current transient of sample **a** PEO-DC and **b** PEO-H-25 arising from application of a potential step of -1 V/SSCsat. held for 45 s.

R is a series resistance related to electrolyte, electrodes, and cables; B is a mass transport index representing the Cottrell equation while F is a current term arising from residual faradaic reactions (mainly HER in this case). Results, in terms of cathodic i Vs time, are plotted in **Figure 81** in case of cathodic potential applied for 45 s on both materials, where the fitting quality (green line) was evaluated according to χ^2 values. Sample PEO-H-25 demonstrated larger deviations from the theoretical model probably caused by the higher residual *I* due to HER, continuously increasing along all the selected time windows. Fitting parameters are collected in **Table 36** where it is possible to see that generally PEO-DC was characterized by higher C_{edl}, growing according to the polarization time as charges continued to accumulate in the EDL according to the abundant H_{ads}. The value of B, dependent on diffusion, was high during the first 30 s of polarization ($D^{H+} \sim 10^{-9}$ $cm^2 \cdot s^{-1}$) according to the prevalence of liquid phase diffusion. If longer polarization times are considered D^{H+} approached numbers associated to solid state-diffusion as in previous analysis. Generally, a higher residual *I* on sample PEO-H-25 was indicative of a faster kinetics of HER occurring on the oxide surface limiting adsorbed hydrogen to penetrate the semiconductor eventually reaching the metallic substrate: this can be considered as an important mechanism retarding oxide debonding. The lower HER kinetics verified on PEO-DC can be attributed to the high content of S retained during PEO carried out with a DC anodic field and verified according to GD - OES. Sulfur species, in fact, are well known cathodic poisoners inhibiting hydrogen recombination. Accounting now for the role of crystal structure on hydrogen evolution kinetics can appear strange HER to be faster over an oxygen reach oxide. In fact, the latter reaction was generally found to be favored in the presence of oxygen vacancies, particularly over Ti_2O_3 (with band gap ~ 0.1 eV [270]) or even better TiO [271] showing a

metallic behavior. However, it is important to keep in mind that the 3rd layer composing PEO-DC, surmounting previous structures as in **Figure 62f** (i.e. ~ 12 nm of TiO and ~ 47 nm of Ti_2O_3), corresponds to a mixed Ti^{3+}/Ti^{4+} phase (with prevalence of the former valence) as can be demonstrated according to analysis of the EELS spectrum visualized in **Figure 82** in green (~ 131 nm thick). As a result, the intrinsic defected nature can be tough as partially responsible for the polarization of the hydrogen evolution reaction. Demonstrated the inhomogeneity and the lower oxidation state of the cation by looking at O_x parameter and ΔL_3 it is acceptable to say that the presence of oxygen vacancies, and related Ti^{3+} centers, can favor strong H_{ads} making unlikely the desorption step required for gas evolution.

The same kinetic result can be verified according to EIS considering **Figure 79c** and **d** where the charge transfer resistance R_{ct} was extracted from the diameter of the high frequency semicircle: 24.1 and 5.5 $\Omega \cdot cm^2$ for PEO-DC and PEO-H-25 respectively. Upon evaluation of the characteristic frequency (ω_{max}), from the value in correspondence of the maximum of $-Z''$ it is possible to calculate C_{edl} using **Equation 40**:

$$C_{edl} = \frac{1}{2\pi R_{ct}\omega_{max}} \tag{40}$$

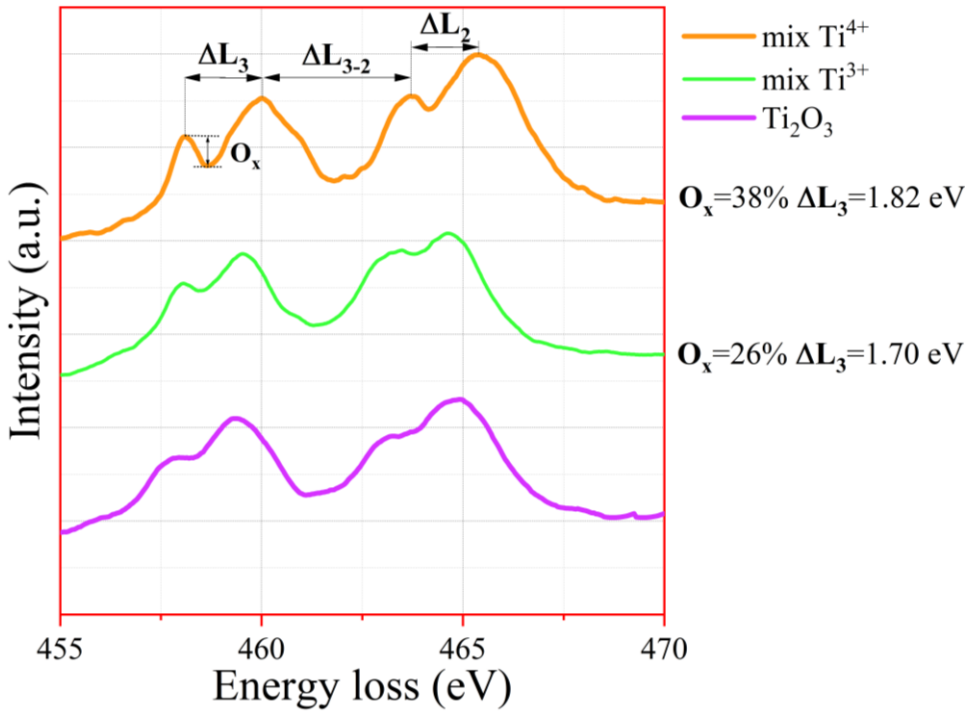

Figure 82: EEL spectra and fine structure related parameters indicating different oxidation levels, corresponding to mix-Ti^{4+} (in orange), mix-Ti^{3+} (in green) and Ti_2O_3 (in purple).

obtaining $2.97 \cdot 10^{-3}$ and $3.07 \cdot 10^{-4}$ $F \cdot cm^{-2}$ thus establishing a good correlation with values extracted from previous current transient analysis, demonstrating that such high values of C did not merely

arise from charge separation but also accumulation in the EDL. The faster kinetics of HER on PEO-H-25, expressed by the lower R_{ct} and C_{edl}, can favor the idea of higher near-surface pH of the electrode, altering the material stability and so the electrochemistry occurring on it.

After kinetics and mass transport provided all the reactions responsible for the increase of C_{redox} of the material charge saturation occurred resulting in oxide debonding by the formation of a growing bubble (red arrow in **Figure 83a**) developed at the metal - oxide interface. Once the gas bubble reached a critical thickness the coating was detached mechanically as can be seen in the insert of **Figure 83b** highlighted by the blue arrow. Bubble formation can always be detected by the presence of a capacitive low frequency loop with negative real impedances in the Nyquist representation.

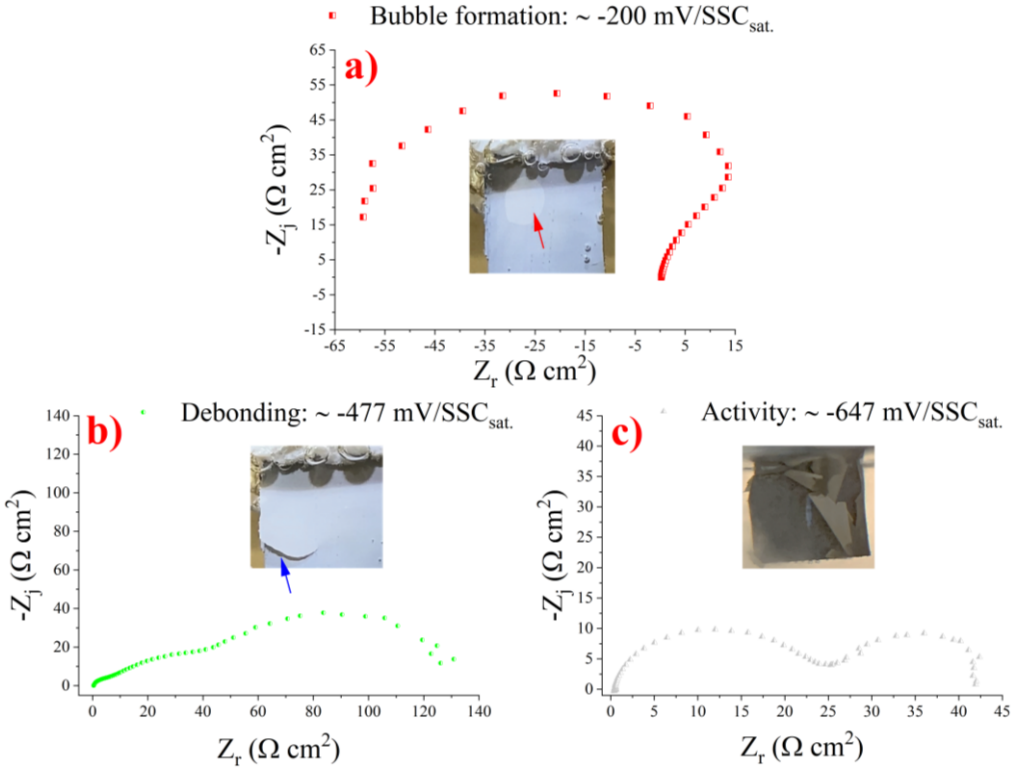

Figure 83: Nyquist representation of PEO-DC with corresponding images collected during the evolution of the corrosion process.

To get insight in this apparently strange behavior linear polarization resistance test (LPR) (displayed in **Figure 84**) was performed immediately after EIS confirming the presence of a negative differential resistance as a consequence of the negative slope of the *V-I* plot in the anodic overpotential region. The only presence of anodic *I*, during LPR test, is indicative of the natural tendency of the electrode to shift cathodically as the result of oxide debonding. The progressively decreasing *I* in case of increasing anodic overvoltages (responsible for the negative differential resistance) depends on the abundant release of charges retained inside C_{redox} during the oxide immersion suddenly returned to the potentiostat once the coating failed.

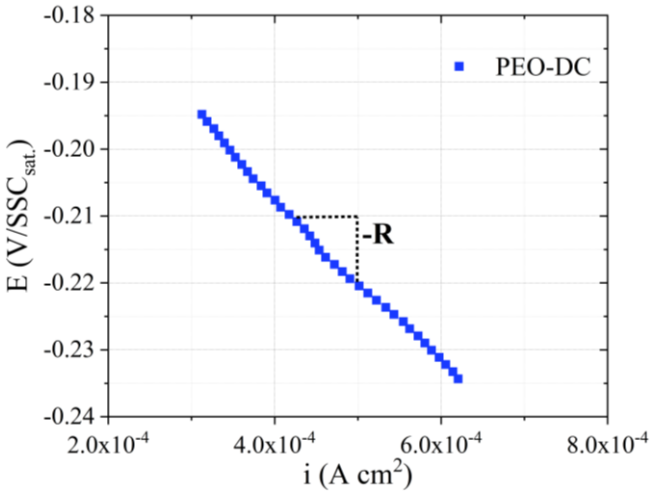

Figure 84: LPR plot for sample PEO-DC.

A similar behavior was already observed in different fields: researchers working on capacitors [272] found a similar trend after complete charging of the electronic device due to the occurrence of *V* relaxation phenomena inducing charge release back to the system. Even in the corrosion field this trend is not new: Boukamp *et al.* [273,274] found it in case of corroding Cr electrodes immersed in H_2SO_4. The author addressed the observation to surface coverage variations during the active-passive transition.

After manifestation of the negative real impedance data and consequent oxide debonding three capacitive loops are generally observed before the two typical relaxations, referring to HER on an active metal [190,194,275], stabilized (as in **Figure 85b**).

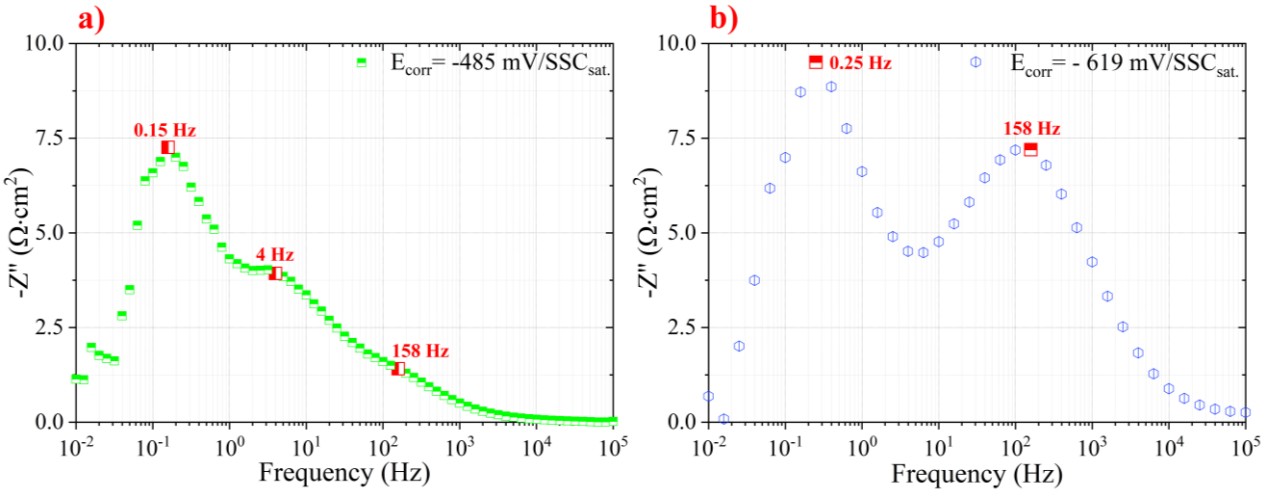

Figure 85: Imaginary impedance versus frequency showing **a** three and **b** two time constants for active Ti electrode.

According to Lasia *et al.* [194] the appearance of the third time constant appears as the result of a slower kinetics of H absorption. The reason why immediately after coating debonding kinetic limitations to the former process should be present can be related to the aggressive condition employed in the

present analysis (pH ~ -2 at 60 °C). In fact, it is reasonable to assume the critical solubility of H in Ti for hydride formation (~ 0.002 ÷ 0.004 in H:Ti atomic ratio) to be reached leading to the establishment of a layer of titanium hydrides initially acting as a diffusion barrier, similarly to the first monolayers of oxide/hydroxides always present on Ti when in contact with an aqueous solution. This made possible the appearance of the third middle frequency time constant whose relaxation frequency (4 Hz) can be easily extracted from **Figure 85a**. However, as E_{corr} moved below ~ - 620 mV/$SSC_{sat.}$ (near the TiO_2 stability limit as highlighted in **Figure 72**) H absorption became so fast to make the process no more easily discernable, a result coming from the loss of protectiveness of even the few layers of oxide/hydroxide (the thermodynamic stability limit of TiO_2 was reached).

6.4 Summary

According to the present analysis crystal structure was found to be an important PEO oxide feature to be considered for corrosion resistance control. In particular, it was shown that upon using high frequency (1000 Hz) and a hybrid duty cycle it was possible to induce the formation of an oxide barrier layer composed by a homogeneous stoichiometry, comprising mainly Ti^{4+}, and a relatively low content of S. This allowed to retard oxide debonding (not observed for 24 h immersion in our test solution) as the result of decreased protons diffusion coefficient, evaluated electrochemically to be ~ 10^{-12} $cm^2 \cdot s^{-1}$, and enhanced HER occurring at the oxide - electrolyte interface. On the other hand, using PEO in DC preserved the natural three - layer structure present on untreated Ti, resulting in the following key points responsible for oxide debonding and high corrosion rate ~ 6.2 $mm \cdot year^{-1}$:

- oxygen vacancies enhance H_{ads} and favor proton diffusion (D^{H^+} ~ 10^{-11} $cm^2 \cdot s^{-1}$).
- The presence of S species acts as a cathodic poison limiting hydrogen recombination and increasing dramatically H accumulation in correspondence of the metal - oxide interface.
- Oxide debonding incubation time increases with the content of Ti^{4+}: after reduction of ~ 85 % ± 9 % of Ti^{4+} cations coating debonding occurred as a result of the continuous increase of the protonic conductivity of the material.
- This resulted in the formation of an H_2 bubble, over the metallic substrate, causing mechanical debonding of the oxide layer. This can be detected by looking the Nyquist plot where the formation of a low frequency capacitive loop with negative real impedance always anticipated the coating failure.

Chapter 7 Conclusions

In conclusion several plasma electrolytic oxidation (PEO) conditions were tested and found to be effective in promoting surface functionalization for corrosion resistance enhancement. This allowed to pursue the final goal of the present dissertation, i.e. the research of a PEO coating outperforming corrosion resistance offered by Ti grade 7 in acidic environment. Among all the experimental evidences the following interesting findings deserve to be summarized:

- *Sulfuric acid* was found to be the most aggressive reducing acid for Ti grade 2 and 7 among: HCl, H_3PO_4, sulfamic, and oxalic acid. This was verified according to weight - loss and electrochemical tests, like EIS and cathodic polarization, evidencing the use of Ti grade 7 as a necessary condition when dealing with H_2SO_4, HCl, and oxalic acid at high T and concentration.

- Despite the opportunity to decrease the high electrical power demand of PEO only small improvements, in terms of corrosion resistance tested in 10 %v/v H_2SO_4 at 60 °C, were obtained when using PEO in *unipolar regime*. In fact only treatments performed at 220 V with high duty cycle (90 % anodic) and frequency (1000 Hz) manifested ~ 30 % improvement with respect to untreated Ti grade 2. Corrosion resistance was improved by using *bipolar PEO*, where the combination of high frequency (1000 Hz) and a moderate amount of cathodic polarization permitted to obtain CR ~ 0.03 mm·year^{-1} in low pH environments.

- The use of *electron energy loss spectroscopy* (EELS) allowed to understand structural details with a spatial resolution down to the nanometre. Cathodic current was found to be particularly advantageous in promoting a more uniform stoichiometry along all the oxide thickness, smoothing the strong Ti valence gradient observed when using PEO in direct current regime.

- *Electrochemical impedance spectroscopy* (EIS) was used to get insights about the corrosion mechanism leading to oxide debonding in a low pH environment. The degradation phenomenon was found to occur in correspondence of the formation of a gas bubble, localized at the metal - oxide interface, developing after charge saturation of the material. Outstanding improvements were found upon the selection of high frequency (1000 Hz) and a hybrid duty cycle, recognized to be important features promoting the design of a barrier layer mainly composed by Ti^{4+} and a low content of S. This choice allowed to decrease the corrosion rate by almost one order of magnitude with respect to performances offered by Ti grade 7 in hot concentrated sulfuric acid.

Bibliography

(1) Mahmoud, MHH.; Afifi, AAI.; Ibrahim, IA. Reductive leaching of ilmenite ore in hydrochloric acid for preparation of synthetic rutile. *Hydrometallurgy*. **2004**, 73, 99–109.

(2) Nagesh, CRVS.; Ramachandran, CS.; Subramanyam, RB. Methods of titanium sponge production. *Trans. Indian Inst. Met.* **2008**, 61, 341–348.

(3) Ono, K.; Suzuki, RO. A new concept for producing Ti sponge: Calciothermic reduction. *Jom*. **2002**, 54, 59–61.

(4) Shi, M.; Liu, B.; Li, S.; Zhao, H. Electrolytic Reduction of Titanium Dioxide in Molten LiCl–Li2O. *Electrochem*. **2021**, 2, 224–235.

(5) Platacis, E.; Kaldre, I.; Blumbergs, E.; Goldšteins, L.; Serga, V. Titanium production by magnesium thermal reduction in the electroslag process. *Sci. Rep.* **2019**, 9, 1–13.

(6) Heckman, JJ.; Pinto, R.; Savelyev, PA. 済無No Title No Title No Title. *Angew. Chemie Int. Ed. 6(11), 951–952*. **1967**.

(7) McCafferty, E.; Wightman, JP. X-ray photoelectron spectroscopy sputter profile study of the native air-formed oxide film on titanium. *Appl. Surf. Sci.* **1999**, 143, 92–100.

(8) Carley, AF.; Chalker, PR.; Riviere, JC.; Roberts, MW. The identification and characterisation of mixed oxidation states at oxidised titanium surfaces by analysis of X-ray photoelectron spectra. *J. Chem. Soc. Faraday Trans. 1 Phys. Chem. Condens. Phases*. **1987**, 83, 351–370.

(9) Lu, G.; Bernasek, SL.; Schwartz, J. Oxidation of a polycrystalline titanium surface by oxygen and water. *Surf. Sci.* **2000**, 458, 80–90.

(10) Zaremba, LS.; Smoleński, WH. Optimal portfolio choice under a liability constraint. *Ann. Oper. Res.* **2000**, 97, 131–141.

(11) Pouilleau, J.; Devilliers, D.; Garrido, F.; Durand-Vidal, S.; Mahé, E. Structure and composition of passive titanium oxide films. *Mater. Sci. Eng. B*. **1997**, 47, 235–243.

(12) Nanci, A.; Wuest, JD.; Peru, L. et al. Chemical modification of titanium surfaces for covalent attachment of biological molecules. *J. Biomed. Mater. Res.* **Published Online First: 1998**. doi:10.1002/(SICI)1097-4636(199805)40:2<324::AID-JBM18>3.0.CO;2-L

(13) Yi, JH.; Bernard, C.; Variola, F. et al. Characterization of a bioactive nanotextured surface created by controlled chemical oxidation of titanium. *Surf. Sci.* **Published Online First: 2006**. doi:10.1016/j.susc.2006.07.053

(14) Wang, XX.; Hayakawa, S.; Tsuru, K.; Osaka, A. Bioactive titania gel layers formed by chemical treatment of Ti substrate with a H2O2/HCl solution. *Biomaterials*. **Published Online First: 2002**. doi:10.1016/S0142-9612(01)00254-X

(15) Wu, JM. Low-temperature preparation of titania nanorods through direct oxidation of titanium with hydrogen peroxide. *J. Cryst. Growth*. **Published Online First: 2004**. doi:10.1016/j.jcrysgro.2004.05.023

(16) Prando, D.; Nicolis, D.; Ormellese, M.; Bolzoni, F.; Pedeferri, M. Chemical oxidation as repairing technique of damaged corrosion resistance enhanced anodic oxide film. ,, 1–15.

(17) Ormellese, M.; Prando, D.; Nicolis, D.; Bolzoni, F.; Pedeferri, MP. Chemical oxidation as repairing technique to restore corrosion resistance on damaged anodized titanium. *Surf. Coatings Technol.* **Published Online First: 2019**. doi:10.1016/j.surfcoat.2019.03.005

(18) Liu, J.; Alfantazi, A.; Asselin, E. A new method to improve the corrosion resistance of titanium for hydrometallurgical applications. *Appl. Surf. Sci.* **2015**, 332, 480–487.

(19) Lin, N.; Xie, R.; Zou, J. et al. Surface damage mitigation of titanium and its alloys via thermal oxidation: A brief review. *Rev. Adv. Mater. Sci.* **2019**, 58, 132–146.

(20) Aniołek, K.; Kupka, M.; Barylski, A. Sliding wear resistance of oxide layers formed on a titanium surface during thermal oxidation. *Wear*. **2016**, 356–357, 23–29.

(21) Arslan, E.; Totik, Y.; Demirci, E.; Alsaran, A. Influence of surface roughness on corrosion and tribological behavior of CP-Ti after thermal oxidation treatment. *J. Mater. Eng. Perform.*

2010, 19, 428–433.
(22) Bailey, R.; Sun, Y. Unlubricated sliding friction and wear characteristics of thermally oxidized commercially pure titanium. *Wear*. **2013**, 308, 61–70.
(23) Bailey, R.; Sun, Y. Corrosion and Tribocorrosion Performance of Thermally Oxidized Commercially Pure Titanium in a 0.9% NaCl Solution. *J. Mater. Eng. Perform.* **2015**, 24, 1669–1678.
(24) Dearnley, PA.; Dahm, KL.; Çimenoğlu, H. The corrosion-wear behaviour of thermally oxidised CP-Ti and Ti-6Al-4V. *Wear*. **2004**, 256, 469–479.
(25) Jamesh, M.; Kumar, S.; Sankara Narayanan, TSN. Effect of thermal oxidation on corrosion resistance of commercially pure titanium in acid medium. *J. Mater. Eng. Perform.* **2012**, 21, 900–906.
(26) Hanaor, DAH.; Sorrell, CC. Review of the anatase to rutile phase transformation. *J. Mater. Sci.* **2011**, 46, 855–874.
(27) Dachille F.,; Simons P.Y.,; Roy R., Pressure-Temperature Studies of Anatase, Brookite, Rutile and TiO2-Ii. *Am. Mineral.* **1968**, 53, 1929–1939.
(28) Ghosh, TB.; Dhabal, S.; Datta, AK. On crystallite size dependence of phase stability of nanocrystalline TiO2. *J. Appl. Phys.* **Published Online First: 2003**. doi:10.1063/1.1604966
(29) Zhang, H.; Banfield, JF. Thermodynamic analysis of phase stability of nanocrystalline titania. *J. Mater. Chem.* **Published Online First: 1998**. doi:10.1039/a802619j
(30) Bonnet, M.; Massard, C.; Veisseire, P.; Camares, O.; Awitor, KO. Environmental Toxicity and Antimicrobial Efficiency of Titanium Dioxide Nanoparticles in Suspension. *J. Biomater. Nanobiotechnol.* **Published Online First: 2015**. doi:10.4236/jbnb.2015.63020
(31) Zhang, J.; Xu, Q.; Feng, Z.; Li, M.; Li, C. Importance of the relationship between surface phases and photocatalytic activity of TiO2. *Angew. Chemie - Int. Ed.* **2008**, 47, 1766–1769.
(32) Diamanti, M V.; Codeluppi, S.; Cordioli, A.; Pedeferri, MP. Effect of thermal oxidation on titanium oxides' characteristics. *J. Exp. Nanosci.* **2009**, 4, 365–372.
(33) Gamboa, JA.; Pasquevich, DM. Effect of Chlorine Atmosphere on the Anatase-Rutile Transformation. *J. Am. Ceram. Soc.* **Published Online First: 1992**. doi:10.1111/j.1151-2916.1992.tb04367.x
(34) Syarif, DG.; Miyashita, A.; Yamaki, T.; Sumita, T.; Choi, Y.; Itoh, H. Preparation of anatase and rutile thin films by controlling oxygen partial pressure. *Appl. Surf. Sci.* **Published Online First: 2002**. doi:10.1016/S0169-4332(02)00532-9
(35) Shannon, DR.; Pask, JA. Kinetics of the Anatase-Rutile Transformation. *J. Am. Ceram. Soc.* **Published Online First: 1965**. doi:10.1111/j.1151-2916.1965.tb14774.x
(36) Suyama, Y.; Kato, A. Mechanism of Action of Additives on Anatase-Rutile Transition. *J. Soc. Mater. Sci. Japan*. **Published Online First: 1978**. doi:10.2472/jsms.27.632
(37) Yu, JC.; Yu, J.; Ho, W.; Jiang, Z.; Zhang, L. Effects of F- doping on the photocatalytic activity and microstructures of nanocrystalline TiO2 powders. *Chem. Mater.* **Published Online First: 2002**. doi:10.1021/cm020027c
(38) Takahashi, Y.; Matsuoka, Y. Dip-coating of TiO2 films using a sol derived from Ti(O-i-Pr)4-diethanolamine-H2O-i-PrOH system. *J. Mater. Sci.* **Published Online First: 1988**. doi:10.1007/BF01115798
(39) Muñoz-Mizuno, A.; Cely-Bautista, M.; Jaramillo-Colpas, J.; Hincapie, D.; Calderón-Hernández, JW. Effect on thermal oxidation in TiO2 nanostructures on nanohardness and corrosion resistance. *Ingeniare*. **2020**, 28, 362–372.
(40) Sarraf, M.; Zalnezhad, E.; Bushroa, AR.; Hamouda, AMS.; Rafieerad, AR.; Nasiri-Tabrizi, B. Effect of microstructural evolution on wettability and tribological behavior of TiO2 nanotubular arrays coated on Ti-6Al-4V. *Ceram. Int.* **Published Online First: 2015**. doi:10.1016/j.ceramint.2015.02.136
(41) Mohan, L.; Anandan, C.; Rajendran, N. Electrochemical behaviour and bioactivity of self-

organized TiO2 nanotube arrays on Ti-6Al-4V in Hanks' solution for biomedical applications. *Electrochim. Acta*. **Published Online First: 2015**. doi:10.1016/j.electacta.2014.12.032
(42) Biswas, A.; Manna, I.; Chatterjee, UK.; Bhattacharyya, U.; Majumdar, JD. Evaluation of electrochemical properties of thermally oxidised Ti-6Al-4V for bioimplant application. *Surf. Eng.* **Published Online First: 2009**. doi:10.1179/174329409X379264
(43) Chen, T.; Koyama, S.; Nishida, S.; Yu, L. Influence of oxidation processing temperature on the structure, mechanical and tribological properties of titanium using carbon sheets. *Metals (Basel)*. **2021**, 11. doi:10.3390/met11040585
(44) Bansal, R.; Singh, JK.; Singh, V.; Singh, DDN.; Das, P. Optimization of Oxidation Temperature for Commercially Pure Titanium to Achieve Improved Corrosion Resistance. *J. Mater. Eng. Perform.* **2017**, 26, 969–977.
(45) Kumar, S.; Narayanan, TSNS.; Raman, SGS.; Seshadri, SK. Thermal oxidation of CP-Ti: Evaluation of characteristics and corrosion resistance as a function of treatment time. *Mater. Sci. Eng. C*. **2009**, 29, 1942–1949.
(46) Wang, G.; Li, J.; Lv, K. et al. Surface thermal oxidation on titanium implants to enhance osteogenic activity and in vivo osseointegration. *Sci. Rep.* **2016**, 6, 1–13.
(47) Bloyce, A.; Qi, PY.; Dong, H.; Bell, T. Surface modification of titanium alloys for combined improvements in corrosion and wear resistance. *Surf. Coatings Technol.* **1998**, 107, 125–132.
(48) Casanova, L.; Belotti, N.; Pedeferri, MP.; Ormellese, M. Sealing of porous titanium oxides produced by plasma electrolytic oxidation. *Mater. Corros.* **2021**,, 1–5.
(49) Simchen, F.; Sieber, M.; Lampke, T. Electrolyte influence on ignition of plasma electrolytic oxidation processes on light metals. *Surf. Coatings Technol.* **2017**, 315, 205–213.
(50) Martin, J.; Melhem, A.; Shchedrina, I. et al. Effects of electrical parameters on plasma electrolytic oxidation of aluminium. *Surf. Coatings Technol.* **2013**, 221, 70–76.
(51) Rokosz, K.; Hryniewicz, T.; Raaen, S.; Chapon, P.; Dudek, Ł. GDOES, XPS, and SEM with EDS analysis of porous coatings obtained on titanium after plasma electrolytic oxidation. *Surf. Interface Anal.* **2017**, 49, 303–315.
(52) Jiang, BL.; Wang, YM. Plasma electrolytic oxidation treatment of aluminium and titanium alloys. *Surf. Eng. Light Alloy. Alum. Magnes. Titan. Alloy.* **2010**,, 110–154.
(53) Jiang, BL.; Ge, YF. Micro-arc oxidation (MAO) to improve the corrosion resistance of magnesium (Mg) alloys. In: Corrosion Prevention of Magnesium Alloys: A volume in Woodhead Publishing Series in Metals and Surface Engineering. 2013 doi:10.1533/9780857098962.2.163
(54) Hung, JC.; Ku, CY.; Fan, ZW. Fabrication of an Electrode Insulated by Using Hot Dip Aluminizing and Micro-arc Oxidation Method for Electrochemical Microhole Machining. *Procedia CIRP*. **2018**, 68, 438–443.
(55) Diamanti, M V.; Pedeferri, MP. Effect of anodic oxidation parameters on the titanium oxides formation. *Corros. Sci.* **2007**, 49, 939–948.
(56) Mizukoshi, Y.; Ohtsu, N.; Masahashi, N. Structural and characteristic variation of anodic oxide on pure Ti with anodization duration. *Appl. Surf. Sci.* **2013**, 283, 1018–1023.
(57) Karambakhsh, A.; Afshar, A.; Ghahramani, S.; Malekinejad, P. Pure commercial titanium color anodizing and corrosion resistance. *J. Mater. Eng. Perform.* **2011**, 20, 1690–1696.
(58) Diamanti, MV.; Ormellese, M.; Pedeferri, MP. Application-wise nanostructuring of anodic films on titanium: a review. *J. Exp. Nanosci.* **2015**, 10, 1285–1308.
(59) Saraswati, WC.; Anawati, A.; Jujur, IN.; Gumelar, MD. Effect of coloring by anodizing on the corrosion behavior of Ti-6Al-4V alloy. *AIP Conf. Proc.* **2020**, 2232. doi:10.1063/5.0001483
(60) Prando, D.; Brenna, A.; Bolzoni, FM.; Diamanti, M V.; Pedeferri, M.; Ormellese, M. Electrochemical anodizing treatment to enhance localized corrosion resistance of pure titanium. *J. Appl. Biomater. Funct. Mater.* **2017**, 15, e19–e24.

(61) Karambakhsh, A.; Afshar, A.; Malekinejad, P. Corrosion resistance and color properties of anodized Ti-6Al-4V. *J. Mater. Eng. Perform.* **2012**, 21, 121–127.
(62) Kahar, SD.; Macwan, A.; Oza, R.; Oza, V.; Shah, S. Characterization and Corrosion Study of Titanium Anodized Film Developed in KOH Bath. *J. Eng. Res. Appl. www.ijera.com*. **2013**, 3, 441–445.
(63) Aliofkhazraei, M.; Macdonald, DD.; Matykina, E. et al. Review of plasma electrolytic oxidation of titanium substrates: Mechanism, properties, applications and limitations. *Appl. Surf. Sci. Adv.* **2021**, 5, 100121.
(64) Clyne, TW.; Troughton, SC. A review of recent work on discharge characteristics during plasma electrolytic oxidation of various metals. *Int. Mater. Rev.* **2019**, 64, 127–162.
(65) Jeffes, JHE. Ellingham Diagrams. In: Encyclopedia of Materials: Science and Technology. 2001 doi:10.1016/b0-08-043152-6/00490-3
(66) Klapkiv, MD. Simulation of synthesis of oxide-ceramic coatings in discharge channels of a metal-electrolyte system. *Mater. Sci.* **1999**, 35, 279–283.
(67) Sundararajan, G.; Rama Krishna, L. Mechanisms underlying the formation of thick alumina coatings through the MAO coating technology. *Surf. Coatings Technol.* **2003**, 167, 269–277.
(68) Dehnavi, V.; Luan, BL.; Shoesmith, DW.; Liu, XY.; Rohani, S. Effect of duty cycle and applied current frequency on plasma electrolytic oxidation (PEO) coating growth behavior. *Surf. Coatings Technol.* **2013**, 226, 100–107.
(69) Yerokhin, AL.; Lyubimov, V V.; Ashitkov, R V. Phase formation in ceramic coatings during plasma electrolytic oxidation of aluminium alloys. *Ceram. Int.* **1998**, 24, 1–6.
(70) Matykina, E.; Arrabal, R.; Scurr, DJ.; Baron, A.; Skeldon, P.; Thompson, GE. Investigation of the mechanism of plasma electrolytic oxidation of aluminium using 18O tracer. *Corros. Sci.* **2010**, 52, 1070–1076.
(71) Hussein, R. O.; Nie, X.; Northwood, D. O.; Yerokhin, A.; Matthews, A. Spectroscopic study of electrolytic plasma and discharging behaviour during the plasma electrolytic oxidation (PEO) process. *J. Phys. D. Appl. Phys.* **2010**, 43. doi:10.1088/0022-3727/43/10/105203
(72) Hussein, R. O.; Nie, X.; Northwood, D. O. An investigation of ceramic coating growth mechanisms in plasma electrolytic oxidation (PEO) processing. *Electrochim. Acta*. **2013**, 112, 111–119.
(73) Jovović, J.; Stojadinović, S.; Šišović, NM.; Konjević, N. Spectroscopic characterization of plasma during electrolytic oxidation (PEO) of aluminium. *Surf. Coatings Technol.* **Published Online First: 2011**. doi:10.1016/j.surfcoat.2011.06.031
(74) Cheng, YL.; Xue, ZG.; Wang, Q. et al. New findings on properties of plasma electrolytic oxidation Coatings from study of an Al-Cu-Li alloy. *Electrochim. Acta*. **2013**, 107, 358–378.
(75) Wang, Y.; Tang, H.; Wang, R.; Tan, Y.; Zhang, H.; Peng, S. Cathodic voltage-dependent composition, microstructure and corrosion resistance of plasma electrolytic oxidation coatings formed on Zr-4 alloy. *RSC Adv.* **2016**, 6, 34616–34624.
(76) Su, P.; Wu, X.; Jiang, Z.; Guo, Y. Effects of working frequency on the structure and corrosion resistance of plasma electrolytic oxidation coatings formed on a ZK60 Mg alloy. *Int. J. Appl. Ceram. Technol.* **2011**, 8, 112–119.
(77) Salami, B.; Afshar, A.; Mazaheri, A. The effect of sodium silicate concentration on microstructure and corrosion properties of MAO-coated magnesium alloy AZ31 in simulated body fluid. *J. Magnes. Alloy.* **2014**, 2, 72–77.
(78) Asoh, H.; Asakura, K.; Hashimoto, H. Effect of alcohol addition on the structure and corrosion resistance of plasma electrolytic oxidation films formed on AZ31B magnesium alloy. *RSC Adv.* **2020**, 10, 9026–9036.
(79) Shokouhfar, M.; Dehghanian, C.; Montazeri, M.; Baradaran, A. Preparation of ceramic coating on Ti substrate by plasma electrolytic oxidation in different electrolytes and evaluation of its corrosion resistance: Part II. *Appl. Surf. Sci.* **2012**, 258, 2416–2423.

(80) Hussain, T.; Kaseem, M.; Ko, YG. Hard acid–hard base interactions responsible for densification of alumina layer for superior electrochemical performance. *Corros. Sci.* **2020**, 170, 108663.
(81) Tomashov, ND. Studies on the mechanism of the electrochemical corrosion of titanium. III. *Zhur. Fiz. Khim*. **1961**, 35, 1068–1077.
(82) Brubaker, SK. Corrosion: Environments and Industries. In: ASM International. Ohio, 2018, 659.
(83) Beretta, S.; Diamanti, MV.; Pedeferri, M. et al. Corrosion of titanium: Part 1: aggressive environments and main forms of degradation. *J. Appl. Biomater. Funct. Mater.* **2017**, 15, 0–0.
(84) Nair, RB.; Kabir, MM.; Lennartsson, PR.; Taherzadeh, MJ.; Horváth, IS. Integrated Process for Ethanol, Biogas, and Edible Filamentous Fungi-Based Animal Feed Production from Dilute Phosphoric Acid-Pretreated Wheat Straw. *Appl. Biochem. Biotechnol.* **2018**, 184, 48–62.
(85) Jalil, MJ.; Ahmad, AH.; Azmi, IS. Recovery of gold in solution from electronic waste by di(2-ethylhexyl) phosphoric acid. *AIP Conf. Proc.* **2018**, 2030. doi:10.1063/1.5066830
(86) LU, J shu. Corrosion of titanium in phosphoric acid at 250 °C. *Trans. Nonferrous Met. Soc. China (English Ed.* **2009**, 19, 552–556.
(87) Yoshikubo, K.; Suzuki, M. Sulfamic Acid and Sulfamates. In: Kirk-Othmer Encyclopedia of Chemical Technology. 2004 doi:10.1002/0471238961.1921120625151908.a01
(88) Wahl, R.; Kallee, E. Oxalic Acid in Saliva, Teeth and Tooth Tartar. *Clin. Chem. Lab. Med.* **1994**, 32, 821–826.
(89) ASTM Standards: G31-72. *Annu. B. ASTM Stand.* **2012**, 72, 1–8.
(90) ASTM G-1, Standard Practice for Preparing , Cleaning , and Evaluating Corrosion Test Specimens. *Significance*. **1999**, 90, 1–9.
(91) ASTM G5 Standard Reference Test Method for Making Potentiodynamic Anodic Polarization Measurements. *Annu. B. ASTM Stand.* **Published Online First: 2014**. doi:10.1520/G0005-13E02.2
(92) Vaughan, J.; Alfantazi, A. Corrosion of Titanium and Its Alloys in Sulfuric Acid in the Presence of Chlorides. *J. Electrochem. Soc.* **2005**, 153, B6.
(93) Beukenkamp, J.; Herrington, KD. Ion-Exchange Investigation of the Nature of Iron (II) in Sulfuric and Perchloric Acid. *J. Am. Chem. Soc.* **1960**, 82, 3022–3025.
(94) Bazeleva, NA. Influence of oxalic acid on the corrosion of VT1-0 titanium in a water-ethylene-glycol heat carrier. *Mater. Sci.* **2006**, 42, 691–697.
(95) Fekry, AM. The influence of chloride and sulphate ions on the corrosion behavior of Ti and Ti-6Al-4V alloy in oxalic acid. *Electrochim. Acta*. **2009**, 54, 3480–3489.
(96) Brossia, CS.; Cragnolino, GA. Effect of palladium on the corrosion behavior of titanium. *Corros. Sci.* **2004**, 46, 1693–1711.
(97) Pedeferri, P. *Corrosion Science and Engineering*. Engineerin. Milan: Springer, 2018 doi:10.1007/978-3-319-97625-9_1
(98) Rodríguez, MA.; Carranza, RM. Properties of the Passive Film on Alloy 22 in Chloride Solutions Obtained by Electrochemical Impedance. *J. Electrochem. Soc.* **2011**, 158, C221.
(99) Brug, G. J.; Van den Eeden, A. L. G.; Sluyters-Rehbach, M.; Sluyters, J. H. The analysis of electrode impedances complicated by the presence of a constant phase element. *J. Electroanal. Chem.* **1984**, 176, 275–295.
(100) Levi, M. D.; Lu, Z.; Aurbach, D. Application of finite-diffusion models for the interpretation of chronoamperometric and electrochemical impedance responses of thin lithium insertion V2O5 electrodes. *Solid State Ionics*. **2001**, 143, 309–318.
(101) Mortazavi, G.; Jiang, J.; Meletis, EI. Investigation of the plasma electrolytic oxidation mechanism of titanium. *Appl. Surf. Sci.* **Published Online First: 2019**. doi:10.1016/j.apsusc.2019.05.250

(102) Ao, N.; Liu, D.; Zhang, X.; Liu, C. Enhanced fatigue performance of modified plasma electrolytic oxidation coated Ti-6Al-4V alloy: Effect of residual stress and gradient nanostructure. *Appl. Surf. Sci.* **2019**, 489, 595–607.
(103) Chung, CJ.; Su, RT.; Chu, HJ.; Chen, H Te.; Tsou, HK.; He, JL. Plasma electrolytic oxidation of titanium and improvement in osseointegration. *J. Biomed. Mater. Res. - Part B Appl. Biomater.* **2013**, 101B, 1023–1030.
(104) Yao, Z.; Jiang, Y.; Jia, F.; Jiang, Z.; Wang, F. Growth characteristics of plasma electrolytic oxidation ceramic coatings on Ti-6Al-4V alloy. *Appl. Surf. Sci.* **2008**, 254, 4084–4091.
(105) Lim, SG.; Choe, HC. Bioactive apatite formation on PEO-treated Ti-6Al-4V alloy after 3rd anodic titanium oxidation. *Appl. Surf. Sci.* **2019**, 484, 365–373.
(106) Casanova, L.; Pedeferri, MP.; Diamanti, M V. et al. Effetto della frequenza di anodizzazione e della polarizzazione catodica sulla resistenza a corrosione del titanio CP Study of evolution of microstructure and mechanical properties of high silicon austempered steel. **Published Online First: 2021**. doi:10.1002/srin.200405831.Di
(107) Bleck, W.; Bonollo, F.; Buchmayr, B.; Mariano, E. Metallurgia. **2021**.
(108) Casanova, L.; Padula, M La.; Pedeferri, M.; Diamanti, MV.; Ormellese, M. An insight into the evolution of corrosion resistant coatings on titanium during bipolar plasma electrolytic oxidation in sulfuric acid. *Electrochim. Acta*. **2021**, 379, 138190.
(109) Tang, Y.; Zhao, X.; Jiang, K.; Chen, J.; Zuo, Y. The influences of duty cycle on the bonding strength of AZ31B magnesium alloy by microarc oxidation treatment. *Surf. Coatings Technol.* **2010**, 205, 1789–1792.
(110) Diamanti, M V.; Del Curto, B.; Masconale, V.; Passaro, C.; Pedeferri, MP. Anodic coloring of titanium and its alloy for jewels production. *Color Res. Appl.* **2012**, 37, 384–390.
(111) Prando, D.; Brenna, A.; Diamanti, MV.; Pedeferri, M.; Ormellese, M. Electrochemical anodizing treatment to improve the corrosion resistance of commercially pure titanium. *Metall. Ital.* **2016**.
(112) Prando, D.; Brenna, A.; Pedeferri, MP.; Ormellese, M. Enhancement of pure titanium localized corrosion resistance by anodic oxidation. *Mater. Corros.* **2018**, 69, 503–509.
(113) Diamanti, M V.; Spreafico, FC.; Pedeferri, MP. Production of anodic TiO2 nanofilms and their characterization. *Phys. Procedia*. **2013**, 40, 30–37.
(114) Kuromoto, NK.; Simão, RA.; Soares, GA. Titanium oxide films produced on commercially pure titanium by anodic oxidation with different voltages. *Mater. Charact.* **2007**, 58, 114–121.
(115) Sobolev, A.; Kossenko, A.; Zinigrad, M.; Borodianskiy, K. An investigation of oxide coating synthesized on an aluminum alloy by plasma electrolytic oxidation in molten salt. *Appl. Sci.* **2017**, 7, 889.
(116) Torres-Cerón, D. A.; Gordillo-Delgado, F.; Moya-Betancourt, S. N. Effect of the voltage pulse frequency on the structure of TiO2 coatings grown by plasma electrolytic oxidation. *J. Phys. Conf. Ser.* **2017**, 935. doi:10.1088/1742-6596/935/1/012067
(117) Williamson, RS.; Disegi, J.; Janorkar, A V.; Griggs, JA.; Roach, MD. Effect of duty cycle on the crystallinity, pore size, surface roughness and corrosion resistance of the anodized surface on titanium. *Surf. Coatings Technol.* **2015**, 277, 278–288.
(118) Barati Darband, G.; Aliofkhazraei, M.; Hamghalam, P.; Valizade, N. Plasma electrolytic oxidation of magnesium and its alloys: Mechanism, properties and applications. *J. Magnes. Alloy.* **2017**, 5, 74–132.
(119) S. Uttiya, D. Contarino, S. Prandi, M.M. Carnasciali, G. Gemme, L. Mattera, R. Rolandi, M. Canepa, OC. Anodic Oxidation of Titanium in Sulphuric Acid and Phosphoric Acid Electrolytes. *J. Mater. Sci. Nanotechnol.* **2014**, 1. doi:10.15744/2348-9812.1.s106
(120) Engelkamp, B.; Fischer, B.; Schierbaum, K. Plasma electrolytic oxidation of titanium in H2SO4-H3PO4 Mixtures. *Coatings*. **2020**, 10, 1–11.
(121) Ittah, R.; Malka, I.; Bar, I.; Itzhak, D. Pitting corrosion evaluation of titanium in NaBr

solutions by electrochemical methods and Raman spectroscopy. *Int. J. Electrochem. Sci.* **2015**, 10, 1326–1342.
(122) Prando, D.; Brenna, A.; Diamanti, M. V. et al. Corrosion of titanium: Part 2: Effects of surface treatments. J. Appl. Biomater. Funct. Mater. . **2018**. doi:10.5301/jabfm.5000396
(123) Britain, G.; Press, P. Corrosion Science,. *Corros. Sci.* **1990**, 31, 281–286.
(124) Prando, D.; Nicolis, D.; Pedeferri, M.; Ormellese, M. Pitting corrosion on anodized titanium: Effect of halides. *Mater. Corros.* **2018**, 69, 1441–1446.
(125) The Materials Information Society, Vol 13A - Corrosion: Fundamentals, testing, and protection. *ASM Handb.* **2003**,, 2597.
(126) Scanlon, DO.; Dunnill, CW.; Buckeridge, J. et al. Band alignment of rutile and anatase TiO2. *Nat. Mater.* **2013**, 9, 798–801.
(127) Ohtsuka, T.; Otsuki, T. The aging of the anodic oxide of titanium during potentiostatic condition by ellipsometry. *Corros. Sci.* **2003**, 45, 1793–1801.
(128) Garsivaz Jazi, MR.; Golozar, MA.; Raeissi, K.; Fazel, M. Surface characteristics and electrochemical impedance investigation of spark-anodized Ti-6Al-4V alloy. *J. Mater. Eng. Perform.* **2014**, 23, 1270–1278.
(129) Cotton, J. B. Pitting corrosion of titanium. *Br. Corros. J.* **1972**, 7, 59–60.
(130) Zou, B.; Lü, GH.; Zhang, GL.; Tian, YY. Effect of current frequency on properties of coating formed by microarc oxidation on AZ91D magnesium alloy. *Trans. Nonferrous Met. Soc. China (English Ed.* **2015**, 25, 1500–1505.
(131) Hwang, IJ.; Hwang, DY.; Ko, YG.; Shin, DH. Correlation between current frequency and electrochemical properties of Mg alloy coated by micro arc oxidation. *Surf. Coatings Technol.* **2012**, 206, 3360–3365.
(132) Erfanifar, E.; Aliofkhazraei, M.; Nabavi, HF.; Rouhaghdam, AS. Growth kinetics and morphology of microarc oxidation coating on titanium. *Surf. Coatings Technol.* **2017**, 315, 567–576.
(133) Rakoch, A. G.; Khokhlov, V. V.; Bautin, V. A.; Lebedeva, N. A.; Magurova, Y. V.; Bardin, I. V. Model concepts on the mechanism of microarc oxidation of metal materials and the control over this process. *Prot. Met.* **2006**, 42, 158–169.
(134) Nominé, A.; Troughton, SC.; Nominé, A V.; Henrion, G.; Clyne, TW. High speed video evidence for localised discharge cascades during plasma electrolytic oxidation. *Surf. Coatings Technol.* **2015**, 269, 125–130.
(135) Lima, RN de.; Vitoriano, J de O.; Ferreira Jr, M.; Alves Junior, C. Plasma Species and Coating Compositions in Aluminum Treated by PEO Using Shot Square Pulse. *Mater. Res.* **2020**, 23. doi:10.1590/1980-5373-mr-2019-0444
(136) Aliasghari, S.; Skeleton, P.; Thompson, GE. Plasma electrolytic oxidation of titanium in a phosphate/silicate electrolyte and tribological performance of the coatings. *Appl. Surf. Sci.* **2014**, 316, 463–476.
(137) Kamil, M. P.; Kaseem, M.; Ko, Y. G. Soft plasma electrolysis with complex ions for optimizing electrochemical performance. *Nature*. **2017**, 7, 1–15.
(138) Pourbaix, M. *Atlas of electrochemical equilibria in aqueous solutions*. 1974
(139) Li, Z.; Gan, F.; Mao, X. A study on cathodic protection against crevice corrosion in dilute NaCl solutions. *Corros. Sci.* **2002**, 44, 689–701.
(140) Chin, DT. Current distribution and electrochemical environment in a cathodically protected crevice. *Corrosion*. **1999**, 55, 229–237.
(141) Chen, X.; Li, XG.; Du, CW.; Cheng, YF. Effect of cathodic protection on corrosion of pipeline steel under disbonded coating. *Corros. Sci.* **2009**, 51, 2242–2245.
(142) Li, M.; Jin, ZX.; Zhang, W. et al. Comparison of chemical stability and corrosion resistance of group IV metal oxide films formed by thermal and plasma-enhanced atomic layer deposition. *Sci. Rep.* **2019**, 9, 1–12.

(143) Torresi, RM.; Cámara, OR.; De Pauli, CP. Influence of the hydrogen evolution reaction on the anodic titanium oxide film properties. *Electrochim. Acta*. **1987**, 32, 1357–1363.
(144) Contu, F. The cathodic behavior of titanium: Serum effect. *J. Biomed. Mater. Res. - Part B Appl. Biomater.* **2012**, 100 B, 544–552.
(145) Thomas, N. T.; Nobe, K. Kinetics of the Hydrogen Evolution Reaction on Titanium. *J. Electrochem. Soc.* **1970**, 117, 622–626.
(146) Nominé, A.; Nominé, A V.; Braithwaite, N. S. J.; Belmonte, T.; Henrion, G. High-Frequency-Induced Cathodic Breakdown during Plasma Electrolytic Oxidation. *Phys. Rev. Appl.* **2017**, 8. doi:10.1103/PhysRevApplied.8.031001
(147) Troughton, S. C.; Clyne, T. W. Cathodic discharges during high frequency plasma electrolytic oxidation. *Surf. Coatings Technol.* **2018**, 352, 591–599.
(148) Ishino, M.; Hashimoto, H.; Asoh, H. Effect of Cathodic Current on the Structural Features of Oxide Films formed by AC Anodization of Aluminum. *J. Electrochem. Soc.* **2017**, 164, C939–C944.
(149) Takahashi, H.; Fujiwara, K.; Seo, M. The cathodic polarization of aluminum covered with anodic oxide films in a neutral borate solution-II. Film breakdown and pit formation. *Corros. Sci.* **1994**, 36, 689–705.
(150) Yao, Z.; Liu, Y.; Xu, Y.; Jiang, Z.; Wang, F. Effects of cathode pulse at high frequency on structure and composition of Al2TiO5 ceramic coatings on Ti alloy by plasma electrolytic oxidation. *Mater. Chem. Phys.* **2011**, 126, 227–231.
(151) Diamanti, M. V.; Bolzoni, F.; Ormellese, M.; Pérez-Rosales, E. A.; Pedeferri, M. Characterisation of titanium oxide films by potentiodynamic polarisation and electrochemical impedance spectroscopy. *Corros. Eng. Sci. Technol.* **2010**, 45, 428–434.
(152) Devilliers, D.; Dinh, MT.; Mahé, E.; Krulic, D.; Larabi, N.; Fatouros, N. Behaviour of titanium in sulphuric acid - Application to DSAs. *J. New Mater. Electrochem. Syst.* **2006**, 9, 221–232.
(153) Gnedenkov, S. V.; Sinebryukhov, S. L. Electrochemical impedance spectroscopy of oxide layers on the titanium surface. *Russ. J. Electrochem.* **2005**, 41, 963–971.
(154) Delgado, D.; Minakshi, M.; Kim, D. J. Electrochemical impedance spectroscopy studies on hydrogen evolution from porous raney cobalt in alkaline solution. *Int. J. Electrochem. Sci.* **2015**, 10, 9379–9394.
(155) Thomas, N. T.; Nobe, K. Electrochemical Behavior of Titanium. *J. Electrochem. Soc.* **1972**, 119, 1450.
(156) Liu, W.; Yang, J.; Qiu, Y.; Liu, Y.; Deng, K. Titanium carbide's effects on coatings formed on D16T aluminum alloy by plasma electrolytic oxidation. *Anti-Corros Method M*. **2020**, 67, 48–58.
(157) Abdulraheem, YM.; Ghoraishi, S.; Arockia-Thai, L.; Zachariah, SK.; Ghannam, M. The effect of annealing on the structural and optical properties of titanium dioxide films deposited by electron beam assisted PVD. *Adv. Mater. Sci. Eng.* **2013**, 2013. doi:10.1155/2013/574738
(158) Zhou, B.; Jiang, X.; Liu, Z.; Shen, R.; Rogachev, A V. Preparation and characterization of TiO2 thin film by thermal oxidation of sputtered Ti film. *Mater. Sci. Semicond. Process.* **2013**, 16, 513–519.
(159) Hussein, R. O.; Nie, X.; Northwood, D. O.; Yerokhin, A.; Matthews, A. Spectroscopic study of electrolytic plasma and discharging behaviour during the plasma electrolytic oxidation (PEO) process. *J. Phys. D. Appl. Phys.* **2010**, 43. doi:10.1088/0022-3727/43/10/105203
(160) Rogov, A. B.; Yerokhin, A.; Matthews, A. The Role of Cathodic Current in Plasma Electrolytic Oxidation of Aluminum: Phenomenological Concepts of the 'soft Sparking' Mode. *Langmuir*. **2017**, 33, 11059–11069.
(161) Hakimizad, A.; Raeissi, K.; Golozar, M. A.; Lu, X.; Blawert, C.; Zheludkevich, M. L. Influence of cathodic duty cycle on the properties of tungsten containing Al2O3/TiO2 PEO nano-composite coatings. *Surf. Coatings Technol.* **2018**, 340, 210–221.

(162) Tsai, D. S.; Chou, C. C. Review of the soft sparking issues in plasma electrolytic oxidation. *Metals (Basel).* **2018**, 8, 1–22.
(163) Tsai, D. S.; Chen, G. W.; Chou, C. C. Probe the micro arc softening phenomenon with pulse transient analysis in plasma electrolytic oxidation. *Surf. Coatings Technol.* **2019**, 357, 235–243.
(164) Xiao, W.; Cao, P.; Liang, Q. N. et al. Adsorption behavior and mechanism of Bi(III) ions on rutile–water interface in the presence of nonyl hydroxamic acid. *Trans. Nonferrous Met. Soc. China*. **2018**, 28, 348–355.
(165) Kosmulski, M. Isoelectric points and points of zero charge of metal (hydr)oxides: 50 years after Parks' review. *Adv. Colloid Interface Sci.* **2016**, 238, 1–61.
(166) Parks, G. A. The isoelectric points of solid oxides, solid hydroxides, and aqueous hydroxo complex systems. *New Zeal. Entomol.* **1964**,, 177–195.
(167) Budarz, J. F.; Turolla, A.; Piasecki, A. F. et al. Influence of Aqueous Inorganic Anions on the Reactivity of Nanoparticles in TiO2 Photocatalysis. **2019**, 33, 2770–2779.
(168) Babauta, J. T.; Medina, A.; Beyenal, H. EQCM and Surface pH Studies on Lanthanum Accumulation on Electrodes in Aqueous Solution. *J. Electrochem. Soc.* **2016**, 163, H866–H870.
(169) Nominé, A.; Martin, J.; Noël, C. et al. Surface Charge at the Oxide/Electrolyte Interface: Toward Optimization of Electrolyte Composition for Treatment of Aluminum and Magnesium by Plasma Electrolytic Oxidation. *Langmuir*. **2016**, 32, 1405–1409.
(170) Arifuku, F.; Yoneyama, H.; Tamura, H. The behavior of incorporated impurities in tantalum anodic oxide films at the dielectric breakdown. *Electrochim. Acta*. **Published Online First: 1980**. doi:10.1016/0013-4686(80)90039-0
(171) Jaeggi, C.; Kern, P.; Michler, J.; Patscheider, J.; Tharian, J.; Munnik, F. Film formation and characterization of anodic oxides on titanium for biomedical applications. *Surf. Interface Anal.* **2006**,, 182–185.
(172) Rogov, AB.; Shayapov, VR. The role of cathodic current in PEO of aluminum: Influence of cationic electrolyte composition on the transient current-voltage curves and the discharges optical emission spectra. *Appl. Surf. Sci.* **2017**, 394, 323–332.
(173) Mazzarolo, A.; Curioni, M.; Vicenzo, A.; Skeldon, P.; Thompson, G. E. Anodic growth of titanium oxide: Electrochemical behaviour and morphological evolution. *Electrochim. Acta*. **2012**, 75, 288–295.
(174) Lukes, P.; Clupek, M.; Babicky, V.; Sunka, P. The role of surface chemistry at ceramic/electrolyte interfaces in the generation of pulsed corona discharges in water using porous ceramic-coated rod electrodes. *Plasma Process. Polym.* **2009**, 6, 719–728.
(175) Atkins, P.; Paula, J De. Atkins' Physical chemistry 8th edition. Chemistry (Easton). . **2009**. doi:10.1021/ed056pA260.1
(176) Rogov, A. B.; Yerokhin, A.; Matthews, A. The Role of Cathodic Current in Plasma Electrolytic Oxidation of Aluminum: Phenomenological Concepts of the 'soft Sparking' Mode. *Langmuir*. **2017**, 33, 11059–11069.
(177) E. J. Bockris,; E. B. Conway, Modern aspects of electrochemistry, n 6. doi:10.1524/zpch.1999.213.part_2.216
(178) Gudla, VC.; Bordo, K.; Jensen, F. et al. High frequency anodising of aluminium-TiO2 surface composites: Anodising behaviour and optical appearance. *Surf. Coatings Technol.* **2015**, 277, 67–73.
(179) Bononi, M.; Giovanardi, R.; Bozza, A. Pulsed current hard anodizing of heat treated aluminum alloys: Frequency and current amplitude influence. *Surf. Coatings Technol.* **2016**, 307, 861–870.
(180) Martin, J.; Nominé, A.; Brochard, F. et al. Delay in micro-discharges appearance during PEO of Al: Evidence of a mechanism of charge accumulation at the electrolyte/oxide interface.

Appl. Surf. Sci. **2017**, 410, 29–41.
(181) Geebarowski, W.; Pietrzyk, S. Influence of the cathodic pulse on the formation and morphology of oxide coatings on aluminium produced by plasma electrolytic oxidation. *Arch. Metall. Mater.* **2013**, 58, 241–245.
(182) Jaspard-Mécuson, F.; Czerwiec, T.; Henrion, G. et al. Tailored aluminium oxide layers by bipolar current adjustment in the Plasma Electrolytic Oxidation (PEO) process. *Surf. Coatings Technol.* **2007**, 201, 8677–8682.
(183) Gębarowski, W.; Pietrzyk, S. Growth characteristics of the oxide layer on aluminium in the process of plasma electrolytic oxidation. *Arch. Metall. Mater.* **2014**, 59, 407–411.
(184) Xin, S.; Song, L.; Zhao, R.; Hu, X. Influence of cathodic current on composition, structure and properties of Al2O3 coatings on aluminum alloy prepared by micro-arc oxidation process. *Thin Solid Films*. **2006**, 515, 326–332.
(185) Cotte, JM.; Fairfield, N.; Us, NY.; Stein, KJ.; Hook, S.; Us, CT. (12) United States Patent. **2006**, 2.
(186) Timoshenko, AV.; Magurova, YV. Application of oxide coatings to metals in electrolyte solutions by microplasma methods. *Rev. Metal.* **2000**, 36, 323–330.
(187) Spurr, RA.; Myers, H. Quantitative Analysis of Anatase-Rutile Mixtures with an X-Ray Diffractometer. *Anal. Chem.* **1957**, 29, 760–762.
(188) Harrington, D. A.; Conway, B. E. ac Impedance of Faradaic reactions involving electrosorbed intermediates-I. Kinetic theory. *Electrochim. Acta*. **1987**, 32, 1703–1712.
(189) Harrington, D. A. Electrochemical impedance of multistep mechanisms: Mechanisms with static species. *J. Electroanal. Chem.* **1998**, 449, 29–37.
(190) Conway, B. E.; White, R. E.; Plenum, K.; York, N.; Lasia, A. *"Applications of the Electrochemical Impedance Spectroscopy to Hydrogen Adsorption, Evolution and Absorption into Metals "*. 2002 doi:10.1007/0-306-47604-5
(191) Armstrong, R. D.; Edmondson, K. The impedance of metals in the passive and transpassive regions. *Electrochim. Acta*. **1973**, 18, 937–943.
(192) Lvovich, V. F. *Impedance Spectroscopy: Applications to Electrochemical and Dielectric Phenomena*. 2012 doi:10.1002/9781118164075
(193) Conwey, B. E. *Electrochemical Supercapacitors: Scientific Fundamentals and Technological Applications*. New York, 1999
(194) Lasia, A. Applications of Electrochemical Impedance Spectroscopy to Hydrogen Adsorption, Evolution and Absorption into Metals. In: Modern Aspects of Electrochemistry. 2005 doi:10.1007/0-306-47604-5_1
(195) Thomas, NT.; Nobe, K. The Electrochemical Behavior of Titanium. *J. Electrochem. Soc.* **1969**, 116, 1748.
(196) Kelly, E. J. Electrochemical Behaviour of Titanium. In: Modern Aspects of Electrochemistry. 1982, 557–639.
(197) Dubenko, A. V.; Nikolenko, M. V.; Aksenenko, E. V.; Kostyniuk, A.; Likozar, B. Mechanism, thermodynamics and kinetics of rutile leaching process by sulfuric acid reactions. *Processes*. **2020**, 8. doi:10.3390/pr8060640
(198) Casanova, L.; Arosio, M.; Taghi Hashemi, M.; Pedeferri, M.; Botton, GA.; Ormellese, M. A nanoscale investigation on the influence of anodization parameters during plasma electrolytic oxidation of titanium by high-resolution electron energy loss spectroscopy. *Appl. Surf. Sci.* **2021**, 570, 151133.
(199) Mortazavi, G.; Jiang, J.; Meletis, EI. Investigation of the plasma electrolytic oxidation mechanism of titanium. *Appl. Surf. Sci.* **2019**, 488, 370–382.
(200) Peña, F de la.; Prestat, E.; Fauske, VT. hyperspy/hyperspy: Release v1.6.2. **Published Online First: 13 April 2021**. doi:10.5281/ZENODO.4683076
(201) Puippe, JC. Influence of Charge and Discharge of Electrical Double Layer in Pulse Plating.

Theory Pr. Pulse Plat. **1986**, 10, 41–54.
(202) Mortazavi, G.; Jiang, J.; Meletis, EI. Investigation of the plasma electrolytic oxidation mechanism of titanium. *Appl. Surf. Sci.* **2019**, 488, 370–382.
(203) Abdallah, I.; Dupressoire, C.; Laffont, L.; Monceau, D.; Vande Put, A. STEM-EELS identification of TiO X N Y , TiN, Ti 2 N and O, N dissolution in the Ti2642S alloy oxidized in synthetic air at 650 °C. *Corros. Sci.* **2019**, 153, 191–199.
(204) Terada, S.; Asayama, K.; Tsujimoto, M.; Kurata, H.; Isoda, S. Chemical shift of electron energy-loss near-edge structure on the nitrogen K-edge and titanium L3-edge at TiN/Ti interface. *Microsc. Microanal.* **2009**, 15, 106–113.
(205) Stoyanov, E.; Langenhorst, F.; Steinle-Neumann, G. The effect of valence state and site geometry on Ti L 3,2 and O K electron energy-loss spectra of Ti x O y phases. *Am. Mineral.* **2007**, 92, 577–586.
(206) Cheynet, M.; Pokrant, S.; Irsen, S.; Krüger, P. New fine structures resolved at the ELNES Ti-L2,3 edge spectra of anatase and rutile: Comparison between experiment and calculation. *Ultramicroscopy*. **2010**, 110, 1046–1053.
(207) Radtke, G.; Lazar, S.; Botton, GA. High-resolution EELS investigation of the electronic structure of ilmenites. *Phys. Rev. B - Condens. Matter Mater. Phys.* **2006**, 74, 1–8.
(208) Radtke, G.; Maunders, C.; Lazar, S.; De Groot, FMF.; Etheridge, J.; Botton, GA. The role of Mn in the electronic structure of Ba3Ti 2MnO9. *J. Solid State Chem.* **2005**, 178, 3426–3430.
(209) Ohtomo, A.; Muller, DA.; Grazul, JL.; Hwang, HY. Artificial charge-modulation in atomic-scale perovskite titanate superlattices. *Nature*. **2002**, 419, 378–380.
(210) Muller, DA.; Nakagawa, N.; Ohtomo, A.; Grazul, JL.; Hwang, HY. Atomic-scale imaging of nanoengineered oxygen vacancy profiles in SrTiO3. *Nature*. **2004**, 430, 657–661.
(211) Lazar, S.; Botton, GA.; Wu, MY.; Tichelaar, FD.; Zandbergen, HW. Materials science applications of HREELS in near edge structure analysis and low-energy loss spectroscopy. *Ultramicroscopy*. **2003**, 96, 535–546.
(212) Heiliger, C.; Heyroth, F.; Syrowatka, F. et al. Orientation-dependent electron-energy-loss spectroscopy of Ti O2: A comparison of theory and experiment. *Phys. Rev. B - Condens. Matter Mater. Phys.* **2006**, 73. doi:10.1103/PhysRevB.73.045129
(213) Zhang, J.; Visinoiu, A.; Heyroth, F. et al. High-resolution electron energy-loss spectroscopy of BaTiO 3/SrTiO 3 multilayers. *Phys. Rev. B - Condens. Matter Mater. Phys.* **2005**, 71. doi:10.1103/PhysRevB.71.064108
(214) Gloter, A.; Ewels, C.; Umek, P.; Arcon, D.; Colliex, C. Electronic structure of titania-based nanotubes investigated by EELS spectroscopy. *Phys. Rev. B - Condens. Matter Mater. Phys.* **2009**, 80. doi:10.1103/PhysRevB.80.035413
(215) De Groot, FMF.; Fuggle, JC.; Thole, BT.; Sawatzky, GA. L2,3 x-ray-absorption edges of d0 compounds: K+, Ca2+, Sc3+, and Ti 4+ in Oh (octahedral) symmetry. *Phys. Rev. B Condens. Matter*. **1990**, 41, 928–937.
(216) Sefat, AS.; Amow, G.; Wu, MY.; Botton, GA.; Greedan, JE. High-resolution EELS study of the vacancy-doped metal/insulator system, Nd1-xTiO3, x = O to 033. *J. Solid State Chem.* **2005**, 178, 1008–1016.
(217) Li, Y.; Wang, Q.; An, M. et al. Nanoscale Chemical and Valence Evolution at the Metal/Oxide Interface: A Case Study of Ti/SrTiO3. *Adv. Mater. Interfaces*. **2016**, 3. doi:10.1002/admi.201600201
(218) Bertoni, G.; Beyers, E.; Verbeeck, J. et al. Quantification of crystalline and amorphous content in porous TiO2 samples from electron energy loss spectroscopy. *Ultramicroscopy*. **2006**, 106, 630–635.
(219) Tian, M. Structural characterizations of photo-catalytic titanium oxide nanoparticles made from amorphous building blocks. *" PhD diss. Univ. Tennessee*. **2015**.
(220) Calvert, CC.; Rainforth, WM.; Sinclair, DC.; West, AR. Characterisation of grain boundaries

in CaCu3Ti 4O12 using HREM, EDS and EELS. *J. Phys. Conf. Ser.* **2006**, 26, 65–68.
(221) Asadabad, MA.; Eskandari, MJ. electron diffraction. *Intech*. **2013**, 32, 137–144.
(222) Chen, B.; Lu, K. Influence of patterned concave depth and surface curvature on anodization of titania nanotubes and alumina nanopores. *Langmuir*. **2011**, 27, 12179–12185.
(223) Bickley, RI.; Gonzalez-Carreno, T.; Lees, JS.; Palmisano, L.; Tilley, RJD. A structural investigation of titanium dioxide photocatalysts. *J. Solid State Chem.* **1991**, 92, 178–190.
(224) Habazaki, H.; Shimizu, K.; Nagata, S.; Skeldon, P.; Thompson, GE.; Wood, GC. Ionic transport in amorphous anodic titania stabilised by incorporation of silicon species. *Corros. Sci.* **2002**, 44, 1047–1055.
(225) Habazaki, H.; Uozumi, M.; Konno, H.; Shimizu, K.; Skeldon, P.; Thompson, GE. Crystallization of anodic titania on titanium and its alloys. *Corros. Sci.* **2003**, 45, 2063–2073.
(226) Raj, V.; Rajaram, MP.; Balasubramanian, G.; Vincent, S.; Kanagaraj, D. Pulse anodizing - An overview. *Trans. Inst. Met. Finish.* **2003**, 81, 114–121.
(227) Torrescano-Alvarez, JM.; Curioni, M.; Skeldon, P. Effects of oxygen evolution on the voltage and film morphology during galvanostatic anodizing of AA 2024-T3 aluminium alloy in sulphuric acid at −2 and 24 °C. *Electrochim. Acta*. **2018**, 275, 172–181.
(228) Xiao, D. *Dielectric Strength of Atmosphere Air*. 2016 doi:10.1007/978-3-662-48041-0_6
(229) Rumble, JR. CRC Handbook of Chemistry and Physics, 101 Edition (Internet Version 2020). *CRC Press. Taylor Fr. Boca Rat. FL*. **2020**.
(230) Kramida, A., Ralchenko, Yu., Reader, J., and NAT (2020). NIST Atomic Spectra Database (ver. 5.8). **2020**. doi:https://doi.org/10.18434/T4W30F
(231) Stojadinović, S.; Vasilić, R.; Perić, M. Investigation of plasma electrolytic oxidation on valve metals by means of molecular spectroscopy-a review. *RSC Adv.* **2014**, 4, 25759–25789.
(232) Stojadinović, S.; Vasilić, R.; Petković, M. et al. Characterization of the plasma electrolytic oxidation of titanium in sodium metasilicate. *Appl. Surf. Sci.* **2013**, 265, 226–233.
(233) Shin, H.; De Guire, MR.; Heuer, AH. Electrical properties of TiO2 thin films formed on self-assembled organic monolayers on silicon. *J. Appl. Phys.* **1998**, 83, 3311–3317.
(234) Dunleavy, CS.; Golosnoy, IO.; Curran, JA.; Clyne, TW. Characterisation of discharge events during plasma electrolytic oxidation. *Surf. Coatings Technol.* **2009**, 203, 3410–3419.
(235) Kitamura, T.; Shibata, K.; Takeda, K. In-flight Reduction of Fe2O3, Cr2O3, TiO2 and Al2O3 by Ar-H2 and Ar-CH4 Plasma. *Isij Int.* **1994**, 33, 1150–1158.
(236) Bullard, DE.; Lynch, DC. Reduction of Titanium Dioxide in a Nonequilibrium Hydrogen Plasma. **1997**, 28, 1069–1080.
(237) Huet, S.; Belmonte, T.; Thiébaut, JM.; Bockel, S.; Michel, H. Reduction of TiO2 assisted by a microwave plasma at atmospheric pressure. *Thin Solid Films*. **2005**, 475, 63–67.
(238) Nowotny, J.; Radecka, M.; Rekas, M. Semiconducting properties of undoped TiO2. *J. Phys. Chem. Solids*. **1997**, 58, 927–937.
(239) Ali, S.; Orell, O.; Kanerva, M.; Hannula, SP. Effect of Morphology and Crystal Structure on the Thermal Conductivity of Titania Nanotubes. *Nanoscale Res. Lett.* **2018**, 13. doi:10.1186/s11671-018-2613-3
(240) Permanasari, AA.; Kuncara, BS.; Puspitasari, P.; Sukarni, S.; Ginta, TL.; Irdianto, W. Convective heat transfer characteristics of TiO2-EG nanofluid as coolant fluid in heat exchanger. *AIP Conf. Proc.* **2019**, 2120. doi:10.1063/1.5115691
(241) Bleck, W.; Bonollo, F.; Buchmayr, B.; Mariano, E. *Metallurgia*. 2021
(242) Briant, CL.; Wang, ZF.; Chollocoop, N. Hydrogen embrittlement of commercial purity titanium. *Corros. Sci.* **2002**, 44, 1875–1888.
(243) Andijani, IN.; Ahmad, S.; Malik, AU. Corrosion behavior of titanium metal in the presence of inhibited sulfuric acid at 50°C. *Desalination*. **2000**, 129, 45–51.
(244) Prando, D.; Brenna, A.; Diamanti, M. V. et al. Corrosion of titanium: Part 1: aggressive environments and main forms of degradation. *J. Appl. Biomater. Funct. Mater.* **2017**, 15.

doi:10.5301/jabfm.5000387
(245) Casanova, L.; Vicentini, L.; Pedeferri, M.; Ormellese, M. Unipolar plasma electrolytic oxidation: Waveform optimisation for corrosion resistance of commercially pure titanium. *Mater. Corros.* **Published Online First: 2020**. doi:10.1002/maco.202012198
(246) Casanova, L.; Gruarin, M.; Pedeferri, MP.; Ormellese, M. A comparison between corrosion performances of titanium grade 2 and 7 in strong reducing acids. *Mater. Corros.* **Published Online First: 2021**. doi:10.1002/maco.202112392
(247) Liu, Y.; Schaller, RF.; Asselin, E. Effect of Fe(III) and Cu(II) on the Passivation of Ti-2 in Acidic Chloride Solutions. *J. Electrochem. Soc.* **2019**, 166, C76–C82.
(248) Ohtsuka, T. Cathodic Reduction of Anodic Oxide Films Formed on Titanium. *J. Electrochem. Soc.* **1987**, 134, 2406.
(249) Hosseini, SMA.; Singh, VB. Active-passive behaviour of titanium and titanium alloy (VT-9) in sulphuric acid solution. *Mater. Chem. Phys.* **1993**, 33, 63–69.
(250) Blackwood, DJ.; Peter, LM.; Williams, DE. Stability and open circuit breakdown of the passive oxide film on titanium. *Electrochim. Acta*. **1988**, 33, 1143–1149.
(251) Blackwood, DJ.; Chooi, SKM. Stability of protective oxide films formed on a porous titanium. *Corros. Sci.* **2002**, 44, 395–405.
(252) Nabavi, HF.; Aliofkhazraei, M.; Rouhaghdam, AS. Electrical characteristics and discharge properties of hybrid plasma electrolytic oxidation on titanium. *J. Alloys Compd.* **2017**, 728, 464–475.
(253) Matykina, E.; Arrabal, R.; Skeldon, P.; Thompson, GE. Transmission electron microscopy of coatings formed by plasma electrolytic oxidation of titanium. *Acta Biomater.* **2009**, 5, 1356–1366.
(254) Friedemann, AER.; Gesing, TM.; Plagemann, P. Electrochemical rutile and anatase formation on PEO surfaces. *Surf. Coatings Technol.* **2017**, 315, 139–149.
(255) Tredici, IG.; Maglia, F.; Ferrara, C.; Mustarelli, P.; Anselmi-tamburini, U. Mechanism of Low-Temperature Protonic Conductivity in Bulk , High-Density , Nanometric Titanium Oxide. **2014**,, 5137–5146.
(256) Ren, R.; Wang, Z.; Meng, X. et al. Tailoring the Oxygen Vacancy to Achieve Fast Intrinsic Proton Transport in a Perovskite Cathode for Protonic Ceramic Fuel Cells. **Published Online First: 2020**. doi:10.1021/acsaem.0c00486
(257) Lin, Z.; Lin, S.; Tian, Y.; Bokkelen, A Van.; Valerio, M.; Gomez, MA. Oxygen Vacancies Altering the Trapping in the Proton Conduction Landscape of Doped Barium Zirconate. **Published Online First: 2020**. doi:10.1021/acs.jpcc.0c09461
(258) Meng, Y.; Gao, J.; Zhao, Z.; Amoroso, J.; Tong, J.; Brinkman, KS. Review : recent progress in low-temperature proton-conducting ceramics. *J. Mater. Sci.* **2019**, 54, 9291–9312.
(259) Sastri, VS. *Green Corrosion Inhibitors: Theory and Practice*. Singapore: Wiley, 2011 doi:10.1002/9781118015438
(260) Elabar, D.; Němcová, A.; Hashimoto, T.; Skeldon, P.; Thompson, GE. Effect of sulphate impurity in chromic acid anodizing of aluminium. *Corros. Sci.* **2015**, 100, 377–385.
(261) Makivić, N.; Cho, JY.; Harris, KD.; Tarascon, JM.; Limoges, B.; Balland, V. Evidence of Bulk Proton Insertion in Nanostructured Anatase and Amorphous TiO2Electrodes. *Chem. Mater.* **2021**, 33, 3436–3448.
(262) Kim, YS.; Kriegel, S.; Harris, KD.; Costentin, C.; Limoges, B.; Balland, V. Evidencing Fast, Massive, and Reversible H+ Insertion in Nanostructured TiO2 Electrodes at Neutral pH. Where Do Protons Come From? *J. Phys. Chem. C*. **2017**, 121, 10325–10335.
(263) Zeng, Y.; Noël, JJ.; Norton, PR.; Shoesmith, DW. Hydrogen transport through thin titanium oxides. *J. Electroanal. Chem.* **2010**, 649, 277–285.
(264) Motupally, S.; Streinz, CC.; Weidner, JW. Proton Diffusion in Nickel Hydroxide Films: Measurement of the Diffusion Coefficient as a Function of State of Charge. *J. Electrochem.*

Soc. **1995**, 142, 1401–1408.
(265) Hupfer, AJ.; Monakhov, E V.; Svensson, BG.; Chaplygin, I.; Lavrov, E V. Hydrogen motion in rutile TiO 2. *Sci. Rep.* **2017**,, 1–10.
(266) Yen, SK. Retardation effects of thermally grown oxide films on the hydrogen embrittlement of commercial pure titanium. *Corros. Sci.* **1999**, 41, 2031–2051.
(267) Tian, H.; Cui, X.; Zeng, L.; Su, L.; Song, Y.; Shi, J. Oxygen vacancy-assisted hydrogen evolution reaction of the Pt/WO3 electrocatalyst. *J. Mater. Chem. A.* **2019**, 7, 6285–6293.
(268) Dupont, MF.; Donne, SW. A Step Potential Electrochemical Spectroscopy Analysis of Electrochemical Capacitor Electrode Performance. *Electrochim. Acta*. **2015**, 167, 268–277.
(269) Hill, C. SciPy. In: Learning Scientific Programming with Python. 2020 doi:10.1017/9781108778039.009
(270) Li, Y.; Yu, ZG.; Wang, L. et al. Electronic-reconstruction-enhanced hydrogen evolution catalysis in oxide polymorphs. *Nat. Commun.* **2019**, 10. doi:10.1038/s41467-019-11124-w
(271) Swaminathan, J.; Subbiah, R.; Singaram, V. Defect-Rich Metallic Titania (TiO1.23) - An Efficient Hydrogen Evolution Catalyst for Electrochemical Water Splitting. *ACS Catal.* **2016**, 6, 2222–2229.
(272) Martynyuk, V.; Ortigueira, M.; Fedula, M.; Savenko, O. Fractional model of the electrochemical capacitor relaxation phenomenon. *Bull. Polish Acad. Sci. Tech. Sci.* **2018**, 66, 441–448.
(273) Losey, MW.; Kelly, JJ. *Electrodeposition*. 2007 doi:10.1016/B978-044452190-3.00010-0
(274) Boukamp, BA. A Linear Kronig-Kramers Transform Test for Immittance Data Validation. *J. Electrochem. Soc.* **1995**, 142, 1885–1894.
(275) Lasia, A. *Electrochemical impedance spectroscopy and its applications*. 2014 doi:10.1007/978-1-4614-8933-7